



**HAL**  
open science

## Contribution to the development of IDEAL-Cell, a new concept of intermediate temperature fuel cell

Joao Abreu

► **To cite this version:**

Joao Abreu. Contribution to the development of IDEAL-Cell, a new concept of intermediate temperature fuel cell. Materials. École Nationale Supérieure des Mines de Paris, 2011. English. NNT : 2011ENMP0093 . pastel-00711493

**HAL Id: pastel-00711493**

**<https://pastel.hal.science/pastel-00711493>**

Submitted on 25 Jun 2012

**HAL** is a multi-disciplinary open access archive for the deposit and dissemination of scientific research documents, whether they are published or not. The documents may come from teaching and research institutions in France or abroad, or from public or private research centers.

L'archive ouverte pluridisciplinaire **HAL**, est destinée au dépôt et à la diffusion de documents scientifiques de niveau recherche, publiés ou non, émanant des établissements d'enseignement et de recherche français ou étrangers, des laboratoires publics ou privés.

École doctorale n°432 :  
Sciences des Métiers de l'Ingénieur

## THÈSE

pour obtenir le grade de docteur délivré par

**l'École Nationale Supérieure des Mines de Paris**

**Spécialité « Sciences et Génie des Matériaux »**

*présentée et soutenue publiquement par*

**João ABREU**

le 5 Décembre 2011

**Contribution au développement d'IDEAL-Cell, un nouveau  
concept de pile à combustible à température intermédiaire**

**Contribution to the development of IDEAL-Cell,  
a new concept of intermediate temperature fuel cell**

Directeur de thèse : **Alain THOREL**

co-encadrement de thèse : **Anthony CHESNAUD**

### Jury

<b>Christian GUIZARD</b> , Directeur de recherche, Laboratoire de Synthèse et Fonctionnalisation des Céramiques, Saint-Gobain/CNRS	Président du jury
<b>Rose-Noëlle VANNIER</b> , Professeur, Ecole Nationale Supérieure de Chimie de Lille	Rapporteur
<b>Fabrice MAUVY</b> , Professeur, Université de Bordeaux	Rapporteur
<b>Daria VLADIKOVA</b> , Professeur, Bulgaria Academy of Sciences	Examineur
<b>Dominique JEULIN</b> , Directeur de recherche, Ecole Nationale Supérieure des Mines de Paris	Examineur
<b>Guilhem DEZANNEAU</b> , Chargé de recherche, Ecole Centrale de Paris	Examineur
<b>Anthony CHESNAUD</b> , Chargé de recherche, Ecole Nationale Supérieure des Mines de Paris	Examineur
<b>Alain THOREL</b> , Directeur de recherche, Ecole Nationale Supérieure des Mines de Paris	Examineur

**MINES ParisTech**

**Centre des Matériaux P. M. Fourt**

10, Rue Henri-Auguste Desbrières B.P.87, F-91003 Evry Cedex, France

*"That he not busy being born is busy dying"*  
*Robert Allen Zimmerman*

*"Por pretextos talvez fúteis,  
a alegria é o que nos torna os dias úteis"*  
*Sérgio Godinho*

## Acknowledgements

While writing this thesis I realized how many different people put their talent, passion and knowledge in it. As I realize how much I've grown during these last four years, I think about all these people I met and are now part of my life. As I leave to another destination far from the coast, I think of those who are always with me. In the deepest of the storms or below the bluest sky and over the bluest sea, my family.

I'd like to thank Esteban Busso and Georges Cailletaud, Directors of the Centre des Matériaux and the research unit UMR 7633, respectively, for giving me the opportunity of doing my PhD in the laboratory they supervise.

I want to thank Alain Thorel, my PhD advisor, first of all for giving me the chance to work on such a challenging project, in an international project and multidisciplinary environment. Thank you for trusting me and letting me doing the thesis I wanted to do. I learned a lot.

I would like to thank Mme Vannier and M. Mauvy for having accepted to be the reviewers of my thesis. Thank you for your comments and the fruitful discussions about this work. I want to thank M. Guizard for being president of the jury. I want to thank all the other members of the jury: M. Dezanneau for his always pertinent questions, M. Jeulin for his competence and brightness that I could witness during these years and Mme. Vladikova for her knowledge and for knowing how to share it with such grace and beauty.

I'd like to thank Anthony Chesnaud, scientific manager of the IDEAL-Cell project, who was in the office next door from the first to the last day.

As you'll notice by reading this text, this thesis wouldn't have been possible without the collaboration of many talented researchers: Zdravko Stoykov, Massimo Viviani, Antonio Barbucci, Asif Ansar, Zeynep Ilhan, Charles Peyrega, Mickael Palard, Alessio Bassano, Francesco Deloro, Denis Soysal, Gergana Raikova. I learned so much from you in so many different ways. Thank you for your brightness and your talent!

I want to thank Rémi Costa, former PhD student in our research group, for the good advices, for his scientific accuracy and for being my headlight showing me what was expecting me.

The daily trips to the canteen at noon wouldn't have been such a joy without my friends from hall C: Mohamed, Cécilie, Pierre, Morgane, Marie-Hélène, Régis. Thank you for the good mood, the interesting, serious, scientific or just silly discussions. Life at the laboratory was made so much easier with the help and daily good mood of the Centre des Matériaux administrative staff: Konaly Sar, Sarojinee Bonneville, Liliane Locicero and Catherine Rouil. Thank you!

I want to thank my football friends of every wednesdays, under the sun, rain or snow: one of the main reasons for my good integration and French speaking skills!

I would like to thank in particular my three musketeers: Nicolas Cordero, Angélique Consil and Bahram Sarbandi. Thank you for your friendship and the great parisian nights spent together. I hope we can keep in touch as time goes by. Nicolas Revuz, for the times you made me laugh, for your energy and creativity. Thank you for introducing me to the never ending process of learning how to play the guitar... without it I would probably have finished writing my thesis 3 months earlier!

A very special thank you to Thomas Vilaro, with who I shared the joy of the french "co-location" and the thrill of searching for an apartment in Paris being just a PhD student with a short-term contract.

To the one who one day put me on a train to Toulon to see an Elton John concert! The one who took me to a Cat Stevens concert! The one who hanged on beside me when the waves got bigger an the wind blowed stronger. The one who keeps showing me a new world every day through her eyes, Perrine Fréhaut. Away we go!

To those who are "the reason why I'm traveling on", my family. My grandfather Joaquim, who left me too soon. My grandmother Lurdes who used to tell me the greatest stories to sleep at night. To my father João, the strongest of all. To my beautiful mother Teresa for her brightness and determination. To my little sister Filipa, the beauty of a woman's strength. Thank you for understanding and supporting me in the choices I've made even if they kept us apart for a while.

To all of you who set sail and left the shoreline with me, the wind will keep taking us further. We're still at Cape Bojador! Let's go!





# Contents

<b>I</b>	<b>Introduction</b>	<b>1</b>
I.1	General context . . . . .	2
I.2	Fuel Cells . . . . .	5
I.2.1	General Overview . . . . .	5
I.2.2	Working principle of a fuel cell . . . . .	6
I.2.2.1	Theoretical Performance . . . . .	7
I.2.2.2	Actual Performance . . . . .	8
I.3	Solid Oxide Fuel Cell (SOFC) . . . . .	9
I.3.1	Advantages and Disadvantages . . . . .	10
I.4	Proton Ceramic Fuel Cell (PCFC) . . . . .	11
I.4.1	Advantages and Disadvantages . . . . .	12
I.5	IDEAL-Cell: a new concept of fuel cell . . . . .	13
I.5.1	Expected Advantages . . . . .	14
I.6	Outline . . . . .	15
<b>II</b>	<b>Proof of concept</b>	<b>17</b>
II.1	Introduction . . . . .	18
II.2	Proof of concept (POC) prototypes . . . . .	18
II.3	Electrolyte materials . . . . .	19
II.3.1	Proton electrolyte materials . . . . .	21
II.3.1.1	Proton conduction mechanism . . . . .	21
II.3.1.2	Materials choice . . . . .	22
II.3.2	Oxygen ion electrolyte materials . . . . .	27
II.3.2.1	Oxygen ion conduction mechanism . . . . .	28
II.3.2.2	Material choice . . . . .	31
II.4	Shaping of proof of concept prototypes . . . . .	32
II.4.1	Shaping techniques . . . . .	35
II.4.1.1	Cold Pressing . . . . .	35
II.4.1.2	Tape Casting . . . . .	35
II.4.2	First approach: self-supported samples . . . . .	41
II.4.3	Second approach : proton electrolyte-supported samples . . . . .	45
II.5	Electrochemical testing . . . . .	48
II.5.1	Experimental apparatus . . . . .	48
II.5.2	Experimental Procedure . . . . .	50
II.5.3	Results . . . . .	50
II.6	Discussion . . . . .	54
II.7	Conclusions . . . . .	58

<b>III</b>	<b>The Electrodes: Anode and Cathode</b>	<b>61</b>
III.1	Introduction . . . . .	62
III.2	Anode materials . . . . .	62
III.2.1	State-of-the-art . . . . .	62
III.2.2	Characterization of anode materials . . . . .	64
III.2.2.1	Samples description and fabrication . . . . .	65
III.2.2.2	S.E.M. characterization of samples . . . . .	69
III.2.2.3	Electrochemical testing . . . . .	69
III.2.3	Discussion . . . . .	71
III.2.4	Conclusions . . . . .	71
III.3	Cathode Materials . . . . .	72
III.3.1	State-of-the-art . . . . .	72
III.3.2	Characterization of cathode materials . . . . .	74
III.3.2.1	Samples description and fabrication . . . . .	77
III.3.2.2	S.E.M. characterization of samples . . . . .	79
III.3.2.3	Electrochemical testing . . . . .	80
III.3.3	Development of a composite cathode . . . . .	80
III.3.3.1	Experimental procedure . . . . .	80
III.3.3.2	Sample characterization . . . . .	81
III.3.3.3	Electrochemical testing . . . . .	81
III.3.4	Development of a new cathode material . . . . .	82
III.3.4.1	Experimental Procedure . . . . .	82
III.3.4.2	Electrochemical testing . . . . .	83
III.3.4.3	Discussion . . . . .	84
III.3.5	Conclusions . . . . .	86
III.4	Conclusions . . . . .	86
<b>IV</b>	<b>Complete cell fabrication</b>	<b>89</b>
IV.1	Introduction . . . . .	90
IV.2	Sample description . . . . .	92
IV.3	Experimental procedure . . . . .	92
IV.4	Sample characterization . . . . .	96
IV.5	Discussion . . . . .	97
IV.6	Conclusion . . . . .	98
<b>V</b>	<b>Central membrane characterization</b>	<b>101</b>
V.1	Introduction . . . . .	102
V.2	X-ray microtomography . . . . .	106
V.3	Experimental Procedure . . . . .	109
V.4	X-ray microtomography results . . . . .	115
V.5	Image segmentation . . . . .	117
V.5.1	Porosity . . . . .	117
V.5.2	Ceramic Materials . . . . .	119
V.5.2.1	Halo . . . . .	122
V.5.3	Segmentation of the three phases . . . . .	127
V.6	Morphologic 3D Image Analysis . . . . .	127
V.6.1	Percolation . . . . .	129
V.6.2	Tortuosity . . . . .	130
V.6.3	Active triple phase boundaries . . . . .	131
V.7	Discussion . . . . .	134

---

V.8	Conclusions . . . . .	136
<b>VI</b>	<b>Study of water evacuation in the central membrane</b>	<b>139</b>
VI.1	Introduction . . . . .	140
VI.2	Experimental Procedure . . . . .	140
VI.3	Description of the samples . . . . .	141
VI.4	Model . . . . .	143
	VI.4.1 Momentum transfer . . . . .	143
	VI.4.2 Mass Transfer . . . . .	146
VI.5	Evaluation of the water evacuation . . . . .	148
	VI.5.1 Problem . . . . .	148
	VI.5.2 Velocity Field . . . . .	150
	VI.5.3 Water evacuation . . . . .	152
	VI.5.4 Influence of the mesh density . . . . .	152
	VI.5.5 Influence of the pores shape . . . . .	155
	VI.5.6 Study of the samples anisotropy . . . . .	156
VI.6	Discussion . . . . .	160
VI.7	Conclusions . . . . .	161
	<b>Conclusions – Prospects</b>	<b>165</b>



---

# Chapter -I-

## Introduction

---

### Contents

---

<b>I.1</b>	<b>General context</b> . . . . .	<b>2</b>
<b>I.2</b>	<b>Fuel Cells</b> . . . . .	<b>5</b>
I.2.1	General Overview . . . . .	5
I.2.2	Working principle of a fuel cell . . . . .	6
I.2.2.1	Theoretical Performance . . . . .	7
I.2.2.2	Actual Performance . . . . .	8
<b>I.3</b>	<b>Solid Oxide Fuel Cell (SOFC)</b> . . . . .	<b>9</b>
I.3.1	Advantages and Disadvantages . . . . .	10
<b>I.4</b>	<b>Proton Ceramic Fuel Cell (PCFC)</b> . . . . .	<b>11</b>
I.4.1	Advantages and Disadvantages . . . . .	12
<b>I.5</b>	<b>IDEAL-Cell: a new concept of fuel cell</b> . . . . .	<b>13</b>
I.5.1	Expected Advantages . . . . .	14
<b>I.6</b>	<b>Outline</b> . . . . .	<b>15</b>

---

## I.1 General context

The image you see below (figure I.1) is a composition of pictures taken in the year 2000 during night from one of the thousands of artificial satellites that wander around earth. Nowadays, this image, although beautiful, is not surprising. If it had been taken one hundred years ago, although it would be the result of a true technological miracle at that time, this picture would be much less impressive than it is today; we would see nothing but a black rectangle on a white page.



**Figure I.1** : Planet Earth at night in the year 2000 [1].

The reason why we actually see something in the black rectangle is because in the last century men learned how to convert energy from different sources and use it to operate more and more different devices that allowed us to make tasks that were hardly feasible or completely impossible before. The benefits from the use of energy in our lives are so evident that distribution networks were created in order to spread its access to the largest number of people.

Since the beginning of this true revolution, energy consumption never stopped increasing. In 2009 total energy consumption in the world was 3 times higher than in 1965 having an increase from 3.8 to 11.2 million tons of oil equivalent (see figure I.2) [2].

The impact in our life quality is tremendous. We live better. In this same period, infant mortality decreased from 116 to 47 deaths per 1000 births while life expectancy raised from 52 to 67 years-old. As a result, world population more than doubled from 3.3 to 6.9 billion people [3].

Our lives became not only longer but also completely different than before. We travel much often and much faster; and information travels even faster than us. The world became smaller. The introduction of all kinds of mechanical devices and biochemicals in agriculture made alimentary products accessible to a larger number of people. Health care and sanitary conditions improved in our every day lives. Industries produce more products, in less time, with lower raw material and labor costs at lower prices. From 1960 to 2008 the world's gross domestic product raised from 1.9 to 60.5 billion dollars [4].

For all these reasons, energy became a strategic sector of the uttermost importance.

In its 2009 World Energy Outlook, the International Energy Agency (IEA) predicts that

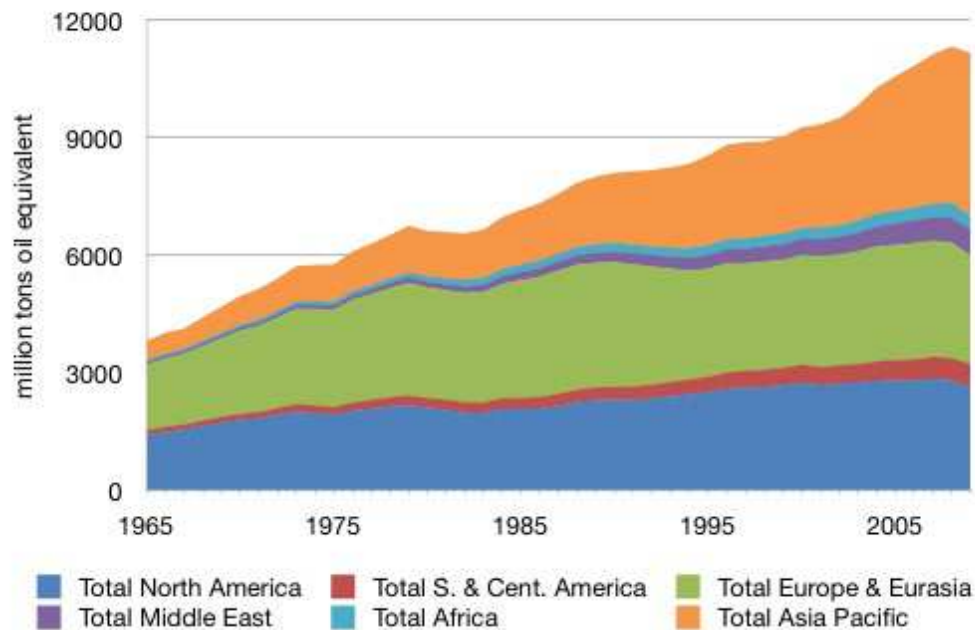


**Figure I.2 :** Total energy consumption in the world from 1990 to 2008 in million tons of oil equivalent [2].

the primary energy demand will increase 40% until 2030; China and India represent over 50% of this increment. Fossil fuels will remain the dominant sources of energy worldwide and electricity consumption will increase 76%. China will overtake USA as the world biggest spender in oil and gas imports soon after 2025.

When in 2100 a new picture of the earth at night will be taken, things will have changed: Europe, North America, Japan and Oceania may be slightly brighter than today but the main increment will be seen in the regions of Asia and South America. However we'll still hardly see Africa's contours.

The IEA predicts that by 2030, 1.3 billion people worldwide will still lack access to electricity compared to 1.5 billion in 2007 [5].

An important effort has been done to spread the access to energy but we didn't diversify enough the sources to obtain it and this has an impact in the planet's sustainability. From 1990 to 2009 the emission of CO<sub>2</sub> in the atmosphere increased at the same rate as the energy consumption: 2.6 times higher from 12000 to 310000 tons per year [2]. One of the main consequences for the planet is the so called global warming. As we can see in figure I.3 most of the planet is in average 1°C or 2°C warmer and in some regions of the north, where ice surfaces are located, the differences reach 5°C. The continuation of current trends would have profound implications for environmental protection and air quality that would cause serious public health issues, particularly in developing countries [5].

This is the challenge we have to face: the need of producing more energy and at the same time of reducing the impact of our presence on the planet.

An effort has been done in the last decade to diversify the sources of energy and the impact of their exploitation in the planet by the use of renewable sources of energy; sources that can be replenished at least as fast as they are consumed. In 2007, renewable energies

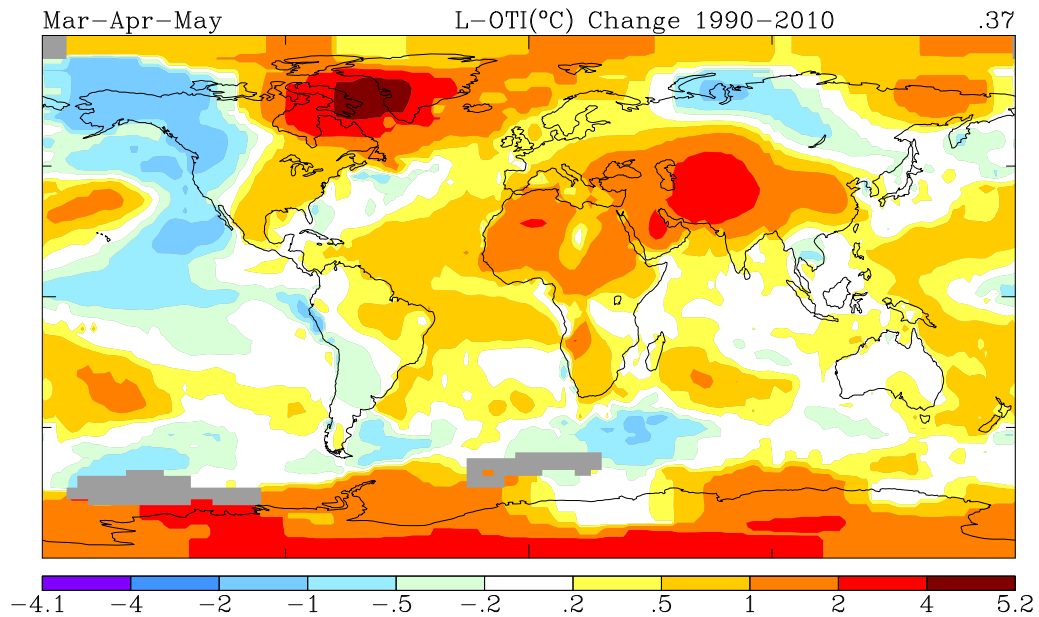


**Figure I.3 :** Temperature difference between 1990 and 2010 during spring in the world [6].

represented 18% of the sources of total energy consumption in the world [2]. In figure I.4 we can see the impressive increase in solar, wind and thermal energy production in the world.

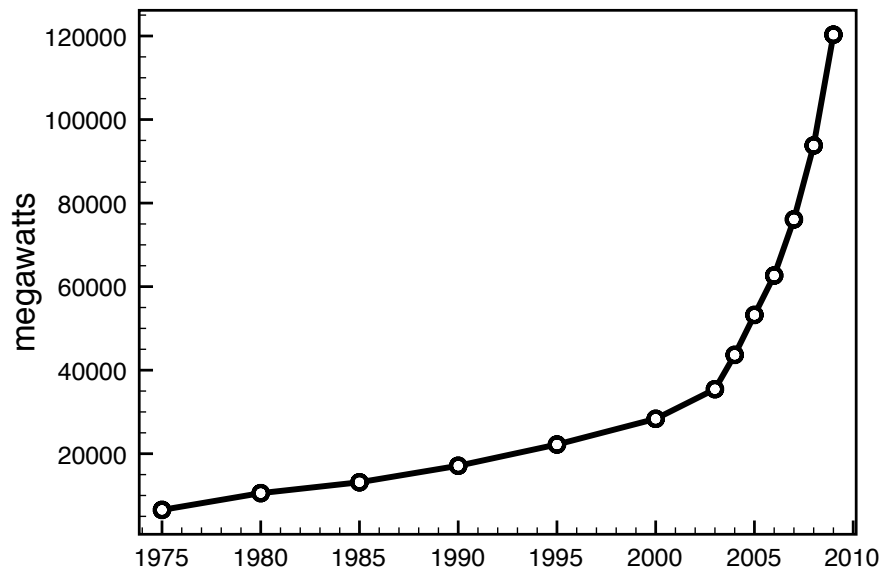


**Figure I.4 :** Solar, wind and thermal energy production in the world from 1975 to 2010 [2].

The five renewable sources used most often in the world are: biomass, water (hydropower), geothermal, wind and solar.

Biomass can be converted into electrical energy with relatively low impact in the

environment through the use of fuel cells.

## I.2 Fuel Cells

### I.2.1 General Overview

Fuel cells are electrochemical devices that convert the chemical energy of the fuels and the combustive directly into electrical energy, producing water as byproduct. In a combustion engine, fuel undergoes a chemical reaction of combustion and electrical energy is produced through an intermediate mechanical step that takes advantage of the expansion of the gases produced to apply a force in a component of the engine making it move.

Instead, in a fuel cell, electrical energy is produced directly by electrochemical processes. Combustion of the fuel cannot occur because it's separated from the oxidant by an electrolyte. The complete structure of a fuel cell - shown in figure I.5 - consists of the electrolyte and two electrodes on each side: the anode and the cathode. During operation, fuel is fed continuously to the anode where it's oxidized while the oxidant is reduced in the cathode creating a flow of ions that goes through the electrolyte and a current of electrons that passes through an external circuit.

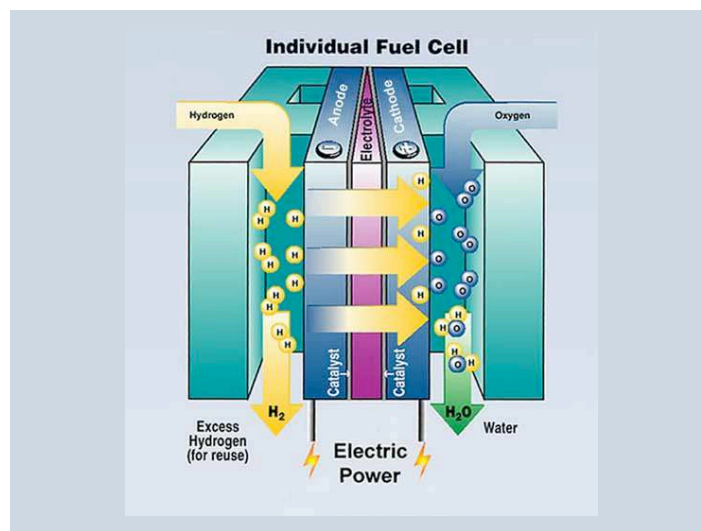


**Figure I.5** : General scheme of a fuel cell [7].

Thus, a fuel cell works like a battery in sense that it also produces electrical energy through electrochemical processes. However, unlike a battery, a fuel cell cannot run out as long as fuel is continuously supplied. This is interesting for applications in which absolutely reliable energy supply is needed like military and health care. Fuel cells also allow the energy generation near the customers rather than central or remote locations which avoids losses over the long transmission and distribution lines [8]. Their ultimate advantage is the high efficiency compared to other energy generation systems but their cost keeps them from being more competitive as it is shown in table I.1.

There are different types of fuel cells in different stages of development. They are commonly classified by the nature of the electrolyte they use. Thus, we can distinguish [9]:

**Polymer Electrolyte Fuel Cells (PEFC)** in which the electrolyte is a polymeric proton exchange membrane where H<sup>+</sup> is the charge carrier. Water management is particularly

**Table I.1** : Comparison of different energy generation systems [8].

	Diesel engine	Photovoltaic	Wind turbine	Fuel cells
Capacity range	500 kW to 5 MW	1 kW to 1 MW	10 kW to 1 MW	200 kW to 2 MW
Efficiency	35%	6-19%	25%	40-60%
Capital cost (\$/kW)	200-350	6600	1000	1500-3000
O&M cost	0.005-0.015	0.001-0.004	0.01	0.0019-0.0153

hard because water cannot be evacuated at a faster rate than it's produced since the membrane must be hydrated to keep its conductive properties. For this reason P.E.F.C. run typically at a temperature range from 60°C to 80°C. These low operating temperatures allow the fast start-up of the system and an immediate response to changes in the demand for power. Its tolerance to shock and vibration due to plastic materials make it suitable for automotive and portable applications. Systems with a power range from 30 W to 250 kW have been tested.

**Alkaline Fuel Cells (AFC)** potassium hydroxide in a matrix plays the role of electrolyte conducting OH<sup>-</sup> ions which are the charge carriers. These systems operate from 65°C to 220°C. Under development since the 1960's, the high reactivity of the electrolyte with CO<sub>2</sub> that may be present in the fuel is one of its main drawbacks. Power delivered by such systems goes from 10 W to 10 kW.

**Phosphoric Acid Fuel Cell (PAFC)** a solution of phosphoric acid in a ceramic matrix conducts H<sup>+</sup> ions. With an operating temperature between 150°C and 220°C, these systems are limited to stationary applications. A wide power range from 100 kW to 1.3 MW has been reached through these systems.

**Molten Carbonate Fuel Cell (MCFC)** uses an electrolyte composed of a mixture of lithium carbonate and potassium through which CO<sub>2</sub><sup>3-</sup> ions circulate. These systems are also suitable for stationary applications since they operate from 600°C to 700°C. Units with delivering power from 10 kW to 2 MW have been tested.

**Solid Oxide Fuel Cell (SOFC)** has dense mixed oxide ceramics as electrolytes; typically a ceramic with a perovskite structure. These materials are good O<sup>2-</sup> (or H<sup>+</sup>) conductors for temperatures from 600°C to 1000°C and this fact determines the system operating temperature. Thus, these cells are also suitable for stationary applications. A power range from 1 kW to 1.7 MW was obtained using these systems.

### I.2.2 Working principle of a fuel cell

A fuel cell can be seen as a charge pump. Just like a mechanical pump creates a pressure difference that makes a fluid to go from a point with higher pressure to a point with lower pressure, a fuel cell creates an electric field with a potential that moves charges from a higher to lower potential.

The potential difference  $\Delta V$ , for an infinitesimal displacement  $dS$ , between two points A and B in an electric field  $E$  is defined as the change in potential energy,  $\Delta U$  of the system divided by the test charge,  $q_0$ :

$$\Delta V = \frac{\Delta U}{q_0} = - \int_A^B E \cdot ds \quad (I.1)$$

The potential difference between points A and B equals the work per unit charge that must be done to move a test charge between the two points in an electric field,  $E$ . The potential

difference  $\Delta V$  is therefore a measure of energy per unit charge with SI units of joules per coulomb, which is defined as volt (V) [10].

### I.2.2.1 Theoretical Performance

The potential of an electric field describes the work done to displace a unit charge in this field. The potential is therefore the driving force for the charge displacement and is equivalent to the open circuit voltage - the voltage when the current is zero. The open circuit voltage of a fuel cell depends on the difference of potential of the electrochemical reactions that take place in the electrodes. The useful energy is extracted from the system directly via the electric circuit. The driving force for this process is the difference in chemical potential (or the activity) between fuel at the anode and of the combustive in the cathode.

**Table I.2** : Electrochemical reactions in the electrodes of the different types of fuel cell [9]

Fuel cell	Anode reaction	Cathode reaction
Polymer electrolyte and Phosphoric acid	$\text{H}_2 \rightarrow 2\text{H}^+ + 2\text{e}^-$	$1/2 \text{O}_2 + 2\text{H}^+ + 2\text{e}^- \rightarrow \text{H}_2\text{O}$
Alkaline	$\text{H}_2 + 2\text{OH}^- \rightarrow 2\text{H}_2\text{O} + 2\text{e}^-$	$1/2\text{O}_2 + \text{H}_2\text{O} + 2\text{e}^- \rightarrow 2\text{OH}^-$
Molten carbonate	$\text{H}_2 + \text{CO}_3^{2-} \rightarrow \text{H}_2\text{O} + \text{CO}_2 + 2\text{e}^-$ $\text{CO} + \text{CO}_3^{2-} \rightarrow 2\text{CO}_2 + 2\text{e}^-$	$1/2\text{O}_2 + \text{CO}_2 + 2\text{e}^- \rightarrow \text{CO}_3^{2-}$
Solid oxide	$\text{H}_2 + \text{O}^{2-} \rightarrow \text{H}_2\text{O} + 2\text{e}^-$ $\text{CO} + \text{O}^{2-} \rightarrow \text{CO}_2 + 2\text{e}^-$ $\text{CH}_4 + 4\text{O}^{2-} \rightarrow 2\text{H}_2\text{O} + \text{CO}_2 + 8\text{e}^-$	$1/2\text{O}_2 + 2\text{e}^- \rightarrow \text{O}^{2-}$
Proton ceramic	$\text{H}_2 \rightarrow 2\text{H}^+ + 2\text{e}^-$	$1/2 \text{O}_2 + 2\text{H}^+ + 2\text{e}^- \rightarrow \text{H}_2\text{O}$

The maximum electrical work  $W_{el}$  that can be obtained in a fuel cell operating at constant temperature and pressure is given by the change in Gibbs free energy  $\Delta G^\circ$  in standard conditions of the global electrochemical reaction:

$$W_{el} = \Delta G^\circ = -nFE^\circ \quad (\text{I.2})$$

where  $n$  is the number of electrons participating in the reaction,  $F$  is the Faraday's constant (96485 C/mol), and  $E^\circ$  is the reversible potential of the cell, considering the reactants and products being in the standard state (25°C, 1 atm).

For the general cell reaction,



the Gibbs free energy  $\Delta G$  of a reaction can be obtained from its value at standard conditions through the equation:

$$\Delta G = \Delta G^\circ - RT \ln \frac{[C]^c [D]^\delta}{[A]^\alpha [B]^\beta} \quad (\text{I.4})$$

When equation I.2 is replaced in I.4, we obtain:

$$E = E^\circ - \frac{RT}{nF} \ln \frac{[C]^c [D]^\delta}{[A]^\alpha [B]^\beta} \quad (\text{I.5})$$

Therefore the concentration of the reactants and the products of the reaction can influence the potential produced by the fuel cell.

The chemical activity is linked to concentration, which in turn is linked to partial pressures  $P$  in gaseous systems. For the simple case of a hydrogen-oxygen fuel cell, where  $2\text{e}^-$  are

exchanged between both the electrodes compartments, the following relation can thus be derived:

$$E = E^\circ + \frac{RT}{2F} \ln \frac{P_{H_2} P_{O_2}^{1/2}}{P_{H_2O}} \quad (\text{I.6})$$

### I.2.2.2 Actual Performance

Compared to an internal combustion engine, fuel cells are not submitted to the limitations of the Carnot cycle thus their theoretical efficiency is higher. The latter is given by the ratio of the Gibbs free energy of water formation  $\Delta G^\circ$  to the thermal energy  $\Delta H^\circ$  delivered by the chemical reaction. The efficiency is 83% when liquid water is formed and 95% for gaseous water at 25°C. At higher temperatures ( $> 900^\circ\text{C}$ ), this efficiency reaches 74% without taking into account the lowering of the potential delivered by the cell in closed circuit. When the circuit is closed, the electrical charges cross the cell, they go through its internal resistance and the potential decreases due to the so called losses or polarizations. These losses are due to three phenomena:

**Activation polarization**,  $\eta_{act}$  is dominant for low current densities when the electrochemical reactions at the electrodes are limited by the charge transfer kinetics. It's a measure of the electrochemical performance of the electrode materials and the ability of the microstructures morphology to facilitate the electrochemical reactions. Electrochemical and chemical reactions are similar in the fact that, in both, the reactants must overcome an activation energy to start the reaction. In the case of an electrochemical reaction for which  $\eta_{act} \geq 50 - 100\text{mV}$ ,  $\eta_{act}$  is given by the general equation

$$\eta_{act} = \frac{RT}{\alpha n F} \ln \frac{i}{i_0} \quad (\text{I.7})$$

in which,  $\alpha$  is the charge transfer coefficient,  $i$  is the current density and  $i_0$  is the exchange current density.

**Ohmic polarization**,  $\eta_{ohm}$  is due to the resistance to the flow of ions in the electrolyte and the flow of electrons in the electrodes. It can be reduced by enhancing the electrolyte conductivity wether through the use of better conducting materials, reducing the electrolyte thickness or increasing the cell's operating temperature. Since most of the electrolyte materials are ohmic, the ratio of the potential loss  $\eta_{ohm}$  to the current,  $I$ , is the resistance,  $R_e$  of the conductor.

$$\eta_{ohm} = R_e I \quad (\text{I.8})$$

**Concentration polarization**,  $\eta_{conc}$  occurs for higher values of current density, when the mass transport of the chemical species in the electrodes control the electrochemical reactions. As the reactants are consumed in the surface of the electrochemical sites, the inability to maintain the bulk concentration creates a concentration gradient. It may be caused by slow diffusion of the gases through the porosity of the electrodes to the electrochemical reaction sites, dissolution of the reactants or products within the electrolyte or diffusion of reactants and products between the reaction sites and the electrolyte. It may be reduced by the optimization of the electrodes morphology. At high current densities, the slow transport of products to the reaction sites is the major contribution to the concentration polarization. These losses can be expressed by:

$$\eta_{conc} = \frac{RT}{nF} \ln \left( 1 - \frac{i}{i_L} \right) \quad (\text{I.9})$$

where  $i_L$  is the limit current.

The actual potential of a fuel cell  $V_{cell}$  is, thus, given by the maximum work determined by equation I.2 less the losses described above:

$$V_{cell} = E^\circ - \eta_{act} - \eta_{ohm} - \eta_{conc} \quad (\text{I.10})$$

The cell potential is function of the current density and it can be represented by a typical I-V curve, displayed in figure I.6. The operating point of a fuel cell will depend on operating variables that will optimize the performance to a specific system requirements, keeping the operating costs as low as possible. For example, operating at higher pressure will increase the cell performance, however more powerful compressors will be needed to compress the reactants and the pipes to feed the fuel and exhaust the gases will have to be adequate, which represents an additional cost.

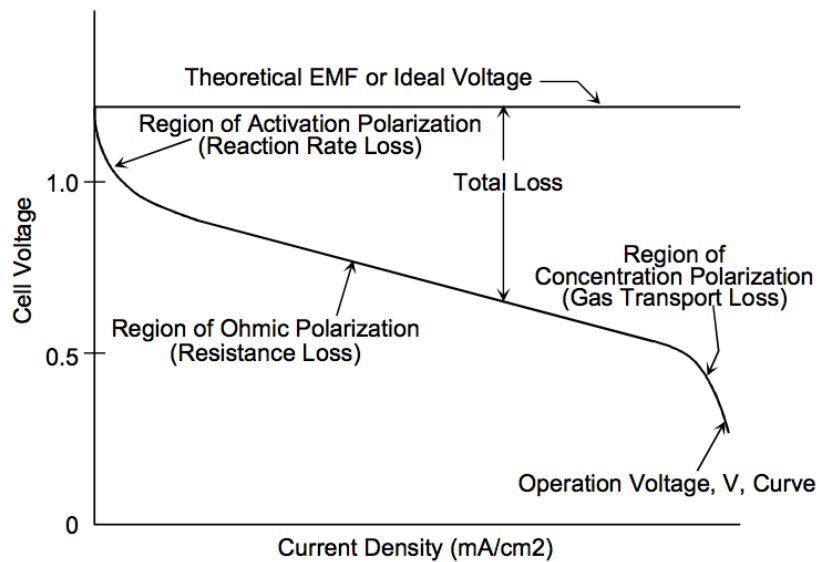


**Figure I.6** : Characteristic current-voltage curve of a fuel cell [9].

The research activities reported here are devoted to a new concept of fuel cell that, due to its characteristics, can be included in the Solid Oxide Fuel Cell family. The following parts I.3 and I.4 state the progress in the field of high temperature fuel cells, SOFC and PCFC, illustrating their advantages and drawbacks.

### I.3 Solid Oxide Fuel Cell (SOFC)

Solid oxide fuel cells (figure I.7) use a solid oxide electrolyte to transfer  $O^{2-}$  ions, the charge carriers, from the cathode to the anode. The fuel (reducing agent) is generally hydrogen and the combustive (oxidant) is oxygen in the air. In the cathode, oxygen is reduced by a current of electrons coming from an external circuit, creating a flow of oxygen ions through the electrolyte (see equation I.11). In the anode, these ions oxidize the fuel forming water

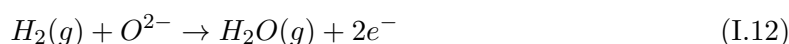
and a current of electrons that passes through the external circuit towards the cathode (see equation I.12). The global reaction is thus given by equation I.13. At standard pressure and temperature ( $T = 25^\circ\text{C}$ ,  $P = 1 \text{ atm}$ ) water formed in this reaction is liquid and therefore  $\Delta G^\circ = -237.3 \text{ kJ/mol}$ . The open-circuit voltage of such system, given by equation I.2, is  $\Delta E^\circ = 1.23 \text{ V}$ . At these same pressure and temperature conditions, if we consider that water is formed as water vapor,  $\Delta G^\circ = -228.6 \text{ kJ/mol}$  and the open-circuit voltage will be  $\Delta E^\circ = 1.19 \text{ V}$  [9].

Solid oxide fuel cells operate at temperatures between  $600^\circ\text{C}$  and  $1000^\circ\text{C}$  where the ionic conductivities of the electrolyte materials is high enough to assure efficiently the transport of  $\text{O}^{2-}$ .

Cathode Reaction:



Anode Reaction:



Overall Reaction:

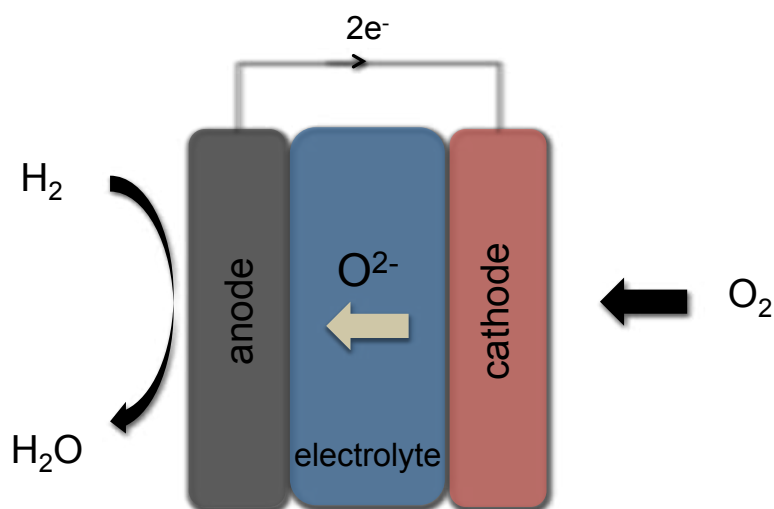
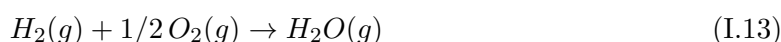


Figure I.7 : Solid oxide fuel cell scheme.

### I.3.1 Advantages and Disadvantages

High temperatures allow the integration of an internal reformer to transform, in situ, methane into hydrogen. This can avoid the development of a hydrogen supply network or storage. At high temperatures the reactions at the electrodes become easier to catalyze and therefore the catalysts used can be cheaper metals than the ones used in low temperature fuel cells. Solid oxide fuel cells produce water as vapor that has a very important energetic value. Thus, this vapor can be used in the heating systems or cogeneration plants. This can increase the efficiency of this type of systems from 40% to 80%. Another advantage is related to the nature and/or composition of the anode gas: carbon monoxide is not a poison anymore for

the catalysts and the tolerance to sulfur is one or two times higher than the ones of phosphoric acid or molten carbonate cells.

Solid Oxide fuel cells present although some disadvantages that keep them from reaching a higher stage of development. Reducing (on the anode side) and oxidant (on the cathode side) atmospheres at such high temperatures create very demanding conditions to the materials used in the cells but also in the interconnects of the stacks. These materials must not be sensitive either to oxidation and reduction at high temperature. This has great impact in the systems performance stability. Other disadvantages are related to the concept itself. The hydrogen oxidation in the anode produces water that has to be evacuated at the same rate that is created while at the same time, in the opposite direction, hydrogen must flow through the microstructure to reach the electrochemical reaction sites. Hydrogen oxidation is the anode's main function, however, water partial pressure must be kept as low as possible to avoid decreasing the cell's potential, as one can see in equation I.6. The function of the anode is dual and somehow incompatible since two gases must flow in opposite directions. Therefore the optimization of the microstructures morphology for this dual function is particularly delicate. The presence of water in the anode dilutes the fuel, decreasing the cell potential and deactivates the electrochemical sites. In these conditions, an increase of hydrogen partial pressure, leads to the formation of more water and therefore a lower potential and a weaker electrochemical reaction rate. W.G. Coors reported that SOFCs with 45-55% efficiency are hampered by poor intrinsic fuel utilization because water vapor is produced at the anode where it dilutes the fuel [11].

The decrease of the SOFC's working temperature is a core objective for its development and it has been attempted through two approaches: the use of thinner electrolytes in electrode supported cells and the development of new materials with higher conductivities.

In this quest, new ionic conduction mechanisms were considered, as it happens in Proton Ceramic Fuel Cells (PCFC).

## I.4 Proton Ceramic Fuel Cell (PCFC)

Proton conduction in solids at temperatures below 100°C had been studied for a long time before the beginning of the years 1980's when H. Iwahara demonstrated that SrCO<sub>3</sub> based sintered oxides had interesting proton conductivities when exposed at hydrogen atmospheres at temperatures between 600°C and 1000°C [12]. These materials can be used as electrolyte of a fuel cell having the characteristics of polymer electrolyte fuel cells but keeping the kinetic and thermal advantages of the solid oxide fuel cells.

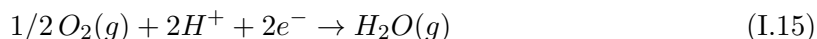
In this concept of fuel cell, H<sup>+</sup> charge carriers are implied instead of O<sup>2-</sup> ions like in the SOFC concept. The relatively lower weight of H<sup>+</sup> ion would imply a lower activation energy associated with ionic transport, and then a better conduction would be expected at lower temperatures (< 800°C).

Thus, in this concept, hydrogen is reduced in the anode yielding a current of protons that is conducted through the electrolyte and a current of electrons that passes by an external circuit towards the cathode (see equation I.14). In the latter, oxygen acts as oxidant and reacts with the protons and the electrons to form water vapor (see equation I.15).

Anode Reaction:



Cathode Reaction:



Overall Reaction:

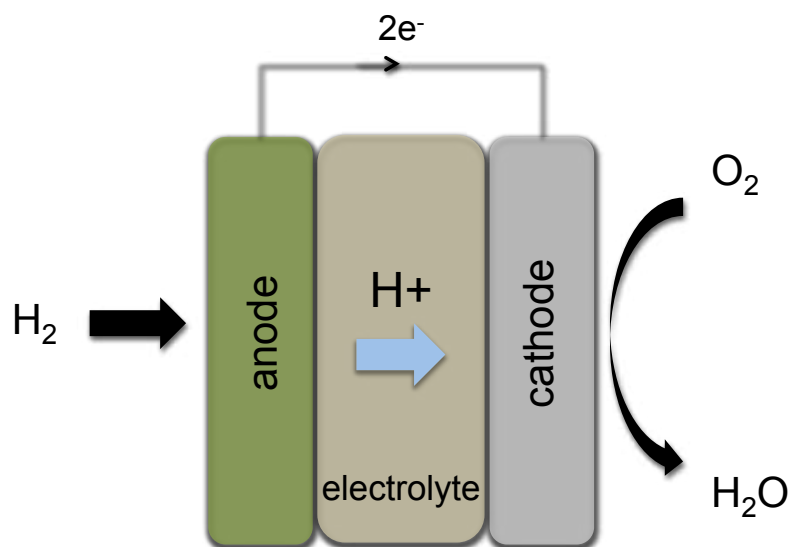


**Figure I.8** : Proton ceramic fuel cell scheme

The overall reaction is the same given in I.13 and therefore, through equation I.2, the open-circuit voltage of a proton ceramic fuel cell has the same value of a SOFC,  $\Delta E^\circ = 1.19 \text{ V}$ , considering water formed as vapor in standard conditions.

#### I.4.1 Advantages and Disadvantages

PCFCs have the advantages of the high temperature fuel cells. They allow higher fuel flexibility because reduction reactions of fossil fuels can be catalyzed at such temperatures. The conditions for the reactions catalysis are so favorable that cheaper metals can be used, instead of platinum or gold used in PEFCs. As in SOFCs, water vapor produced allows the integration of the cells stack in cogeneration plants and increases the global efficiency up to 80%. The advantage of the PCFCs comparing to the SOFCs is the possibility of reducing the operating temperature. Proton conductors have the advantage that the ion migration kinetics are rather faster, and so the cell can run at lower temperatures, which is very important for the materials durability and long-time performance. Another advantage is that water is no longer formed in the anode and therefore fuel is not diluted and then the electrochemical reaction rate is not decreased.

However, this is where the disadvantages of this concept begin. Although fuel dilution is avoided, the problem of water evacuation is exactly the same in the cathode of a PCFC. Oxygen must diffuse to reach the electrochemical sites and at the same time water must be evacuated in the opposite direction. The microstructure of the cathode has to be optimized for this dual and opposing function. The evacuation of water is important because its presence in the oxidizing atmosphere of the cathode at such a high temperature is highly demanding for the cathode and interconnect materials. Chemical stability of the materials is affected and therefore performance of the fuel cell is decreased.

In this context the development of fuel cells can follow two paths: the improvement of the concepts described above through the development of better performing materials and the optimization of the microstructures using different shaping techniques or the development of breakthrough concepts that will allow to overcome the difficulties the research community has been confronted with for many decades.

The second choice was made in the beginning of the years 2000s when a new concept of intermediate temperature fuel cell was conceived. This concept has so far been called *Innovative Dual MEmbrANE Fuel - Cell: IDEAL-Cell*.

## I.5 IDEAL-Cell: a new concept of fuel cell

If we keep the classification of fuel cells according to the electrolyte's nature, IDEAL-Cell is in fact a solid oxide fuel cell, which operating temperature is intermediate between those of PCFCs and SOFCs.

In the previous sections, the major obstacles to the development of high temperature fuel cells were presented. In a SOFC the anode is an obstacle to the cell development because the fuel is diluted which decreases the voltage and the electrochemical activity. Moreover, counter-flow of fuel and water makes the microstructure optimization difficult. Although PCFC present some advantages that allow us to overcome the limitations of the SOFCs systems, the presence of water in the cathode creates an extremely severe atmosphere for the materials durability and the counter-flow of oxygen and water is a problem similar to the one found in SOFC anodes.

The idea behind the IDEAL Cell concept is to keep from both concepts the most performing components and to connect them through a new membrane. This innovative system that combines the advantages of state-of-the-art fuel cells (SOFC and PCFC) while avoiding their drawbacks, consists in the anode and proton conducting electrolyte of a PCFC connected to the cathode and oxygen ion conducting electrolyte of a SOFC through a porous ceramic central membrane, as one can see in figure I.9. In this cell, hydrogen is oxidized in the anode through reaction I.17 creating a current of electrons that pass through an external circuit and a flow of protons that are conducted through the electrolyte. On the other electrode, oxygen is reduced by the electrons coming from the external system creating a flow of oxygen ions that go through the electrolyte. The central membrane must allow the recombination of the two types of ions in order to react and form water (see reaction I.18) that must be evacuated through this porous central structure.

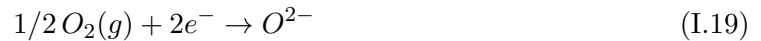
Anode reaction:



Central membrane reaction:



Cathode Reaction:



Overall Reaction:



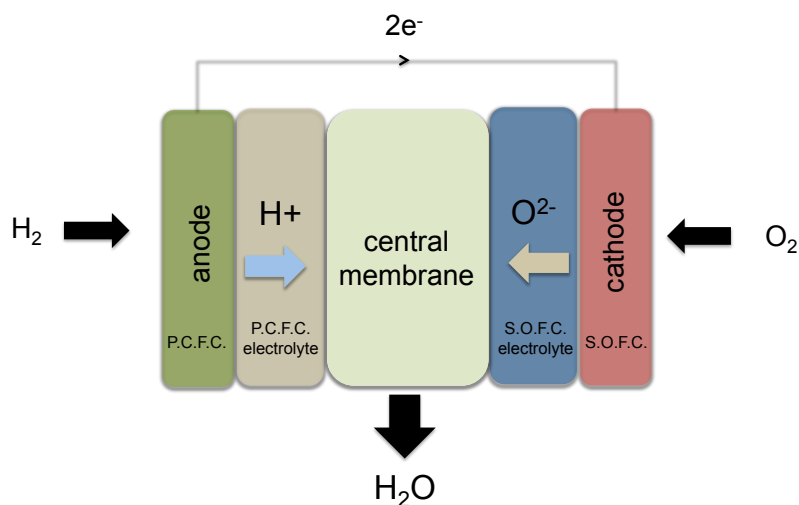


**Figure I.9** : Innovative dual membrane fuel cell - a new concept of fuel cell

### I.5.1 Expected Advantages

Proposing a new concept of fuel cell to the scientific community wouldn't make sense if it couldn't bring advantages with respect to the already existing concepts. What was written in the two previous sections allows us to conclude the advantages expected from IDEAL-Cell.

The innovation of this concept lies on the central membrane, which is the core of the device [13]. The idea of a mixed dedicated proton and oxygen ion conducting membrane that can allow water formation and evacuation simplifies the role the electrodes have to play. Compared to the already existing systems, the constraints in terms of microstructures are decreased. Thus, materials and microstructures of the anode and the cathode can now be optimized to their main purpose: fuel and combustive diffusion and their electrochemical reactions. It is no longer necessary to take into account the gas counter-flow to evacuate water out of the electrodes microstructures. Since water is not present in the electrodes, the electrochemical sites activity is no longer decreased. In fact, oxygen and hydrogen chambers are almost closed (single gas flow, no exhaust pipe); the stack architecture design is therefore made simpler than that of SOFC and PCFC, and offers the possibility of applying a pressure independently at both anode and cathode sides. This will allow the optimization of operating conditions and will drastically limit the polarization losses. In the anode, fuel is not diluted and the cell's potential is not decreased. In the cathode, a dry oxidizing atmosphere is less demanding both for the cathode and the interconnects materials. Since some oxygen ion electrolyte materials have been reported to have good performances at 600°C, this new concept would operate at a temperature close to the one of a PCFC, which has the advantages described in I.4.1. Within the central membrane, the reaction of  $\text{H}^+$  and  $\text{O}^{2-}$  ions recombination is an exothermal reaction, giving rise to local increases of temperature that will improve ion diffusion. In addition to this role, the central membrane must have the optimal architecture to easily evacuate water. Therefore, it will be open to the exterior via an exhaust pipe; these thermodynamic conditions will force water to condense in cooler parts of the system generating a pressure drop and thus the enhancement of the water formation reaction in the central membrane according to the Le Chatelier principle. Due to the pressure drop in the central membrane, the equilibrium of the reaction will shift to counteract the imposed change and a new equilibrium is established towards an increase of water formation. Water produced in the central membrane can be used in an internal system with an electrolyzer to

produce hydrogen or in a vapor-reforming stage. This water also has an important energetic value that can be very efficiently recovered through a heat exchanger. Recovering this steam is made easier than in SOFC or PCFC systems since it is no longer diluted with anode or cathode gases.

## I.6 Outline

This concept is protected by a French [?] patent since 2005 and in the rest of Europe, USA and Japan since 2007. In order to develop this idea, the European commission agreed to sponsor a research program under the seventh framework program. This project called *IDEAL Cell: Innovative Dual mEmbrane fueL Cell* began in January 2007 gathering ten partners from five different european countries. The results presented here were obtained in the last three years in the scope of this project at the *Centre des Matériaux* from Mines ParisTech, the project coordinator.

Thus, in the following chapters are reported the results on the fabrication and testing of the first IDEAL-Cell prototypes that lead to the proof of concept, which was the first objective of the project. After this phase, efforts were focused on the development of the electrodes and the shaping of a complete cell that could have better performances than the prototypes. The optimization of the cell also took us to study how to improve the shaping procedure of the central membrane in order to increase its ability to produce and evacuate water.

En 2009, la consommation mondiale d'énergie était trois fois plus élevée qu'elle ne le fut en 1965. Parallèlement, la qualité de vie s'est fortement améliorée : la mortalité infantile est passée de 116 à 47 par mille et l'espérance de vie a connu une hausse de 29% en 44 ans en passant de 52 à 67 ans. Néanmoins, l'amélioration de notre qualité de vie, liée aux activités anthropiques, est la cause directe du bouleversement climatique qui ne cesse de s'aggraver. Selon l'agence internationale de l'énergie (AIE), l'augmentation de la consommation d'énergie dans le monde aura un impact certain sur la santé publique. En raison de son caractère écologique, la pile à combustible est une solution d'avenir pour produire de l'énergie électrique "propre" directement par conversion de l'énergie chimique d'un combustible et d'un comburant, l'eau et la chaleur étant les seuls produits de combustion. Parmi les piles à combustible fonctionnant haute température, deux sont en voie d'industrialisation : les piles à combustible à oxydes solides (SOFC) et à conduction protonique (PCFC). Cependant, ces deux dispositifs électrochimiques présentent des inconvénients majeurs, directement liés à la présence d'eau aux électrodes, qui freinent leur développement. Pour obvier à ces limitations, un nouveau concept de pile à combustible a été inventé Centre des Matériaux et breveté par ARMINES. Il consiste en l'assemblage des compartiments anodique et cathodique respectivement d'une PCFC et d'une SOFC par l'intermédiaire d'une membrane centrale poreuse et conductrice anionique et protonique qui permet la formation et l'évacuation de l'eau. La présente thèse contribue au développement de cette cellule innovante de pile à combustible dans le cadre d'un projet Européen.

---

---

# Chapter -II-

## Proof of concept

---

### Contents

---

<b>II.1</b>	<b>Introduction . . . . .</b>	<b>18</b>
<b>II.2</b>	<b>Proof of concept (POC) prototypes . . . . .</b>	<b>18</b>
<b>II.3</b>	<b>Electrolyte materials . . . . .</b>	<b>19</b>
II.3.1	Proton electrolyte materials . . . . .	21
II.3.1.1	Proton conduction mechanism . . . . .	21
II.3.1.2	Materials choice . . . . .	22
II.3.2	Oxygen ion electrolyte materials . . . . .	27
II.3.2.1	Oxygen ion conduction mechanism . . . . .	28
II.3.2.2	Material choice . . . . .	31
<b>II.4</b>	<b>Shaping of proof of concept prototypes . . . . .</b>	<b>32</b>
II.4.1	Shaping techniques . . . . .	35
II.4.1.1	Cold Pressing . . . . .	35
II.4.1.2	Tape Casting . . . . .	35
II.4.2	First approach: self-supported samples . . . . .	41
II.4.3	Second approach : proton electrolyte-supported samples . . . . .	45
<b>II.5</b>	<b>Electrochemical testing . . . . .</b>	<b>48</b>
II.5.1	Experimental apparatus . . . . .	48
II.5.2	Experimental Procedure . . . . .	50
II.5.3	Results . . . . .	50
<b>II.6</b>	<b>Discussion . . . . .</b>	<b>54</b>
<b>II.7</b>	<b>Conclusions . . . . .</b>	<b>58</b>

---

## II.1 Introduction

The IDEAL-Cell concept is, first of all, an effort to overcome the difficulties which the scientific community has been confronted with in order to enhance fuel cells performances. Two typical approaches have been followed so far: (1) synthesizing new materials with higher conductivities and better catalytic properties, or (2) optimizing the microstructures through new or better-tuned techniques. In both cases the objective is to converge the actual performance of the systems to their theoretical values, keeping the operating temperatures as low as possible. The introduction of a new concept of fuel cell represents a third path to reach the same objectives. Due to its original configuration the IDEAL-Cell concept (see chapter I) can be an answer to some of the relevant drawbacks of the SOFC and PCFC systems. However, this third strategy is worthy to be carried out only if it represents a simplification and not a source of new and more complex scientific and technical questions that will not add anything to the state-of-art fuel cell systems. In this perspective, our first goal was to demonstrate that IDEAL-Cell is not only a promising possibility but that it actually behaves as a fuel cell, when a difference of potential is created between its electrodes.

In this chapter, the activities developed in what was called the *proof of concept* (POC) phase are described. These activities go from the materials choice and characterization to the fabrication and testing of the first prototypes. As every new concept, its first units are prototypes designed to demonstrate that the idea is valid, feasible and has reproducible performances. Therefore, factors such as the cost of production and the possibility of industrial scale-up of the shaping processes were not taken into account in the decisions on the first cell prototypes. The most important criterion was performance but in a qualitative and not in a quantitative point of view; for example it was more important to detect the electrical current produced than to reach a high current density. Thus, it made sense that the materials chosen to fabricate the first samples were well known for their performances and reliability in the field of fuel cells. The shaping techniques used were chosen for being used routinely in the last years in our laboratory and therefore for producing reproducible results. At last, the samples were tested in typical fuel cell operating conditions in a dedicated electrochemical tester.

The results that allowed us to demonstrate this new concept are presented and discussed here.

## II.2 Proof of concept (POC) prototypes

The first step in demonstrating the IDEAL-Cell concept was to decide the configuration of the POC prototypes in terms of microstructures, materials used in each functional layer and shaping techniques. These decisions were taken keeping in mind the mechanical reliability of the samples during testing, the reproducibility of the microstructures and, consequently, of the performances as well. As it was shown in figure I.9, a complete IDEAL-Cell is an electrochemical device with five different layers, each of them with different compositions, functions and microstructures. Each compartment of the cell was described in I.5. The anode and the cathode are mixed conductors with porous structures that must allow electrochemical reactions to take place and the transport of fuel and combustive, respectively. The electrolytes must be dense layers of purely ionic conductor materials. The central membrane, the innovative part of this concept, must be a porous structure that permits the conduction and the reaction of  $H^+$  and  $O^{2-}$  ions and the transport of water to sweep it out of the system. The choice of the electrodes must take into account different aspects related to

the materials properties and to the microstructures optimization. The electrodes must be chemically compatible with the electrolytes at high temperature, in order to ensure that secondary phases are not created at the respective interfaces, which would decrease the performance of the cell. In the case of composite electrodes (as it is the case of the anode), in which the interface between an electronic conductor and an ion conductor creates the active electrochemical reaction sites, the reactivity between the two materials is a key issue. The concentration of these interfaces, called the *triple-phase boundaries* (TPB), can be optimized through the shaping procedure by changing the proportion and grain size of the two materials and the volume and shape of the porosity.

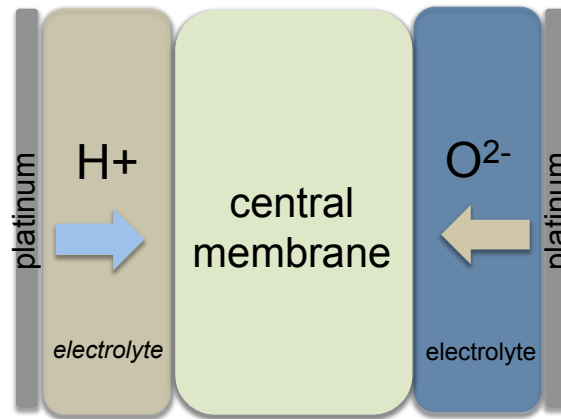


**Figure II.1** : Proof of concept prototypes scheme.

For these reasons, it was decided that, in a first phase, the POC prototypes would not include typical electrodes because the variability of the microstructures and the compatibility of the materials would have an important impact in the system's performance that should be studied later. Thus, the first prototypes have a three layer structure constituted by the two dense electrolytes and the porous central membrane, as it is shown in figure II.1. The electrodes are constituted by a platinum coating. Obviously, the electrolytes are constituted by a proton conductor and an oxygen-ion conductor. The central membrane must conduct both ions and therefore will be a composite of both electrolyte materials. Such a layered structure is new in field of fuel cells and therefore, at this point, many questions don't have an answer. It is not known if the ion recombination will occur or if it needs the use of a catalyst neither what is the better percentage of each of the materials and what is the best porosity volume that allows the reaction to occur.

Once the design of the prototypes was chosen, a decision about the materials used to shape them was made.

## II.3 Electrolyte materials

An electrical charge can be conducted by a material in the form of an ion or an electron. The electrical conductivity ( $\sigma$ ) of a material is, thus, the sum of electronic parts ( $\sigma_e, \sigma_h$ ) and an ionic contribution ( $\sigma_{ion}$ ):

$$\sigma = \sigma_e + \sigma_h + \sigma_{ion} = e_0(n\mu_n + p\mu_p) + z e_0 N_{ion} \mu_{ion} \quad (\text{II.1})$$

where  $n$ ,  $p$ , and  $N_{ion}$  are the concentrations of electrons  $e$ , holes  $h$ , and ions, respectively, and  $\mu_n$ ,  $\mu_p$ , and  $\mu_{ion}$  their mobilities ( $e_0$  is the elementary charge and  $z$  is the valence of the ion).

Materials can be classified by their prevailing type of conductivity: in the electronic conductors the electrical charge is conducted in the form of electrons; in the mixed ionic-electronic materials, both ions and electrons are responsible for the charge conduction; and in the ionic conductors, such as several metal oxides, a specific ion generally acts as the charge carrier.

In an electrochemical device, the function of an electrolyte is to separate its electrodes, blocking electronic conduction but allowing charge to pass in the form of selected ions because any electronic conduction would short-circuit the system. An electrolyte must also be gastight in order to avoid the direct reaction of combustion between the fuel in the anode and the oxygen in the cathode. Thus, each electrolyte is in contact with one of the electrodes and, in an IDEAL-Cell, with the central membrane. Therefore they must be stable under oxidizing and reducing conditions and must not react with the electrodes and central membrane materials to avoid the formation of secondary phases that would decrease the performance of the cell. The materials must also be mechanically adjusted because during production and operation, they undergo temperature cycles that cause their expansion and contraction. If the materials have a similar behavior at high temperature, cracking and delamination of the electrode/electrolyte and central membrane/electrolyte interfaces are prevented during thermal cycling.

An electrolyte is defined by its ability to conduct electrical charge in the form of ions and not in the form of electrons and therefore the materials used as electrolytes are ionic conductors with negligible electronic conduction. A solid material with ionic conductivity must contain in its crystal structure a high concentration of mobile ions that can move relatively easily from the equilibrium position in a long-range path through which they can migrate. In order to understand the choice of an electrolyte material, it is important to understand how the ionic conduction occurs.

In an oxide, when an ion moves in a lattice, it has to occupy a new position in the crystal structure - a vacant or interstitial position - and in the act of migrating it generates a vacant site. Both vacant and interstitial oxygen ions are considered as point defects with regard to the ideal crystal structure of a material. Thus the mobility and concentration of defects in a material are linked to its conduction properties. The specific conductivity,  $\sigma$  is a thermally activated process given by equation II.2.

$$\sigma = \frac{\sigma_0}{T} \exp\left(\frac{-E_a}{kT}\right) \quad (\text{II.2})$$

where  $\sigma_0$  is called the prefactor,  $E_a$  is the activation energy for the diffusion process and  $k$  is the Boltzmann constant.

However, for a material to be an ionic conductor, the presence of a high concentration of mobile ions may not be enough. It must have a structure that is favorable to ions mobility, there must be an interconnected equivalent sites for the mobile ion, which are only partially occupied. At low temperatures, the normal sites are fully occupied and the interstitial sites are empty. But as the temperature increases, intrinsic thermal disorder generates large numbers of self interstitial-vacancy pairs and results in partial occupancy of the combined sub-lattices. The defects created like this are called intrinsic defects.

Partial occupation of equivalent sites can also be obtained by non-stoichiometry by doping the material with aliovalent cations to produce extrinsic defects [14].

In general, a material has a high specificity in the type of ions that are transported in its crystal structure. In the case of an electrochemical device like an IDEAL-Cell, two electrolytes

conduct two different ions: protons in the anode compartment and oxygen ions in the cathode compartment.

### II.3.1 Proton electrolyte materials

Proton-conducting materials can be classified in two categories: those that contain protons in their stoichiometry and those in which protons are introduced from an external source during their synthesis or exist in equilibrium with hydrogen or water in the surrounding atmosphere. Whatever the nature of the material is, because of their charge and size, protons do not exist as free ions but always in interaction with other ions of its structure. In a solid oxide, a proton can interact with a lattice oxygen but commonly they are part of a larger molecule such as  $\text{OH}^-$ ,  $\text{H}_3\text{O}^+$  or  $\text{NH}_4^+$ . Some of the better studied proton conductors require a high degree of hydration to be performing. A good review about the conduction mechanism in these materials can be found in [15]. However, these materials are not stable at temperatures higher than  $300^\circ\text{C}$  since they dehydrate which causes a loss in their performances [16].

At higher temperatures, in the  $600\text{--}800^\circ\text{C}$  range, the highest mobilities of proton defects have been reported for perovskite-type oxides [15].

Recently, fast proton conduction has been reported in non-perovskite structured materials. These materials have conductivities about ten times lower than the state-of-the-art perovskite proton conductors but they show improved stability in  $\text{CO}_2$ - and water-containing atmospheres [14].

#### II.3.1.1 Proton conduction mechanism

The perovskite structured materials draw considerable interests since they are the better known and better performing high temperature proton conductors. These ceramic oxide materials have been found to have protonic conductivity by H. Iwahara *et al.* in  $\text{SrCO}_3$ -based solutions under hydrogen-containing atmosphere [12]. These materials are extrinsic systems since the proton defects, which are the charge carriers, are introduced in the crystal structure by dissolution of water vapor. The reaction can be written, in Kröger-Vink notation, as:



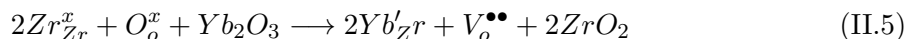
where  $\text{O}_o^x$  is a lattice oxygen and  $\text{V}_o^{\bullet\bullet}$  is an oxygen vacancy and  $\text{OH}_o^\bullet$  is a proton defect.

When the proton defects  $\text{OH}_o^\bullet$  have replaced oxygen vacancies, the electrolyte can diffuse the protons coming from the anode:



and are then removed at the central membrane, in the case of an IDEAL-Cell.

Thus, one single oxygen vacancy generates two proton defects that are free to move acting as charge carriers. The concentration of oxygen vacancies in the perovskite crystal structure is, therefore, the driving force for the formation of proton defects. These vacancies are created intrinsically through the Frenkel and Schottky mechanisms but in too low concentrations to generate fast ionic conductivity. Therefore, these structures have to be substituted by lower valence ions. In order to compensate the missing charge, oxygen vacancies are created in the crystal structure. This is, for example, the case of doping  $\text{Yb}^{3+}$  for  $\text{Zr}^{4+}$  according to the solid solution  $\text{BaZr}_{1-x}\text{Yb}_x\text{O}_{3-x/2}$ . In Kröger-Vink notation, this can be written as [14]:



The highest proton defect mobilities have been found in cubic perovskite oxides ( $ABO_3$ ). These perovskites structure are called cubic because, in its ideal configuration, B ions form a cube with the A cation in its center and one oxygen in each of its corners, as shown in figure II.2(a) and (b).

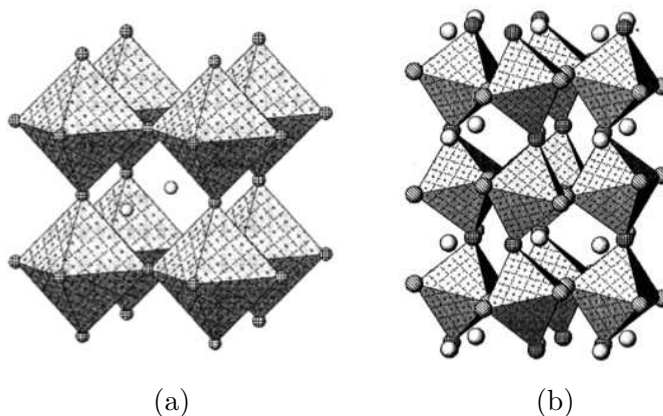


**Figure II.2** : The aristotype structure of an  $ABO_3$  perovskite with the A-cation surrounded by four  $BO_6$  octahedra (a). Oxygen ions are in the corners of the octahedra and the B-cation is in its center. The crystal structure of  $BaCeO_3$  at room temperature (b) [17].

In such a structure, the mechanism of conduction happens in two steps: the rotation of the proton defect and the transfer of the proton to the neighboring oxide ion. The latter step seems to be the rate-limiting one since the rotation of the defect has low activation barriers. According to this mechanism, the proton would be the only mobile species, while oxygen has a fixed position in the materials crystal structure. However, in most perovskite-type oxides, oxygens are separated by a distance greater than 290 pm which is too high for the formation of a strong hydrogen bonds [15]. Thus, the proton can only be transferred if the lattice undergoes a distortion in order to reduce the distance between the oxygen atoms. The energy that the lattice needs to deform is equivalent to the energy it gains with hydrogen bond, therefore, short oxygen and large oxygen separations have the same probability of occurring. The first are advantageous for defect reorientation while the latter favor the proton transfer. However high activation energies of the protonic defects mobility in these structures show that the path through which protons are conducted is not linear. Proton actually is transferred outside the  $BO_6$  octahedron, creating a highly deformed hydrogen bond as one can see in figure II.3 (a) and (b).

This path allows the transfer of the proton minimizing the interactions with the B cation charge. The influence of these interactions is shown by the difference between proton mobilities in cubic perovskites with pentavalent B-site (I-V perovskites) and tetravalent B-site (II-IV perovskites) perovskites, as shown in II.4 [15].

### II.3.1.2 Materials choice

Amongst the perovskite structured oxides that have been reported to be suitable for proton electrolyte applications, Y:BaCeO<sub>3</sub> solutions seem to be those that present higher

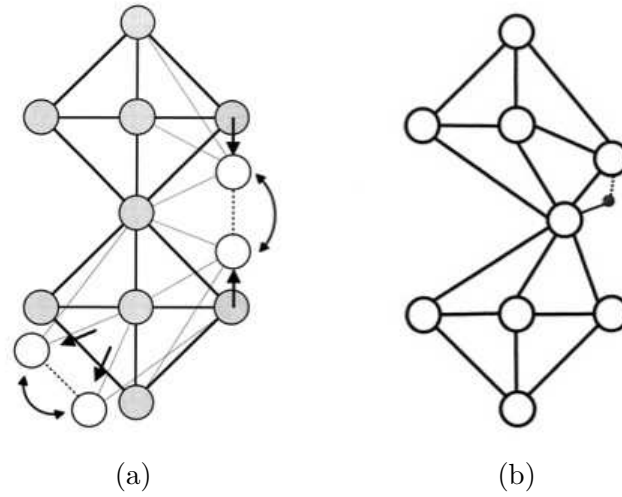


**Figure II.3** : Deformation of the perovskite structure in (a) [18] to allow the transfer of the proton, in black, to the neighboring oxygen ion (b) [15].

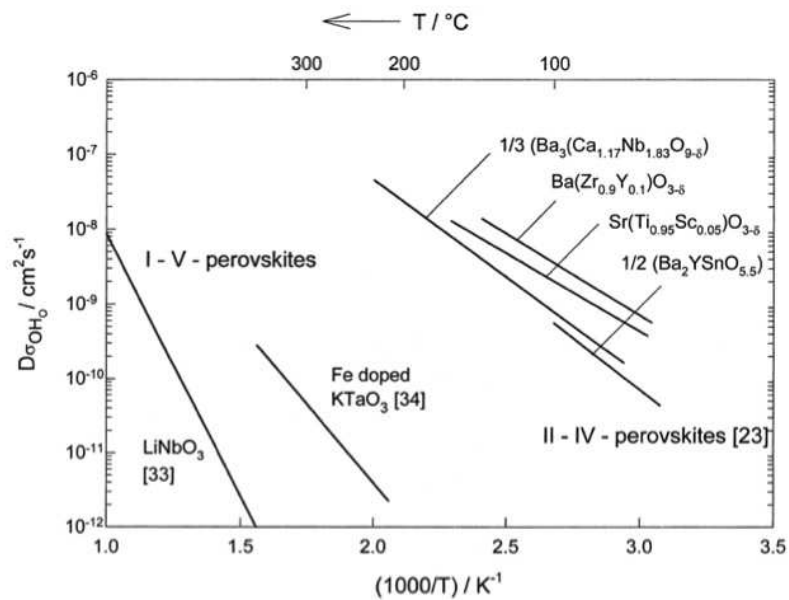


**Figure II.4** : Proton diffusion coefficients in I-V and II-IV perovskite-type oxides [15].

conductivities, as it can be seen in figure II.5. However, these materials have a low chemical stability under CO<sub>2</sub>-containing atmosphere.

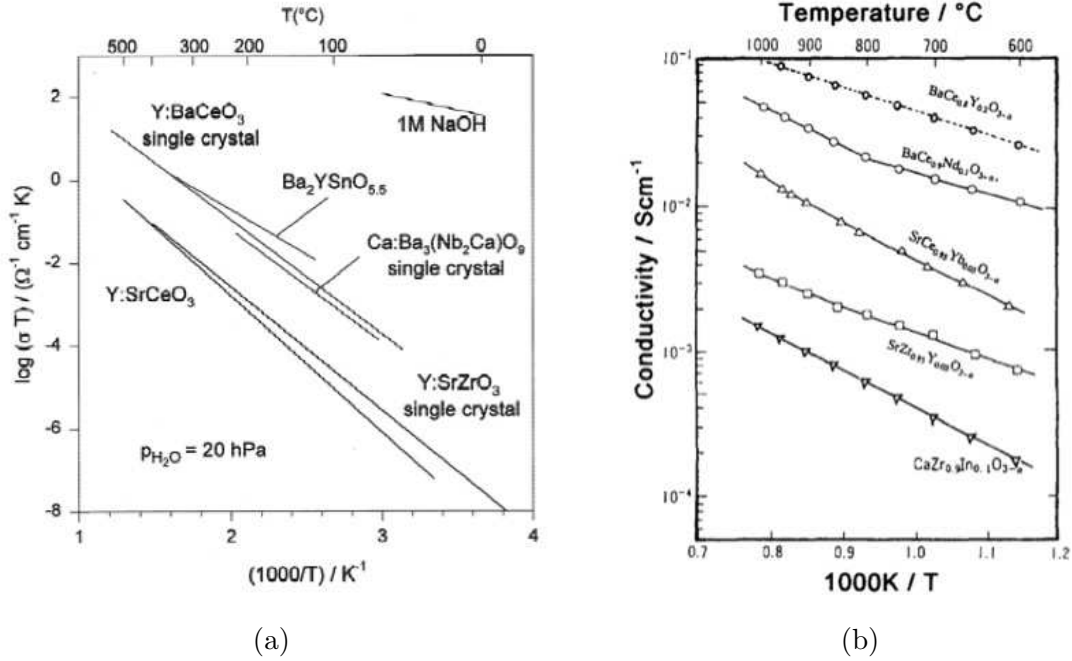


**Figure II.5** : Proton conductivities for several perovskite-structured proton conductors [17] [16].

Ma *et al.* [19] studied these materials and found that BaCe<sub>0.9</sub>Y<sub>0.1</sub>O<sub>3-δ</sub> (BCY10) has one of the highest proton conductivities at 700°C with  $\sigma = 20 \text{ mS cm}^{-1}$  in wet hydrogen.

From the experiments carried out in our laboratory by J. Hafsouli [20], the barium cerate-based solution with higher conductivity is BaCe<sub>0.85</sub>Y<sub>0.15</sub>O<sub>3-δ</sub>. Therefore this was the material chosen as proton conductor.

Yttrium doped barium cerate, BaCe<sub>0.85</sub>Y<sub>0.15</sub>O<sub>3-δ</sub>, was supplied by *Marion Technologies*, a company specialized in ceramic materials production.

The composition of the powder was confirmed by X-ray diffraction as it can be seen in figure II.6. Residual impurities of BaCeO<sub>3</sub> were also detected.

According to the information given by the supplier, this powder has a narrow particle size distribution centered in 0.23  $\mu\text{m}$ , with the granulometric parameters presented in table II.1.

**Table II.1** : Granulometric data for the BaCe<sub>0.85</sub>Y<sub>0.15</sub>O<sub>3-δ</sub> powder.

d <sub>10</sub>	d <sub>50</sub>	d <sub>90</sub>
0.15 $\mu\text{m}$	0.23 $\mu\text{m}$	0.71 $\mu\text{m}$

However, the particle size distribution is wider than what the granulometric values may indicate. As shown in figure II.7, the powder particle size distribution includes particles from 0.2  $\mu\text{m}$  to 2  $\mu\text{m}$ .

Observations with scanning electron microscope show that this powder is agglomerated in clusters from 100  $\mu\text{m}$  to 20  $\mu\text{m}$  of small particles of a few micrometers, as it can be seen in figures II.8 (a) and (b).

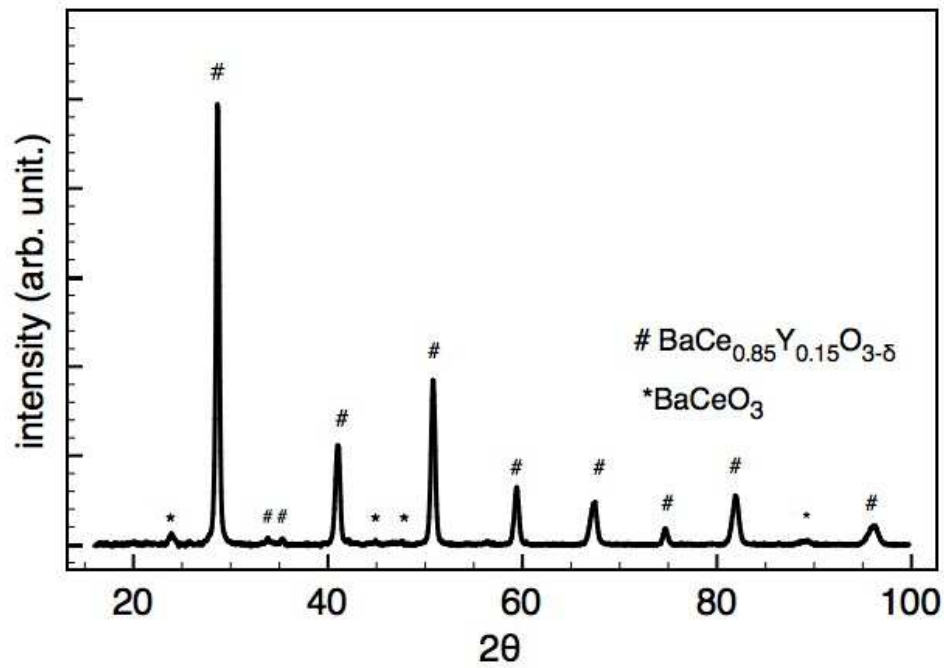


Figure II.6 : Particle size distribution in volume for  $\text{BaCe}_{0.85}\text{Y}_{0.15}\text{O}_{3-\delta}$  powder.

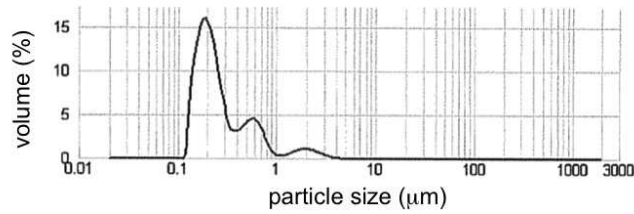


Figure II.7 : Particle size distribution in volume for  $\text{BaCe}_{0.85}\text{Y}_{0.15}\text{O}_{3-\delta}$  powder.

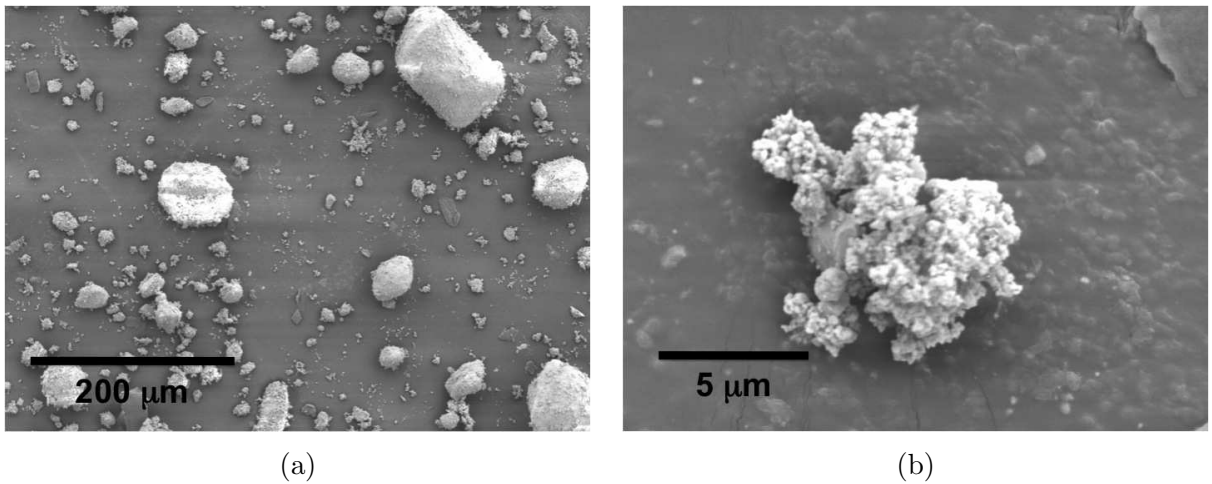
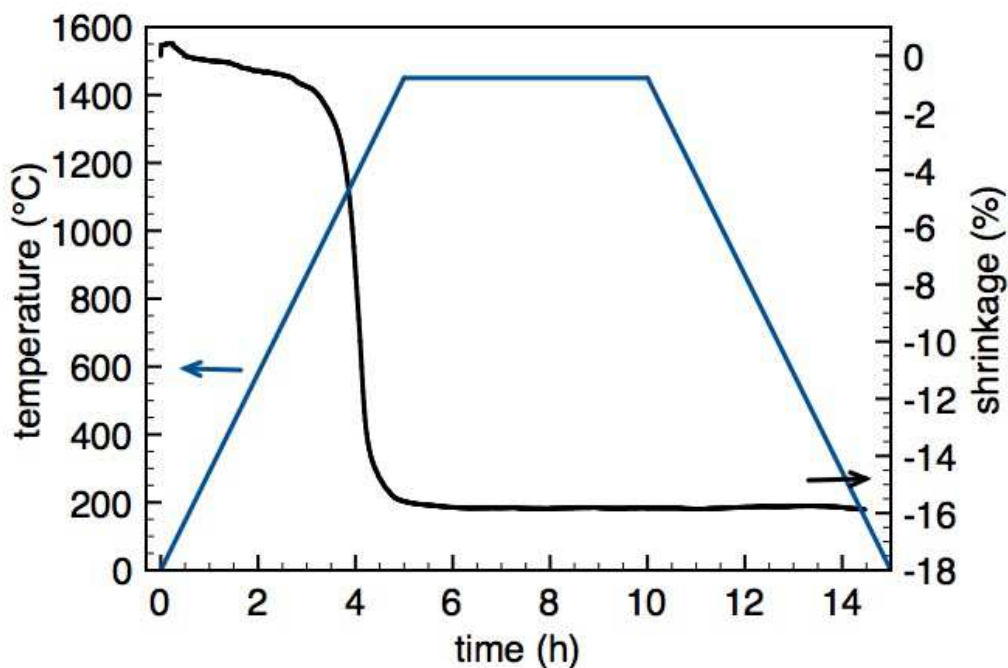


Figure II.8 : Morphology of the  $\text{BaCe}_{0.85}\text{Y}_{0.15}\text{O}_{3-\delta}$  powder.

A dilatometric study of this powder was carried out in pellets of 5.2 mm thickness and 10 mm diameter pressed at 100 MPa for 5 minutes. They were then put in the tester between two platinum foils to keep the alumina ( $\text{Al}_2\text{O}_3$ ) of the experimental apparatus from reacting with the barium cerate. A load of 5 g was applied in order to assure that the apparatus was in contact with the pellet during the whole experiment and would follow the sample's shrinkage. The behavior of the platinum foils during the same thermal cycle was previously studied and it was taken into account in the analysis of the behavior of the ceramic pellet. As shown in figure II.9 the thermal cycle used consisted in heating the sample at  $5^\circ\text{C}/\text{min}$  until  $1450^\circ\text{C}$ , where the temperature is held for 5h. The sample is then cooled at  $5^\circ\text{C}/\text{min}$  until room temperature.



**Figure II.9** : Thermal treatment used for the study of the thermo-mechanic behavior of  $\text{BaCe}_{0.85}\text{Y}_{0.15}\text{O}_{3-\delta}$ .

The behavior of the  $\text{BaCe}_{0.85}\text{Y}_{0.15}\text{O}_{3-\delta}$  pellet during the thermal treatment is shown in figure II.9. The sample volume decreases slightly with the increasing of temperature until  $900^\circ\text{C}$ . At this temperature, the sample shrinkage strongly increases. The sample's shrinkage rate can be obtained through the expression:

$$\text{shrinkage rate} = \frac{l_{t+1} - l_t}{(t+1) - t} \quad (\text{II.6})$$

where  $l_t$  is the height of the sample at time  $t$ .

In figure II.10 the evolution of the shrinkage rate with the sample temperature is plotted. These data allow us to conclude that  $\text{BaCe}_{0.85}\text{Y}_{0.15}\text{O}_{3-\delta}$  powder reaches its highest shrinkage rate at  $1260^\circ\text{C}$ .

A pellet of  $\text{BaCe}_{0.85}\text{Y}_{0.15}\text{O}_{3-\delta}$  powder was sintered at  $1300^\circ\text{C}$  at different durations. It was found that the density of the pellet after sintering didn't change significantly after 5h. The density of the pellets after sintering (see figure II.11(a) and (b)) was 94% of the theoretical

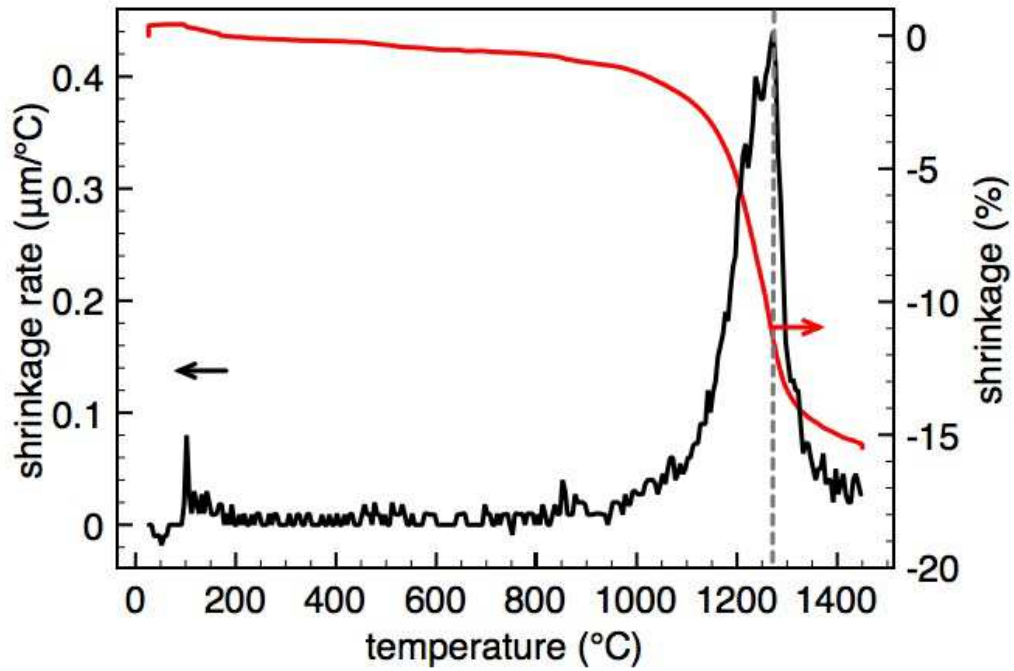


**Figure II.10** : Shrinkage rate and shrinkage of  $\text{BaCe}_{0.85}\text{Y}_{0.15}\text{O}_{3-\delta}$  powder as function of temperature.

one.

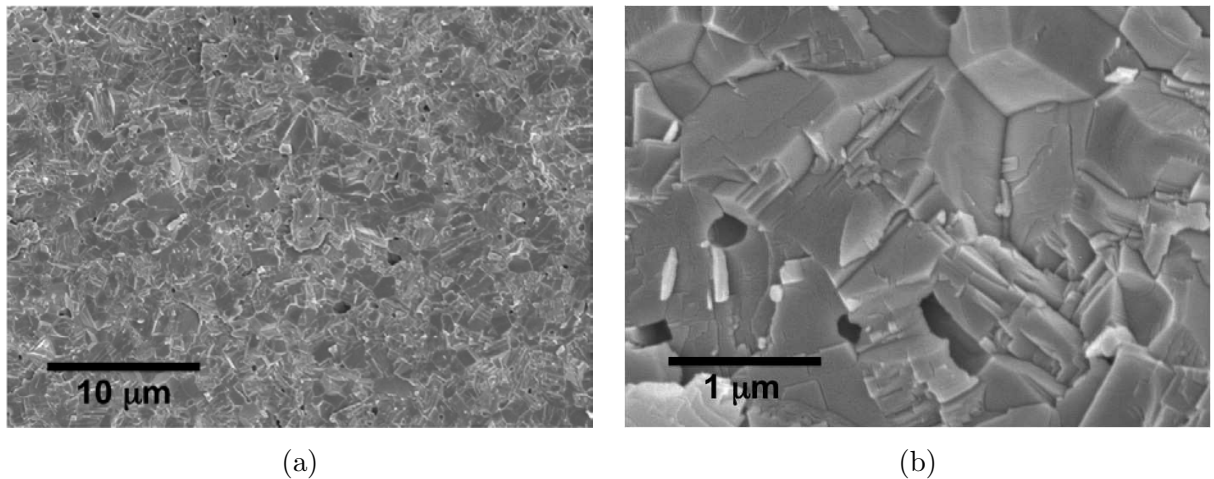


**Figure II.11** : S.E.M. image of a  $\text{BaCe}_{0.85}\text{Y}_{0.15}\text{O}_{3-\delta}$  pellet sintered at  $1300^\circ\text{C}$  for 5h.

### II.3.2 Oxygen ion electrolyte materials

An oxygen ion electrolyte must fulfill the same requirements of the proton electrolyte material except that  $\text{O}^{2-}$  ions are the charge carriers instead of  $\text{H}^+$ . In the operating conditions of temperature and atmosphere, these materials must be specific oxygen-ion conductors. This

type of conductivity was first observed in doped zirconia ( $\text{ZrO}_2$ ) by Walther Nernst in the last decade of the nineteenth century. In the late 1930s, the first SOFC concept used yttria-stabilized zirconia (YSZ) as oxygen-ion electrolyte material which remains until today the state-of-the-art material [21].

### II.3.2.1 Oxygen ion conduction mechanism

As for proton conduction, the oxygen ion conduction depends on the mobility and concentration of the defects in the structure of the oxide.

Fluorite structured doped oxides are the most well known and better understood oxygen ion conductors [22]. These materials are not fast oxygen ion conductors until they are doped with aliovalent cations. The introduction of these ions into the host lattice introduces oxygen vacancies, as for example the addition of  $\text{Gd}_2\text{O}_3$  to ceria. This process can be translated by the following defect equation in Kröger-Vink notation:



where  $\text{Gd}'_{\text{Ce}}$  is a gadolinium atom replacing in a cerium position,  $\text{O}_{\text{O}}^{\times}$  is an oxygen atom in its position and  $\text{V}_{\text{O}}^{\bullet\bullet}$  is a vacancy in an oxygen site.

In this case the neutrality condition implies that  $[\text{Gd}'_{\text{Ce}}] = 2[\text{V}_{\text{O}}^{\bullet\bullet}]$ . Since this condition is valid for any trivalent metal substitutional ions, the vacancy concentration will be linearly dependent upon the dopant concentration. However, as it can be seen in figure II.12(a), the conductivity of ceria solutions reaches a maximum for a certain dopant level.

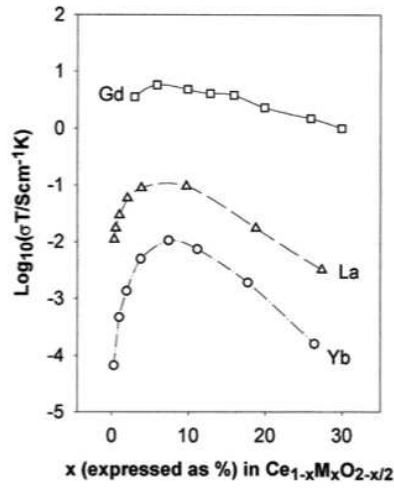
The main reason for this maximum is the presence of a minimum energy barrier necessary to activate ionic conduction. This term is obviously very important because it determines the temperature dependence of the ionic mobility [22] [23]. As one can see in figure ??, Faber et al. [24] have determined the minimum of the activation energy for oxygen ion conduction in five different ceria solid solutions. The minimum determined coincides only roughly with the minimum in conductivity because it is not the only parameter having an influence in the conductivity depending on the concentration of the dopant. Two theories are proposed to understand this minimum. Wang et al. [25], explain it by the presence of a minimum of the electrostatic effect of the charged dopant ions, lowering the activation energy for conduction. On the other hand, Faber et al. [24] attribute the presence of the minimum to the change in the energy of oxygen sites in the vicinity of a dopant cation in the interaction radius,  $r_c$ . The spheres of influence of each dopant ion would overlap with the increase of its concentration, creating an interconnected pathway with a lower activation energy for conduction.

Faber et al. [24] also showed that the minimum of activation energy changed differently according to the chemical identity of the dopant cation (see figure II.12(b)).

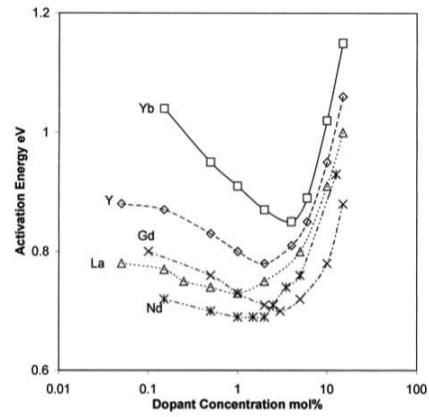
Kilner [26] has pointed out that both calculated and experimental data for the activation enthalpies are correlated with the ionic radius of the dopant, as shown in figure II.13, finding a new minimum when the ionic radius of the host and the dopant approximately matched.

Thus, two conclusions can be drawn about the doping of fluorites with a dopant of effective charge  $-1$ : (a) the activation energy is concentration dependent with a minimum at low dopant concentrations; (b) for a given concentration the activation enthalpy is dependent upon the size of the dopant with a minimum when the radii of the host and the dopant are approximate.

Even though it is not the oxide with the highest ionic conductivity, YSZ has stable ionic conductivity in a large range of oxygen partial pressure while the low mobility of the electronic charge carriers make its electronic conductivity negligible with respect to the ionic one. Zirconia has a fluorite structure that has the same conduction mechanism explained



(a)



(b)

**Figure II.12** : Isothermal conductivity for different ceria-based solutions. [22]. Activation energies for oxygen ion conductivities in several doped ceria solutions [24](b).

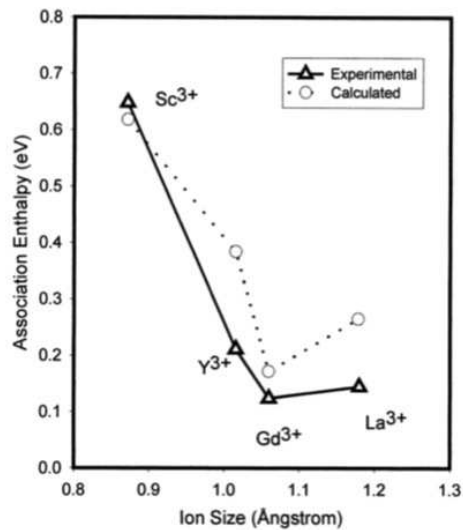


**Figure II.13** : Association enthalpy of several ions in ceria-based solutions as a function of the ions radius [22].

above. Thus, zirconia's conductivity can be enhanced by different dopants, as it can be seen in figure II.14. Amongst these dopants a maximum of conductivity is reached for scandium since its ionic radius is closest to that of zirconia (figure II.13)

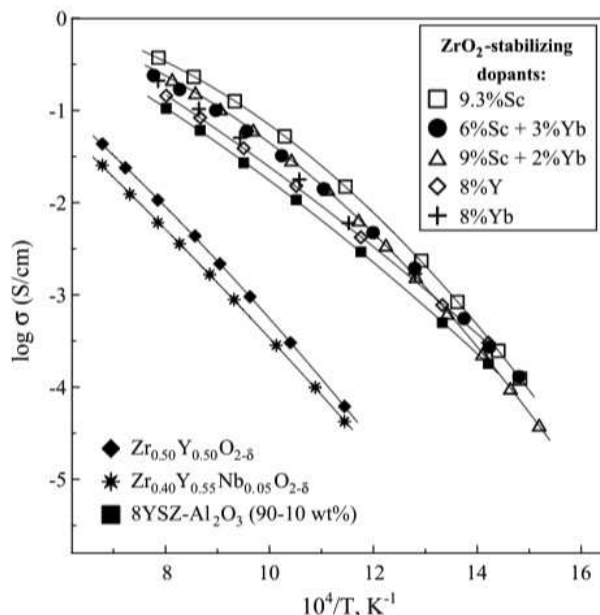


**Figure II.14** : Conductivities of several zirconia-based solutions doped with different cations [27].

Zirconia has, however, disadvantages that made the scientific community search for better alternatives. At operating conditions of about  $1000^{\circ}\text{C}$ , a degradation of zirconia's ionic conductivity is observed after less than 1000 h. This could be overcome by decreasing the systems operating temperature but since ionic conductivity is a thermally activated process (as seen above), the transport properties would not be high enough to achieve satisfactory cell performances. Electrolyte performances can be improved by reducing its thickness, which would allow it to have lower ohmic losses. However, alternative electrolytes that have higher conductivities than zirconia-based materials can be used in order to do so.

Amongst the alternatives to zirconia-based electrolytes, cerium dioxide,  $\text{CeO}_2$ , another fluorite-structured oxide, presents higher oxygen-ion conductivities. As the fluorites mentioned above, its transport properties can be improved by doping with rare earth cations that will reach a maximum for a certain concentration that will depend on the dopant's ionic radius, as explained before. In figure II.15 we can see that ceria-based solid solutions  $\text{Ce}_{1-x}\text{M}_x\text{O}_{2-\alpha}$  reach its best performance for  $\text{M} = \text{Gd}$  or  $\text{Sm}$  and  $x = 0.10 - 0.20$ .

Doped ceria is also chemically stable towards potential electrode materials. Fuel cells with doped ceria electrolyte, Ni/ceria anode and  $\text{La}_{1-x}\text{Sr}_x\text{Co}_y\text{Fe}_{1-y}\text{O}_{3-\delta}$  cathode have reached high power densities of  $400 \text{ mW cm}^{-2}$  [27]. These materials have, however, disadvantages related to the low stability of the cerium ion that changes its valence from  $\text{Ce}^{4+}$  to  $\text{Ce}^{3+}$  in reducing atmospheres becoming mixed conductors which can lead to the short-circuit of the cell. Such problem can be overcome by reducing the operating temperature of the system to  $<550^{\circ}\text{C}$ . In an IDEAL-Cell system the oxide-ion conducting electrolyte material is not in contact with the anode and therefore it isn't in reducing atmosphere, which can be another advantage of this concept.

Thanks to the growing interest in SOFC systems many electrolyte materials with

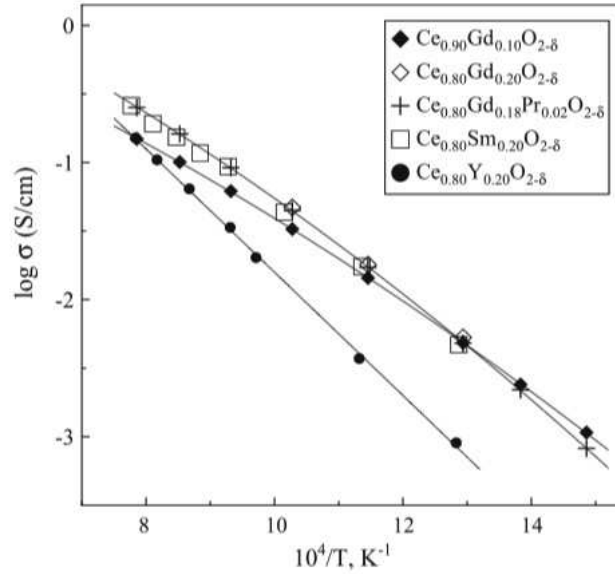


**Figure II.15** : Conductivities of ceria-based solutions for different dopant ions [27].

structures other than fluorite have been investigated and have been found to have high ionic conductivities.

Some perovskite structured materials have been reported to have oxygen-ion conductivities comparable to those of zirconia-based electrolytes. However, very few perovskites are pure ion conductors. Lanthanum gallate ( $\text{LaGaO}_3$ ) based materials doped with strontium in the A-site and magnesium in the B-site exhibit high ionic conductivity and good chemical compatibility with cathode materials. However, they show reactivity with state-of-the-art Ni-containing anode materials and, in reducing atmospheres, gallium evaporates compromising the electrolyte stability. Again, like for doped ceria solutions, these materials may be used in an IDEAL-Cell since the oxygen ion electrolyte is separated from the anode and its reducing atmosphere.

A similar phenomena occurs for bismuth oxide ( $\text{Bi}_2\text{O}_3$ ) systems known since the early 1970's for having higher conductivities than zirconia-based electrolytes but become mixed conductors in reducing atmospheres due to the change in the oxidation degree of bismuth.

High oxygen ion conductivities have also been reported in apatites,  $\text{La}_2\text{Mo}_2\text{O}_9$ - based (LAMOXY),  $\text{Bi}_4\text{V}_2\text{O}_{11}$ -based (BIMEVOX) materials but their weak chemical stability and limited purely ionic conductivity domain keep them from being used for practical applications.

The fast developments in this field resulted in a lack of knowledge of important properties such as the conduction mechanism, the electronic conductivity domain and the long-term chemical stability.

### II.3.2.2 Material choice

Due to the innovative nature of this fuel cell concept, the choice of the materials must be conservative in order to reduce the unknown phenomena that can occur during the processing and testing of the different cell components. Thus, for all the reasons explained above, it was decided to choose a fluorite structured material since their long-term stability and ionic conductivity domains have already been tested. Between zirconia-based and ceria-based

**Table II.2** : Granulometric data for the  $\text{Ce}_{0.85}\text{Y}_{0.15}\text{O}_{2-\delta}$  powder.

$d_{10}$	$d_{50}$	$d_{90}$
$0.14\mu\text{m}$	$0.19\mu\text{m}$	$1.86\mu\text{m}$

solutions, the last ones were chosen as oxygen ion conducting electrolyte materials. Zirconia presents a high degradation of the transport properties at high temperatures. Even though this is observed for temperatures around  $1000^\circ\text{C}$  and the new concept is expected to operate  $600^\circ\text{C}$  -  $700^\circ\text{C}$  this was a risk we didn't want to take, specially considering the advantages of doped ceria solutions. Doped ceria has higher ionic conductivity than zirconia-based solutions, however, it is not stable in reducing atmospheres. In an IDEAL-Cell this should not be a problem since the oxygen-ion electrolyte is not in contact with the anode compartment of the cell.

Amongst the doped ceria solutions, the one that presents higher level of performances at  $600^\circ\text{C}$  is, as we can see in figure II.15,  $\text{Ce}_{0.9}\text{Gd}_{0.1}\text{O}_{2-\alpha}$ . However, this was not our choice. The proton electrolyte material chosen is an yttrium-doped solution and, since both electrolyte materials will be in contact in the central membrane, it is important that they are chemically compatible. Thus, it seemed a wiser choice for the oxygen ion electrolyte, the same dopant cation used in proton electrolyte material. The concentration of the dopant chosen was the same used in the proton electrolyte in order to avoid a concentration gradient that would act as the driving force for the diffusion of the dopant.

Thus, the oxygen electrolyte material chosen is  $\text{Ce}_{0.85}\text{Y}_{0.15}\text{O}_{2-\delta}$ , here called YDC15.

This powder was also supplied by the company Marion Technologies.

It is a powder with a particle size distribution centered in  $0.2\mu\text{m}$  with the granulometric data presented in tableII.2. However, as it is shown in figure II.17, a small volume fraction of powder has particle size of about  $2\mu\text{m}$ .

An X-ray diffraction experiment was carried out and it was verified that the powder supplied was single-phased (figure II.16).

This powder is roughly agglomerated in clusters of different sizes, as it can be seen in figure II.18.

The dilatometric behavior of this material was studied using the same procedure and thermal cycle described in II.3.1.2. The evolution of the sample height with the increase of the temperature is shown in figure II.19.

For this powder, shrinkage strongly increases after  $800^\circ\text{C}$ . The shrinkage rate was determined through equation II.6 and its evolution with the sample's temperature is shown in figure II.20. It's possible to conclude that the highest shrinkage rate is reached for a temperature of  $1190^\circ\text{C}$ .

After sintering this powder for 5h at  $1200^\circ\text{C}$ , a density of 92% of the theoretical density was reached (see figure II.21(a) and (b)).

## II.4 Shaping of proof of concept prototypes

The proof of concept prototypes are three layered samples with a dense proton conducting electrolyte, a dense oxide-ion conducting electrolyte and a porous composite central membrane. The choice of the materials to produce such samples was based on the specificity of each electrolyte, their chemical compatibility and the reliability of the performances. The powders were supplied by Marion Technologies and their morphology, purity, and thermal

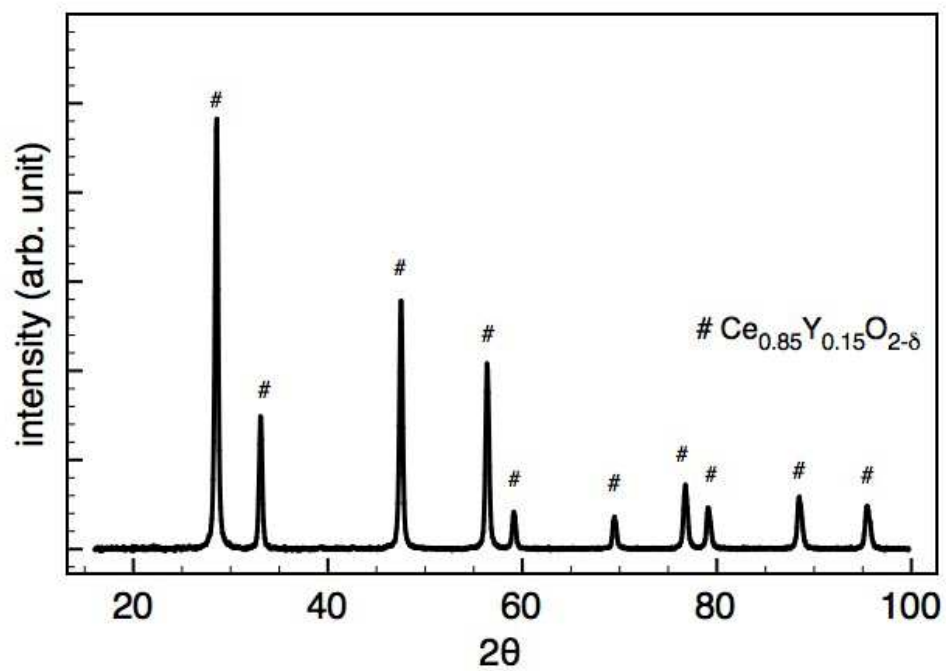


Figure II.16 : X-ray diffraction diagram for  $\text{Ce}_{0.85}\text{Y}_{0.15}\text{O}_{2-\delta}$  powder.

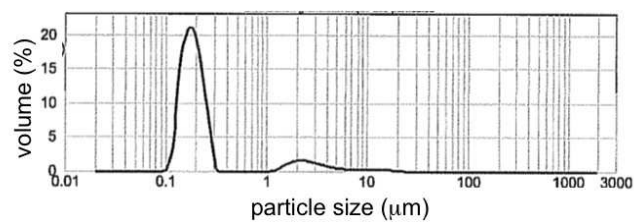


Figure II.17 : Particle size distribution in volume for  $\text{Ce}_{0.85}\text{Y}_{0.15}\text{O}_{2-\delta}$  powder.

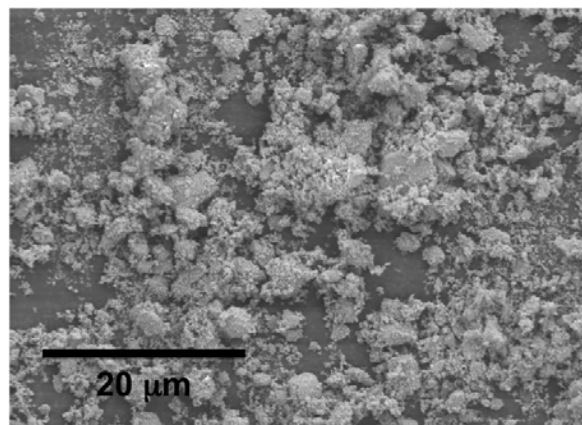
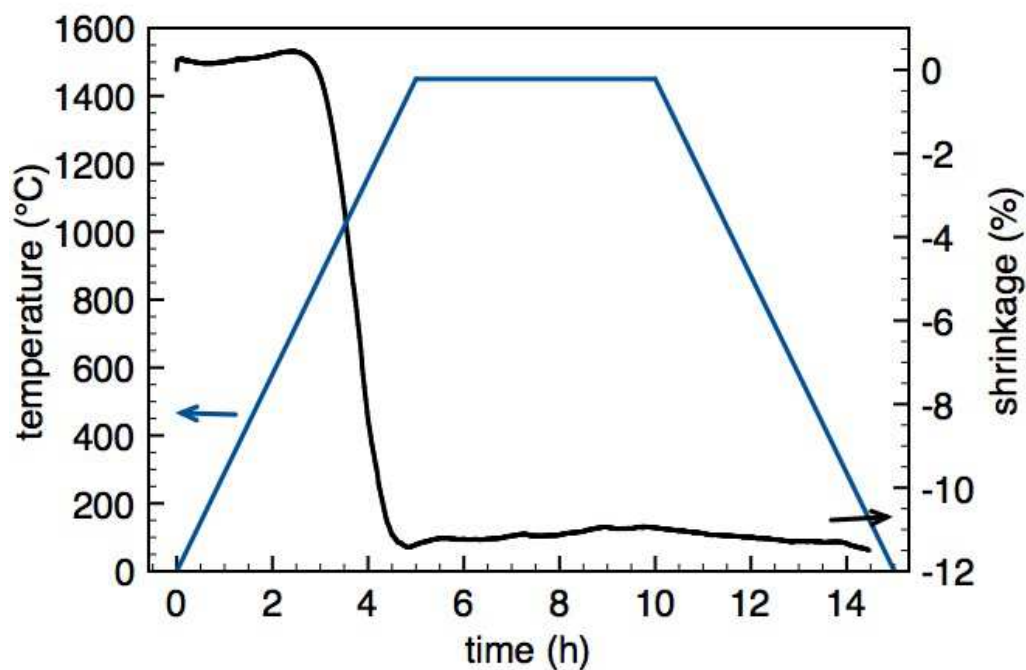
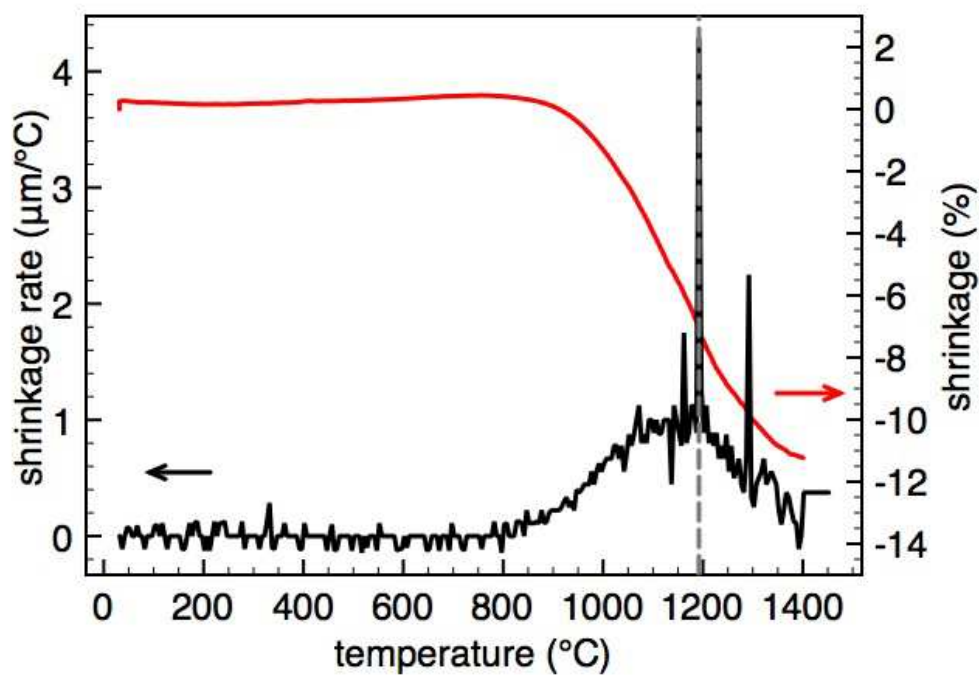


Figure II.18 : S.E.M picture of the  $\text{Ce}_{0.85}\text{Y}_{0.15}\text{O}_{2-\delta}$  powder.



**Figure II.19** : Dilatometry of the  $\text{Ce}_{0.85}\text{Y}_{0.15}\text{O}_{2-\delta}$  sample: in blue the temperature profile used and in black the shrinkage of the sample.



**Figure II.20** : Shrinkage rate (in black) and shrinkage (in red) of  $\text{Ce}_{0.85}\text{Y}_{0.15}\text{O}_{2-\delta}$  powder as function of temperature.

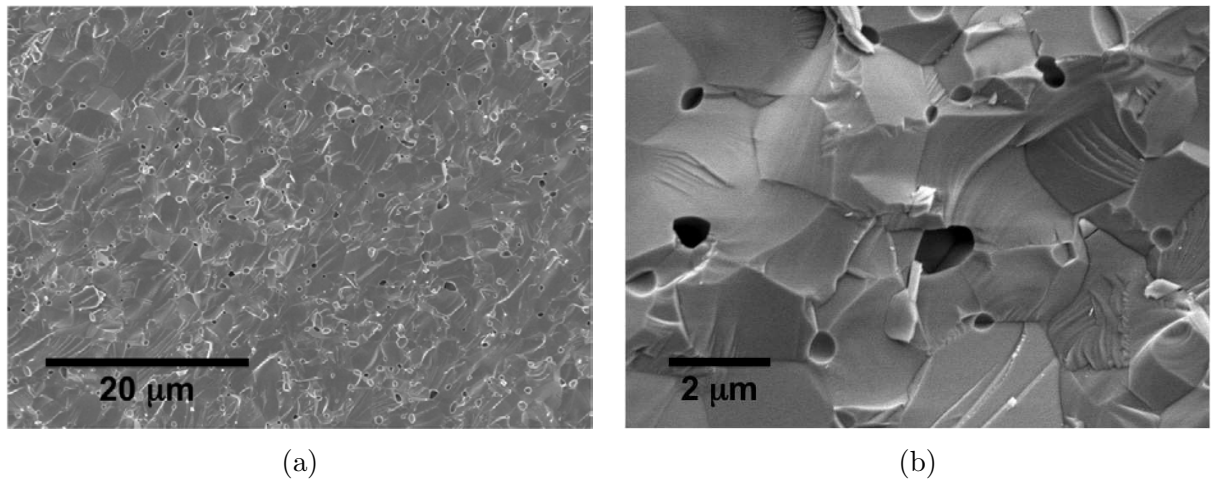


**Figure II.21** : S.E.M. image of a  $\text{Ce}_{0.85}\text{Y}_{0.15}\text{O}_{2-\delta}$  pellet sintered at  $1200^\circ\text{C}$  for 5h.

mechanic behavior were studied.

### II.4.1 Shaping techniques

The fabrication of these samples was a new challenge in the field of fuel cells, however, many techniques that could be adapted to this purpose have been used to produce fuel cells components over the years. At Centre des Matériaux two manufacturing techniques have been used for these applications: cold pressing and tape casting. These were the techniques chosen because the reproducibility of the results that could be achieved was an advantage to the project's reliability.

#### II.4.1.1 Cold Pressing

Cold pressing is generally used to process refractory and ceramic components for electronic applications. In this process, powders are put in a die, sometimes mixed with an organic binder, and pressed uniaxially to acquire the desired shape. After pressing, materials undergo a sintering treatment in order to have the microstructures and the mechanical strength needed.

This procedure is commonly used to produced pieces with different shapes in a fast and precise way.

For fuel cell applications, cold pressing may be used to produce dense or porous pellets that can be the support of a multilayered structure. The thickness of these pellets, after sintering, can vary from  $500\ \mu\text{m}$  to few millimeters.

#### II.4.1.2 Tape Casting

Tape casting is used as a ceramics shaping method since 1947. Previously used in the food industry, this technique has been widely used in new applications related to the electronic industry such as the fabrication of capacitors, gas sensors, solid oxide fuel cells and photovoltaic solar energy cells [28].

Tape casting allows to produce single or multilayered flat structures with good control of the thickness and porosity. The basic principle of tape casting is shown in figure II.23. A slip or slurry of the material being shaped is poured into a puddle or reservoir above a flat surface where a ceramic layer, or tape, will be cast. Behind the slurry puddle there

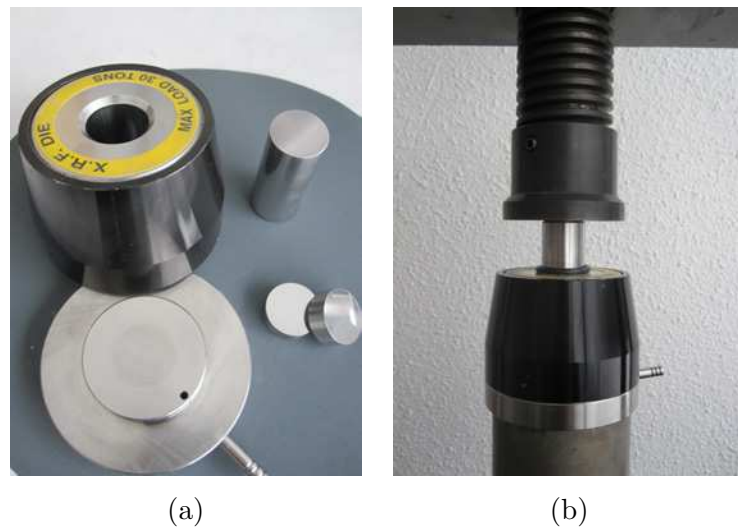


**Figure II.22** : Cold pressing die.

is a blade, also called doctor blade, through which the thickness of the layer is controlled. The layer can be formed through two different mechanisms: (1) the movement of the blade over the puddle, dragging it until the desired thickness is reached or (2) the surface below the puddle is set in motion pushing it against the blade that controls the thickness of the layer.

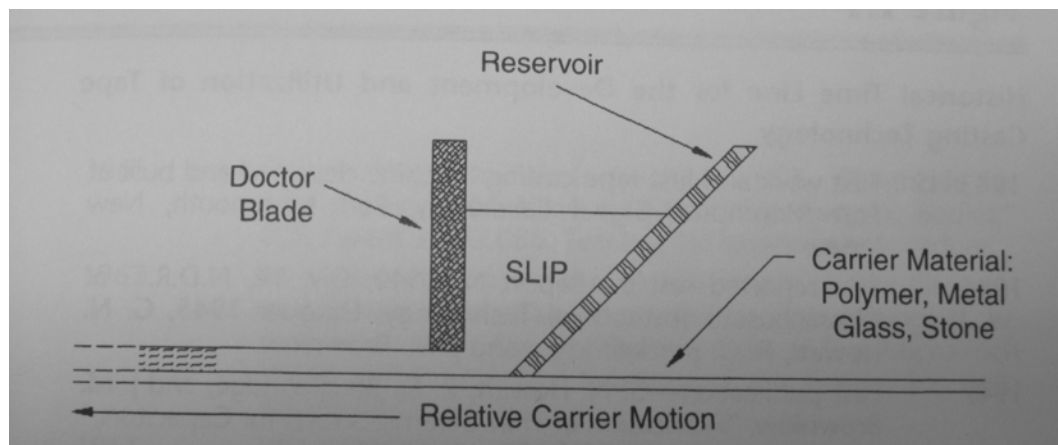


**Figure II.23** : Basic principle of the tape casting technique.

When the tape is cast, it is then dried and the solvents are evaporated, leaving a dry or green tape in the flat surface. Large flat tapes can be produced through this technique and therefore the slurry must produce structures with the necessary strength and flexibility. After drying the tape is sintered to remove all the compounds of the slurry and the material densifies until the desired microstructure and mechanical strength are reached. The sintered structure will be determined by the quality of the green tape that in its turn is strongly influenced by the slurry composition. A tape casting slurry is typically composed by the powder, a solvent, a binder, a plasticizer and a dispersant.

The powder morphology plays a determinant role in the quality of the green tape. For

instance, a highly packed green tape can only be obtained for a small particle size powder. However, a small particle size powder will have a high specific surface which requires high concentration of additives to give the tape the adequate flexibility and mechanical strength. These additives will fill the spaces between the particles keeping them from being in contact. During the sintering treatment of the tapes, mass diffusion occurs through the contact points between the particles and necks are formed. During these phase, the center of the particles remain at the same distance. In the following phase, porosity is closed and the tape shrinks creating a dense structure. Thus, the particle size and additives concentration is a key issue in the control of the microstructures. A powder typically used in tape casting has particle sizes between 1 and 4  $\mu\text{m}$  and specific areas between 2 and 6  $\text{m}^2/\text{g}$ .

Not only the particle size and specific surface are important but also the particle shape of a powder has an influence in the resulting microstructures. Spherical particles yield highly packed tapes while rod-like particles and platelets can have a preferred orientation grain growth during sintering due to the stress created by the blade. Homogeneity of the particles size is an important parameter because, as it was shown by Rémi Costa in his PhD thesis [29], particles of the same material with different sizes have different sintering kinetics. If the two regions of the same tape have different sintering behavior, shrinkage will not occur at the same rate in the whole structure and this will lead to the deformation of the structure. Thus, a narrow particle size distribution with a range of the order of  $\sim 6:1$  for the largest to the smaller particles is recommended. Non-homogeneous sintering kinetics and poor packing density can also occur for powders that are agglomerated as it is the case of the  $\text{BaCe}_{0.85}\text{Y}_{0.15}\text{O}_{3-\delta}$  and  $\text{Ce}_{0.85}\text{Y}_{0.15}\text{O}_{2-\delta}$  powders seen in figs. II.8 and II.18, respectively. For this reason, when powder and additives are mixed, the slurry goes through a ball milling phase in order to break these agglomerates and also to homogenize the mixture.

Tape casting is a "fluid forming process". In order to form flat tapes, the powder has to behave as a fluid. For that reason the powder is suspended in a solvent in which it is chemically stable. Another requirement of the solvent is that it must be able to dissolve the other additives of the slurry. That solvent can be aqueous or non aqueous (organic). In most of the tape casting applications, organic solvents are used. These solvents are more flexible because they can be used with hygroscopic materials. The choice of a solvent depends also on health, safety and environmental impact. The most commonly used organic solvents are ethanol, methanol, toluene, methyl ethyl ketone, xylenes, and 1,1,1, trichloroethylene [30]. There is also the possibility of using two or more solvents in the same slurry. The main advantage of this approach is the increase of the possibility of dissolving different organic additives. The use of azeotropes as solvent is also interesting because it has a higher dissolving capability than a mixture of solvents.

The mixture of the powders and solvent doesn't have the necessary mechanical strength and flexibility that allows the tape to be handled. These properties are given by the binder.

The binder is a continuous phase in the green tape; it acts like the matrix where the powder is in suspension. The choice of the binder depends on its solubility in the solvent, its viscosity, its cost, the burnout temperature and its by-products. Two main families of binders are used: the polyvinils and the polyacrylates. Both of these types have the ability of forming a film because they become long-chain polymers during drying. The main difference between them is the atmosphere to be used for their decomposition.

The most commonly used vinyl binders are PVC ((poly)vinyl chloride), PVA ((poly)vinyl alcohol) and PVB ((poly)vinyl butyral). PVB is the most reported binder used in tape casting and has been extensively studied. PVA is also commonly used but it is a water-based binder

due to its solubility in water. These binders must be fired in oxidizing atmospheres due to the mechanism of decomposition of the polymer. The typical by-product of its decomposition is carbon that can be removed by the presence of oxygen, water vapor or hydrogen.

On the other hand acrylic binders can be removed in reducing atmospheres. Their decomposition mechanism is completely different from the vinyl binders. Acrylics decompose and evaporate from the tape leaving very little carbon residue. Some of the most used acrylic binders are polyacrylate esters, polymethyl methacrylate and polyethyl methacrylate. If we punch a hole in a green tape of powder, solvent and binder - as it will be later necessary in the shaping process - it will probably break because of its lack of flexibility. This property is given by another additive: the plasticizer.

Two types of plasticizers are used in tape casting slurries. They are different in the way they act in the binder molecules in order to give the tape higher flexibility. The first type of plasticizer acts as binder's solvent. It reacts with the long-chain polymer breaking it into several smaller chains. As a result, the glass transition temperature of the polymer decreases below room temperature making the binder able to stretch without breaking. Excessive use of this kind of plasticizers decreases the adhesion of the tape to the neighboring tapes or to the surface carrier due to the liquid behavior given to the tape.

The second kind of plasticizer acts between the long-chain polymer as a lubricant. It does not react with the polymer molecules but it keeps them from crossing each other and allows them to have better mobility. These plasticizers also increase the adhesion of different layers to each other since they have better capability to adapt to the adjacent surfaces. However, an excess of these molecules gives the tape a high plastic deformation that will result in the tapes deformation after sintering. The most common plasticizers used in tape casting are from the family of the phthalates (n-Butyl (dibutyl), Butyl benzil, Dimethyl), glycols (poly ethylene, polyalkylene, poly propylene) and several others like glycerine and propylene carbonate.

As it was said before, the homogeneity of the green tapes is a key issue to obtain flat samples since it is necessary that the sintering kinetics is homogeneous in the whole tape. Thus, it is not only important that the powder has an uniform morphology and narrow particle size distribution but also that, particle deposition occurs homogeneously through the green tape structure. This homogeneous particle deposition depends on the stability of the powder particles in the slurry. All particles tend to get closer to each other through the action of London-van der Waals forces. In particular, when powder doesn't have a tendency to wet, particle clusters can form to lower the free energy of the suspension by reducing the solid-liquid interface area. A slurry will be stable when a repulsive force of the same magnitude of the attractive forces is provided to the particles. The magnitude of the particle's repulsion can be increased through the addition of another component to the slurry: the dispersant.

There are two types of mechanisms that increase the repulsive forces between particles: the electrostatic repulsion and the polymeric stabilization. Electrostatic repulsion keeps particles from attracting to each other through the formation of a layer of ions around the surface of the particle with opposite charge and a diffuse double layer in which the concentration of these ions decreases as the distance increases. When a particle and these layers move in a liquid, create a difference of potential between them. The gradient of electrical potential between the particle's ionic layer and the solvent is given by the zeta potential. Thus, following the evolution of the zeta potential as the dispersant is added allow to measure the stability of the slurry. When the concentration of positively charged species will be equal to the negatively charged ones, the zeta potential of the solution will be zero. Since the concentration of ions play an important role in the particles repulsion, the stabilization of the slurry may depend on its pH.

Due to water's high dielectric constant, this kind of repulsion plays an important role in

**Table II.3** : Non aqueous tape casting compounds chosen in this project and their respective functions.

function	compound	short name
solvent	ethanol	-
binder	poly(vinyl butyral)	PVB
plasticizer	polyethylene glycol	PEG

aqueous, whereas in non aqueous media electrostatic repulsion may come into play with the addition of some additives. But since the tapes are generally dense, particles are separated by small distances and polymeric stabilization is the most important method.

Polymeric stabilization is as effective in aqueous and non aqueous suspensions and for this reason it is the most used method to stabilize powders suspensions. Polymers may act according to two mechanisms: steric stabilization in which the molecules attach to the particles surface and depletion stabilization in which molecules stay in suspension between the particles. The latter mechanism is not well understood and researches on the subject are being carried on. Steric stabilization occurs when the polymer attaches to the particle surface and the rest of the long chain keeps the particles from approaching to each other more than about 10 nm. The best steric stabilizers are polymers that have a long chain that is soluble in the solvent and a functional group that acts as an anchor and attaches the molecule to the surface of the particle. A steric stabilizer effectiveness depends on the polymers ability to cover and attach to the particle's surface. Some of the most commonly used dispersants are oleic acid, blown menhaden fish oil, glycerol trioleate, phosphate ester.

There is, however, a competition between the dispersant and the binder since, as it was said before, the binder is the matrix where particles are in suspension and that gives the membrane its mechanical strength. Adsorption to the particle surface is a key step both to the actions of both the binder and the dispersant. Some binders can act as dispersants since they have the ability to attach to the powder particles and they are, in most of the cases, long-chain polymers. Some authors consider poly(vinyl butyral), a typical non aqueous tape casting binder, as a dispersant. Mistler and Twiname [28] consider, from their experimental results, that the binder has "by far" the largest effect on particle separation in a green tape.

Non aqueous tape casting has been used in our laboratory with good results since the PhD works of J. Hafsaoui and R. Costa [20] [29]. Therefore it was chosen to use the same slurry compounds that have been reported to be effective rather than to search one amongst the many possible new compositions that would have to be adapted to each of the powders used in this project. The compounds used are presented in table II.3.

Amongst the typical solvents used in non aqueous tape casting, ethanol is one of the most common ones, chosen for its low toxicity, stability with the ceramic materials, and its moderate volatility at room temperature. The fact that ethanol allows the dissolution of most organic compounds leaves a wide choice for the other slurry compounds. The use of anhydrous ethanol is not common since the benefits of having a tape without water don't justify the higher costs of this option.

We chose one of the most common binders used in non aqueous tape casting that also has been reported to have the same properties of a dispersant [28]: poly(vinyl) butyral with an average molecular weight between 30.000 and 35.000, supplied by Acros Organics.

As a plasticizer the choice of polyethylene glycol is justified by the fact that it is also

known for having dispersant properties.

Since the benefits of using a dispersant to stabilize the slurries are not clear, due to the competition with the binder for surface adsorption, and the stabilizing properties of the binder and the plasticizer used, it was decided not to add a specific compound for this function. The addition of a dispersant would increase the amount of organic products in the tapes which could have an influence on the microstructures obtained after sintering. This would be one more parameter to optimize the slurry composition and its presence is not sure to improve its stability.

The amounts of binder must be adapted to each powder, since their interaction with the particles surface is very important and not all powder have the same particle size. Then the proportions of plasticizer and solvent must be optimized in order to provide the tape the desired flexibility and to allow the dissolution of all the organic compounds.

Powders are mixed with all slurry compounds in a plastic container of 100 mL and are ball milled with 8 mm zirconia balls for four hours. Then the slurry is de-aired in vacuum and poured in a glass surface where the tape will be cast (see figure II.24).

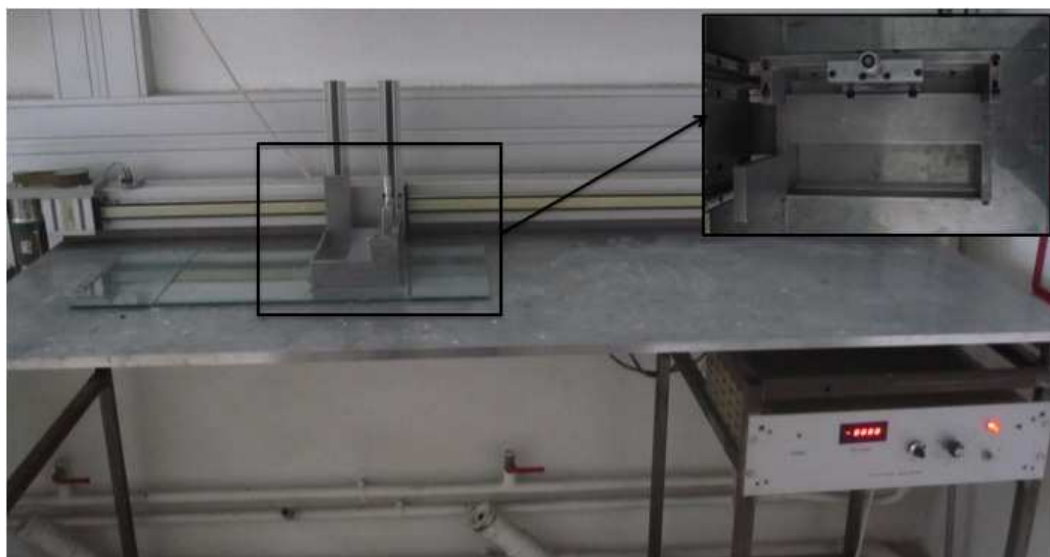


**Figure II.24** : Tape casting equipment used for ceramic materials shaping.

Then the desired thickness is set with a micrometer and it is put in motion at the desired speed. As the blade passes over the slurry, it creates a layer over the glass surface. The tape is then left to dry at room temperature for 2h if a single layer structure is made or 45 min if a second tape will be cast over the first one. After drying the tapes may have strong adherence with the glass support which doesn't allow an easy handling without deforming it. In order to avoid so, the glass surface can be coated with a mixture of glycerol and ethanol before the tape is cast. Once the tape is dry it is punched in different diameter circles by die cutting with a metallic ring and then detached from the glass.

A sintering treatment is then required to give the structures its final mechanical strength and adequate microstructures.

Our objective is, thus, to produce POC prototypes (see figure II.1) that will allow to demonstrate the IDEAL-Cell concept, using cold pressing and tape casting to process the  $\text{BaCe}_{0.85}\text{Y}_{0.15}\text{O}_{3-\delta}$  and  $\text{Ce}_{0.85}\text{Y}_{0.15}\text{O}_{2-\delta}$  powders characterized above.

### II.4.2 First approach: self-supported samples

Having these tools available to produce the POC prototypes, our first approach was a conservative one. The first samples were totally produced by cold pressing. The advantage of this technique, from a shaping point of view, is that it allows to produce thick layers in which their local lack of homogeneity will have a smaller influence in the global sintering behavior of the samples. This can be an important advantage for different reasons. These samples are three-layered structures of which two are dense, each one made of a different material, and a third porous layer that is a composite of the two materials. Intrinsically, due to their final microstructures, the two dense layer will have different shrinkage rates than the porous one. It is also likely that the two dense electrolytes will have a different sintering behavior, as it was shown in figures II.10 and II.19. This difference is due to their different particle size that plays a role in the sintering kinetics but most of all due to their different chemical nature. Each of the powders also present a "tail" in their particle size distribution. The fact that the particles distribution isn't narrower contributes to local differences in the powders shrinkage during sintering.

The dilatometric study of the electrolyte materials also shows that the densification of  $\text{BaCe}_{0.85}\text{Y}_{0.15}\text{O}_{3-\delta}$  is the limiting process of the shaping procedure, since its corresponding electrolyte must be dense. Therefore the sintering temperature of these samples must reach at least  $1300^\circ\text{C}$ . This temperature is high enough to densify the  $\text{Ce}_{0.85}\text{Y}_{0.15}\text{O}_{2-\delta}$  electrolyte, that has a sintering temperature of  $1200^\circ\text{C}$  but it is too high if we want to keep the porous microstructure of the central membrane. In order to solve this, a sequential shaping procedure in which the  $\text{BaCe}_{0.85}\text{Y}_{0.15}\text{O}_{3-\delta}$  electrolyte is sintered separately from the other two layers is not possible by cold pressing and sintering of a material over an already dense one is not favorable because the specific surface of the dense layer was severely reduced during sintering. Therefore, the solution found to create a porous structure in the central membrane at high temperature is the introduction of a pore former; a compound that decomposes during sintering creating voids between the particles without reacting with them. Many different pore formers have been used in tape casting such as potato starch, rice starch, and graphite with different particle sizes [31]. These compounds decompose at different temperatures creating different pore shapes and sizes in the structure of the tapes after sintering.

Our choice was graphite because it is an inert material that decomposes in oxidizing atmospheres at high temperatures. The graphite used has irregular shape particles of about  $5\ \mu\text{m}$  - as shown in figure II.25 - that create relatively small pores in the sintered pieces without a preferential orientation.

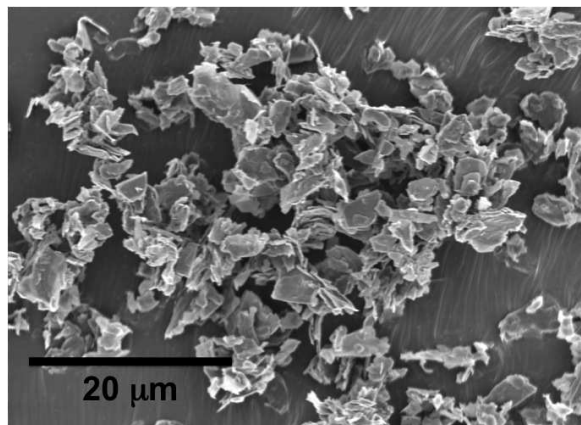
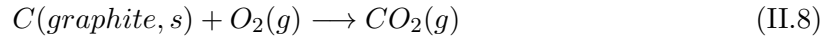


**Figure II.25** : S.E.M. image of the graphite used as pore former in the central membrane.

As temperature rises during sintering, graphite will react with oxygen in air, according to reaction II.8.



which is an exothermic reaction with  $\Delta H_c^\circ = -393 \text{ kJ/mol}$ . Thus, at a certain temperature, heat and  $CO_2(g)$  will be released from the ceramic body. A sudden release of the gases, trapped in the sample, can cause the deformation of its initial shape and that's why it is important to hold the furnace's temperature when the reaction takes place. In order to know at which temperature the reaction takes place and the higher weight loss occurs, differential thermal analysis of graphite was carried out. The sample weight was followed from room temperature to  $900^\circ\text{C}$  in air, yielding the curve shown in figure II.26.

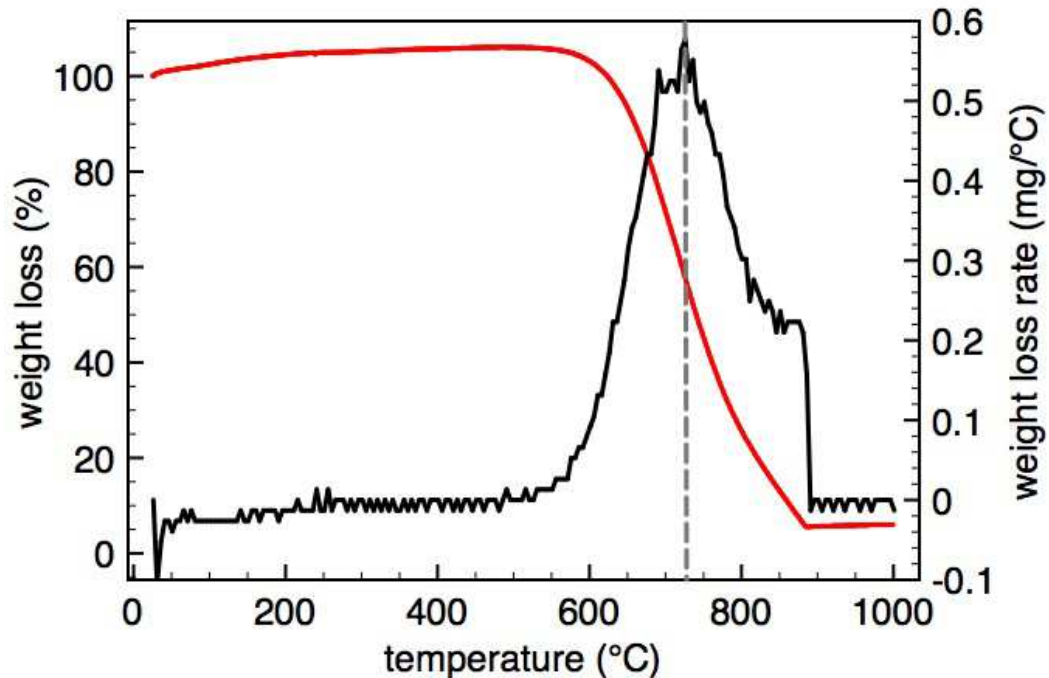


**Figure II.26** : Differential thermal analysis of a sample of graphite in air.

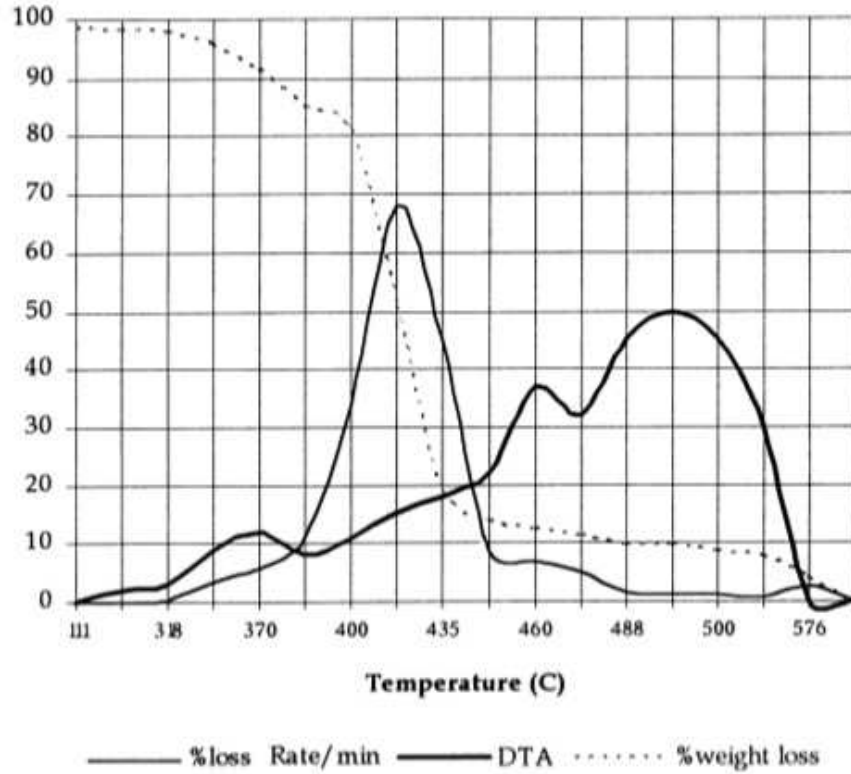
As we can see, the highest weight loss is detected at  $700^\circ\text{C}$  and, therefore, temperature must be held to allow graphite combustion at low rate.

During the fabrication of the first samples using this method, it was observed the delamination of the  $Ce_{0.85}Y_{0.15}O_{2-\delta}$  electrolyte layer from the central membrane sometimes before and always after the sintering treatment. This was due to a bad bonding of the two layers, even if the central membrane contains  $Ce_{0.85}Y_{0.15}O_{2-\delta}$ . This was avoided by adding the organic binder used in tape casting - poly(vinyl butyral) - in the central membrane in order to improve the adherence of the two layers. These molecules will decompose at high temperatures in oxidizing atmospheres and therefore, for the same reasons as for graphite, the thermal cycle used in sintering must be changed in order to allow the compounds slow decomposition. Since, poly(vinyl butyral) has been widely used in tape casting, its behavior at high temperature is known. Salam *et al.* found that approximately 85% of the PVB's

**Table II.4** : Composition of each layer used in the fabrication of proof of concept prototypes by tape casting and sintering.

	proton conducting electrolyte	central membrane	oxygen ion conducting electrolyte
$\text{BaCe}_{0.85}\text{Y}_{0.15}\text{O}_{3-\delta}$	2.00 g	0.91 g	-
$\text{Ce}_{0.85}\text{Y}_{0.15}\text{O}_{2-\delta}$	-	1.00 g	2.00 g
graphite	-	0.20 g	-
poly(vinyl butyral)	-	0.10 g	-

weight loss in air occurred in the temperature range of 350-450°C as it can be seen in figure II.27. Thus, the temperature chosen for the burnout of PVB was 450°C.

**Figure II.27** : Differential thermal analysis of poly(vinyl butyral) [32].

After several trials, an optimal fabrication procedure was found. The composition of each layer is presented in table II.4.

Each powder mixture of powder was ball milled for 2h in 100 mL plastic containers with zirconia balls for 2h. Then each of powder and the central membrane mixture were put sequentially in a 25 mm diameter die. The three layers were then pressed at 100 MPa for 5 minutes.

The green pellet was then put on a  $\text{Al}_2\text{O}_3$  support over a  $\text{BaCe}_{0.85}\text{Y}_{0.15}\text{O}_{3-\delta}$  powder bed to avoid the reaction between the support and the pellet. The sintering cycle, shown in figure II.28 was defined taking into account the reaction of the binder and the pore former and the

densification of the electrolytes as it was explained before. The heating rate was  $1^{\circ}\text{C}/\text{min}$  until  $700^{\circ}\text{C}$  to approach smoothly the decomposition temperatures of PVB and graphite and then  $2^{\circ}\text{C}/\text{min}$ . Temperature was held at  $450^{\circ}\text{C}$  and at  $700^{\circ}\text{C}$  for 2h and at  $1300^{\circ}\text{C}$  for 5h to densify the electrolytes. The cooling rate was  $2^{\circ}\text{C}/\text{min}$ .

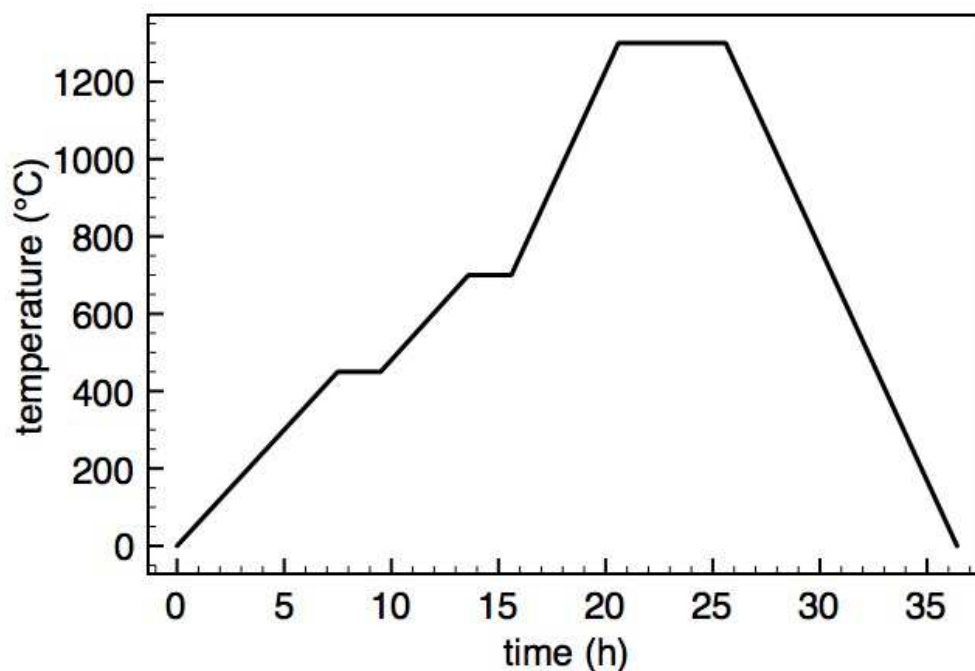


**Figure II.28** : Thermal cycle used in the sintering of the proof of concept samples produced by cold pressing.

After sintering, flat samples of 21 mm diameter were obtained with the microstructures that can be seen in figure II.29.

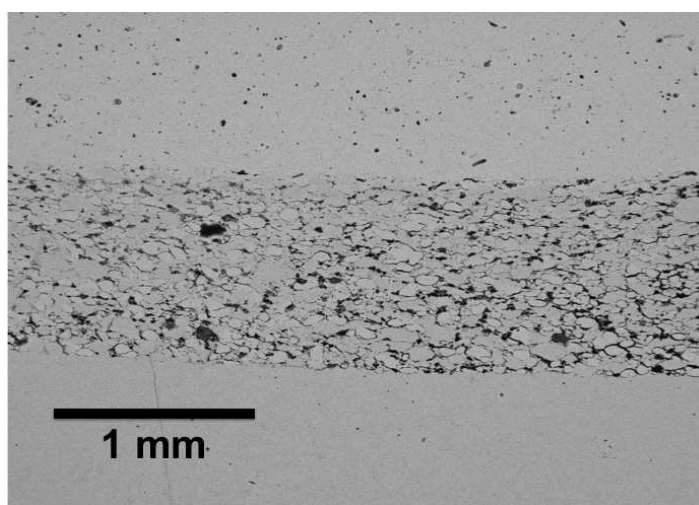


**Figure II.29** : Proof of concept sample made by cold pressing.

Both electrolytes were successfully densified, although it is clear that the  $\text{BaCe}_{0.85}\text{Y}_{0.15}\text{O}_{3-\delta}$  electrolyte (on the top) is less dense and shows some closed porosity whereas the central membrane has the desired highly porous structure due to the action of graphite. It is also clear the quality of the interfaces between the three layers that create a continuous phase for the ions conduction from the electrolytes to the central membrane thus limiting the interface polarization. As expected, this sample is very thick: 2.5 mm of total thickness. The electrical performances obtained from such cell are obviously low but useful since they are likely to demonstrate, from a qualitative point of view, that the concept operates as a fuel cell.

### II.4.3 Second approach : proton electrolyte-supported samples

While trying to decrease the thickness of the POC samples, a new fabrication procedure was found. It was clear that thinner layers would imply the use of tape casting but although green POC samples were easily obtained, due to the sintering different behavior of each of the layers, it wasn't possible to obtain flat samples totally fabricated by tape casting.

The new approach consists in supporting the sample in one of the layers that would be much thicker than the others, as it is the case for anode-supported fuel cells. Since the  $\text{BaCe}_{0.85}\text{Y}_{0.15}\text{O}_{3-\delta}$  powder has the higher sintering temperature and yet again the limiting step of the process, the central membrane and the  $\text{Ce}_{0.85}\text{Y}_{0.15}\text{O}_{2-\delta}$  electrolyte would be cast sequentially over the already sintered proton conducting electrolyte. The three layers would then be sintered at the  $\text{Ce}_{0.85}\text{Y}_{0.15}\text{O}_{2-\delta}$  sintering temperature in order to densify the electrolyte. The porosity in the central membrane would be assured by a higher volume of organic compounds in the green tape and also by the presence of  $\text{BaCe}_{0.85}\text{Y}_{0.15}\text{O}_{3-\delta}$  that wouldn't be densified at such low temperature.

However such approach turned out to be very complex. It was constantly observed the delamination of the tapes cast over the dense proton conducting pellet, although the degree of this delamination changed with the tapes slurry composition. Another sensitive point was to find the slurries composition for the central membrane and oxygen ion electrolyte that would give both layers a compatible shrinkage rate taking into account their completely different microstructures after sintering. In most of the trials the interface of these two layers didn't have good quality in the whole diameter of the samples.

The best solution found for this problem was to sinter a  $\text{BaCe}_{0.85}\text{Y}_{0.15}\text{O}_{3-\delta}$  pellet at low temperature to keep some porosity that would act as a mechanical attachment for the central membrane layer. The slurries compositions were changed iteratively until the central membrane has good interfaces with both electrolytes in the whole surface of the sample. It was chosen to create the central membrane's porosity by the addition of an excess of binder and plasticizer. It was found that this approach allowed better adhesion with the other layers, rather than adding another compound like graphite that would release additional amount of products in gas phase. Part of this iterative process was also the oxygen ion electrolyte slurry that would assure both the adhesion of the layer to the central membrane and the adequate microstructure of the electrolyte.

Thus, 2.0 g of  $\text{BaCe}_{0.85}\text{Y}_{0.15}\text{O}_{3-\delta}$  powder were pressed in a 25 mm die at 100 MPa for 5 minutes. The pellet was then sintered at 1200°C for 5h with heating and cooling rates of 5°C/min. Over the sintered pellet, central membrane and oxygen ion electrolyte layers were cast. The pellet was put in the glass surface shown in figure II.24 and the blade was set 200µm above the pellet or layer above. The central membrane was a composite of 50 vol.% of both electrolyte materials. After the first tape was cast it was left to dry for 2h before the second one's deposition. The slurries composition are shown in table II.5.

The sintering cycle had to be adapted to the decomposition of the organic compounds

**Table II.5** : Composition of the slurries used in the fabrication of proof of concept prototypes by cold pressing, tape casting and sintering.

	central membrane	oxygen ion conducting electrolyte
$\text{BaCe}_{0.85}\text{Y}_{0.15}\text{O}_{3-\delta}$	2.72 g	-
$\text{Ce}_{0.85}\text{Y}_{0.15}\text{O}_{2-\delta}$	3.00 g	6.00 g
poly(vinyl butyral)	1.70 g	1.40 g
polyethylene glycol	0.40 g	0.30 g
ethanol	5.50 g	5.00 g

added to the slurries. In order to know the temperatures in which this occurs, differential thermal analysis of a membrane with binder, plasticizer and solvent was carried out. The results are presented in figure II.30. As it can be seen, the higher weight lost rate is detected at 350°C. Therefore, taking into account the materials, the slurries compositions and the desired microstructures, the samples were sintered at 1200°C for 5h with a previous step at 350°C for 2h to allow slow decomposition of the organic compounds. The sintering cycle is presented in figure II.31.

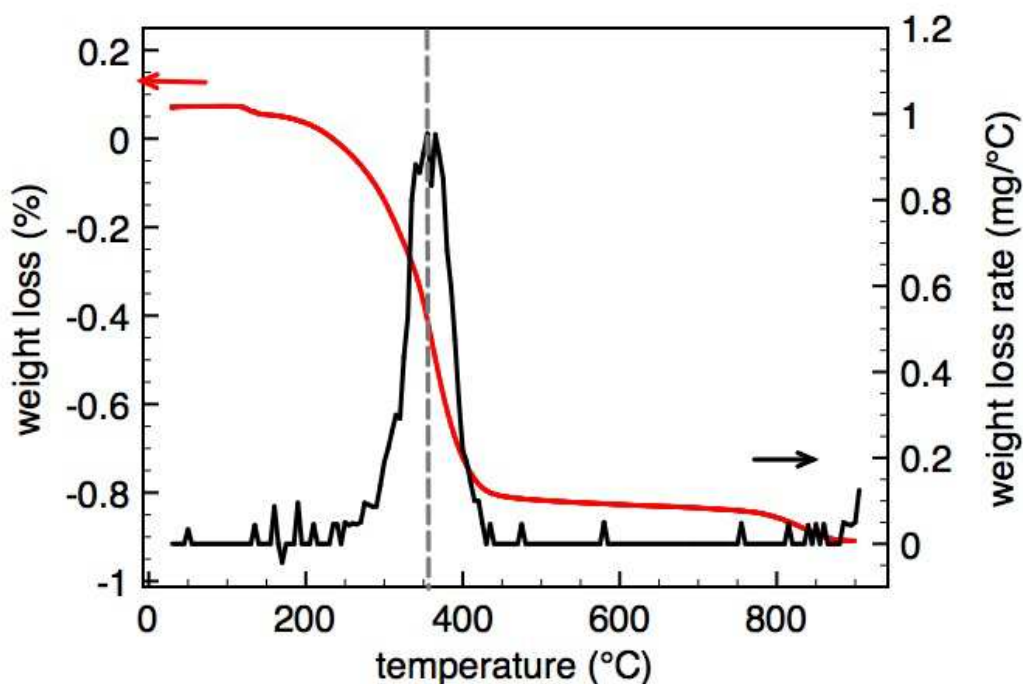


**Figure II.30** : Differential thermal analysis of a polymer membrane made of poly(vinylbutyral) (binder), polyethylene glycol (plasticizer) and ethanol (solvent).

Flat samples of 21 mm diameter were obtained after sintering. The interfaces between the three layers were satisfying as it can be seen in figure II.32 of a sample after electrochemical testing.

The proton conducting electrolyte is a flat layer with 600  $\mu\text{m}$  of thickness. We can see

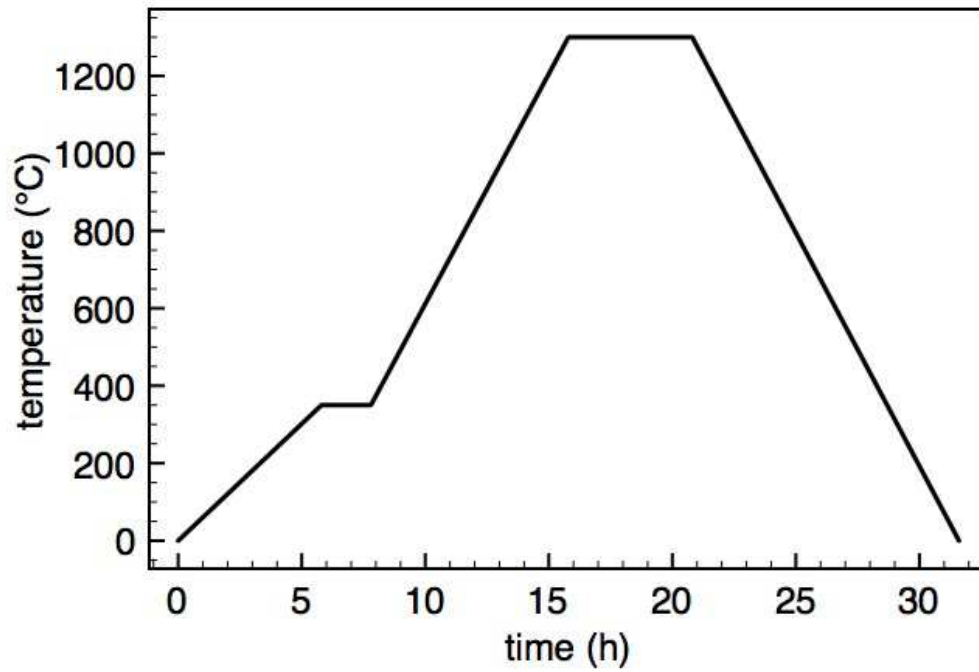


**Figure II.31** : Thermal cycle used in the sintering proof of concept samples made by cold pressing and tape casting.

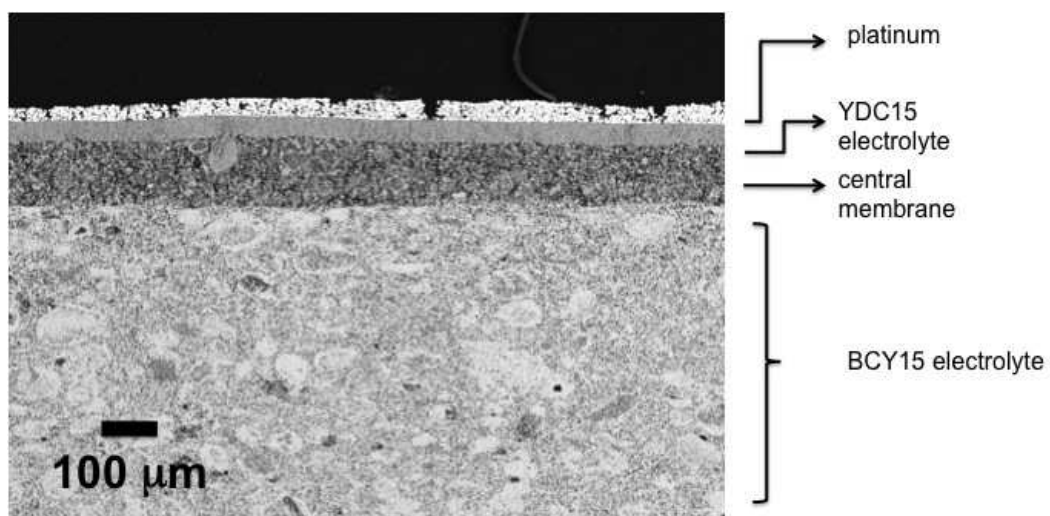


**Figure II.32** : Proof of concept sample made by cold pressing, tape casting and sintering.

that the layer is less dense and less homogeneous than the one shown in figure II.29 for the samples made by cold pressing, which was expected from the sintering temperature used. The central membrane is a porous microstructure of about  $100\mu\text{m}$  with good interfaces with both electrolytes. The  $\text{Ce}_{0.85}\text{Y}_{0.15}\text{O}_{2-\delta}$  electrolyte is the densest layer and has a thickness of  $30\mu\text{m}$ .

These dedicated POC samples fabricated at Centre des Matériaux during this project were relevant because their electrochemical tests allowed to demonstrate the IDEAL-Cell concept.

## II.5 Electrochemical testing

One of the most useful and expected characterization methods of these samples is the electrochemical test in typical fuel cell operating conditions. Both types of samples presented above were tested in an electrochemical tester specially developed to allow obtaining as much data as possible to demonstrate that this concept operates as a fuel cell when a difference of potential is created between both electrodes. This fuel cell operates differently from the other classical concepts due to the central membrane, the innovative third compartment where water is produced and evacuated. Thus, operating an IDEAL-Cell taking advantage of its innovative design implies the use of new interconnects (if a stack is tested) and new electrochemical tester (if a single cell is tested) that assure the gas tightness between the three chambers: the anode, the cathode and the central membrane. A new electrochemical tester was developed taking into account the specificities of the new concept and thus allowing to demonstrate its advantages.

All electrochemical activities including the development of the electrochemical tester were carried out in Genoa (Italy) by Antonio Barbucci and his team from Consiglio Nazionale delle Ricerche (C.N.R.).

### II.5.1 Experimental apparatus

The specificity of this electrochemical tester is the fact that it allows to detect water produced in the third compartment of the cell: the central membrane. This is indeed one of the advantages of this cell: the possibility of isolating water produced from the anode and the cathode, which brings the advantages claimed before.

In practice, the electrochemical tester has three chambers instead of two, as it can be seen in figure II.33.

The cell is put between two alumina tubes that feed the oxygen and wet hydrogen to the respective electrodes. The tubes are in contact with the electrolytes and have a larger diameter than electrodes. As it was said before, platinum electrodes were used. They were coated by brushing over the electrolytes and then sintered at  $1000^\circ\text{C}$  in air. Platinum meshes were placed at both sides of the cell. The gas tightness of the contact surfaces of the tubes with the electrolytes is assured by a thermiculite<sup>®</sup> sealing ring supplied by Flexitallic, UK. A quartz tube surrounding the two alumina tubes and the cell, creates the third chamber that is fed with a stream of nitrogen that carries the water vapor produced by the cell into the moisture analyzer (see figure II.34)

The alumina tubes together with thermocouples and platinum wires, welded to the Pt meshes, were connected to a metal support (Probostat, NorEcs) with all the connections for gases and electric contacts.

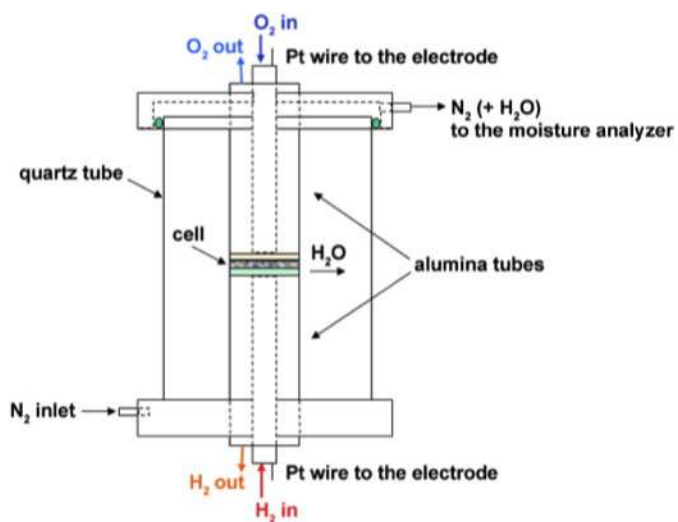


Figure II.33 : Scheme of the electrochemical tester.

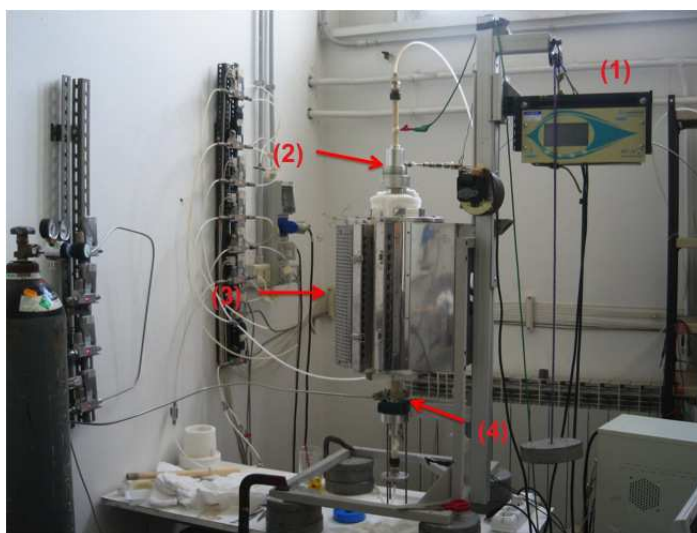


Figure II.34 : Electrochemical tester dedicated to the POC experiments. It can be seen the (1) moisture analyzer, (2) hydrogen feed, (3) furnace, (4) oxygen feed.

## II.5.2 Experimental Procedure

The experiments were carried out to demonstrate that the tested prototypes have typical fuel cell behavior. It was stated that IDEAL-Cell would be considered as a fuel cell if its performances respected four criteria:

1. **a stable open circuit voltage in hydrogen and air:** the open circuit voltage must be recorded as a function of time when the cell was fed with hydrogen and oxygen, in what is called a chronopotential measurement.
2. **a stable polarization curve ( $V/i$ ):** the polarization curve can be obtained by measuring the current density supplied by the cell at different voltages. The cell voltage is changed by connecting the system to external loads with different impedance values (or changing the hydrogen partial pressure of the anode gas stream). Knowing the cell current and voltage, the power generated by the system can be obtained.
3. **a specific impedance fingerprint for the formation of water:** electrochemical impedance spectroscopy is widely used in the field of fuel cells to give information on reaction kinetics, mass transfer and electrolyte membrane resistance losses. For the IDEAL-Cell system, one can expect to obtain a specific impedance spectra due to the formation of water inside the cell structure.
4. **measurement of water formation in the central membrane as a result of the cell operation:** any fuel cell produces an electrical current and water as byproduct. A direct measurement of water produced while the cell is operating is a proof that the system is working.

Thus, the system temperature was set at the cell's operating temperature, i.e. 600°C. Oxygen and hydrogen diluted in nitrogen at different ratios were fed to the cathode and the anode, respectively. The anode gas stream was bubbled in water at 25°C to assure the proton electrolyte conducting properties. In order to record the signals corresponding to each of the proof of concept criteria, different types of experiments were carried out.

Chronopotential, polarization and impedance measurements were carried out by using a potentiostat-impedancemeter (Autolab, Pgstat30).

## II.5.3 Results

Both types of POC prototypes with platinum electrodes were tested following the procedure described above. The first sample being tested was the one produced by cold pressing and tape casting.

The proton electrolyte-supported sample, which microstructures are shown in figure II.32 was put in the tester and fed with 15 NmL/min of wet (3% H<sub>2</sub>O) hydrogen in the anode and 30 NmL/min of oxygen in the cathode side. The system's open circuit voltage was registered and the results are shown in figure II.35.

The cell shows a stable open circuit voltage of 0.90 V at 600°C for the recorded period (about 15 min), which is close to the theoretical value of 1.05V given by the Nernst equation.

In order to test the reliability of this result, the gas feed was switched on and off for several short (figure II.36) periods of time, while the open circuit voltage was measured.

The cell was switched-off for periods of about 5 minutes. Each time it was switched-on, it got its former value of OCV. This result was reproduced in an experiment that lasted about 30 min.

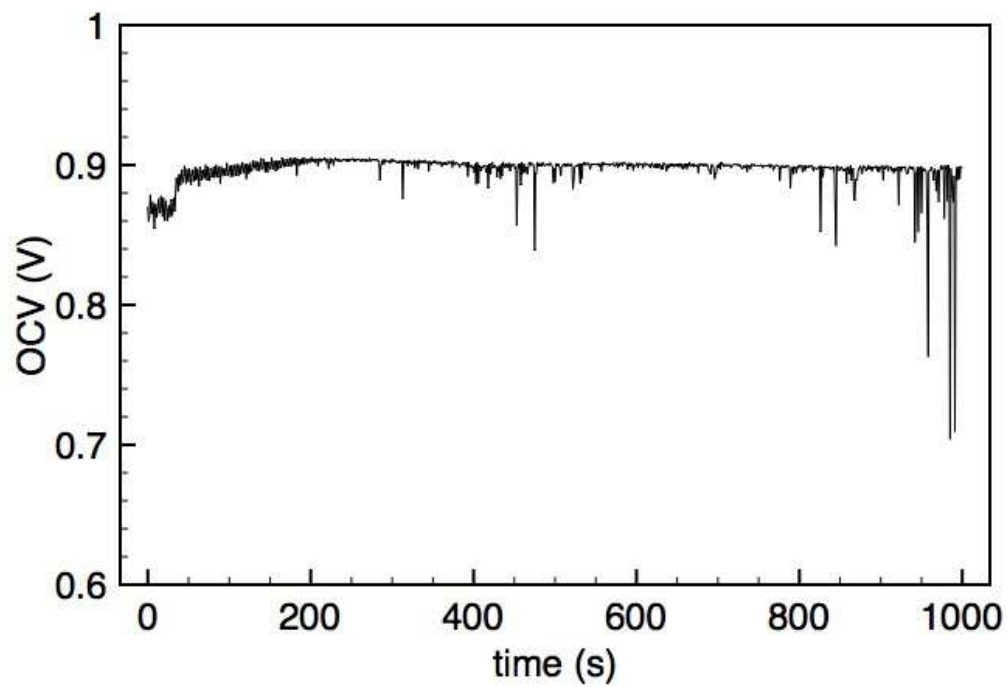


Figure II.35 : Open circuit voltage of the electrolyte-support cell as a function of time.

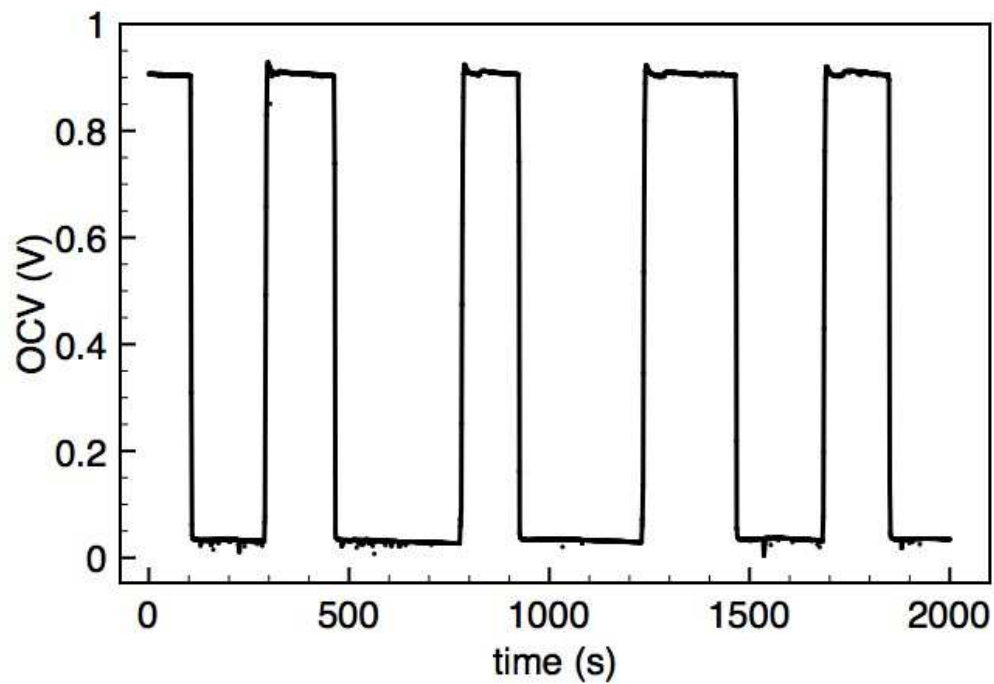
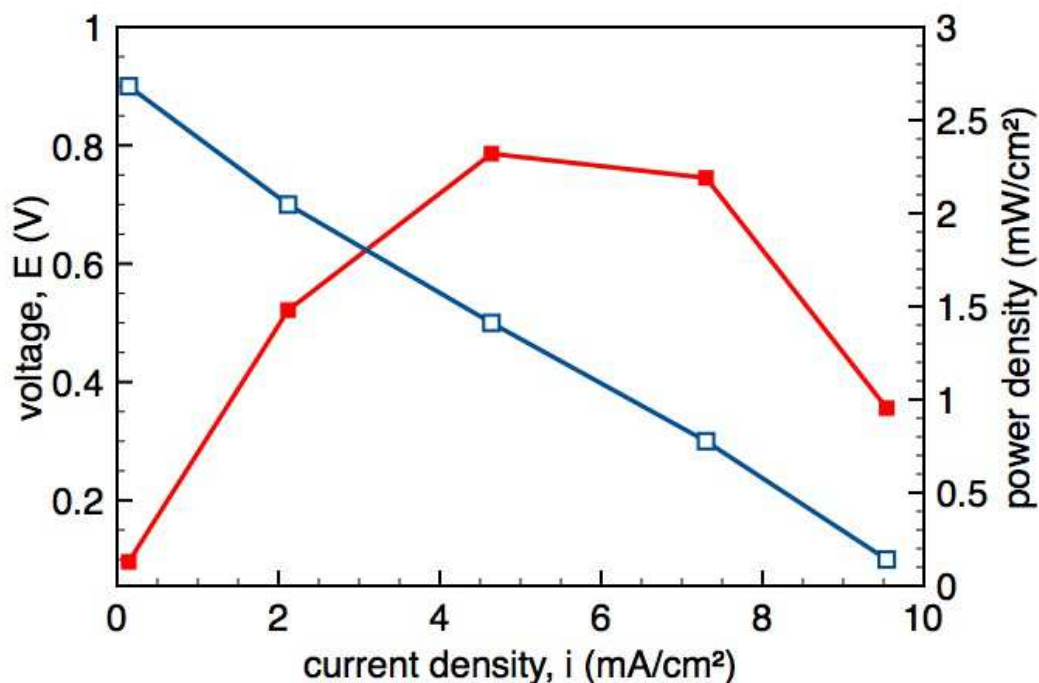


Figure II.36 : Open circuit voltage recorded in a POC prototype wet hydrogen and oxygen feed was switched on an off.

The cell voltage was decreased to 0.7 V, 0.5 V, 0.3 V and 0.1 V. The current produced by the cell for each potential was recorded, yielding the polarization curve displayed in figure II.37



**Figure II.37** : Polarization curve of a proof of concept prototype.

The voltage decreased linearly with the increase of the current demand. The power delivered by the cell was also determined, reaching a maxima of 2.3 mW/cm<sup>2</sup> at 0.5V and a current density of 4.6 mA/cm<sup>2</sup>.

Impedance spectroscopy measurements were carried out in this sample in order to detect the formation of water at 0.9 V. An alternate current was applied to the sample in order to record the impedance diagram. For both measurements the alternate current frequency range used was 1 MHz-1 Hz and the intensity was about 1/10 of the direct current supplied by the cell when operating. The results can be seen in figure II.38.

The self-supported sample, produced by cold pressing, allowed us to obtain another kind of results. As it can be seen in figure II.39 when the sample was fed with wet hydrogen and oxygen the open circuit voltage increased to a value under 1.0 V. After a period of optimization of the experimental parameters, the sample was left at open circuit for a period of about 1.5h. The open circuit voltage measured was stable at the 1.04 V.

Testing these samples allowed to detect the production of current when the fuel and the combustive were fed to the electrodes and the circuit was closed. When the gases were fed to the cell, the open circuit voltage quickly stabilized at 0.9V. When the circuit was connected to an external load, the cell voltage decreased to 0.2 V and a current was produced, as it can be seen in figure II.40. When the current was produced, the amount of water in the third chamber outflow stream was measured through the moisture analyzer.

A clear increase of the water concentration was detected at the voltage as the cell produces the current. The registered level of humidity before the polarization could be due to the nitrogen flow through the system, to possible leakage, to adsorption of water in the central

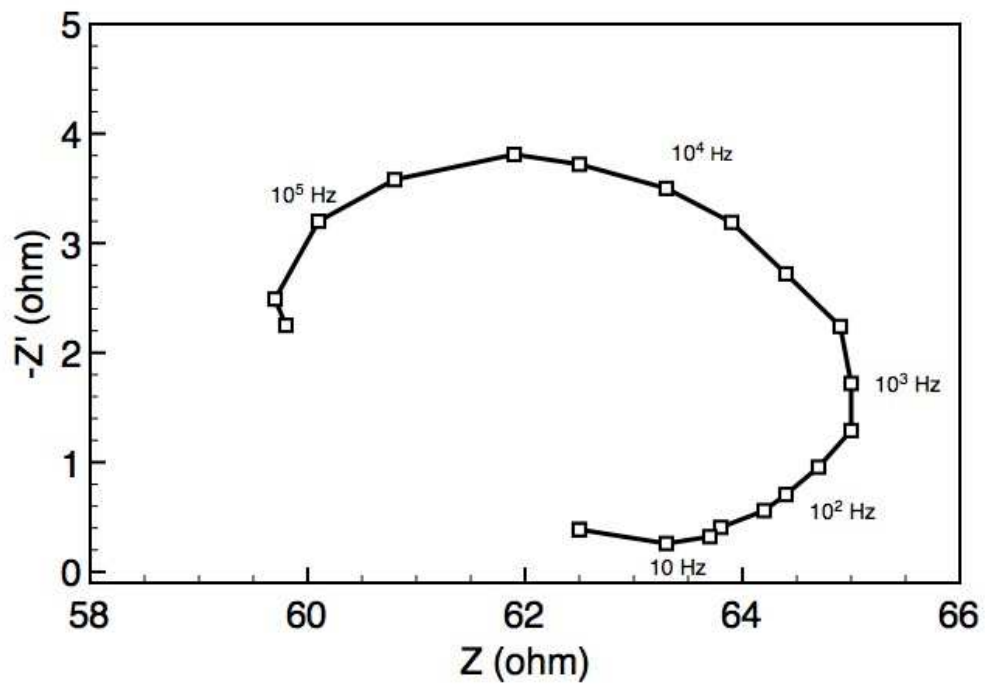


Figure II.38 : Nyquist plot of a proof of concept sample at 0.9 V.

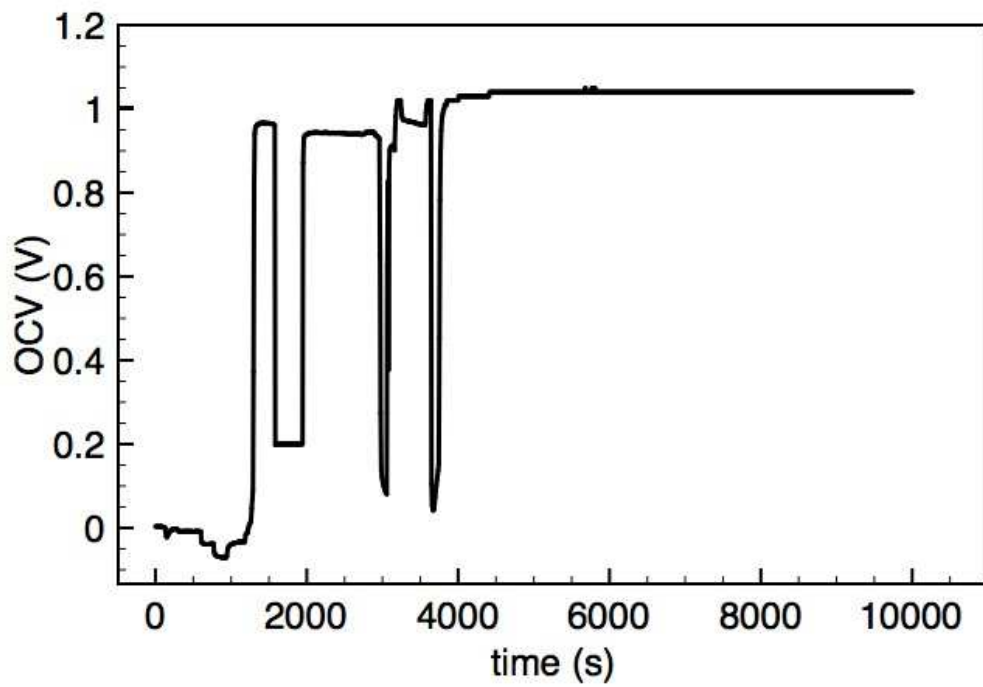
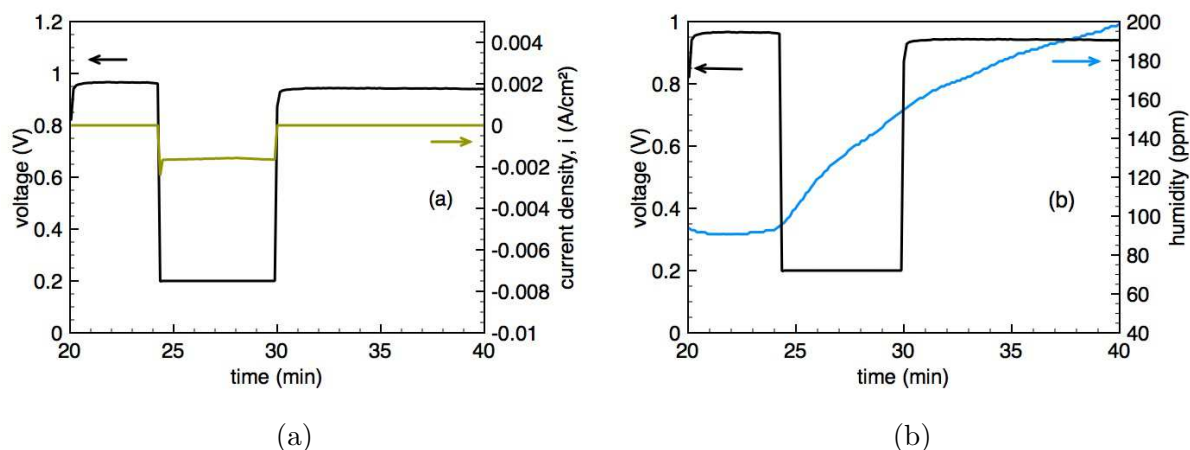


Figure II.39 : Open circuit voltage of a the self-supported sample fed with wet hydrogen and oxygen.



**Figure II.40** : Current produced when the cell is switched-on (a) and water produced as a result of the cell operation (b).

membrane and the connecting pipes.

## II.6 Discussion

In the previous parts are described the activities developed to demonstrate a new concept of fuel cell, that go from the choice of the configuration of the first prototypes, to the choice and characterization of the materials, their shaping procedure and electrochemical testing.

The prototypes of the IDEAL-Cell concept is a simplified structure of the five functional layer structure presented in figure I.9. The configuration of the prototypes - called proof of concept samples - consist in a three layer structure of two electrolytes and central membrane. This simplified structure allowed avoiding the issues related with the electrodes performance. The electrodes microstructures, composition and reactivity with the electrolytes materials need further investigation that didn't have to be taken into account with the proof of concept prototypes configuration chosen.

The materials chosen to produce these samples were  $\text{BaCe}_{0.85}\text{Y}_{0.15}\text{O}_{3-\delta}$  as proton conductor and  $\text{Ce}_{0.85}\text{Y}_{0.15}\text{O}_{2-\delta}$  as oxygen ion conductor. Amongst the high temperature proton conducting materials, the ones that show highest proton defects mobilities are the cubic perovskites structured materials. They are not only highly performant but also one of the better studied materials for these applications. The conductivity of these materials is proportional to their proton defects concentration that are created by the introduction of water vapor in the oxygen vacancies of the crystal structure. These oxygen vacancies only exist in sufficiently high concentration if the materials are doped by lower valency ions. The chemical identity and the concentration of the dopant have an influence in the conductivity of the materials, as it was explained in part II.3.1.1. The highest conductivities have been reported for yttrium-doped barium cerate and amongst these compounds the one that was found to have the highest performance [20] at our laboratory was  $\text{BaCe}_{0.85}\text{Y}_{0.15}\text{O}_{3-\delta}$ . For these reasons this was the proton conductor chosen for the for this project.

Oxygen ion conduction depends on the concentration of the pair interstitial ion - vacancy. When an ion moves in the lattice it occupies a new position - an interstitial position. At low temperatures, the normal sites are occupied and the interstitial positions are empty. With a temperature increase the intrinsic thermal disorder and generate interstitial-vacancy pairs. The concentration of these defects can be increased by doping the material with aliovalent

cations. Doped fluorite structure materials are the best understood oxygen ion conductors. In this category the two most important families of materials are the ceria and the zirconia doped oxides. Ceria doped solutions have higher conductivities, however they are unstable in reducing atmospheres. Since in the IDEAL-Cell concept the oxygen ion electrolyte is not in contact with the anode, the material chosen is a ceria solution. These materials have been widely studied and the one that has better conductivity is the gadolinium doped ceria. However, since the dopant used in the proton conductor is yttrium, it was chosen to keep the same dopant at the same concentration in the oxygen ion conductor. Therefore, the oxygen ion conductor chosen was  $\text{Ce}_{0.85}\text{Y}_{0.15}\text{O}_{2-\delta}$ .

The  $\text{BaCe}_{0.85}\text{Y}_{0.15}\text{O}_{3-\delta}$  powder supplied has a particle size distribution centered at  $d_{50} = 0.23 \mu\text{m}$  but with a certain dispersion that causes it to have a  $d_{90} = 0.71 \mu\text{m}$  and a small fraction of particles with  $2 \mu\text{m}$  size. The powder is agglomerated in clusters of  $100 \mu\text{m}$  to  $20 \mu\text{m}$ .  $\text{BaCe}_{0.85}\text{Y}_{0.15}\text{O}_{3-\delta}$  powder is an almost pure compound having residual amounts of  $\text{BaCeO}_3$ . It was chosen not to proceed to a high temperature treatment to eliminate these impurities because it could cause particle coarsening which is not worthy because they are present in residual amounts. Through dilatometry it was found that this powder has a sintering temperature of  $1300^\circ\text{C}$ .

The  $\text{Ce}_{0.85}\text{Y}_{0.15}\text{O}_{2-\delta}$  powder is a single-phase compound with a narrow particle distribution between  $0.1 \mu\text{m}$  and  $0.3 \mu\text{m}$  and with a fraction of particles with size of about  $2 \mu\text{m}$ . This lack of homogeneity of both powders particles size distribution has an important influence on the sintering kinetics of these materials. Since the driving force of the sintering mechanism is the decrease of the particle specific surface, the shrinkage rate of the ceramic bodies will not be homogeneous during the high temperature treatment. The morphology of each powder causes a non-homogeneous sintering behavior in the whole ceramic pieces. The ceramic materials used have different sintering temperatures due to their chemical nature. The dilatometric behavior of the  $\text{Ce}_{0.85}\text{Y}_{0.15}\text{O}_{2-\delta}$  powder shows that it has a sintering temperature of  $1200^\circ\text{C}$ .

In order to produce POC samples, two techniques were used: cold pressing and tape casting. The first allowed producing relatively thick flat samples whereas the latter allowed producing thin layers with controlled porosity. Tape casting was successfully applied using poly(vinyl butyral) as binder, polyethylene glycol as plasticizer and ethanol as solvent. The decomposition of these organic products during sintering create porosity in the ceramic bodies allowing to control the samples microstructures. During sintering, temperature must be held at the value for which organic products decomposition occurs at its highest rate, to allow the release of the gaseous compounds smoothly without deformation of the sample. In the case of the compounds added in the tape casting slurries, its highest decomposition rate occurred at  $350^\circ\text{C}$ .

Tape casting was not the only shaping procedure that allows porosity control. This is also made possible in cold pressing by the addition of graphite and/or poly(vinyl butyral). Their thermal decomposition temperature was also determined by differential thermal analysis. Graphite has higher decomposition rate at  $700^\circ\text{C}$  and poly(vinyl butyral), widely studied for these application, has been reported to decompose at  $450^\circ\text{C}$ .

Two different approaches were used to produce IDEAL-Cell prototypes : (a) samples completely produced by cold pressing and (b) samples produced by cold pressing and tape casting.

Through the first approach, the three layers of the prototype were pressed simultaneously in a  $25 \text{ mm}$  die at  $60 \text{ MPa}$ . The electrolytes were constituted of each ion conducting material and the central membrane is a  $50 \text{ vol.}\%$  composite of the two materials. The complete sample was then sintered at  $1300^\circ\text{C}$ , the sintering temperature of  $\text{BaCe}_{0.85}\text{Y}_{0.15}\text{O}_{3-\delta}$ , the material that densifies at higher temperature. Thus, the  $\text{Ce}_{0.85}\text{Y}_{0.15}\text{O}_{2-\delta}$  electrolyte was also densified.

The porosity of the central membrane had to be assured by the addition of graphite and poly(vinyl butyral). The temperature sintering cycle had a step of 2h at 450°C and another one at 700°C to allow the smooth decomposition of both pore formers. The samples produced by cold pressing - called self-supported samples - were flat samples of 21 mm of diameter. The  $\text{Ce}_{0.85}\text{Y}_{0.15}\text{O}_{2-\delta}$  electrolyte was highly dense whereas the  $\text{BaCe}_{0.85}\text{Y}_{0.15}\text{O}_{3-\delta}$  electrolyte had residual closed porosity. Both fulfill the requirements for an electrolyte explained before. The whole sample had 2 mm of thickness: 700  $\mu\text{m}$  for each electrolyte and 600  $\mu\text{m}$  for the central membrane. Good interfaces between the three layers were successfully achieved as it can be seen in figure(II.32). The structure of the sample allowed transport of the ions in a continuous media from the electrolyte through the central membrane. Contrarily to the electrolytes, a highly porous structure that may allow water evacuation was obtained.

The second approach used consisted in a combination of two shaping techniques: cold pressing and tape casting. The idea behind this approach was to use a thick  $\text{BaCe}_{0.85}\text{Y}_{0.15}\text{O}_{3-\delta}$  layer produced by cold pressing to deposit the central membrane and the  $\text{Ce}_{0.85}\text{Y}_{0.15}\text{O}_{2-\delta}$  electrolyte by tape casting. Since the proton electrolyte material densifies at higher temperature, it was the component of the POC prototype that constrained the shaping procedure. Therefore, it was chosen to pre-sinter this layer separately and then the rest of the sample could be shaped at lower temperature. The use of cold pressing is justified by the need of producing a thick layer that would offer mechanical support to the sample, not only during electrochemical testing, but also during sintering of the rest of the compartments. Thus, the flatness of the sample was assured. Over the flat  $\text{BaCe}_{0.85}\text{Y}_{0.15}\text{O}_{3-\delta}$  sample the central membrane and the  $\text{Ce}_{0.85}\text{Y}_{0.15}\text{O}_{2-\delta}$  electrolyte were deposited by tape casting with a drying step between both layers. These layers were then sintered at 1200°C in order to densify the oxygen ion electrolyte. Both tape casting slurries composition had to be optimized to yield satisfying microstructures for each functional layer. The central membrane slurry composition also had to be tuned keeping in mind the layer adhesion to the proton electrolyte pellet. However, the adhesion of the central membrane over a highly dense electrolyte was never achieved. Therefore, the tapes were cast over  $\text{BaCe}_{0.85}\text{Y}_{0.15}\text{O}_{3-\delta}$  pellets sintered at 1200°C that were less dense than the previous ones. Higher porosity of the proton conducting electrolyte obtained allowed a slight impregnation of the slurry in the pellet that assured its mechanical adhesion during sintering. The  $\text{BaCe}_{0.85}\text{Y}_{0.15}\text{O}_{3-\delta}$  pellet is thus sintered at the same temperature than the layers deposited by tape casting. However, the previous sintering of the proton electrolyte is still necessary. When the central membrane and the oxygen ion electrolyte were successively cast over a green  $\text{BaCe}_{0.85}\text{Y}_{0.15}\text{O}_{3-\delta}$  pellet, their components, mainly the solvent, diffused into the its structure during the drying phase. Then, during sintering, these compounds would react or evaporate from the body of the pellet causing its deformation. The samples produced by this method were closer to an optimized fuel cell structure. The whole thickness of the sample was 730  $\mu\text{m}$ : a proton conducting electrolyte with 600  $\mu\text{m}$ , the central membrane with 100  $\mu\text{m}$  and an oxide-ion conducting electrolyte with 30  $\mu\text{m}$ . Thus reduced thickness of this prototype reduces the ohmic losses in the electrolytes and also in the the central membrane. The sample flatness allows it to be tested electrochemically. The quality of the interfaces allow the transport of the ions from the electrolytes to the central membrane and the central membrane is a composite porous structure that allows water formation and evacuation. Its disadvantage is the lower density of the proton conducting electrolyte. The gas-tightness of the samples relies thus mostly on the oxide-ion conducting electrolyte.

The confirmation that the fabrication procedures developed are valid came from the electrochemical testing of these prototypes. But most of all, the electrochemical tests allowed to prove that IDEAL-Cell is a new concept that operates as a fuel cell with some specificities

linked to its new configuration.

As described in part II.5, the electrochemical activities included the development of a dedicated electrochemical tester. The need of such a device arises from the specific three chambers configuration of this concept of fuel cell. In order to take advantage from the IDEAL-Cell design, the central membrane compartment must be isolated from the electrodes. The electrochemical tester designed for these experiments contains thus three sealed chambers. This configuration also allowed to follow the composition of the exhaust gas from the central membrane through a moisture analyzer.

The two types of samples produced allowed to obtain two different types of results and both of them fulfilled the 4 criteria chosen to prove IDEAL-Cell as a new concept of fuel cell.

The electrolyte-supported sample was tested following the procedure described above. When the cell was fed with wet hydrogen and oxygen, its open circuit voltage rapidly increased to 0.9V, a value close the theoretical one. This value was remarkably stable in time. The reactions taking place in the anode and in the cathode create a difference of potential that is function of the gibbs free energy of the global reaction in standard conditions. The potential created is function of the temperature and the concentration of the reactants as it is described by the Nernst equation. The variation with temperature of the theoretical open circuit voltage of a cell fed with pure hydrogen and oxygen is shown in figure II.41.

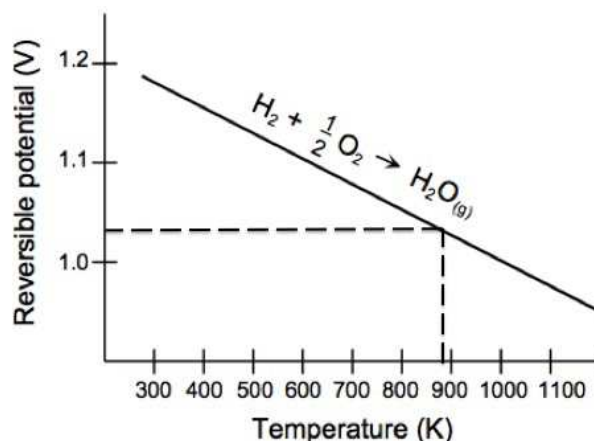


**Figure II.41** : Open circuit voltage of the of fuel cell fed with pure hydrogen and oxygen as a function of temperature.[9]

The fact that the experimental open circuit voltage is slightly lower than the theoretical one may be due to the use of non-pure gases. First of all, the anode gas has 3 wt.% of water to create proton defects in the electrolyte material. It is also possible that there were leakages in the experimental set that reduced even more the concentration of hydrogen in the anode feed stream. And one should not also exclude that gas crossover occurred in the cell, since the electrolytes are less dense than the ones of the self-supported sample. Due the better microstructures of this sample or to a better sealed experimental setup, the open circuit voltage reached was 1.04 V, closer to the theoretical value.

The electrolyte-supported sample was then submitted to galvanostatic polarization measurements. A characteristic V/I curve was obtained. The potential varies linearly with the current translating that the ohmic losses are the limiting-step of the cell performance. The specific power of this prototype is therefore rather low. This is certainly due to the lack of optimization of the whole structure in terms of layers thicknesses, central membrane

porosity and concentration of active reaction sites (triple-phase boundaries).

Impedance analysis was carried out at a potential very close to the OCV. The nyquist plot displays an inductive loop for which the differential resistance is negative, i.e. the values of the real part of the impedance decrease. C. Gabrielli has developed a mathematical model for such impedance spectra considering that a two-steps reaction occurs for which the reaction rate of the second step is higher than the first one [33]. Z. Stoynov and D. Vladikova in a catalogue of impedance models also identify a very similar nyquist plot as representing a two step reaction model [34]. Epelboin *et al.* report the same type of inductive loop in the study of the dissolution and passivation of Fe in an acidified sulfate solution [35]. The presence of an inductive loop is in this case due to the formation of water in the central membrane. Recently, Vladikova *et al.* suggested, based on these results, a model to the water formation in the central membrane [36]. According to the Gibbs theory for formation and growth of new phases, when clusters of the new phase are small, i.e. under a critical size, their growth need additional energy [37]. From an impedance point of view this implies a positive differential resistance. After reaching the critical size, the phase clusters growth becomes a spontaneous process that occurs with smaller external chemical potential. And it is this second process that has a negative differential resistance in the impedance diagram. Capturing this phenomena requires thus the fine-tuning of the experimental conditions that allow to detect the formation of the negative loop. The fuel cell must be in an operating point in which water is formed slowly so that it is possible to detect the formation of the water clusters before reaching the critical size. This operating point was found to be very close to the open circuit voltage, when a low direct current is produced by the cell and therefore a small amount of water is formed at a slow rate. Then a small intensity perturbation of the system is carried out by supplying a low alternate current with about 1/10 the intensity of the direct current produced by the cell. In these conditions, at lower frequencies, it is possible to detect the formation of water clusters and to follow their growth until the critical size. Then the water formation is spontaneous and doesn't need additional energy which is translated in the impedance diagram as a negative resistance, i.e. a negative loop.

Besides showing an improved OCV value, the self-supported samples allowed obtaining a different kind of results. One of them is the production of current at the exact moment the circuit is closed while wet hydrogen and oxygen are fed to the anode and cathode, respectively. But the better contribution from this sample was the direct measurement of water formation in the central membrane. This experiment is particularly difficult due to the low amount of water produced that was further diluted in the gas carrier stream. However, in figure II.40(b), it is clear that when the circuit was closed, the current demand increased, leading to a decrease in the cell voltage and an increase of water concentration in the third chamber stream was measured. This last evidence of water formation in the central membrane, fulfills the last two criteria previously chosen to prove this concept. It is clear, though, that when the circuit is open again, a decrease of water concentration is not measured in the third chamber stream. This may be explained by the distance at which the moisture analyzer was from the sample, causing a delay in the detection of the system's reaction to the change in the experimental parameters.

## II.7 Conclusions

The activities described above showed that IDEAL-Cell is a new concept of fuel cell, a new possibility available in the scientific community to improve fuel cells efficiency. During these activities new challenges in the fields of electrochemical testing and materials shaping came up. The electrochemical testing with direct water measurement and impedance analysis were technically sophisticated experiments, innovative to the scientific community. Fulfilling the

four criteria was a demanding and reliable path for the IDEAL-Cell concept that other fuel cell concepts didn't go through before.

However, the performances of these first prototypes are very low compared to the more mature high and intermediate temperature fuel cells. This is due to the early stage of development of the shaping procedure used to fabricate such a cell. Thus shaping procedure can be improved to optimize both macro and microstructures. The fact that two electrolyte materials are used in the fabrication of this fuel cell is a constraint in what concerns sintering of the materials. The different thermal expansion coefficients and different behavior at high temperature (different shrinkage rates), make producing thin, flat samples, a complicated issue in which many parameters play a role. Therefore the use of materials with a more similar sintering behavior, whether by controlling the particle size or changing their chemical nature or use sintering aids, will be necessary to decrease the cell thickness and reach higher performances. Another important issue is the control of the powders particle size distribution, that should be as narrow as possible in order to yield ceramic pieces with homogeneous sintering kinetics which is a very important parameter for the flatness of such thin layers.

Many questions concerning the central membrane are unanswered, due to the innovative nature of such a structure. The best proportion of the proton and oxygen ion conducting phases, the volume and tortuosity of the porosity that allows highest rate of water production and evacuation are important morphological parameters in the optimization of this cell. Increasing the concentration of the active reaction sites in the central membrane may be a factor as important as the concentration of the electrodes triple-phase boundary in the other more classical fuel cell systems.

Now that it is proven to be a fuel cell, an important axis of development of this concept is the fabrication of the electrodes (chapter III) that will lead to the fabrication of a complete cell (chapter IV), without platinum electrodes. This step would contribute to approach this fuel cell from the stage of development of the more mature ones.

Le premier objectif de ce projet a été de démontrer la faisabilité et le fonctionnement de ce concept innovant de pile à combustible. Pour cela, des échantillons spécifiques ont été fabriqués par combinaison du coulage en bande et pressage à froid, suivi d'un frittage à haute température. Ces échantillons ont une configuration simplifiée comparée à celle de la cellule complète qui consiste à substituer les électrodes conventionnelles par un simple dépôt de platine. Les composés  $\text{BaCe}_{0.85}\text{Y}_{0.15}\text{O}_{3-\delta}$  (BCY15) et  $\text{Ce}_{0.85}\text{Y}_{0.15}\text{O}_{2-\delta}$  (YDC15) ont été sélectionnés respectivement comme électrolytes conducteurs protonique et anionique. Le choix de ces matériaux repose sur le meilleur compromis entre bonnes performances électrochimiques et compatibilité chimique dans les conditions réelles de fonctionnement de la cellule. Des températures de frittage de  $1300^\circ\text{C}$  et  $1200^\circ\text{C}$  pour BCY15 et YDC15 ont été mesurées par dilatométrie, tous deux présentant une distribution granulométrique très proche. Les échantillons dédiés à la preuve du concept ont été testés sur banc de tests électrochimiques et les résultats montrent qu'ils se comportent telle une pile à combustible haute température avec quelques spécificités relatives à sa configuration en 3 chambres indépendantes. Pour valider le concept, 4 critères prédéfinis ont été démontrés : (1) une tension en circuit ouvert et (2) une courbe de polarisation stables, (3) une signature sur les spectres d'impédance complexe caractéristique de la formation d'eau et (4) quantification de la teneur en eau formée en fonction du courant traversant la cellule. A ce stade du projet, la densité de puissance maximale mesurée est de  $2.3 \text{ W cm}^{-2}$ .

---

---

## Chapter -III-

# The Electrodes: Anode and Cathode

---

### Contents

---

<b>III.1</b>	<b>Introduction . . . . .</b>	<b>62</b>
<b>III.2</b>	<b>Anode materials . . . . .</b>	<b>62</b>
III.2.1	State-of-the-art . . . . .	62
III.2.2	Characterization of anode materials . . . . .	64
III.2.2.1	Samples description and fabrication . . . . .	65
III.2.2.2	S.E.M. characterization of samples . . . . .	69
III.2.2.3	Electrochemical testing . . . . .	69
III.2.3	Discussion . . . . .	71
III.2.4	Conclusions . . . . .	71
<b>III.3</b>	<b>Cathode Materials . . . . .</b>	<b>72</b>
III.3.1	State-of-the-art . . . . .	72
III.3.2	Characterization of cathode materials . . . . .	74
III.3.2.1	Samples description and fabrication . . . . .	77
III.3.2.2	S.E.M. characterization of samples . . . . .	79
III.3.2.3	Electrochemical testing . . . . .	80
III.3.3	Development of a composite cathode . . . . .	80
III.3.3.1	Experimental procedure . . . . .	80
III.3.3.2	Sample characterization . . . . .	81
III.3.3.3	Electrochemical testing . . . . .	81
III.3.4	Development of a new cathode material . . . . .	82
III.3.4.1	Experimental Procedure . . . . .	82
III.3.4.2	Electrochemical testing . . . . .	83
III.3.4.3	Discussion . . . . .	84
III.3.5	Conclusions . . . . .	86
<b>III.4</b>	<b>Conclusions . . . . .</b>	<b>86</b>

---

### III.1 Introduction

In the previous chapter it was described how IDEAL-Cell prototypes were fabricated from proton and oxygen ion conducting materials using tape casting and cold pressing as shaping techniques. These prototypes were electrochemically tested and fulfilled pre-defined criteria that proved they behaved as a fuel cell when a difference of potential was created between the electrodes. As it was said before, platinum electrodes were used in the POC prototypes to avoid the problems of materials and microstructure optimization of ceramic electrodes. However, in precious metal electrodes, the electrochemical reactions occur only in the electrode/electrolyte interface whereas in ceramic electrodes they are extended to the whole microstructure. Thus it is expected that the electrodes activation polarizations decrease when ceramic structures are used. Therefore, the use of optimized ceramic electrodes is very important regarding the improvement of a complete IDEAL-Cell performances.

In this chapter, the activities carried out to develop ceramic electrodes are described. The electrodes were electrochemically tested and these results took to the optimization of their composition.

### III.2 Anode materials

The anode of a the IDEAL-Cell concept is the same used in PCFC in which the oxidation of hydrogen takes place creating a flow of electrons that are conducted through an external circuit and a stream of protons that flow towards the electrolyte. Thus, the microstructure of the anode must be porous to allow the diffusion of hydrogen to each electrochemical sites where a metal catalyzes its oxidation. However, these electrochemical sites are only active if the catalyst is in contact not only with a porous network that allows the diffusion of hydrogen but also with a proton conductor that percolates towards to the electrolyte and an electron conductor that percolates in the direction of the current collector. These active electrochemical sites are the so called triple phase boundaries (TPB) and their length in an anode is increased when composite ceramic anodes are used instead of precious metals ones [38].

The anode of a fuel cell must have a high electrical conductivity and high electrochemical catalytic activity, it must be mechanically and chemically stable when in contact with the electrolyte in operating conditions. It must also have a coefficient of thermal expansion that matches those of the other cell components. In the fabrication of an anode it must be taken into account the optimization of the microstructures but also the chemical composition of the materials used.

#### III.2.1 State-of-the-art

Several studies have been carried out on the development of SOFC anodes. The most widely used anode in this kind of fuel cells is a mixture of nickel and yttrium-stabilized zirconia (Ni-YSZ), so-called cermet for its ceramic-metal composition. Nickel acts as an excellent reforming catalyst (if hydrocarbons are used directly as fuel) and as an electrocatalyst for the oxidation of hydrogen while YSZ constitutes a support for the nickel particles and an oxygen ion conductor [39]. However some disadvantages of these materials remain a challenge. Ni-based anodes catalyze the deposition of carbon that block the electrochemical reaction. For this reason, many researchers have suggested different SOFC anode materials such as replacing Ni for Cu. Cu-YSZ composites were reported to be stable in hydrocarbon fuels but it's necessary to add ceria as catalyst for the anode to achieve reasonable performances [40].

This subject has been widely studied for SOFCs since it has a great impact in the activation polarization of the cell. Although this is also a very important subject to improve the performance of PCFCs, very few studies have been carried out on cermet anodes fabrication [38].

Similarly to the Ni-YSZ cermet anodes used in SOFC, the most used ones in PCFC is a cermet anode based on a catalytically active metal to hydrogen oxidation and a high temperature proton conductor because they have TPB extended to the whole structure volume. M.-L. Fontaine *et al.* have proposed a shaping procedure based on tape casting, spin-coating and screen-printing of a fuel cell based on  $\text{La}_{0.995}\text{Sr}_{0.005}\text{NbO}_{4-\delta}$  electrolyte and a cermet  $\text{La}_{0.995}\text{Sr}_{0.005}\text{NbO}_{4-\delta}/\text{NiO}$  anode [41]. G.C. Mather *et al.* studied the stability of  $\text{Ni-SrCe}_{0.9}\text{Yb}_{0.1}\text{O}_{3-\delta}$  and found that there is degradation ceramic component of the cermet in reducing atmospheres [42].

Nickel is the most widely used catalyst in PCFC anodes although some aspects of its action are not well understood. Rossmeisl and Bessler found a relationship between the conductivity of nine different metals that can be used in SOFCs electrodes with the respective surface binding enthalpy of oxygen,  $\Delta E_o$ , as seen in figure III.1(a) [43].

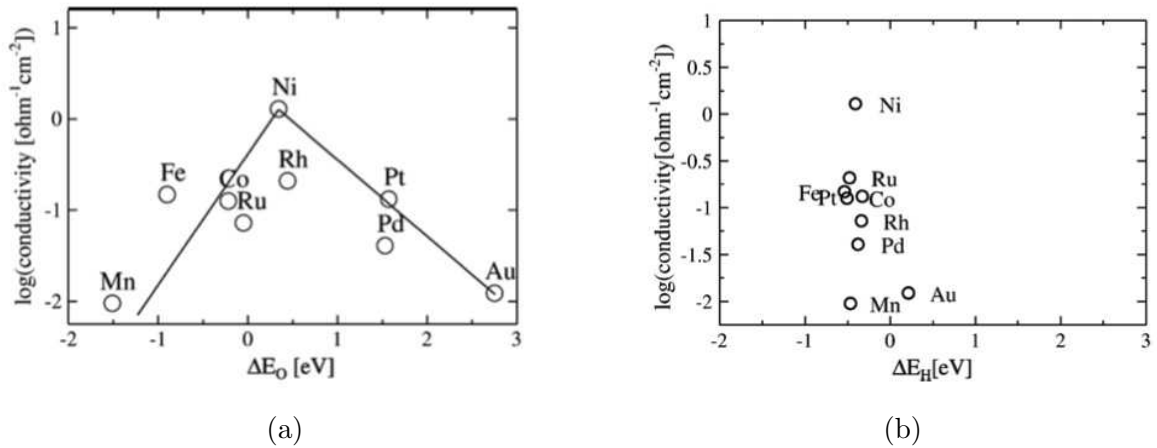


**Figure III.1** : Conductivities of different metals used in SOFCs electrodes plotted against the adsorption energy of (a) oxygen and (b) hydrogen on pure metal surfaces [43].

The fact that the metals' surface affinity towards the oxygen has a strong relationship with the conductivity suggest that the metal-oxygen species are important intermediates in the anode reaction. These results show that the oxygen spillover mechanism is the relevant reaction to investigate. In this same article the hydrogen spillover mechanism was also studied [43]. According to it, hydrogen molecules dissociate on the anode surface and diffuse to the three-phase boundary where a proton is transferred to the electrolyte. This is the same mechanism that occurs in the anode of a PCFC since hydrogen is the only gas present. Thus, the conductivities of each metal was plotted against hydrogen adsorption energy,  $\Delta E_H$ , because this would be relevant step of the mechanism. However, as it is seen in figure III.1(b) the hydrogen adsorption energies of all the metals are very similar and the hydrogen spillover mechanism does not explain nickel's better performance. Further investigations on the catalytic mechanism of nickel are necessary since contradictory studies were reported. Bieberle *et al.* obtained experimental anode data that could be interpreted according to the hydrogen spillover mechanism [44].

### III.2.2 Characterization of anode materials

For the reasons explained above, the anode chosen was a cermet of a metal with catalytic properties towards hydrogen oxidation, and a ceramic proton conductor. Since the anode must be chemically stable in contact with the electrolyte and must have similar coefficient of thermal expansion, the proton conductor chosen was the same used in the electrolyte of the POC prototypes, i.e.  $\text{BaCe}_{0.85}\text{Y}_{0.15}\text{O}_{3-\delta}$ . As an electron conductor and electrochemical catalyst, NiO was used as a precursor of Ni. The fabrication of the anode requires the tuning of the composition that yields an anode with a coefficient of thermal expansion similar to that of the electrolyte. Reducing the percentage of NiO used in the cermet approaches the shrinkages of the two layers during sintering, as studied by R.M.C. Clemmer and S. F. Corbin in Ni-YSZ anodes (figure III.2).

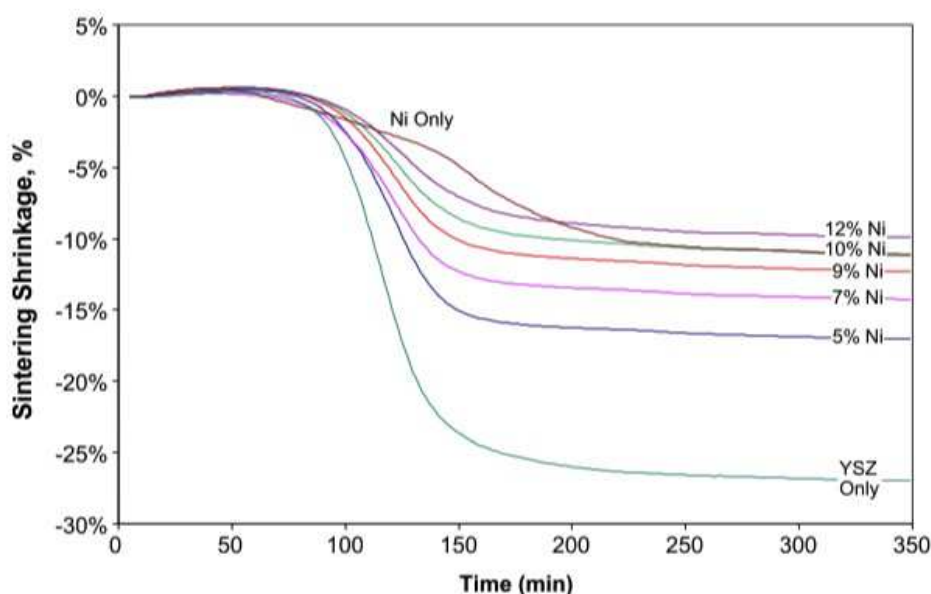


**Figure III.2** : Sintering shrinkage of different cermets with different proportions of Ni and YSZ [45]

The results show that a small variation in the percentage of nickel drastically changes the shrinkage behavior of the cermet during sintering, compared to that of the electrolyte. Thus, the lower is the concentration of nickel in the anode, the more compatible their behavior during sintering will be. However, one must keep in mind that the volume percentage of nickel must be high enough to give the anode a high concentration of TPB and to create percolating paths for electrons towards the current collector. Pratihari *et al.* determined through conductivity measurements in Ni/YSZ cermets that the percolation threshold for nickel is about 30 vol.%, as it can be seen in figs.III.3(a) and (b) [46] [47].

Working above the percolation threshold of both metal and proton conductor phases, Zunic *et al.* tested three different Ni- $\text{BaCe}_{0.9}\text{Y}_{0.1}\text{O}_{3-\delta}$  anodes in complete cells [38]. The proportions of the two phases were changed (40:60, 50:50 and 60:40) in three different fuel cells where the same composite cathode:  $\text{La}_{0.8}\text{Sr}_{0.2}\text{Co}_{0.8}\text{Fe}_{0.2}\text{O}_3 - \text{BaCe}_{0.9}\text{Y}_{0.1}\text{O}_{3-\delta}$ . The three cells were tested in air and pure hydrogen at different temperatures and their performances were compared with platinum anode cell. The results, in figure III.4, show that the fuel cells maximum power has a slight decrease (less than 5%) when the amount of nickel is reduced from 60 vol.% to 40 vol.% in the cermet.

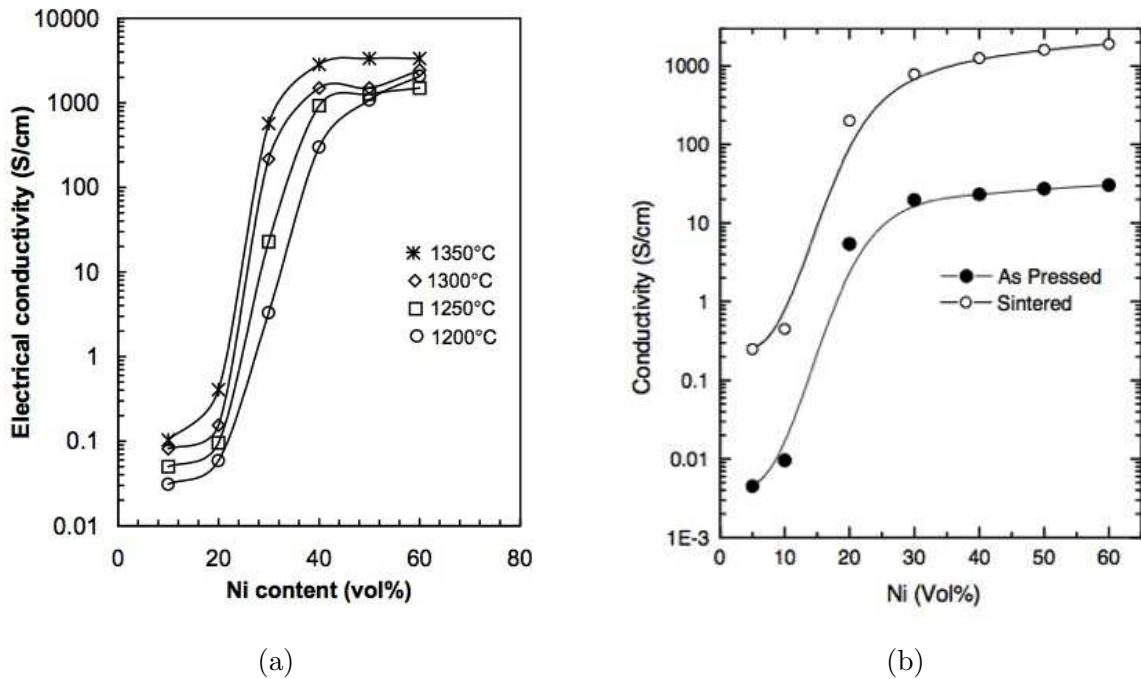


**Figure III.3** : Variation of electrical conductivity measured (a) at 1000°C as a function of nickel concentration in Ni/YSZ anodes sintered at different temperatures [46] and (b) measured at room temperature in Ni/YSZ pellets made from nickel coated powder [47].

The  $\text{BaCe}_{0.85}\text{Y}_{0.15}\text{O}_{3-\delta}$  powder used was the same characterized in chapter II: it's a powder with a particle size distribution centered at  $d_{50} = 0.23 \mu\text{m}$  that is not narrow and includes particles of  $2 \mu\text{m}$ ; this powder has a sintering temperature of 1300°C. The NiO powder was supplied by Novamet. According to the supplier, this powder has a particle size distribution centered at  $d_{50} = 6\text{-}10 \mu\text{m}$  and a specific surface of  $3\text{-}4 \text{ m}^2/\text{g}$ . Through S.E.M. observations, it was verified that the particles have an homogeneous rounded shaped morphology with a large particle size distribution.

The X-ray diffraction pattern in figure III.6 demonstrates that the nickel oxide supplied is a single-phase powder.

In order to identify the behavior of this material at high temperature, a dilatometry was carried out with the same temperature cycle used for the electrolyte materials and shown in figure II.9 and figure II.19. A pellet of nickel oxide was put in the dilatometer with two platinum foils between the alumina tubes of the experimental apparatus and the sample to avoid the reactivity between them. An experiment was carried out only without the ceramic pellet in order to know shrinkage of the platinum and the apparatus itself. The corrected behavior of nickel oxide is displayed in figure III.7. The powder is less refractory than the electrolyte materials since it reaches its highest shrinkage rate at 1050°C.

### III.2.2.1 Samples description and fabrication

In order to study the performances of the electrodes produced with the materials available using tape casting and cold pressing, anode symmetrical cells were produced. A fabrication method was optimized to produce these samples, taking into account their specifications. The anodes must be porous cermets with high density of triple-phase boundaries deposited by tape casting on both sides of a dense proton electrolyte layer of about  $500 \mu\text{m}$  thickness.

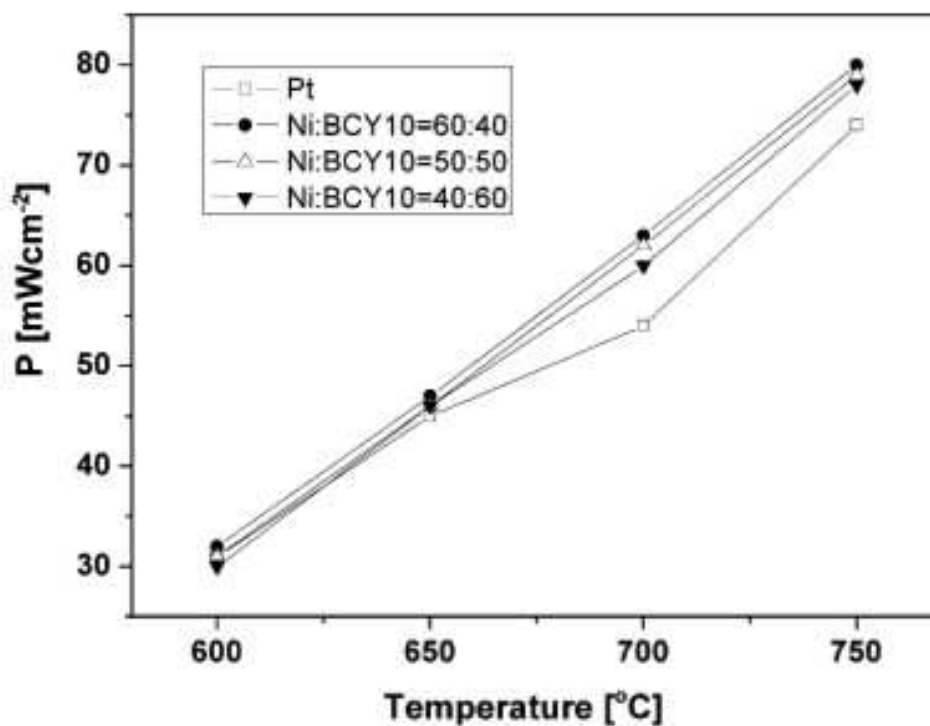


**Figure III.4 :** Performance comparison of a single cell with different anode types at different temperatures [38].

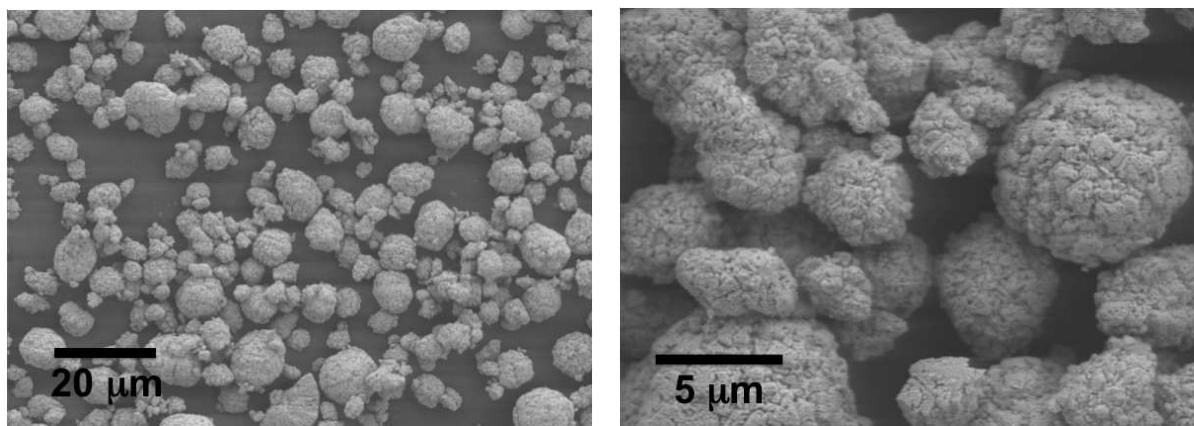


**Figure III.5 :** S.E.M. pictures of the nickel oxide powder used in the anode fabrication.

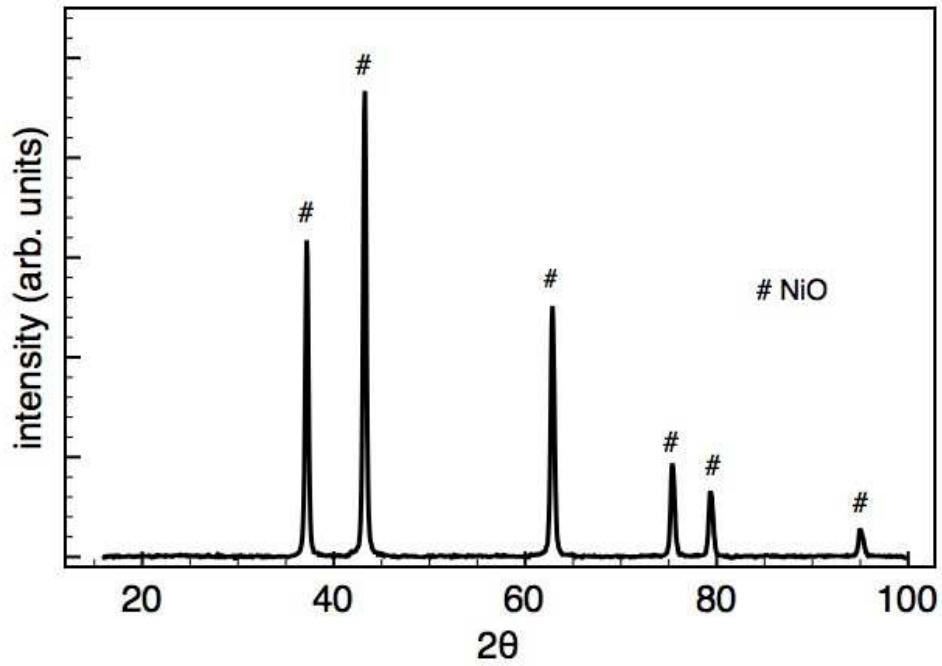


Figure III.6 : X-ray diffraction pattern for the NiO powder.

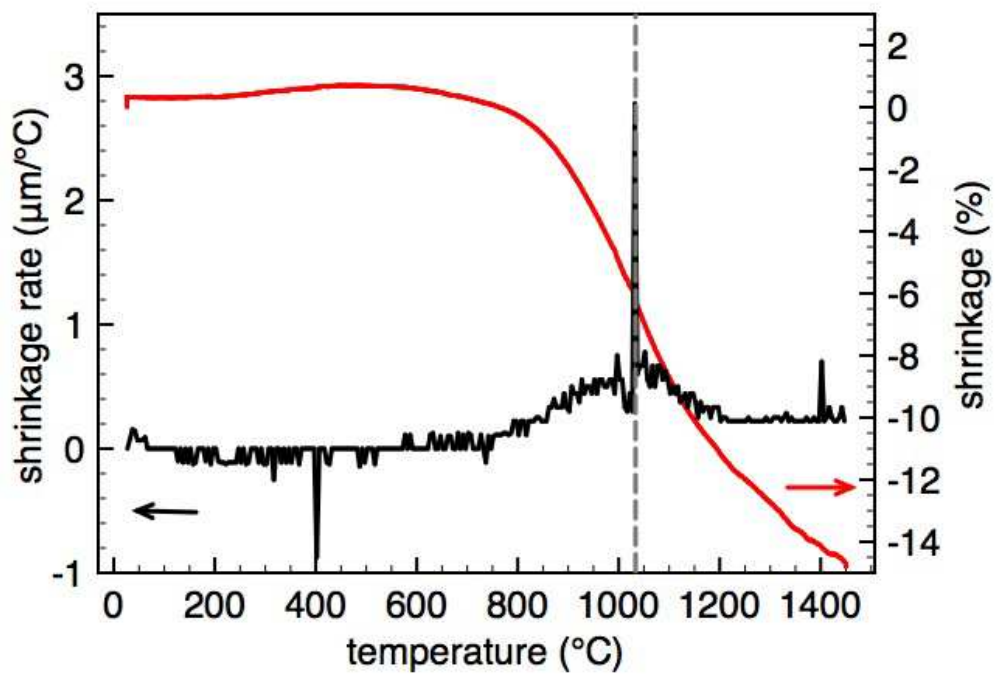


Figure III.7 : Nickel oxide powder shrinkage and shrinkage rate during sintering.

**Table III.1** : Composition of the anode tape casting slurry layer.

	anode layer	short name
NiO	2.80g	-
BaCe <sub>0.85</sub> Y <sub>0.15</sub> O <sub>3-<math>\delta</math></sub>	3.50 g	BCY15
poly(vinyl butyral)	4.50 g	PVB
poly(ethyleneglycol)	3.50 g	PEG
ethanol	7.00 g	-

The whole sample must have a diameter of at least 20 mm for reasons of compatibility with the electrochemical tester. The configuration of the samples is illustrated in figure III.8.

**Figure III.8** : Scheme of an anode symmetrical cell.

The fabrication procedure of anode symmetrical cells must take into account the performance of the electrode and the electrolyte and therefore their microstructures and composition. While the electrolyte is a pure proton conductor, the anode composition must be tuned to create electron conducting, proton conducting and porosity percolating paths. Where these paths are in contact with each other is where the electrochemical reaction takes place. However, performance criteria are not the only ones to be taken into account; the material behavior during sintering is important to ensure the samples flatness and the layers interfaces. The shrinkage of the porous anode must be compatible with that of the dense electrolyte and the composition of the anode plays an important role, as seen in figure III.7. Since NiO has a sintering temperature lower than BaCe<sub>0.85</sub>Y<sub>0.15</sub>O<sub>3- $\delta$</sub> , the anode will densify at a lower temperature than the electrolyte. The porosity of the anode may be ensured by the composition adding a higher volume of binder to the tape casting slurry or by sintering the cell at lower temperature. However, lowering the sintering temperature may obviously keep the electrolyte from densifying. On the other hand, above a certain temperature, the anode would stop shrinking and would not follow the same behavior of the electrolyte. This would cause the "delamination" of the anode layer and a cell with poor interfaces would be obtained.

With these constraints, an experimental procedure was found. Since the electrolyte should have at least 500  $\mu\text{m}$  of thickness, it could be easily produced by cold pressing. Thus, 2.0g of BaCe<sub>0.85</sub>Y<sub>0.15</sub>O<sub>3- $\delta$</sub>  were pressed at 100 MPa in a 25 mm diameter die. Then, in order to avoid the difference of shrinkage, the electrolyte was sintered at 1300°C for 5h with cooling and heating rates of 5°C/min. The electrolytes obtained have a density of 93%, measured through the weight and volume of the pellet. The anode layer was then cast over the sintered electrolyte. The slurry composition, in table III.1, and the sintering treatment were optimized to avoid the delamination of the anode and the electrolyte.

The anode has, thus, 40 vol.% of NiO (expected 35 vol.% after reduction) and 35 vol.% of BaCe<sub>0.85</sub>Y<sub>0.15</sub>O<sub>3- $\delta$</sub>  which may ensure the conduction paths of both electrons and protons, reaching the percolation threshold shown in figure III.3. The anode and electrolyte assembly were then sintered at 1100°C for 5h, according to the cycle shown in figure III.9.

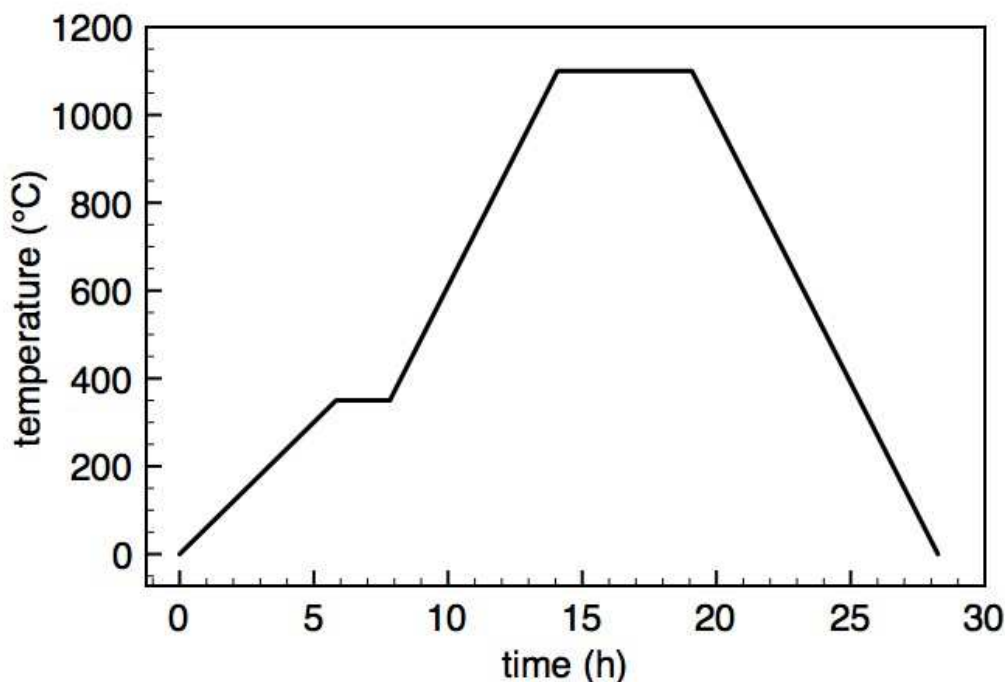


Figure III.9 : Sintering cycle for the anode layer in symmetrical cells.

### III.2.2.2 S.E.M. characterization of samples

The samples were sintered using a  $ZrO_2$  support over a  $BaCe_{0.85}Y_{0.15}O_{3-\delta}$  powder bed. The first layer was cast and sintered and only afterwards the second layer was deposited and sintered on the other side of the electrolyte. It was verified that when the two green anodes were sintered simultaneously, the one that was between the powder bed and the electrolyte was delaminated. This happened because the anode was sintered under a constraint and it wasn't able to shrink normally.

The samples obtained, shown in figures III.10 and III.11, were flat with 21 mm of diameter. The electrolyte was dense with about 6 vol.% of closed porosity and about  $800\mu m$  of thickness. The composite electrodes were highly porous with a thickness of about  $30\mu m$ . A good quality of the interfaces between the electrodes and the electrolyte was obtained.

### III.2.2.3 Electrochemical testing

Anode symmetrical cells were electrochemically tested in wet hydrogen in order to determine its area specific resistance. These experiments were carried out at the Institute of Electrochemistry and Energy Systems (I.E.E.S.) from Bulgaria by Daria Vladikova and her team.

Before these experiments were carried out, the anodes were reduced in 5% hydrogen at  $800^\circ C$  for 2h in order to reduce the nickel oxide to nickel, as used by Lee *et al.* [48].

Electrochemical impedance experiments were carried out in wet hydrogen from 0.1 Hz to 1 MHz and from  $420^\circ C$  to  $700^\circ C$ . The results, shown in figure III.12, show that the anodes produced have a resistance of  $21.06\ \Omega.cm^2$  at  $611^\circ C$ . Measuring the electrode's conductivity at different temperatures, an activation energy of 0.74 eV was determined.

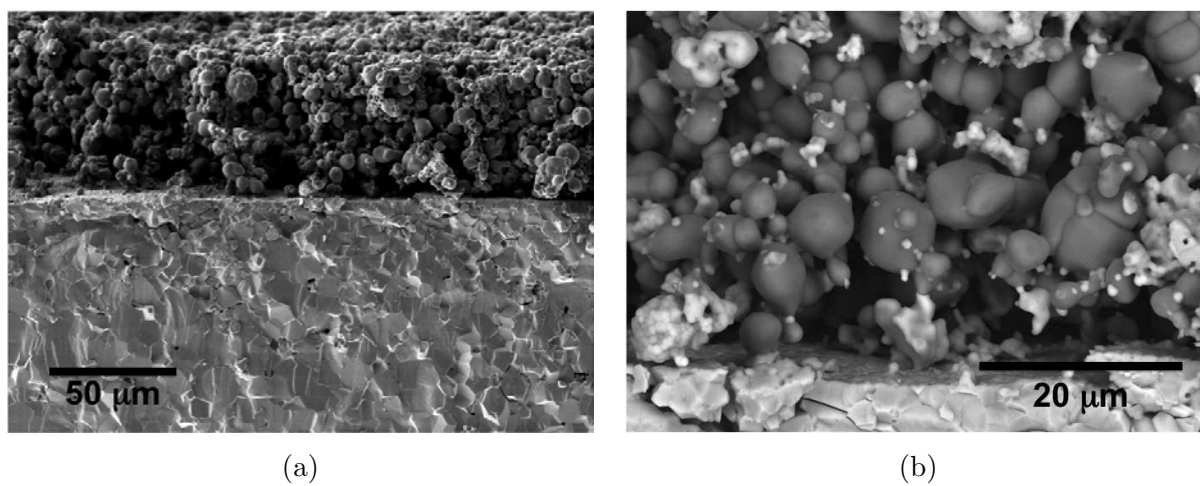


Figure III.10 : B.S.E.-S.E.M. anode symmetrical cell.

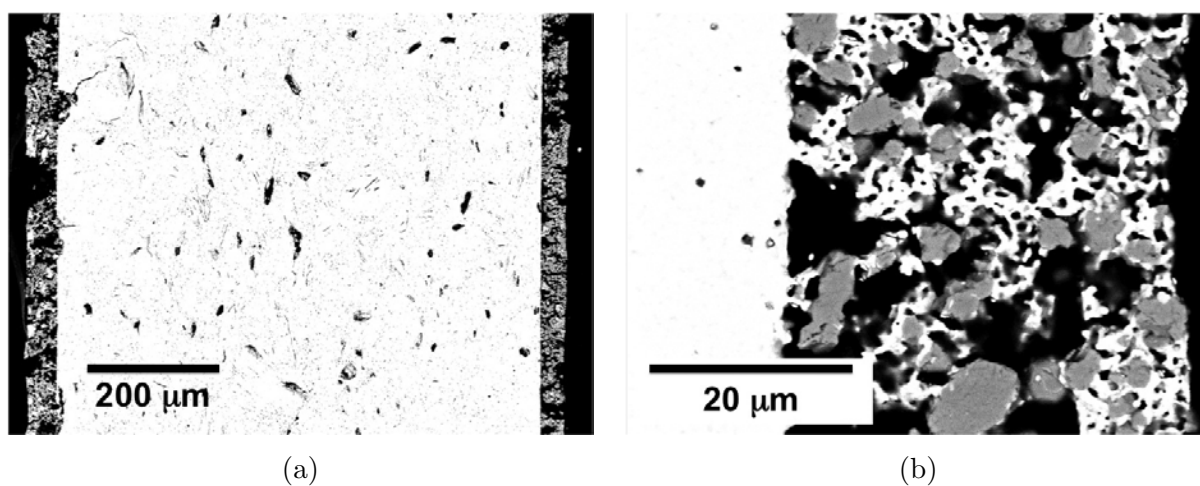
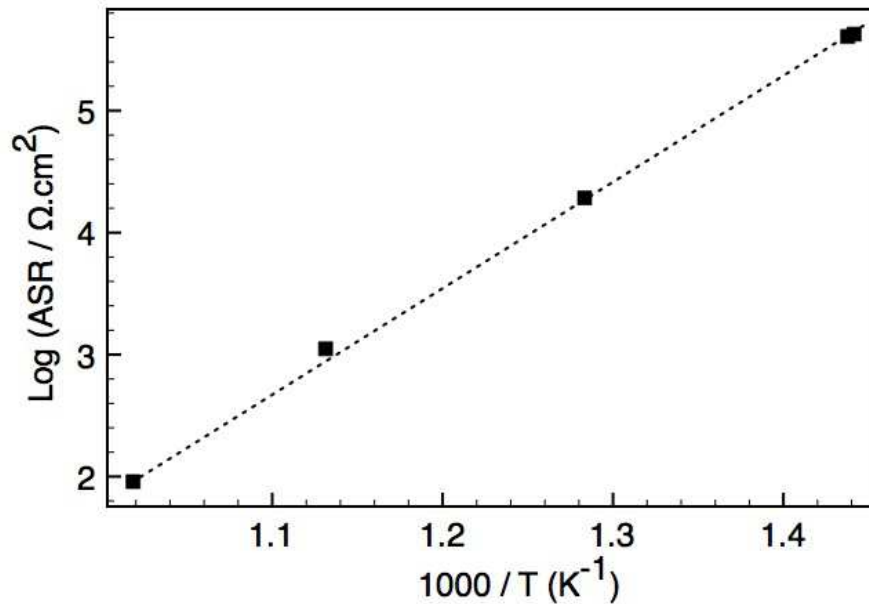


Figure III.11 : B.S.E.-S.E.M. anode symmetrical cell.



**Figure III.12** : Arrhenius plot of the Ni/BaCe<sub>0.85</sub>Y<sub>0.15</sub>O<sub>3- $\delta$</sub>  anode.

### III.2.3 Discussion

Due to the materials different sintering temperatures, a two step shaping procedure was developed in order to produce anode symmetrical cells. This procedure allowed avoiding that the two materials, with different shrinking rates, sintered simultaneously. Otherwise the delimitation and deformation of the layers would have occurred. A thick electrolyte could be obtained by cold pressing and sintering after determining the adequate sintering cycle. The procedure described before allowed producing symmetrical anode cells with good quality microstructures. The samples obtained were flat with dense electrolytes that didn't allow the diffusion of the gases through its structure. The anodes had good interfaces with the electrolyte and the necessary porosity to allow the diffusion of the fuel. It is a composite metallic and ceramic structure that assures both electron and proton conductivities. Each phase percolates and creates active reaction sites in the so called triple phase boundaries, the anode's active sites. The proportion of the two materials and the porosity of the layer must allow the formation of active reaction sites. Milan Zunic *et al.* reported that changing the two phases from 40 vol.% to 60 vol.% changes the power delivered by the cell from 30 mW/cm<sup>2</sup> to 32 mW/cm<sup>2</sup> at 600°C. Zunic *et al.* use in this study a very similar cermet as anode: Ni-BaCe<sub>0.90</sub>Y<sub>0.10</sub>O<sub>3- $\delta$</sub> . These anodes were produced by cold pressing and sintering. The activation energies reported are in the range of 0.084 eV and 0.072 eV in wet hydrogen which is about ten times smaller than the activation energy obtained for the anodes produced by the method described above [38]. The anodes produced have thus very low performance when compared to state-of-the-art ones using similar cermet.

### III.2.4 Conclusions

Anode symmetrical cells based on a BaCe<sub>0.85</sub>Y<sub>0.15</sub>O<sub>3- $\delta$</sub>  electrolyte and a Ni/BaCe<sub>0.85</sub>Y<sub>0.15</sub>O<sub>3- $\delta$</sub>  cermet anode. The method uses cold pressing to produce the electrolyte and tape casting to deposit the anode layer. The two compartments are sintered in two different treatments due to

the need to densify the electrolyte and avoid the delamination of the anode that has a different high temperature sintering behavior. The procedure developed allowed producing flat samples with about 21 mm of diameter and 700  $\mu\text{m}$  of thickness and appropriate microstructures. The electrolyte was dense, to allow a good effective conductivity and the electrode was porous to allow the diffusion of the fuel. The volume percentage of the two phases of the cermet was in the range that the percolation theory predicts necessary to allow the transport of the electrons and protons and was the same reported to be effective by others authors, the anode produced had an area specific resistance of 21.06  $\Omega\cdot\text{cm}^2$  at 600°C and an activation energy of 0.74 eV. This value of activation energy is ten times higher than the one reported by Zunic *et al.* [38]. Therefore, since the quality of the microstructures is satisfying, the reason for these low performances must be related with the formation of an insulating phase in the interface of Ni and  $\text{BaCe}_{0.85}\text{Y}_{0.15}\text{O}_{3-\delta}$  that blocks the electron conductivity. This phenomena need further investigation.

### III.3 Cathode Materials

In an IDEAL-Cell, the cathode is identical to that used in an SOFC. In this cathode, oxygen diffuses and reacts with the electrons coming from the anode to create oxygen ions, according to the reaction of reduction I.11. Thus the cathode must be a porous structure made of a mixed oxygen ion and electron conducting material. The configuration of a cathode is thus very similar to that of an anode in the sense that percolating paths for ions, electrons and porosity must be created and the electrochemical reaction takes place where they intersect. The concentration of these active electrochemical sites is higher when ceramic cathodes are used instead of platinum cathodes, where reaction only takes place in its interfaces with the electrolyte.

Similarly to the anode, the cathode of a fuel cell must have a high electrical conductivity and high electrochemical catalytic activity. It must be chemically stable when in contact with the electrolyte in operating conditions and must have a coefficient of thermal expansion that matches those of the other cell components so that mechanical failure during operation doesn't occur. In the fabrication of a cathode, it must be taken into account the optimization of the microstructures but also the chemical composition of the materials used.

#### III.3.1 State-of-the-art

In a fuel cell, the cathode is responsible for very important losses due to the mass transfer of air or oxygen in the microstructure and to the activation of the electrochemical reaction. The proportion of these losses are illustrated for PAFCs in figure III.13.

Therefore it is very important to select materials with higher conductivities and better electrochemical activity to improve fuel cells performances. The criteria for the materials choice must also allow to avoid technical problems such as cracking of the components at high temperatures which are due to the mismatch of thermal expansion coefficients between the cathode and the electrolyte [49].

The majority of the activities currently in progress on the development of SOFCs cathodes are dedicated to perovskite-type oxides [49]. Amongst these materials the ones that have drawn more interest were Sr-doped  $\text{LaCoO}_3$  and Sr-doped  $\text{LaMnO}_3$  due to their high oxide ion and electronic conductivities [50] [49]. These properties make them interesting mixed ionic-electronic conductors.  $\text{La}_{1-x}\text{Sr}_x\text{CoO}_{3-\delta}$  were the first perovskites to be reported as good conductors for SOFC cathodes. However, in operating conditions, the performance of these materials is not stable due to the high thermal expansion coefficient with respect to the one of yttria-stabilized zirconia, the most used electrolyte material in SOFCs [50].

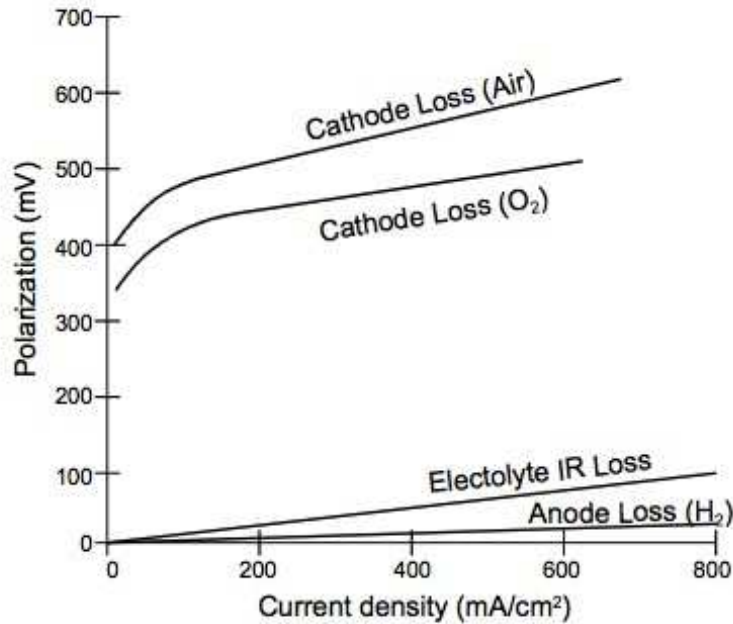


**Figure III.13** : Cathode and anode contribution to a fuel cell polarization. [9]

$\text{La}_{1-x}\text{Sr}_x\text{CoO}_{3-\delta}$  oxides are also chemically incompatible with yttria-stabilized zirconia since they react at high temperatures (about  $1000^\circ\text{C}$  [51]). This electrode is interesting when used with ceria-based electrolytes due to their higher conductivity compared to the one of yttrium-stabilized zirconia which allows to decrease the system operating temperature to  $700^\circ\text{C}$ - $800^\circ\text{C}$  and therefore avoid the reactivity with the cathode [52] [53] [54]. While trying to replace  $\text{La}_{1-x}\text{Sr}_x\text{CoO}_{3-\delta}$  oxides, different materials such as  $\text{Gd}_{1-x}\text{Sr}_x\text{CoO}_3$ ,  $\text{GdCoO}_3$ ,  $\text{Sm}_{1-x}\text{Sr}_x\text{CoO}_3$  have been tested as SOFC cathodes. However, these materials were reported to be reasonable but less conductive than La-doped analogues [49].

Different strategies have been followed to improve the compatibility of these materials. One of the most promising ones is substituting the B-site of the perovskite ( $\text{ABO}_3$ ) with Fe for Co. Tai *et al.* studied the influence of the concentration of iron and strontium on the electrical conductivity and linear thermal expansion coefficient of the materials. It was shown that replacing Co with Fe decreases the thermal expansion coefficient, making the behavior of the cathode at higher temperature closer to the one of the electrolyte. On the other hand it is also shown that the increase of Fe leads to the decrease of electrical conductivity (see figures III.14 (a) and (b)) [55] [56]. The objective is to reach the best compromise between a high electrochemical performance and a thermal expansion coefficient compatible with the electrolyte material.

For the case of the A-site doping with Sr, it was reported that the decrease of La leads to the increase of the thermal expansion coefficient, making it less compatible with ceria-based. However the lower is the percentage of Sr is in the material, the lower is its conductivity. The maximum electrical conductivities of  $\text{La}_{1-x}\text{Sr}_{0.4}\text{Co}_x\text{Fe}_{0.8}\text{O}_3$  were found for  $x = 0.2$ - $0.4$  at temperatures between  $600^\circ\text{C}$  and  $800^\circ\text{C}$  in air. These conductivities were in the range of 200-330 S/cm [56].

SOFCs with  $\text{La}_{0.58}\text{Sr}_{0.4}\text{Co}_{0.2}\text{Fe}_{0.8}\text{O}_3$  cathodes have successfully been developed giving

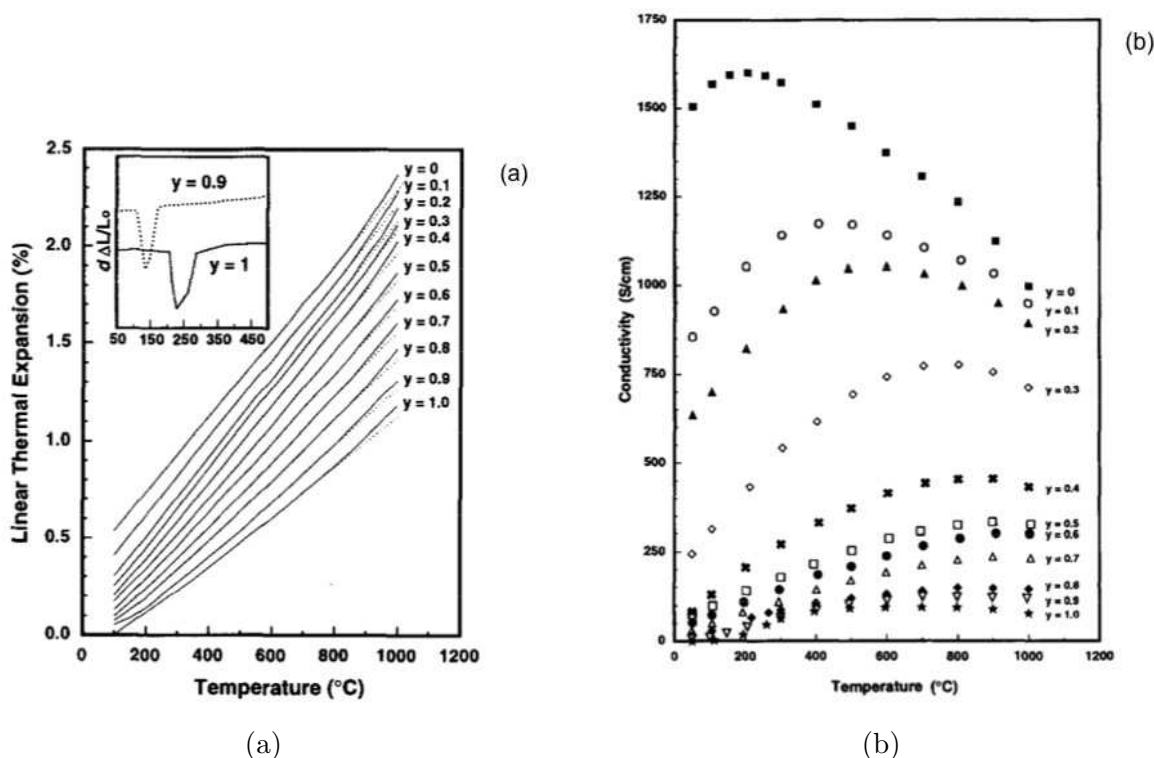


**Figure III.14** : Linear thermal expansion curves for  $\text{La}_{0.8}\text{Sr}_{0.2}\text{Co}_{1-y}\text{Fe}_y\text{O}_3$  in (a) and electrical conductivity of the same material as a function of temperature in air in (b) [55].

reproducibly a power output of 1.0-1.2W/cm<sup>2</sup> at 800°C and 0.7V with hydrogen as fuel gas. Compared with conventional cathodes based on (La,Sr)MnO<sub>3</sub> the higher power densities allow to reduce the operating temperature of about 100°C [57]. Different  $\text{La}_{1-x}\text{Sr}_x\text{Co}_y\text{Fe}_{1-y}\text{O}_3$  cathode compositions have been tested with Ni-YSZ anodes and YSZ electrolytes. A  $\text{Ce}_{1-x}\text{Gd}_x\text{O}_2$  layer was screen printed between the electrolyte and the cathode to avoid reactivity. The performances were compared with (La,Sr)MnO<sub>3</sub>/YSZ composite cathodes and the results at 800°C and 700°C are shown in figure III.15.

It is seen that the best performances are reached using the  $\text{La}_{0.8}\text{Sr}_{0.2}\text{Co}_{0.2}\text{Fe}_{0.8}\text{O}_3$  cathode at both operating temperatures. At 800°C, cells with LSM/YSZ cathodes have similar performances to the ones of  $\text{La}_{0.6}\text{Sr}_{0.4}\text{Co}_{0.2}\text{Fe}_{0.8}\text{O}_3$  cathodes. However at 700°C the performance of the  $\text{La}_{1-x}\text{Sr}_x\text{Co}_{1-y}\text{Fe}_y\text{O}_3$  cathode is much higher.

### III.3.2 Characterization of cathode materials

For the reasons exposed above the material used as cathode was  $\text{La}_{0.4}\text{Sr}_{0.6}\text{Co}_{0.2}\text{Fe}_{0.8}\text{O}_{3-\delta}$ . The powder used was supplied by Marion Technologies and, as it can be seen in figures III.16(a) and (b), it is a powder with agglomerates from 5 μm to 20 μm.

The particle size distribution given by the supplier (figure III.17) indicates that these are agglomerates of particles with a narrow size distribution centered at  $d_{50}$  of 1,30μm. The composition of the powder was confirmed by X-ray diffraction and, as it can be seen in figure III.18, it was found out that the powder contained small amounts of SrCO<sub>3</sub> as secondary phase.

In order to characterize the behavior at high temperature of this material, a dilatometry experiment was carried out using the same procedure than the one used for the former three

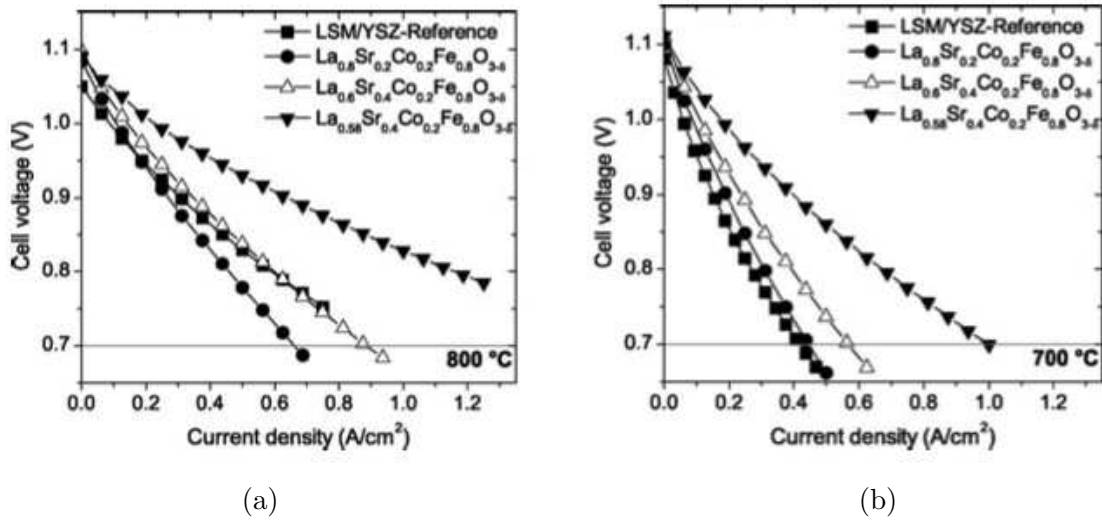


Figure III.15 : Performances of different fuel cells with different cathodes at 700°C and 800°C [57].

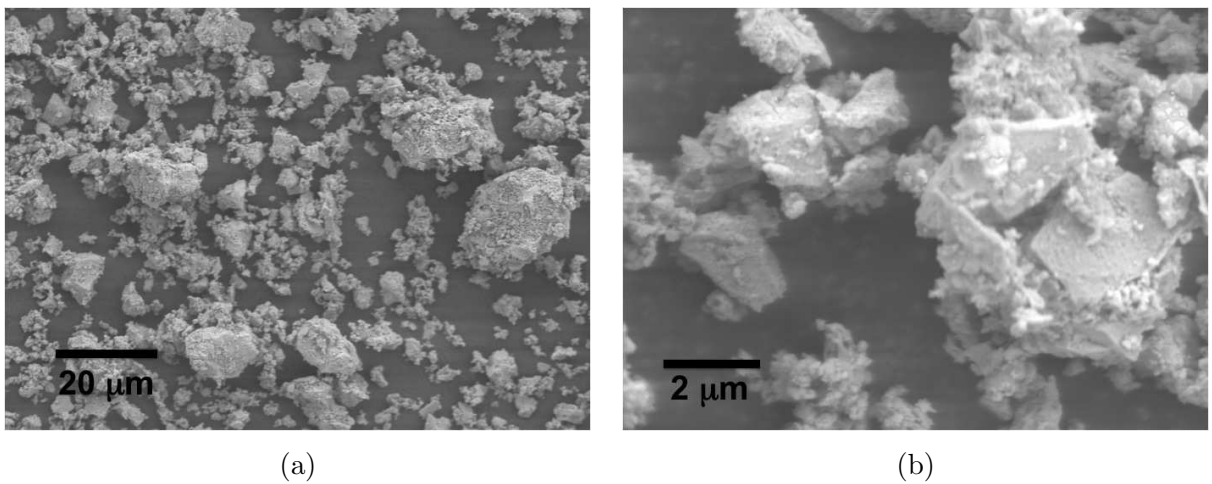


Figure III.16 : S.E.M. pictures of the  $\text{La}_{0.4}\text{Sr}_{0.6}\text{Co}_{0.2}\text{Fe}_{0.8}\text{O}_{3-\delta}$  powder used in the cathode symmetrical cells fabrication.

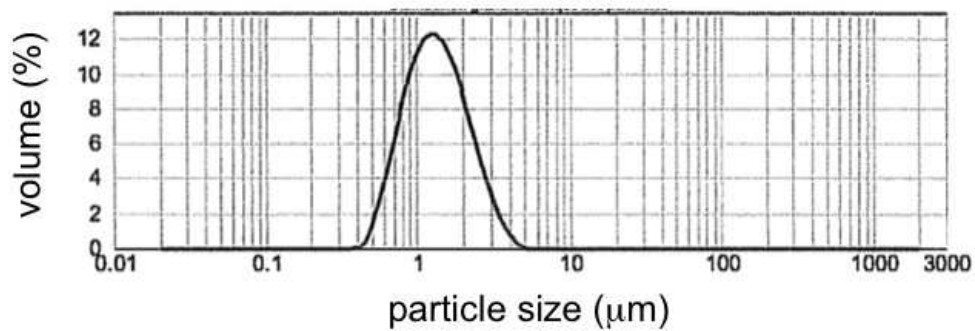


Figure III.17 : Granulometry of  $\text{La}_{0.4}\text{Sr}_{0.6}\text{Co}_{0.2}\text{Fe}_{0.8}\text{O}_{3-\delta}$  powder.

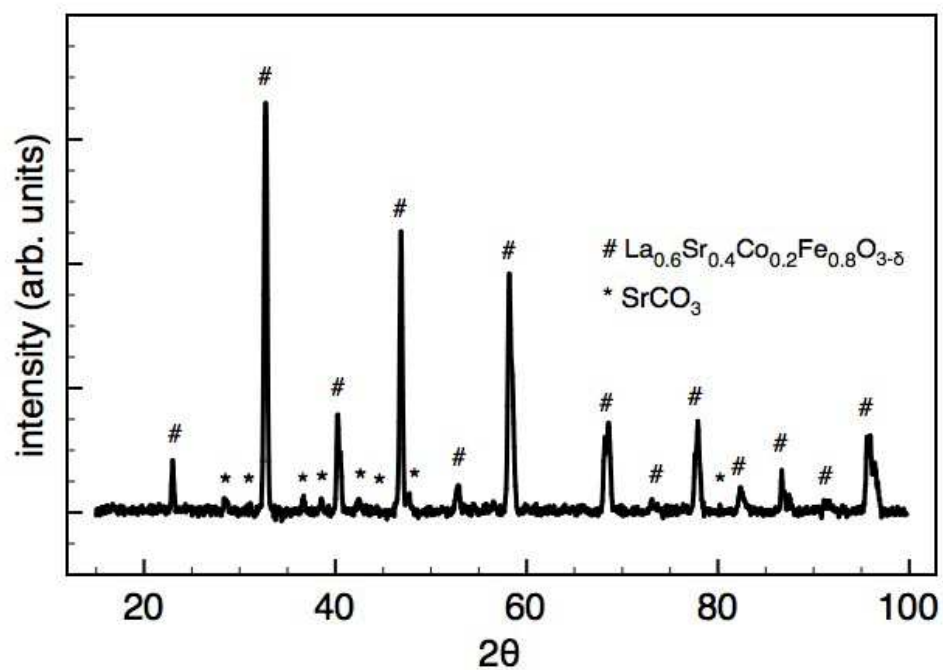
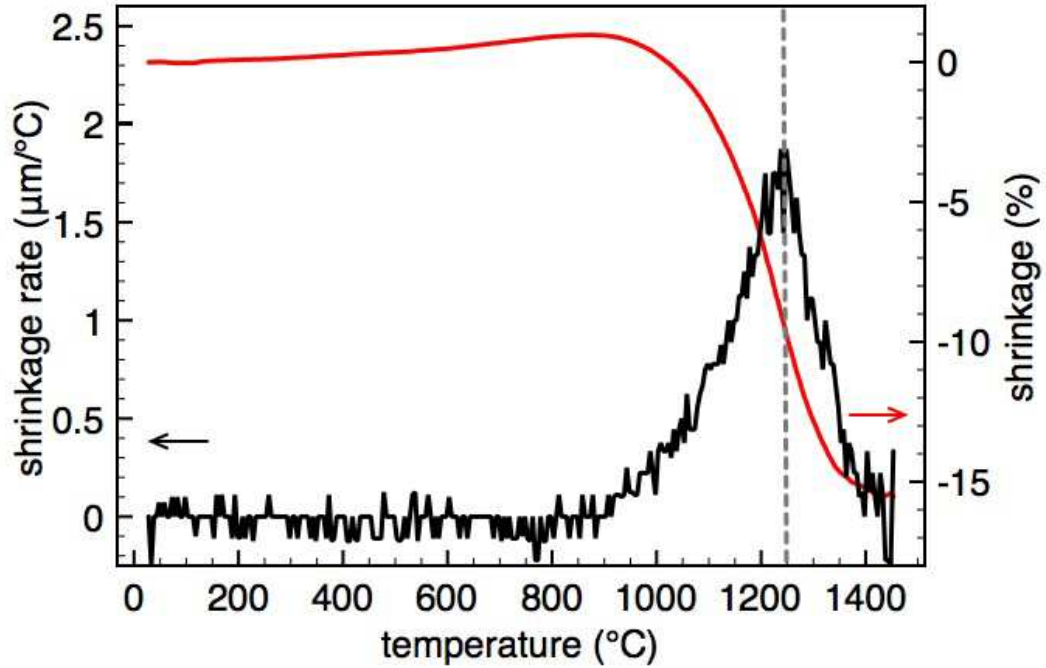


Figure III.18 : X-ray diffraction diagram of  $\text{La}_{0.4}\text{Sr}_{0.6}\text{Co}_{0.2}\text{Fe}_{0.8}\text{O}_{3-\delta}$  powder.

Table III.2 : Granulometric data for the  $\text{La}_{0.4}\text{Sr}_{0.6}\text{Co}_{0.2}\text{Fe}_{0.8}\text{O}_{3-\delta}$  powder.

$\text{La}_{0.4}\text{Sr}_{0.6}\text{Co}_{0.2}\text{Fe}_{0.8}\text{O}_{3-\delta}$		
$d_{10}$	$d_{50}$	$d_{90}$
$0.72\mu\text{m}$	$1.30\mu\text{m}$	$2.43\mu\text{m}$

powders (BCY15, YDC15 and NiO).



**Figure III.19** :  $\text{La}_{0.4}\text{Sr}_{0.6}\text{Co}_{0.2}\text{Fe}_{0.8}\text{O}_{3-\delta}$  powder shrinkage and shrinkage rate during sintering.

This material reaches its highest shrinkage rate at  $1250^{\circ}\text{C}$ . This information is only qualitative since the densification of the cathode is not an objective.

### III.3.2.1 Samples description and fabrication

The configuration of these samples, displayed in figure III.20 is the same as those of the anode symmetrical cells. The cathodes, made of  $\text{La}_{0.4}\text{Sr}_{0.6}\text{Co}_{0.2}\text{Fe}_{0.8}\text{O}_{3-\delta}$ , must be porous structures to allow the diffusion of the oxygen deposited on both sides of an oxygen ion conducting electrolyte. Again, the electrolyte must be dense, at least  $500\ \mu\text{m}$  thick, and have a diameter 20 mm to fit the electrochemical tester. The oxide-ion electrolyte material chosen was the  $\text{Ce}_{0.85}\text{Y}_{0.15}\text{O}_{2-\delta}$  which was presented in chapter II.



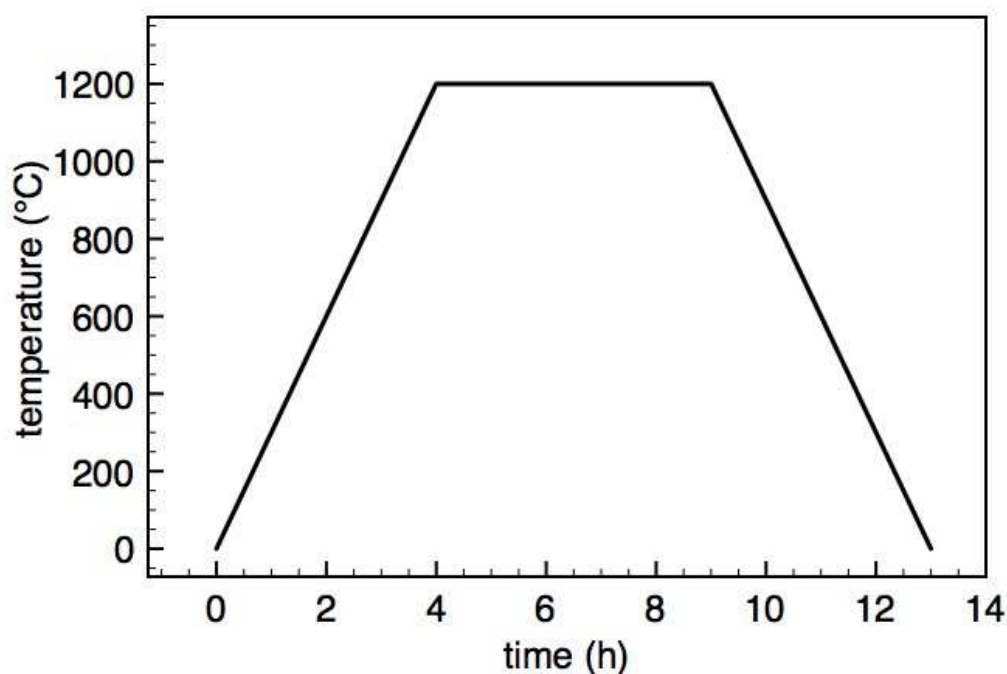
**Figure III.20** : Scheme of a cathode symmetrical cell.

An experimental procedure was developed to produce these samples, taking into account the specificity of the microstructures of their respective components. The electrolyte and the cathode were made of two different materials with different sintering temperatures. In order to avoid the incompatibility of the high temperature behavior of the two materials, the samples are produced in two steps. The electrolyte is pressed at 5 MPa in a 25 mm die and

**Table III.3** : Composition of the cathode tape casting slurry layer.

	cathode layer
$\text{La}_{0.4}\text{Sr}_{0.6}\text{Co}_{0.2}\text{Fe}_{0.8}\text{O}_{3-\delta}$	5.00 g
poly(vinyl butyral)	1.50 g
poly(ethyleneglycol)	1.50 g
ethanol	3.50 g

then sintered at 1200°C for 5h with heating and cooling rates of 5°C/min, according to the figure III.21.

**Figure III.21** : Sintering cycle used to sinter the  $\text{Ce}_{0.85}\text{Y}_{0.15}\text{O}_{2-\delta}$  electrolyte.

The cathode layer was then cast over the electrolyte and then sintered. A cathode slurry composition and a sintering treatment was found iteratively until a layer with good interfaces with the electrolyte and highly porous structure was obtained. Thus, a slurry with the composition shown in figure III.3 was ball-milled for 4h and then cast over the electrolyte. The blade was set to zero over the pellet and then the thickness was increased to 100  $\mu\text{m}$ .

The cathode and the already dense electrolyte were sintered at 1100°C with a burn-out step at 350°C for 2h, according to the cycle shown in figure III.22. After sintering, the second cathode was cast on the other surface of the electrolyte using the same tape casting procedure and sintering treatment than the first one.

The samples are sintered over a  $\text{ZrO}_2$  sintering support with a powder bed of the same material that is in contact with the support.

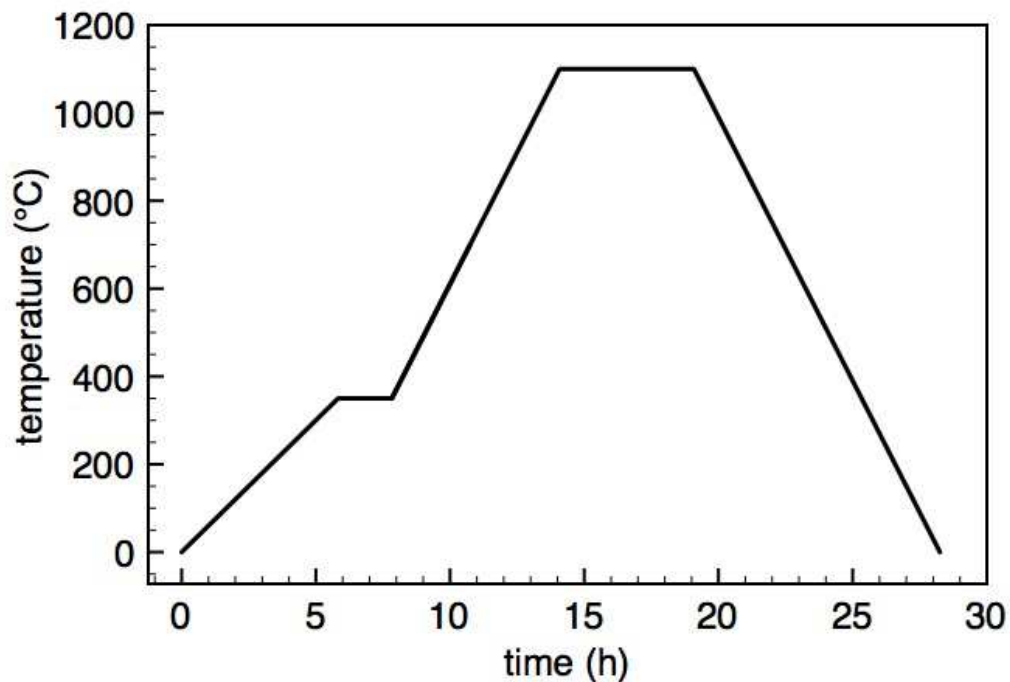


Figure III.22 : Temperature cycle used to sinter the cathode in symmetrical cells.

### III.3.2.2 S.E.M. characterization of samples

The samples obtained using this fabrication procedure were flat with 20 mm of diameter. The electrolyte's density after sintering was measured through the weight and the dimensions of the pellet. It reached 92% of the theoretical density. The porosity is closed and thus the electrolyte assures the gas tightness. The electrode is a porous layer about 10  $\mu\text{m}$  thick with good interfaces with the electrolyte as it can be seen in figures III.23 (a) and (b).

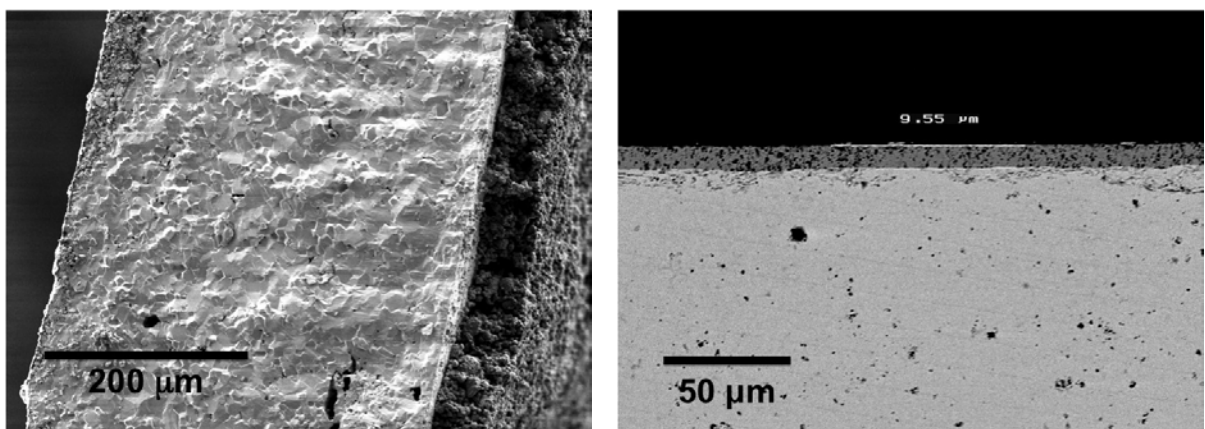


Figure III.23 : S.E.M.-B.S.E. pictures of the  $\text{La}_{0.4}\text{Sr}_{0.6}\text{Co}_{0.2}\text{Fe}_{0.8}\text{O}_{3-\delta}$  cathode symmetrical cells.

### III.3.2.3 Electrochemical testing

Electrochemical impedance spectroscopy experiments were carried out in this cathode from 0.1 Hz to 1 MHz at temperatures from 500°C to 700°C in air. This cathode has a specific area resistance of 9.98  $\Omega\cdot\text{cm}^2$  at 611°C. The Arrhenius plot showing the area specific resistance as a function of the temperature in figure III.24 allowed to determine an activation energy of 1.50 eV.

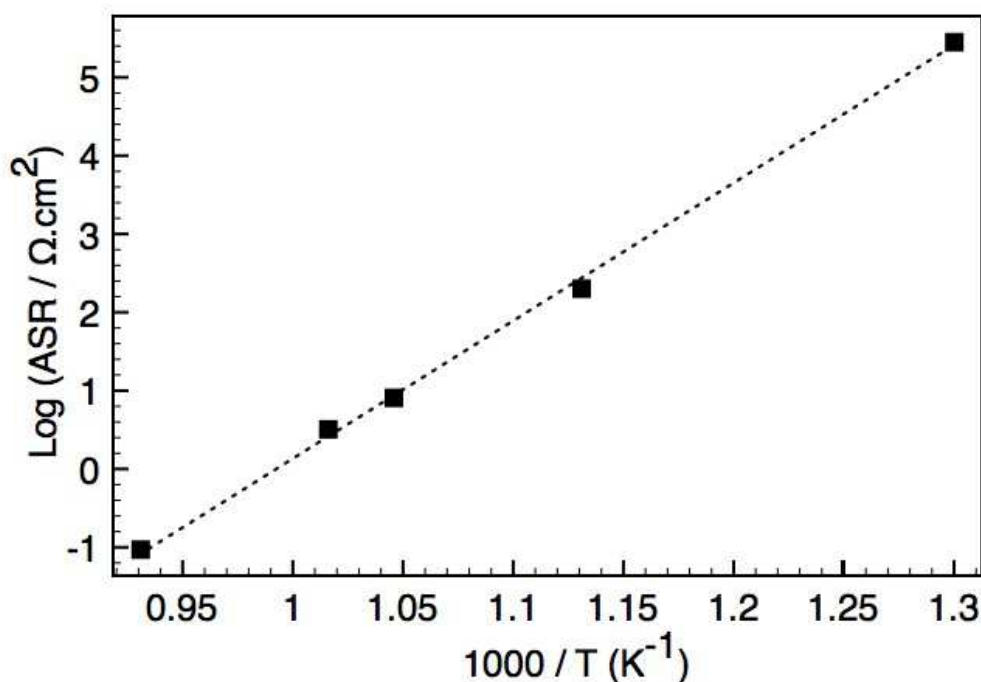


Figure III.24 :  $\text{La}_{0.4}\text{Sr}_{0.6}\text{Co}_{0.2}\text{Fe}_{0.8}\text{O}_{3-\delta}$  cathode resistance measurement.

### III.3.3 Development of a composite cathode

Although the anode is the electrode that is farer from state-of-the-art performances, the cathode should also be optimized to allow reaching higher cell performances. Thus, a path followed to improve the cathode materials was developed. The first approach consists in changing the cathode composition from a single-phase to a composite structure, as it is the case for the optimization of the anode. Thus, the strategy consists in improving the ion conduction in the cathode by introducing a pure oxygen ion conductor in its composition. The electron conductivity would still be assured by  $\text{La}_{0.4}\text{Sr}_{0.6}\text{Co}_{0.2}\text{Fe}_{0.8}\text{O}_{3-\delta}$  that is also an ion conductor. For reasons of chemical compatibility with the electrolyte,  $\text{Ce}_{0.85}\text{Y}_{0.15}\text{O}_{2-\delta}$  powder will be used to create the composite structure.

#### III.3.3.1 Experimental procedure

The experimental procedure is very similar to the one developed to produce the previous cathodes. Since the electrolyte material is the same, dense electrolytes were prepared pressing the powder at 25 MPa for 5 min in a 25 mm die. These pellets were then sintered at 1200°C

**Table III.4** : Composition of the cathode tape casting slurry layer.

	composite cathode layer	short name
$\text{La}_{0.4}\text{Sr}_{0.6}\text{Co}_{0.2}\text{Fe}_{0.8}\text{O}_{3-\delta}$	2.50 g	LSCF48
$\text{Ce}_{0.85}\text{Y}_{0.15}\text{O}_{2-\delta}$	2.50 g	YDC15
poly(vinyl butyral)	1.60 g	PVB
poly(ethyleneglycol)	1.75 g	PEG
ethanol	2.60 g	-

for 5h with heating and cooling rates of  $5^\circ\text{C}/\text{min}$ , according to the temperature profile shown in figure III.21.

The composite cathode was then deposited over the electrolyte pellet by tape casting and sintered at  $1100^\circ\text{C}$  for 5h, according to the cycle shown in figure III.22. The slurry composition was optimized in an iterative process in order to assure the porosity of the layer and the good quality of the interfaces. The best result was obtained for the slurry composition shown in table III.4.

### III.3.3.2 Sample characterization

The samples obtained were flat, with a diameter of about 20 mm. The electrolyte was thick, as it had already been determined for the previous samples and had a thickness of about  $700\ \mu\text{m}$ , as it can be seen in figure III.25. The cathode layer had a thickness of about  $60\ \mu\text{m}$ . The interfaces between the electrolyte and the electrode had good quality which allowed a continuous conductive pathway for the ion conduction.

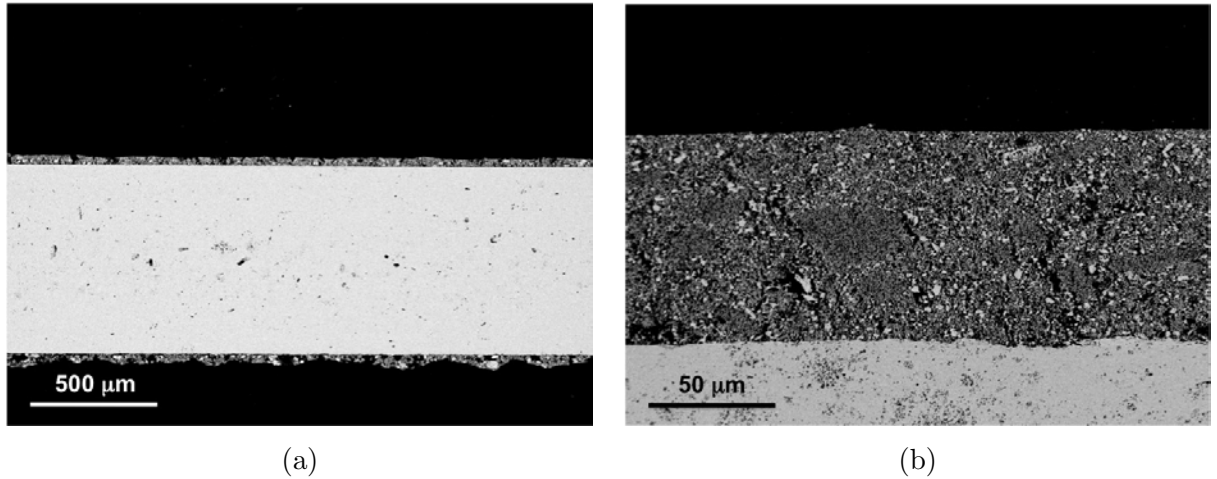


**Figure III.25** : S.E.M.-B.S.E. images of the  $\text{La}_{0.4}\text{Sr}_{0.6}\text{Co}_{0.2}\text{Fe}_{0.8}\text{O}_{3-\delta}\text{-Ce}_{0.85}\text{Y}_{0.15}\text{O}_{2-\delta}$  cathode symmetrical cells.

### III.3.3.3 Electrochemical testing

These cathode also were electrochemically tested. Electrochemical impedance spectroscopy was carried out from 0.1 Hz to 1 MHz and in a temperature range from  $550^\circ\text{C}$  to  $700^\circ\text{C}$ . The data obtained allowed to determine the total resistance of the electrode at different temperature. This cathode has an area specific resistance of  $0.988\ \Omega\cdot\text{cm}^2$  at  $594^\circ\text{C}$ . These

data are plotted as function of the temperature in figure III.26. The slope of the curve is the value of the activation energy, which is, in this case, 1.09 eV.

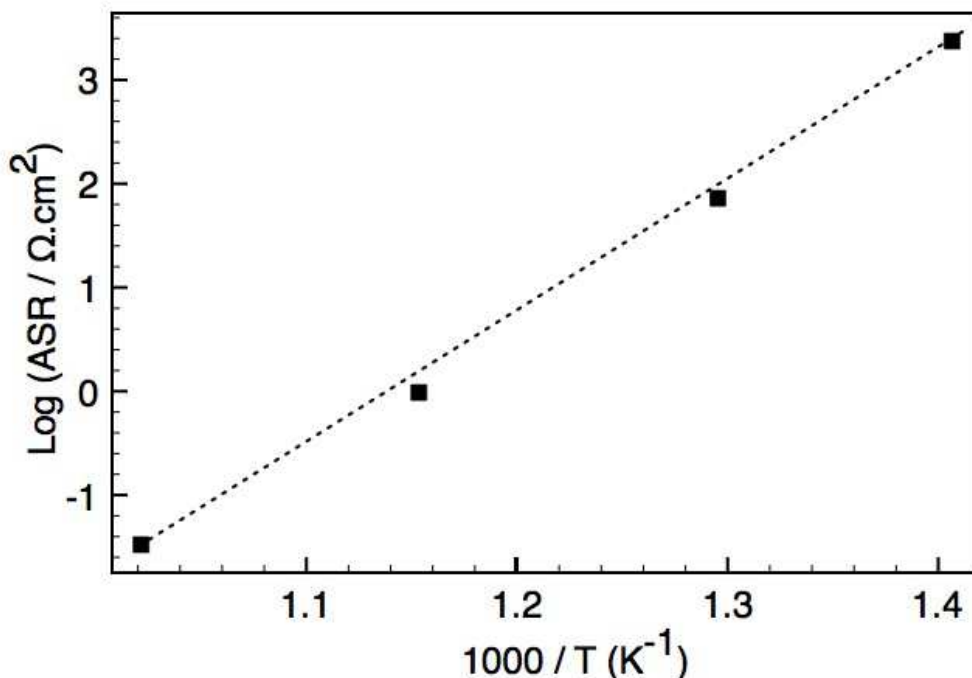


**Figure III.26** :  $\text{La}_{0.4}\text{Sr}_{0.6}\text{Co}_{0.2}\text{Fe}_{0.8}\text{O}_{3-\delta}-\text{Ce}_{0.85}\text{Y}_{0.15}\text{O}_{2-\delta}$  cathode resistance measurement.

### III.3.4 Development of a new cathode material

A second strategy comes from the fact that  $\text{BaCe}_{0.85}\text{Y}_{0.15}\text{O}_{3-\delta}$  is not only a proton conductor but also an oxygen ion conductor. This is certainly due to the presence of oxygen vacancies that, in an oxygen-rich atmosphere, conduct the oxygen ions through its structure. Electrochemical impedance spectroscopy carried out by IEES showed that proton and oxide-ion conductivities of BCY15 increase with temperature and tend to equalize at 600°C. Obviously, the transport of  $\text{H}^+$  and  $\text{O}^{2-}$  ions in such a material is associated with different activation energies. Thus, the third cathode studied was based on a  $\text{BaCe}_{0.85}\text{Y}_{0.15}\text{O}_{3-\delta}$  electrolyte and a composite cathode of the same material and  $\text{La}_{0.4}\text{Sr}_{0.6}\text{Co}_{0.2}\text{Fe}_{0.8}\text{O}_{3-\delta}$ . This feature opens the possibility of developing a performing cathode based on the material that is used as a proton conductor. The interest of this approach is the possibility of eliminating one of the two electrolyte materials, what would simplify the *IDEAL Cell* configuration from the shaping point of view. The adoption of such an approach will be a compromise between the cathode's performance and the gain in the simplification of the complete cell microstructures quality, the materials stability and therefore of the cell performance stability.

#### III.3.4.1 Experimental Procedure

These cathodes have the same configuration of the previous two: the cathode layer is deposited by tape casting over a dense electrolyte pellet. The electrolyte will be a  $\text{BaCe}_{0.85}\text{Y}_{0.15}\text{O}_{3-\delta}$  pellet and the cathode will be a porous  $\text{BaCe}_{0.85}\text{Y}_{0.15}\text{O}_{3-\delta}$  and  $\text{La}_{0.4}\text{Sr}_{0.6}\text{Co}_{0.2}\text{Fe}_{0.8}\text{O}_{3-\delta}$

**Table III.5** : Composition of the cathode tape casting slurry layer.

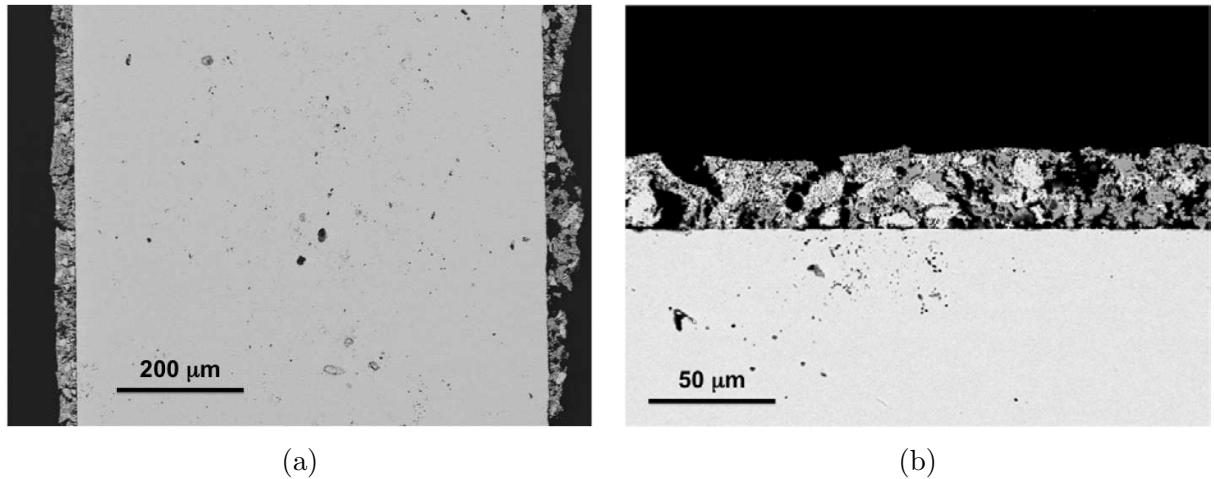
	composite cathode layer
$\text{La}_{0.4}\text{Sr}_{0.6}\text{Co}_{0.2}\text{Fe}_{0.8}\text{O}_{3-\delta}$	2.50g
$\text{BaCe}_{0.85}\text{Y}_{0.15}\text{O}_{3-\delta}$	2.50g
poly(vinyl butyral)	1.30g
poly(ethyleneglycol)	1.25g
ethanol	3.30g

composite layer. The latter assures once again the electron conduction while the first one acts as oxide-ion conductor.

The electrolyte powder was, thus, pressed at 25 MPa in a 25 mm die and then sintered at 1300°C for 5h with 5°C/min heating and cooling rates. This is the same procedure used before for the anode symmetrical cells electrolyte. The composite cathode slurry composition and the sintering treatment were then developed iteratively until the cathode's good microstructures and interfaces with the electrolyte were obtained. The optimized slurry composition is given in table III.5.

The sintering cycle that yielded the most satisfying microstructures is the same used to sinter the anode layers in the anode symmetrical cells and is shown in figure III.9.

The samples obtained were flat with about 20 mm of diameter. The electrolyte was dense and about 650  $\mu\text{m}$  thick, while the cathode was a porous structure with a thickness of about 20  $\mu\text{m}$ , as it can be seen in figure III.27.

**Figure III.27** : S.E.M.-B.S.E. pictures of the  $\text{La}_{0.4}\text{Sr}_{0.6}\text{Co}_{0.2}\text{Fe}_{0.8}\text{O}_{3-\delta}$ - $\text{BaCe}_{0.85}\text{Y}_{0.15}\text{O}_{3-\delta}$  cathode symmetrical cells.

#### III.3.4.2 Electrochemical testing

Electrochemical impedance spectroscopy experiments were carried out to investigate the performances of the cathode. The experiments were performed between 0.1 Hz and 1 MHz and in a temperature range between 500 °C and 700 °C. This cathode has a area specific resistance of 1.43  $\Omega\cdot\text{cm}^2$  at 610°C. The arrhenius plot is displayed in figure III.28 indicates the activation energy value, which is 0.65 eV.

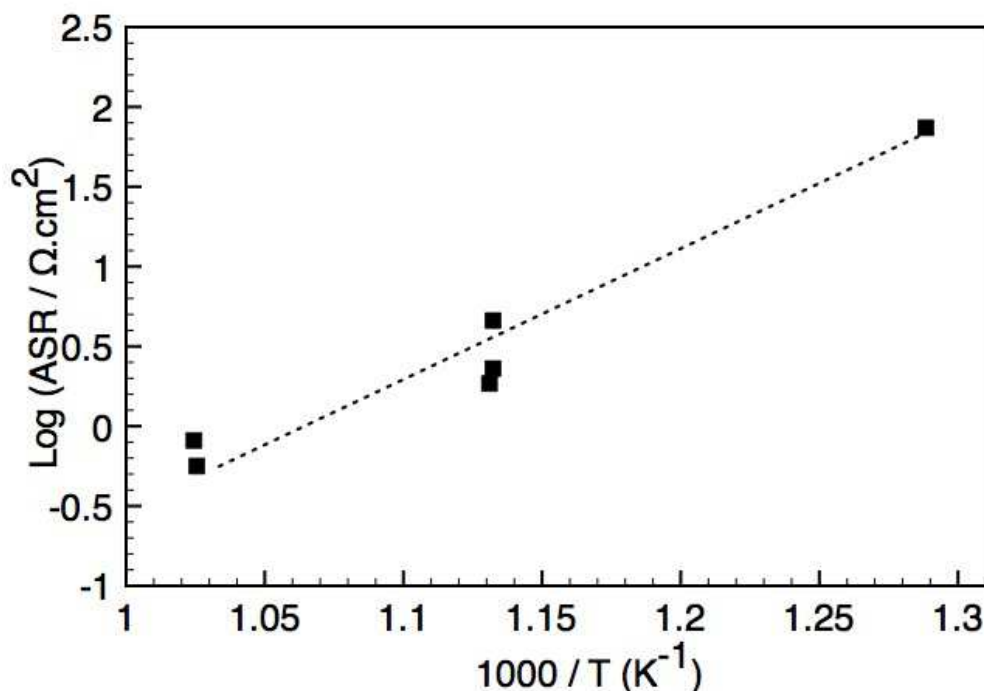


**Figure III.28** :  $\text{La}_{0.4}\text{Sr}_{0.6}\text{Co}_{0.2}\text{Fe}_{0.8}\text{O}_{3-\delta}$ - $\text{BaCe}_{0.85}\text{Y}_{0.15}\text{O}_{3-\delta}$  cathode resistance measurement.

### III.3.4.3 Discussion

Three different cathodes were developed in order to obtain the best performing IDEAL-Cell. The fabrication procedure was very similar to the one developed for the anode symmetrical cells; the electrolyte was pressed and sintered previously and then the cathode was deposited by tape casting and sintered. The electrolytes were densified to over 92% while the electrodes were porous structures with good interfaces between the layers. The samples were flat with about 20 mm of diameter and 700  $\mu\text{m}$  of thickness. The electrodes had the same diameter of the electrolyte and thicknesses between 10  $\mu\text{m}$  and 50  $\mu\text{m}$ . The first cathode developed was a single-phase  $\text{La}_{0.4}\text{Sr}_{0.6}\text{Co}_{0.2}\text{Fe}_{0.8}\text{O}_{3-\delta}$ -based electrode that is both an oxygen ion and electron conductor. This cathode (cathode (1) in figure III.29) has an area specific resistance of 9.98  $\Omega\cdot\text{cm}^2$  at 611°C and an activation energy of 1.50 eV. These performances are less limiting than the ones of the anode, however, in order to reach performances closer to state-of-the-art cells, the cathodes performances should be improved. Therefore, a new approach was followed and consists in adding an oxide-ion conductor and use a composite electrode as it was done before for the anode. The same fabrication procedure was followed adapting the tape casting slurry for the new powder mixture. The microstructures were similar to the ones of the former cathode, however, the performances were improved. The composite  $\text{La}_{0.4}\text{Sr}_{0.6}\text{Co}_{0.2}\text{Fe}_{0.8}\text{O}_{3-\delta}$ - $\text{Ce}_{0.85}\text{Y}_{0.15}\text{O}_{2-\delta}$  (cathode (2) in figure III.29) has an area specific resistance of 0.988  $\Omega\cdot\text{cm}^2$  at 594°C and an activation energy of 1.09 eV.

A new cathode was developed based on the fact that  $\text{BaCe}_{0.85}\text{Y}_{0.15}\text{O}_{3-\delta}$  is an oxide-ion conductor in air. It is also a composite cathode:  $\text{La}_{0.4}\text{Sr}_{0.6}\text{Co}_{0.2}\text{Fe}_{0.8}\text{O}_{3-\delta}$ - $\text{BaCe}_{0.85}\text{Y}_{0.15}\text{O}_{3-\delta}$ . The microstructures are similar to the previous cathodes. In terms of performances, this cathode (cathode (3) in figure III.29) has an area specific resistance of 1.43  $\Omega\cdot\text{cm}^2$  at 610°C.

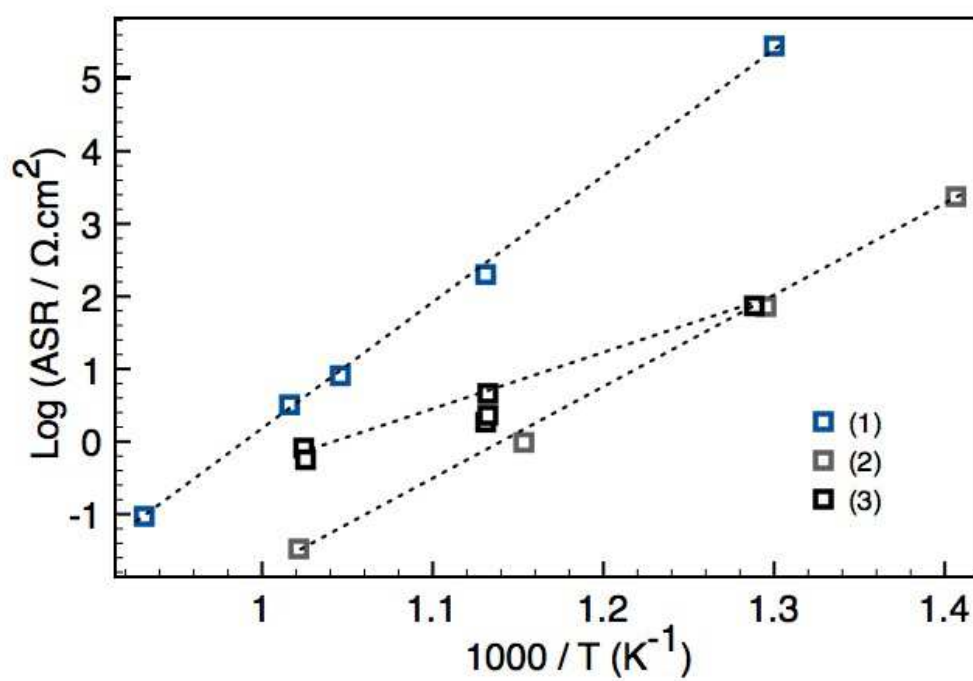


**Figure III.29** : Resistance measurement of the  $\text{La}_{0.4}\text{Sr}_{0.6}\text{Co}_{0.2}\text{Fe}_{0.8}\text{O}_{3-\delta}$  cathode (1),  $\text{La}_{0.4}\text{Sr}_{0.6}\text{Co}_{0.2}\text{Fe}_{0.8}\text{O}_{3-\delta}\text{-Ce}_{0.85}\text{Y}_{0.15}\text{O}_{2-\delta}$  composite cathode (2) and  $\text{La}_{0.4}\text{Sr}_{0.6}\text{Co}_{0.2}\text{Fe}_{0.8}\text{O}_{3-\delta}\text{-BaCe}_{0.85}\text{Y}_{0.15}\text{O}_{3-\delta}$  cathode (3).

### III.3.5 Conclusions

The composite cathodes proved to be better performing than a single-phase mixed conductor cathode with similar microstructures fabricated using the same procedure. A composite cathode based on oxygen ion conductor, has lower area specific resistance than the single-phase cathode in the range of temperatures in which IDEAL-Cell is expected to operate.

### III.4 Conclusions

A fabrication procedure was developed to produce both electrodes of the IDEAL-Cell using the combination of cold pressing, tape casting and sintering. The electrolytes were successfully densified and the porosity of the electrodes was assured by tuning the composition of the slurry. Good interfaces between both layers were obtained. The anode obtained, a Ni-BaCe<sub>0.85</sub>Y<sub>0.15</sub>O<sub>3- $\delta$</sub>  cermet, has a specific area resistance of 21.06  $\Omega\cdot\text{cm}^2$  at 611°C, and the Arrhenius plot allowed determining an activation energy of 0.74 eV. These performances are about ten times inferior to the ones reported by other authors for a similar anode. This can keep the IDEAL-Cell from reaching higher performances and needs further investigation. Three different cathodes were developed regarding their application to the IDEAL Cell concept. The most performing one was a composite La<sub>0.4</sub>Sr<sub>0.6</sub>Co<sub>0.2</sub>Fe<sub>0.8</sub>O<sub>3- $\delta$</sub> -Ce<sub>0.85</sub>Y<sub>0.15</sub>O<sub>2- $\delta$</sub>  cathode that has an area specific resistance of 0.988  $\Omega\cdot\text{cm}^2$  at 594°C.

---

Après avoir démontré le concept IDEAL-Cell, les activités se sont orientées vers le développement des matériaux d'électrode. L'anode choisie, un composite poreux céramique/métal (appelé cermet) conducteur ionique et électronique, représente à ce jour la meilleure formulation assurant la catalyse de la réaction de dissociation des molécules d'hydrogène, présente dans la porosité, grâce à la présence de particules de Ni. La zone active, point de rencontre de ces trois propriétés électrochimiques, est appelée point triple (TPB). Ainsi, augmenter la densité de ces sites réactionnels percolants dans tout le volume de l'électrode permettra d'exacerber les performances électrochimiques de ce composant. La microstructure de l'anode doit être optimisée afin d'assurer la diffusion de l'hydrogène, son oxydation aux TPBs pour générer des protons migrant jusqu'à l'électrolyte adjacent et des électrons circulant vers le circuit électrique extérieur. L'anode doit également être chimiquement et mécaniquement compatible avec l'électrolyte. Pour garantir de cahier des charges, le cermet choisi est un mélange  $\text{BaCe}_{0.85}\text{Y}_{0.15}\text{O}_{3-\delta}$  et NiO. Pour des raisons homologues, mais ici pour des anions et non des protons, la composition de la cathode choisie est  $\text{La}_{0.40}\text{Sr}_{0.60}\text{Co}_{0.20}\text{Fe}_{0.80}\text{O}_{3-\delta}$ . Les deux électrodes doivent être poreuses pour assurer la diffusion des gaz. La morphologie ainsi que le comportement au frittage de ces deux composés ont été caractérisés. Une séquence de procédés, utilisant le coulage en bande et le pressage à froid suivis d'un frittage à haute température, a été mise en œuvre pour fabriquer des demi-cellules symétriques électrode/électrolyte/électrode. Les échantillons ont été testés par spectroscopie d'impédance complexe. L'anode présente de faibles performances comparées à celles extraites de la littérature et mesurées sur des matériaux similaires. Une caractérisation par microscopie électronique en transmission a permis de mettre en évidence la formation d'une phase secondaire ségrégant aux TPBs et interphases. La cathode montre de très bonnes performances électrochimiques, plus spécifiquement en mélange avec YDC15 et BCY15 pour former les composites  $\text{Ce}_{0.85}\text{Y}_{0.15}\text{O}_{2-\delta}/\text{La}_{0.40}\text{Sr}_{0.60}\text{Co}_{0.20}\text{Fe}_{0.80}\text{O}_{3-\delta}$  et  $\text{BaCe}_{0.85}\text{Y}_{0.15}\text{O}_{3-\delta}/\text{La}_{0.40}\text{Sr}_{0.60}\text{Co}_{0.20}\text{Fe}_{0.80}\text{O}_{3-\delta}$ . A  $600^\circ\text{C}$ , température de fonctionnement de IDEAL-Cell, la cathode composite de formulation chimique  $\text{Ce}_{0.85}\text{Y}_{0.15}\text{O}_{2-\delta}/\text{La}_{0.40}\text{Sr}_{0.60}\text{Co}_{0.20}\text{Fe}_{0.80}\text{O}_{3-\delta}$  (50/50 en proportion volumique) montre les meilleures performances avec une résistance spécifique de  $0.988 \text{ ohm.cm}^2$ .

---



---

# Chapter -IV-

## Complete cell fabrication

---

### Contents

---

IV.1	Introduction . . . . .	90
IV.2	Sample description . . . . .	92
IV.3	Experimental procedure . . . . .	92
IV.4	Sample characterization . . . . .	96
IV.5	Discussion . . . . .	97
IV.6	Conclusion . . . . .	98

---

## IV.1 Introduction

In the previous chapters, different shaping procedures for each compartment of the IDEAL-Cell are described. A three layer stack of the two electrolytes and a central membrane was fabricated by cold pressing or cold pressing and tape casting. It was also shown that the fabrication procedures found allow the production of fuel cell prototypes. It was later demonstrated that the electrodes were successfully produced by tape casting over pellets of electrolyte materials. Both anode and cathode were electrochemically tested. The anode material was reported to need improvements in the fabrication procedure or to be replaced by another one in order to reach good electrochemical performances, since there is probably the formation of an insulating phase in the interface between the electron and proton conductors. On the other hand the cathode composition was improved and shows good electrochemical performances.

In this chapter the activities developed in order to fabricate the first complete IDEAL-Cell by tape casting and sintering are described.

A complete IDEAL-Cell could be produced by coating the electrodes to the POC samples fabricated by cold pressing or tape casting, cold pressing and sintering are presented in chapter II. As it was shown in chapter III, the deposition of anode and cathode materials over electrolyte pellets by tape casting and sintering was successfully accomplished. Thus, the combination of these techniques would allow the fabrication of a complete cell. However, the high thicknesses of the electrolytes, would keep such cells from reaching high performances, and would add few knowledge with respect to the POC sample with platinum electrodes.

Nevertheless the presence of a thick support layer in a fuel cell structure has several advantages and this approach has been the source of many developments in the field of fuel cell fabrication. Thus, researches have been focused on what are called electrolyte-supported, anode-supported and cathode-supported cells.

The electrolyte-supported cell design uses a thick electrolyte to provide mechanical support to the thin electrodes but these systems can only reach high performances if the electrolyte has low ohmic losses. This can be achieved by increasing the system operating temperature. Thus, electrolyte-supported cells with  $100\mu\text{m}$  - 1 mm electrolytes usually operate at temperatures between  $850^\circ\text{C}$  and  $1000^\circ\text{C}$  which require more expensive interconnects and sealing materials [58]. Another way to decrease the ohmic losses is to reduce the electrolyte thickness and to use thicker electrodes that can assure the mechanical support of the cell. Thus, anode-supported cells have electrolytes with  $< 50\mu\text{m}$  and operate at temperatures below  $800^\circ\text{C}$ . In the cathode-supported cells the electrolyte is as thin but the operating temperatures are slightly higher due the higher losses in the cathode.

Although these designs allow decreasing the cell's operating temperature, the thick support layer is made of a ceramic or cermet material, which is not only a brittle support but also contains expensive elements.

The advantage of the metal-supported cell design is that the mechanical support is given by an inexpensive porous material that replaces the surplus of the electrode layer, as it is illustrated in figure IV.1. Thus, the ceramic layers are applied directly over the metal support and their thicknesses can be optimized exclusively for their electrochemical function.

Nickel-based materials were the first choice of researchers to develop fuel cell metal supports. Pure nickel porous tubes and NiCrAlY supports prepared by die pressing have been successfully used to produce fuel cells with good performances [59] [60] [61]. A variety of electrolyte materials have been deposited over these supports using several different techniques. For example, strontium- and magnesium-doped lanthanum gallate (LSGM) have been deposited on nickel supports by atmospheric plasma spray [61] and on Ni-Fe supports

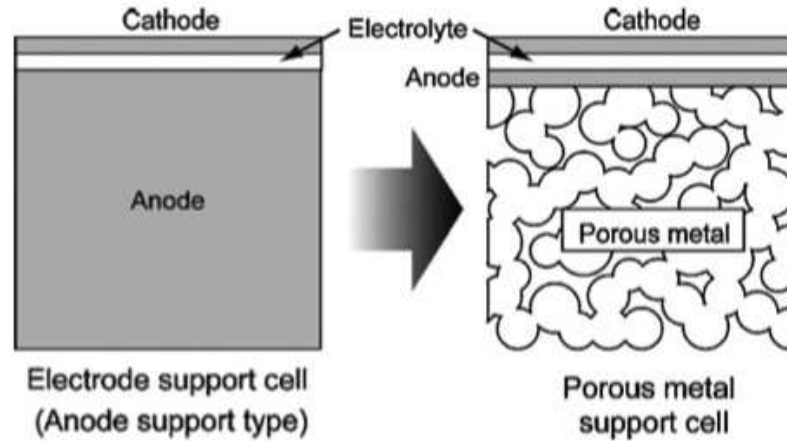


**Figure IV.1** : Metal supported cell scheme [58].

by pulsed laser deposition [62] [63] [64] [65]. However, this electrolyte was reported to be reactive with nickel which decreases the cell's performances. For this reason, gadolinium-doped ceria (GDC) has also been used as electrolyte of metal-supported cells. The advantage of this material, besides its good conductivity at relatively low temperatures ( $\sim 500^\circ\text{C}$ ), is that it can be sintered to high densities under constraint. This allows the use of previously prepared metal supports that have very low or none shrinkage during sintering [58]. Fully dense gadolinium-doped ceria electrolytes have been obtained by sintering at temperatures below  $1000^\circ\text{C}$  [66]. High sintering temperature ( $T \sim 1450^\circ\text{C}$ ) in air have also been used to densify gadolinium-doped electrolytes deposited by drop-coating and wet deposition [67].

Another interesting electrolyte material for these applications is yttrium-stabilized zirconia (YSZ) due to its good conductivity and to its low price. Electrolytes of this material have been deposited over metal-supported anodes by plasma spraying techniques. These methods allow the formation of dense layers avoiding high temperature treatments as therefore they keep the metal substrate highly porous structure. However, the conductivity of the electrolytes produced by plasma spraying is lower than the ones produced by tape casting, which requires that these cells operate at about  $800^\circ\text{C}$  to reach high performances [68]. These operating temperatures may harm the cell long term stability due to the oxidation of the metal support.

Therefore, low-cost deposition techniques such as dip coating, screen printing, tape casting, aerosol spray coating, spin coating and drip coating followed by a high temperature sintering step to achieve high densities have also been used to fabricate metal-supported cells [58]. These techniques are particularly demanding for the metal support because at high temperature it may lose its porous structure needed to allow gas transport during the cell's operation. Sintering treatments at such high temperatures in air also cause the oxidation of the support. In order to avoid so, sintering is carried out under reducing or neutral atmospheres. However, cathode materials are usually unstable under such atmospheres [69]. Therefore, cathodes are usually sintered after the non-oxidizing steps in air below  $900^\circ\text{C}$  to avoid the substrate oxidation. This low temperature sintering requirement limits the cathode material choice since materials such as LSM and LSCF require sintering in air at temperatures between  $1000^\circ\text{C}$  and  $1200^\circ\text{C}$  to reach high performances [58]. Several  $(\text{La,Sr})(\text{Cr,Mn})\text{O}_{3-\delta}$  composition cathodes were sintered in nitrogen at  $1100^\circ\text{C}$  to avoid the support oxidation but none of the compositions showed good electrochemical performances after such treatment.

Sintering metal-supported cells is demanding not only in terms of the materials stability but also in terms of their high temperature behavior. During sintering the electrolyte shrinks about 20%, depending on the density of the green density layer. Thus, the metal support must have a sintering behavior similar to that of the electrolyte. If this is not the case the electrolyte is sintered under constraint which creates cracks in the structure or insufficient density.

For this reason another kind of metal supports have been used for fuel cell applications. Iron-based materials, mostly ferritic stainless steels, that have a high temperature behavior more compatible with electrolyte materials have been used in for these applications [58]. These materials typically contain between 10 wt. % and 26 wt.% of Cr and other elements such as Ni, Mo, Si and Al to improve their physical properties. The disadvantage of these supports is related to their compatibility with anode materials. When in a fuel cell there is direct contact between a stainless steel and Ni-containing anode, interdiffusion of Ni and Fe/Cr occurs. The diffusion of Fe and Cr into the Ni-containing anode can cause the formation of insulating oxides such as  $\text{Cr}_2\text{O}_3$ ,  $\text{NiCr}_2\text{O}_4$ ,  $\text{FeO}$ , which decrease the anode catalytic activity [58].

## IV.2 Sample description

Iron-based metal supports are inexpensive materials that have good high temperature behavior compatibility with electrolyte materials. However, Fe and Cr contained in ferritic stainless steels diffuse into Ni-containing anodes, harming their catalytic activity. The anode material chosen to demonstrate this fuel cell concept is a cermet composed of NiO and  $\text{BaCe}_{0.85}\text{Y}_{0.15}\text{O}_{3-\delta}$ . As shown in chapter III the electrochemical performances of this anode need to be improved. Thus, a stainless steel support is not adequate to the fabrication of a complete IDEAL-Cell for chemical compatibility reasons.

Therefore it was chosen to use a Ni-based material as metal support for this cell. The material used is a porous nickel foam produced by the company INCO. This foam is produced by physical vapor deposition pre-coating and electroplating. It is used in batteries for its high conductivity and uniform pore structure, as catalyst or catalyst support and also as a filter material due to its mechanical strength and temperature and corrosion resistance. According to the supplier this foam, shown in figure IV.2 has a density in the 300-600  $\text{g}/\text{m}^3$  range and a cell size between 450-800  $\mu\text{m}$ .

The complete IDEAL-Cell ceramic layers will be directly applied by tape casting over the foam, using the same materials described before in chapters II and III. The resulting green cell must undergo a sintering treatment in order to acquire the desired microstructures and mechanical strength. The anode layer will be in contact with the metal support. One of the advantages of using a Ni-foam as a fuel cell support is that it is compatible with the NiO used in the anode composition. The other layers will be consecutively cast, forming the five layered structure, shown in figure IV.3. Microstructure requirements for the layers are the same than those stated before: the electrodes and the central membrane must be porous structures with high density of active triple-phase boundaries and the electrolytes must dense enough to ensure gas-tightness. An additional requirement in this cell design is that the foam must keep its porous structure after the sintering step, to allow gas diffusion during operation.

## IV.3 Experimental procedure

The metal-supported IDEAL-Cell was manufactured using the tape casting equipment shown in figure II.24, following the same procedure used to fabricate POC samples and symmetric

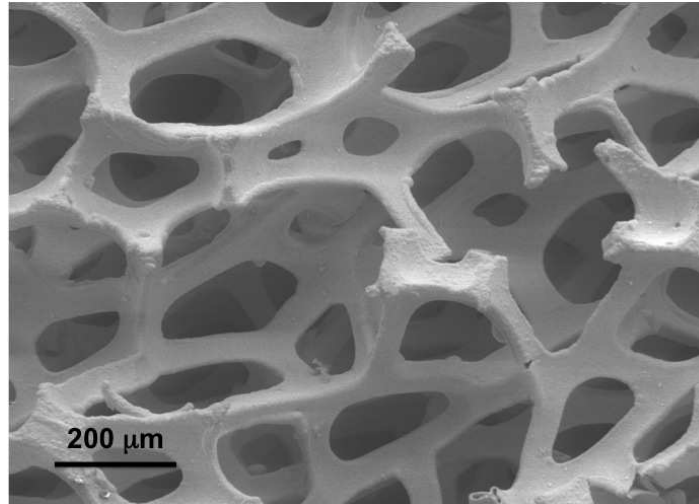


**Figure IV.2** : S.E.M. picture of the nickel foam.



**Figure IV.3** : Nickel foam supported IDEAL-Cell scheme.

**Table IV.1** : Composition of the slurries used in the fabrication metal-supported complete cell.

	anode	proton electrolyte	central membrane	oxide-ion electrolyte	cathode	short name
$BaCe_{0.85}Y_{0.15}O_{3-\delta}$	2.5 g	7.0 g	2.7 g	-	-	BCY15
$Ce_{0.85}Y_{0.15}O_{2-\delta}$	-	-	3.0 g	7.0 g	3.5 g	YDC15
$NiO$	3.8g	-	-	-	-	NiO
$La_{0.6}Sr_{0.4}Fe_{0.2}Co_{0.8}O_{3-\delta}$	-	-	-	-	2.5 g	LSCF48
poly(vinyl butyral)	1.2 g	2.4 g	2.8 g	1.4 g	3.0 g	PVB
polyethylene glycol	0.4 g	0.8 g	0.8 g	0.3 g	0.5 g	PEG
ethanol	6.0 g	7.5 g	7.8 g	4.8 g	6.6 g	-

half cells. The composition of the slurries used for the deposition of each of the five layers slurry was optimized to obtain the desired porous or dense structure. Each slurry is composed of a ceramic or cermet powder, a binder, a plasticizer and a solvent. Their function and the choice of each compound is explained and justified in chapter II. Slurry compounds create a polymer film that assures the mechanical strength and flexibility of the tape. Thus, this film occupies the space between the powder particles to create a homogeneous tape. This compounds decompose during sintering, leaving voids between the particles. As the temperature increases during sintering, mass diffusion between powder particles takes place in the points where they are in contact with each other. These necks grow, and the particles approach of each other in a thermally activated process. The driving force of the sintering process is the reduction of the particles specific surface, phenomenon that decreases the system total energy. Thus, the final density of the layer depends on the particle initial packing in the green tape. Dense green layers, where particles are highly packed, have high density of contact points and therefore will most probably yield dense sintered tapes. The amount of organic products in the slurry must be enough to assure the tape mechanical stability. Thus there is a balance between the adequate tape green density to obtain the desired microstructure and the amount of organic products needed to offer the green tape its mechanical strength and flexibility.

The process of tuning a slurry composition for a certain layer is an iterative process in which each of the slurry compounds are changed until the tape mechanical properties, homogeneity and relative density after sintering requirements are satisfied. The optimized compositions for each layer are shown in table IV.1.

Contrarily to what was done to produce symmetrical half cells, the anode was not directly cast over the support. Deposition of the anode slurry over the nickel foam would lead to the partial or complete closing of its porosity. Therefore, the complete cell was cast over a glass support coated by a mixture of ethanol and glycerol that acts as an anti-adhesive, assuring that the layers are easily detached from the support after drying.

The five ceramic layers were cast consecutively from the cathode to the anode. Each tape was left to dry for 1h before the following tape was cast. After drying of each layer the blade was put in touch with green tape to reset the point where the thickness is zero. Afterwards the blade's height was then adjusted to obtain the thickness of the tape above. This procedure was repeated to produce each compartment of the cell until the anode layer was cast. Over this layer, previously punched 20 mm disks of nickel foam were put over the anode before it was dry. In order to avoid the nickel foam to penetrate the proton conducting electrolyte, two anode layers were cast. The first one was left to dry during 2h and then the second one was cast. The nickel foam was then put over the second anode after being 30 minutes drying. The whole structure was then left to dry for 24h and then the complete cell

were punched with the same diameter of the nickel foam support.

The slurry composition of each tape was tuned in order to obtain dense electrolytes and porous electrodes and central membrane. After each trial the cell was sintered and the quality of its microstructures was investigated by scanning electron microscope (SEM) observations. The objective of this sintering treatment is the burnout of the organic products and the densification of the ceramic materials but attention must be paid to the metal support stability. If a nickel foam-supported cell is sintered in air, the support will oxidate at high temperature. This reaction causes the increase of the foam's volume which has an influence in the sintering behavior of the rest of the whole structure. The oxidation of the nickel into nickel oxide also renders the foam very brittle, and that may cause the failure of the cell during operation. Therefore, the sintering must be carried out in controlled atmosphere, as long as the decomposition of the organic products is assured. Thus, instead of burning-out the organic tape in air, it can be decomposed at high temperature in argon, to avoid the nickel oxidation. In order to verify if this decomposition occurs in the absence of oxygen, a differential thermal analysis was carried out in argon from room temperature to 900°C.

As it is shown in figure IV.4, the weight loss occurs at the highest rate at 370°C and it reaches 5% of the initial weight. Therefore, the cells were sintered in controlled atmosphere, using the thermal treatment shown in figure IV.5.

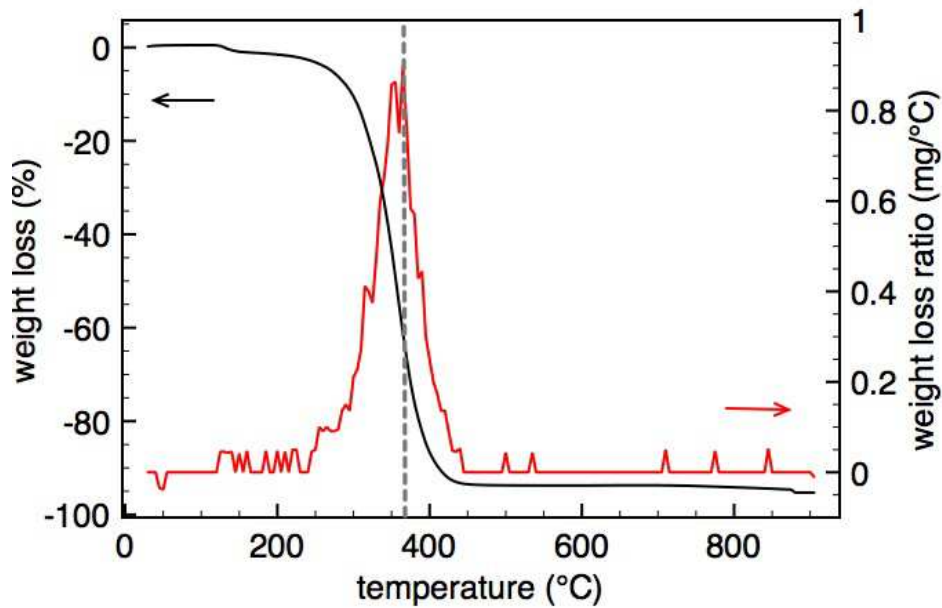


**Figure IV.4** : Weight loss and weight loss ratio of an organic tape as a function of temperature in argon.

Thus, the furnace temperature is raised from room temperature until 370°C in argon at 1°C/min where it is held for 2h. This step allows decomposing the organic products used in tape casting. The temperature is then raised from 370°C to 1300°C at 2°C/min in argon. At 1300°C the temperature is held for 5h in order to densify the ceramic layers and then it is decreased at 2°C/min until room temperature, always in argon.

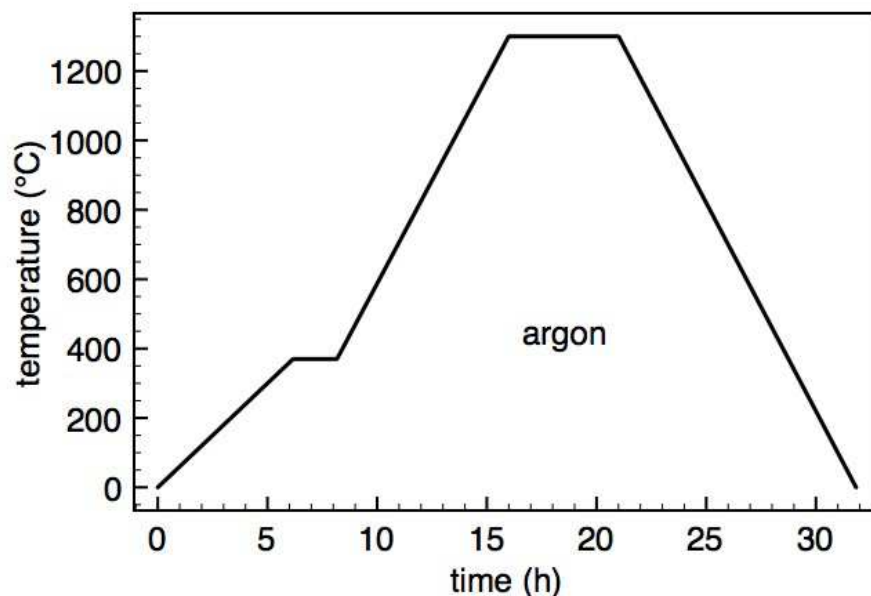


**Figure IV.5** : Sintering temperature cycle for nickel foam supported cell.

#### IV.4 Sample characterization

The microstructure of the samples obtained after sintering is shown in figure IV.6. It can be seen that the boundaries of each layer are neat, therefore there wasn't any diffusion between the layers during tape casting. It is also clear that the layers which materials have lower sintering temperatures are more dense, since the sintering cycle was optimized to densify the proton-conducting electrolyte that has the highest sintering temperature. This high temperature treatment allow densifying the oxide-ion conducting electrolyte and has therefore a good microstructure. However, although the cathode slurry has high volume of organic products, it has very low porosity. On the other hand, the central membrane has the desired porous structure, necessary to evacuate the water produced during the cell's operation.

Although the sintering cycle was chosen taking into account the sintering temperature of the  $\text{BaCe}_{0.85}\text{Y}_{0.15}\text{O}_{3-\delta}$  material, the proton-conducting electrolyte is less dense than the oxide-ion electrolyte, which decreases its effective conductivity and may not assure the gas tightness of the structure. On the other hand, the anode has a porous structure in which the nickel foam penetrates, assuring the cohesion of the metal foam and the ceramic layers. The strategy of casting two anode layers was effective in keeping the nickel foam from penetrating the proton conducting electrolyte. An interesting aspect of the microstructures obtained is the presence of cracks in the layers that densify more easily: the oxide-ion electrolyte and cathode. This is probably due to the action of the metal support and the other layers of the cell that shrink at higher temperatures and keep the oxide-ion electrolyte and the cathode from shrinking freely at lower temperature. Their particles are kept apart in areas of concentration of stress, and later yield cracks because they are not able to connect and create necks that grow by mass diffusion mechanism that would allow the densification of the material. The metal support did not keep the cell from deforming during sintering. The complete cell, with about 25 mm of diameter, was not flat and could not be used in a stack.

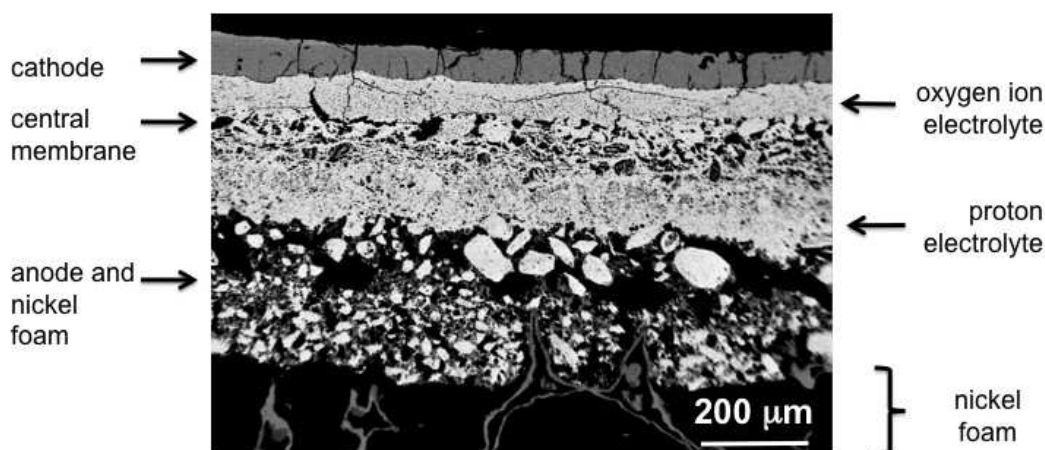


**Figure IV.6** : Nickel foam supported IDEAL-Cell B.S.E.-S.E.M. picture.

The sintering treatment at controlled atmosphere was not enough to avoid the oxidation of the nickel foam to a certain extent. This was probably due to the presence of residual oxygen in the furnace.

## IV.5 Discussion

After demonstrating the IDEAL-Cell concept and producing its electrodes, we were now interested in developing a fabrication procedure that allowed to obtain a complete cell. Instead of adapting a POC prototype by applying the electrodes directly onto the electrolytes, another approach was followed that could lead to a complete cell with higher performances. Thus, it was decided to apply a metal support architecture to this fuel cell because, as it was said before, it allows optimizing the ceramic layers exclusively for their functions in the cell. The ceramic layers were deposited over a glass support from the cathode to the anode by tape casting. Each slurry was optimized so that the adequate microstructures were obtained for each layer. The metal support, a nickel foam with 200  $\mu\text{m}$  pores, was then deposited over the anode. In order to avoid that the foam would enter the electrolyte, a double anode layer was cast. As it can be seen in figure IV.6, this strategy was successful, however it has the disadvantage of increasing the anode's thickness and therefore its polarization as well. The green cell was then sintered at 1300°C for 5h, which was the cycle appropriate to densify the proton conducting electrolyte material, the one with the highest sintering temperature. In order to avoid the oxidation of the nickel foam, this thermal treatment was carried out in argon. In the absence of oxygen, it was verified that the high temperature was enough to decompose the organic products used in tape casting. However, a residual weight of about 5% remains probably as carbon. One way to avoid this is using binders and plasticizers that decompose completely in reducing or neutral atmospheres.

Although the slurries and the sintering cycle were optimized to do so, the proton conducting electrolyte was not fully densified. A solution for this would be the use of a sintering aid, to change the powder's morphology and particle size in order to change its sintering temperature. The oxide-ion conducting electrolyte reaches a higher density, since it's a material that has a lower sintering temperature. The sintering temperature wasn't high enough to densify the proton electrolyte but on the other hand it was too high for the cathode that is too dense, although the tape casting slurry was tuned to avoid so.

It can be seen in figure IV.6 that the cathode and the oxide-ion electrolyte have cracks

in their structures. This happens because these materials, with lower sintering temperature, were the first to reach its highest density, while the other layers kept shrinking. Since the dense layers couldn't follow the shrinkage of the rest of the structure, and the interfaces kept the layers together, cracks were created in the points of higher stress concentration.

## IV.6 Conclusion

A fabrication procedure was developed to produce a complete IDEAL-Cell. It had to take into account that this five-layered structure is made of four different materials with different shrinkage behaviors and, amongst those layers, the electrolytes must be dense and the electrodes and the central membrane must have a porous structure. It was developed a metal supported-architecture allows optimizing the layers thicknesses to their electrochemical application. The metal support used is a highly porous nickel foam with 200  $\mu\text{m}$  pores. The ceramic layers were produced by tape casting and then the foam was deposited over the anode. Each layer slurry was optimized to obtain the adequate layer microstructure. The porosity in the layers is created by the burning-out, in oxygen, of the organic products used in the slurries. However, in the presence of oxygen, the nickel foam oxidizes and becomes brittle and therefore can lead to the cell's premature failure. In order to avoid so, sintering was carried out in argon and the organic tape casting additives were thermally decomposed. However, a residue of about 5wt.% was left after sintering. The oxidation of the nickel foam was not completely avoided due to the presence of residual oxygen in the furnace. To overcome the disadvantages of this thermal treatment two strategies were proposed; the first consists in considering a reducing treatment at high temperature in hydrogen to eliminate the residues resulting from the tape burnout and the second in reducing the oxidized nickel foam or sintering in vacuum but using tape casting binders and plasticizers that decompose in reducing atmospheres without leaving residues.

The nickel foam offers a mechanical support to the cell but it doesn't avoided its deformation during sintering due to the different high temperature behavior of the materials. The fact that some layers keep shrinking when others reached their highest density, creates areas of high stress concentration where cracks are created in order to follow the cell's shrinkage.

The limiting point of this shaping procedure is the high sintering temperature of  $\text{BaCe}_{0.85}\text{Y}_{0.15}\text{O}_{3-\delta}$  that makes densifying the electrolyte a hard task. As a solution, it can be used a sintering aid to lower the sintering temperature or try to decrease the powder's particle size in order to increase its specific area and therefore increase the sintering driving force. However, smaller particle size powder requires higher volume of tape casting binder and plasticizer to create a mechanically stable tape and therefore its densification less likely to happen.

---

Suite au développement des composants de IDEAL-Cell pris séparément, une séquence de procédés a été définies et mise en place pour fabriquer une cellule complète. L'obtention de très bonnes performances impose une succession de couches minces, pour limiter les chutes ohmiques, associées à des microstructures optimisées pour chacun des composants. A contrario, une bonne tenue mécanique de la cellule en fonctionnement est assurée par une couche épaisse appelé support. Dans ce chapitre, une séquence de procédés est proposée pour la fabrication d'une cellule complète supportée par une mousse de nickel. La différence de comportement au frittage des différents matériaux a été prise en compte dans la formulation des barbotines pour obtenir les microstructures désirées après traitement thermique. En raison de cette différence, les cellules présentent des déformations et fissures dans les couches successives.

---



---

## Chapter -V-

# Central membrane characterization

---

### Contents

---

<b>V.1</b>	<b>Introduction . . . . .</b>	<b>102</b>
<b>V.2</b>	<b>X-ray microtomography . . . . .</b>	<b>106</b>
<b>V.3</b>	<b>Experimental Procedure . . . . .</b>	<b>109</b>
<b>V.4</b>	<b>X-ray microtomography results . . . . .</b>	<b>115</b>
<b>V.5</b>	<b>Image segmentation . . . . .</b>	<b>117</b>
	V.5.1 Porosity . . . . .	117
	V.5.2 Ceramic Materials . . . . .	119
	V.5.2.1 Halo . . . . .	122
	V.5.3 Segmentation of the three phases . . . . .	127
<b>V.6</b>	<b>Morphologic 3D Image Analysis . . . . .</b>	<b>127</b>
	V.6.1 Percolation . . . . .	129
	V.6.2 Tortuosity . . . . .	130
	V.6.3 Active triple phase boundaries . . . . .	131
<b>V.7</b>	<b>Discussion . . . . .</b>	<b>134</b>
<b>V.8</b>	<b>Conclusions . . . . .</b>	<b>136</b>

---

## V.1 Introduction

The previous chapters describe the activities that lead to the development of POC prototypes, the development and optimization of the electrodes and a first approach to fabricate highly performant IDEAL-Cells. Although the fabrication procedure of the complete cell still requires further researches on materials development and shaping techniques optimization, it was soon anticipated theoretically which compartment will be the limiting step of the cell performance. Bessler *et al.* developed an electrochemical model for an IDEAL-Cell, that, when fitted with the testing results of the first prototypes, showed that the central membrane is responsible for most of the polarization losses of the cell (see figure V.1). And, as expected by the configuration of the system, the polarization losses of the electrodes are very low since they play one single role. Thus, our activities focused on the optimization of the central membrane by tape casting and sintering.

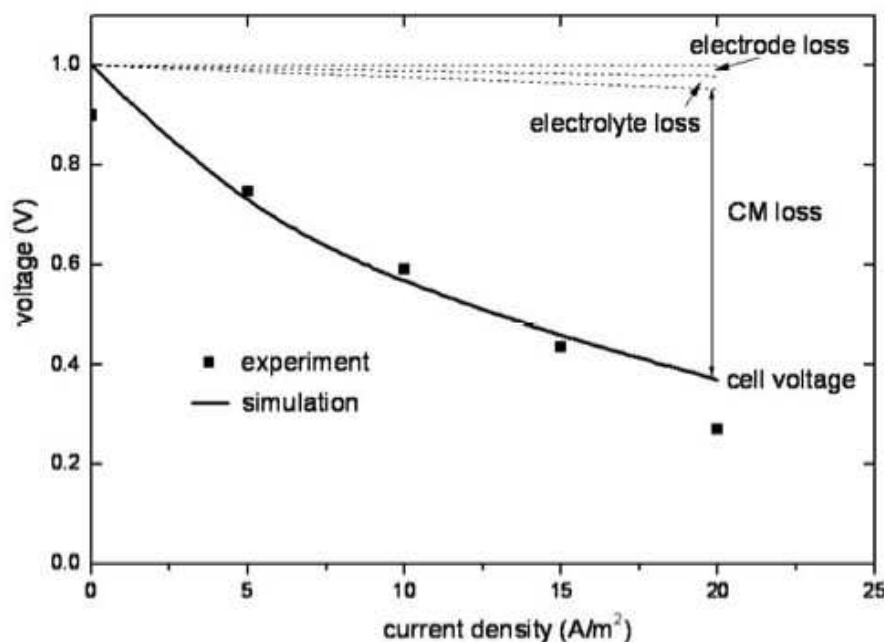


**Figure V.1** : I-V curve predicted through modeling for an IDEAL-Cell. The polarizations of the electrodes, the electrolytes and the central membrane are identified [70].

The central membrane, as it was already written before, must have a high density of active reaction sites where the  $O^{2-}$  and  $H^+$  ions recombine to create water, that must then be evacuated through a porous structure. The active reaction sites of the central membrane are all the morphologic sites where the proton electrolyte phase connected to its electrolyte is in contact with the oxygen ion electrolyte phase also connected to its corresponding electrolyte. Here, the ions coming from the electrolytes meet and recombine but these sites only remain active if water is evacuated. Therefore, the two phases must also be in contact with the porosity network that leads to the exterior of the cell. This notion is very similar to the so-called triple phase boundaries that are the active electrochemical reaction sites of an anode

or cathode of an SOFC.

Different studies have been carried out to quantify the triple phase boundaries of SOFC electrodes using different approaches. Deng and Patric developed a geometrical model to measure the length of the triple phase boundaries of an electrode of an SOFC. They considered that the ion conducting material and the electron conducting material are powders which all particles have one size and that size is the same for the both of them. Two particles with diameter  $D$  have an intersection length of  $\alpha D$  (figure V.2). The triple phase boundaries are determined by the perimeter of the circle with diameter  $\alpha D$ .

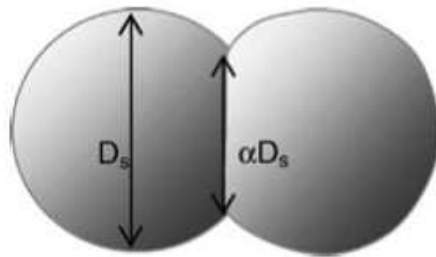


**Figure V.2** : Single diameter particle size intersection.

The triple phase boundaries length was determined, as it can be seen in figure V.3, for different particle sizes, pore sizes and porosity volume percentages.

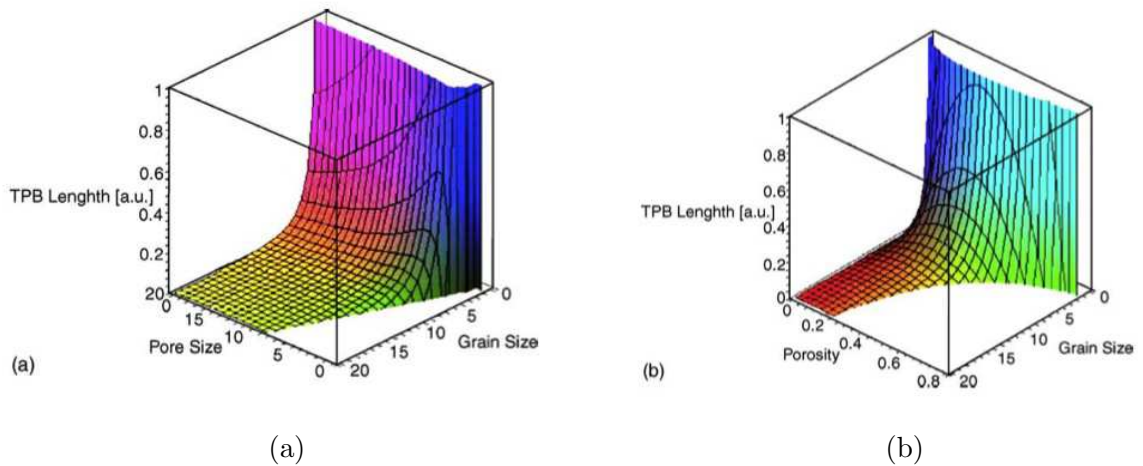


**Figure V.3** : Triple phase boundaries determined as function of the porosity volume, particle size and pore size [71].

This is a very simple and unrealistic approach since powders never have such narrow particle size distribution and it's even more unlikely that two different powders have the same particle size. It is also missing the notion of percolation of the phases to determine the active triple phase boundaries. Wilson *et al.* used the first experimental method to estimate the triple phase boundary length. Studying a NiO-YSZ composite SOFC anode, they used F.I.B-S.E.M. to obtain a 3D section of the real structure of the anode, as it can be seen in figure V.4(a).

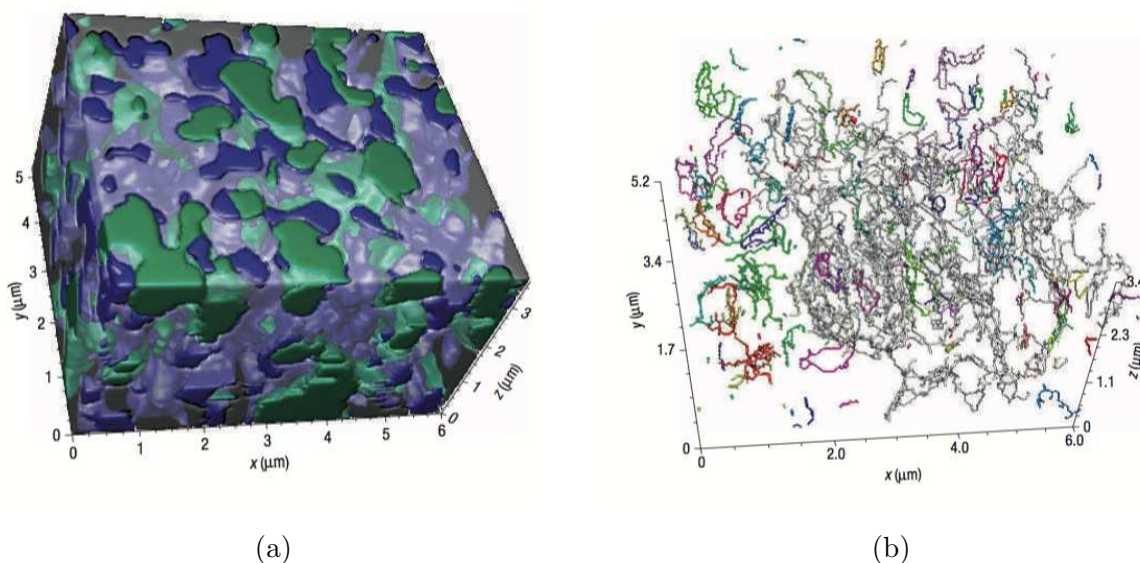


**Figure V.4** : 3D image of a NiO-YSZ anode obtained by F.I.B.-S.E.M. (a) and the active triple phase boundaries in white (b) [72].

Then, using image processing operations and taking into account the notion of phase percolation, the total and active triple phase boundaries were determined, as it can be seen in figure V.4(b). In the sample studied, 63% of its triple phase boundaries were active, representing a density of  $2696 \text{ m/mm}^3$ . This study, although of high quality and groundbreaking at the time, has its drawbacks. The technique only allows to study a volume of  $6 \times 5 \times 4 \text{ } \mu\text{m}^3$  which probably is not representative of the whole sample.

Kenney *et al.* developed purely modeling approach to solve this problem. Using spheres to represent the powders particles, they represented each powder with different particle sizes distributions. Then, using random models that allow a certain percentage of overlapping of the elements, they created 3D randomly packed structures representative of an electrode produced using materials with the features considered (figures V.5 (a) and (b)). Using algorithms to determine the active triple phase boundaries of these structures they could determine their length as a function of the porosity volume, fraction of each phase and even different particle size distributions.

The method developed is rather powerful since it allows to determine the triple phase boundaries length as a function of the powders particle size distribution (figure V.6(a) and (b)). However, using spheres as particle models is an approach more or less rough depending on the actual powder morphology. The shaping technique used, whether it is tape casting and sintering or plasma spraying, changes the morphology of the layers even when using the same materials. Therefore these models cannot take into account all the experimental factors that influence the structure of the final layers morphology.

Since the central membrane is the component that is keeping IDEAL-Cell from reaching better performances, a method based in experimental measures to determine the active triple phase boundaries has been developed. Unlike the other experimental-based technique we know, this one should allow obtaining a representative image of the whole sample which would be a step forward in this field. This technique could then be used to optimize the central membrane. The technology used to obtain 3D images of the microstructures was the X-ray microtomography.

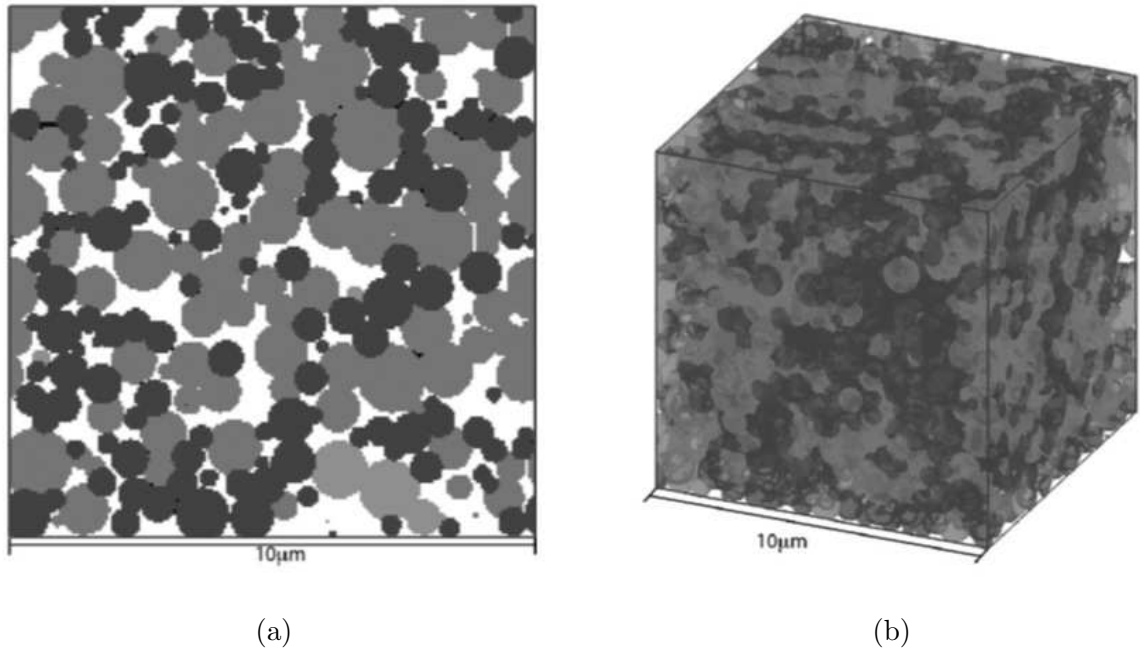


**Figure V.5** : A 2D image of a random anode structure (a) and its respective 3D representation (b) [73].

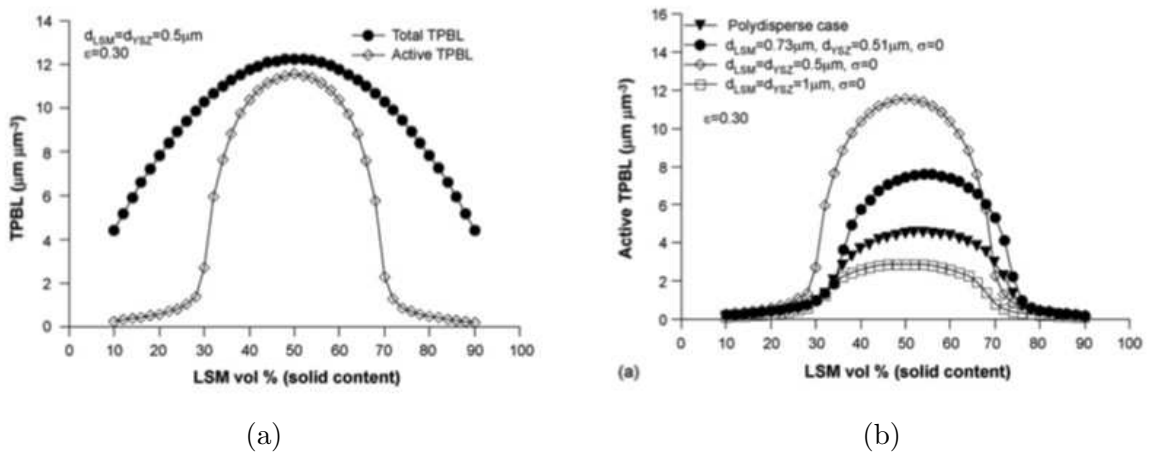


**Figure V.6** : Total and active triple phase boundaries length for a single-size particle distribution (a) and different particle size distributions (b) [73].

## V.2 X-ray microtomography

X-ray microtomography allows obtaining images of microstructures through the same principle of X-ray scans commonly used in medical applications for example. When a beam of X-rays crosses an object, some photons go through it without interacting with its particles while others are scattered or absorbed. This phenomenon of scattering and absorption is called attenuation and it depends on the energy of the beam, the thickness of the sample and the density and atomic number of the material. For the same beam energy, photons can travel different distances on the same sample based on the probability of encountering a particle on their path. Thus, the probability of a photon to interact with the material increases exponentially with its thickness.

For a mono-energetic beam of photons, the change in X-ray beam intensity crossing the material in a certain thickness can be expressed as:

$$dI(x) = -I(x) n \alpha dx \quad (\text{V.1})$$

where,  $dI$  is the change in intensity,  $I$  is the initial intensity,  $n$  is the number of atoms/cm<sup>3</sup>,  $\alpha$  is the proportionality constant that reflects the total probability of a photon being scattered or absorbed and  $dx$  is the thickness crossed by the beam .

When integrated, the equation becomes

$$I = I_0 e^{-n\alpha x} \quad (\text{V.2})$$

The number of atoms/cm<sup>3</sup>,  $n$ , and the proportionality constant,  $\alpha$ , are usually combined to yield the linear attenuation coefficient,  $\mu$ .

$$I = I_0 e^{-\mu x} \quad (\text{V.3})$$

where,  $I$  is the intensity of photons transmitted across the distance  $x$ ,  $I_0$  is the intensity of the incident photon beam,  $\mu$  is the linear attenuation coefficient and  $x$  is the distance crossed by the beam through the sample.

The linear attenuation coefficient describes the fraction of X-rays that are absorbed or scattered per unit thickness of materials. This coefficient allows to determine the energy of the photons that allow a better contrast between different materials of a sample and the maximum thickness required to allow the detection of the signal crossing the sample [74] [75].

The X-ray microtomography experiments were carried out at the European Synchrotron Radiation Facility (ESRF) in Grenoble, France. A synchrotron produces X-ray radiation when the trajectory of high energy electrons circulating at nearly the speed of light is deviated by magnetic fields. Several laboratory tomographs have been commercially produced, however, the best images in terms of spatial resolution, signal-to-noise ratio and quantitative exploitation are obtained using synchrotron radiation. This high quality of the image is due to the highly intense, coherent and monochromatic beam. There is no image magnification, and the spatial resolution mainly results from the effective pixel size of the detector. The range of pixel sizes available at the ESRF goes from 0.28  $\mu\text{m}$  to 30  $\mu\text{m}$ . The electrons are emitted by an electron gun and accelerated by a pulsed electric field in vacuum nearly to the speed of light in the linear accelerator of the synchrotron (see figure V.7). After reaching their speed, the electrons reach their final energy (6 billion GeV) in the booster synchrotron. This is done in the booster synchrotron, a 300 m long ring where bending magnets which bend the electrons trajectory. The electric field applied must be synchronized to increase the electrons energy [76].

The electrons are sent to the 844 m long storage ring where they circulate at a pressure of around  $10^{-9}$  mbar. In the storage ring bending magnets change the direction of the electrons

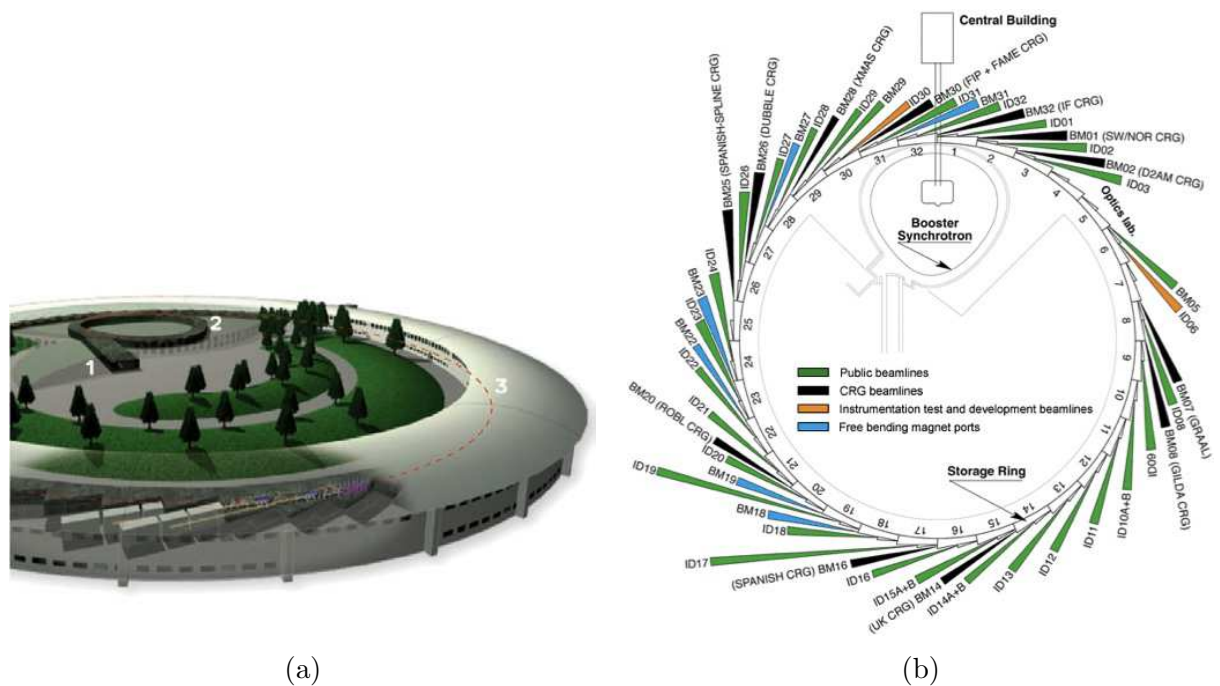


**Figure V.7** : The European Synchrotron Radiation Facility. In (a) we can see 1 the linear accelerator, 2 the booster synchrotron and 3 the storage ring. In (b) a scheme with all the beam lines available including the ID19 used in these experiments. [76]

that emit electromagnetic waves tangentially to the curved trajectory. The light emitted covers a wide range of the spectrum from microwaves to X-rays. The beam goes through focusing magnets that keep it as small as possible and through undulators that increase the intensity of the beam.

In the optics cabin, a monochromator that contains a silicon is used to select a specific energy from the wide spectrum of energies that compose the beam. The beam with the selected energy is then focused into the sample through a mirror. The beam used for these experiments was the ID19, a high resolution diffraction topography beamline. It is a multi-purpose long beam (145 m from the storage ring) that allows using two combined techniques: microtomography and phase contrast imaging. 3D images can be obtained by recording a series of radiographs (typically about 1500) for different angular positions of the sample, which rotates around an axis perpendicular to the beam. Then, a back projection algorithm reconstitutes the image of the sample in 3D.

The phase contrast imaging is obtained using a very coherent beam using a technique called propagation-based imaging technique. It consists in recording the interference pattern produced by choosing one or several sample-to-detector distances. As the beam's coherent X-ray photons cross regions with different X-ray interactions in the sample, they are refracted and undergo a phase shift, lose coherence and create constructive and destructive interference patterns with photons that were not diffracted. It is this patterns that create the contrast imaging of interfaces within the sample [78].

Due to its long length and its particular position in the storage ring, the beam is very coherent and it can be either with a wide homogeneous or a focused in a spot below 100 nm. It can be operated in an energy range from 6 to 100 keV but most of the experiments are performed between 10-35 keV.

The sample position is set in front of the beam with very precise robotic systems. After

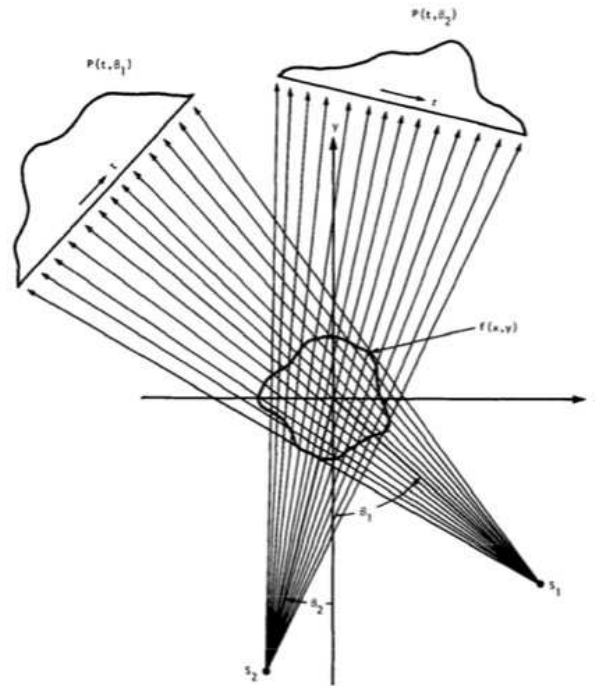


**Figure V.8** : About 1500 images of a sample in different angular positions allow reconstructing its 3D structure using a back projection algorithm. [77]

interacting with the sample, the beam is analyzed with different detectors often tailored for a specific experiment. The beam energy and the position of the sample in front of the beam and its distance from the detector is controlled in the control cabin. Immediately after the experiment a first preview of the data is obtained and the experimental parameters can be tuned to improve the results.

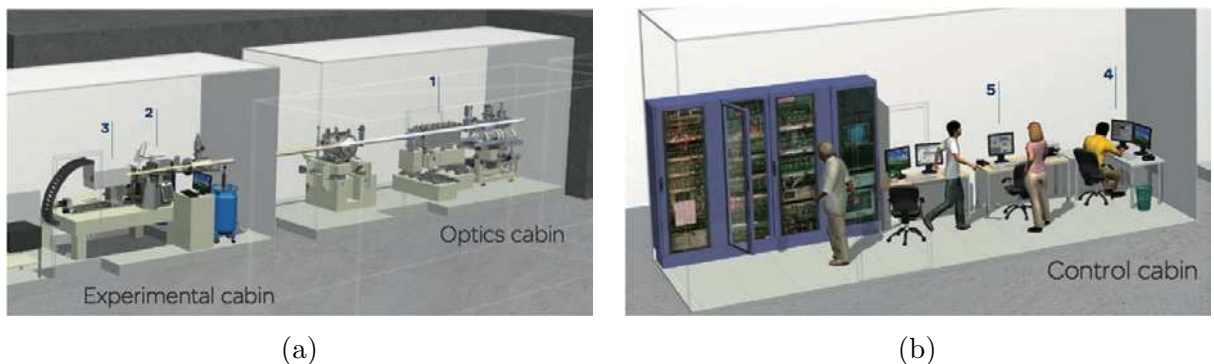


**Figure V.9** : In (a) the optics cabin where it's shown, 1, the X-ray optics, 2, the sample workspace and, 3, the detectors. In (b) we see, 4, where the beam is controlled and, 5, where the first data analysis is made..

### V.3 Experimental Procedure

The influence of the fabrication parameters in the morphology of the central membrane can be studied using X-ray microtomography to obtain their final 3D structure. Our goal was to determine the concentration of the triple phase boundaries in the central membrane. The central membrane was shaped by tape casting and sintering, using the same binder, plasticizer and solvent used in the proof of concept and development of electrodes activities. In addition to these components, corn starch was added to the slurry in order to increase the porosity of the layer.

As it can be seen in figure V.10(a), corn starch has a spherical shape with a diameter between 10  $\mu\text{m}$  and 25  $\mu\text{m}$ .

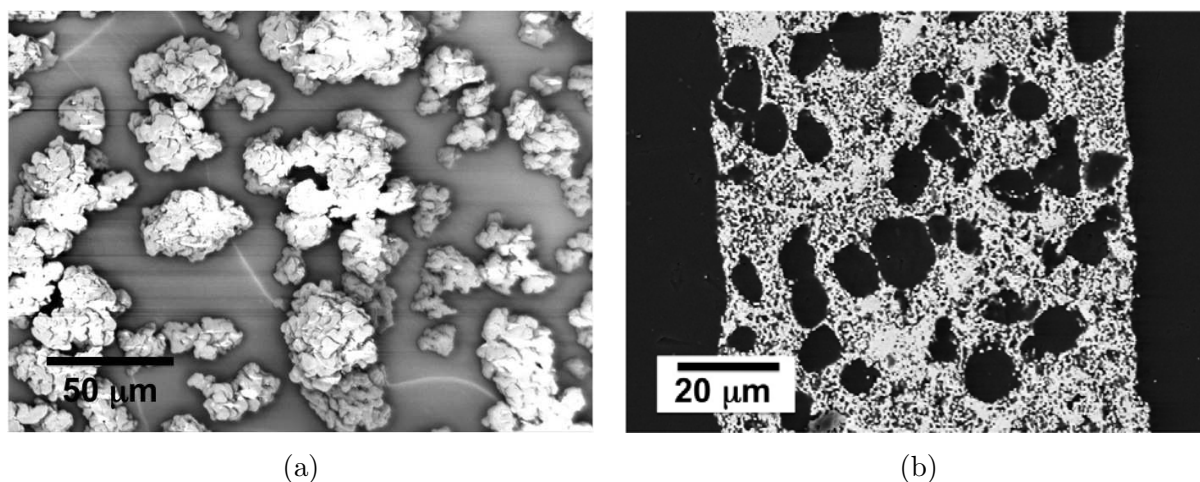


**Figure V.10** : S.E.M image of corn starch (a) and B.S.E-S.E.M. image of a sintered central membrane in which corn starch was used as pore former.

During sintering, corn starch decomposes and leaves voids in the green layer that keep the particles from approaching to each other. These voids will later be pores, in this case, spherical with about 15  $\mu\text{m}$  of diameter, as it can be seen in figure V.10(b).

In order to control the final porosity of the central membrane using corn starch, a calibration of the tape casting slurries was carried out. The volume percentage of corn starch in the slurry was increased and the final porosity volume in the membrane after sintering was determined by image analysis. The central membrane is, as it was said before, a composite layer of  $\text{BaCe}_{0.85}\text{Y}_{0.15}\text{O}_{3-\delta}$  and  $\text{Ce}_{0.85}\text{Y}_{0.15}\text{O}_{2-\delta}$ . The compounds used in the tape casting slurries are the same used in the previous chapters: ethanol as solvent, polyvinyl butyral (PVB) as binder and polyethylene glycol (PEG) as plasticizer. The slurries were ball-milled for 4h, cast at 500  $\mu\text{m}$  thick and left to dry for 24h. The resulting layers were punched into discs and sintered. The sintering temperature cycle was optimized to allow a slow degradation of the pore former. A step of 2h at 350°C was included in the cycle since this is the temperature at which corn starch has its highest weight loss in air, as it can be seen in figure V.11.

The sintering cycle, seen in figure V.12 includes thus one only step for the decomposition of starch and the organic tape at 350°C. The samples were sintered at 1300°C for 5h to use the conditions in which most likely a complete cell will be sintered.

As shown in figure V.10(b), in a B.S.E.-S.E.M. image, the ceramic phase is well distinguished from the porosity in the grey level. Due to their very different average atomic number, the ceramic appears in white or light grey, whereas the porosity is in black. The

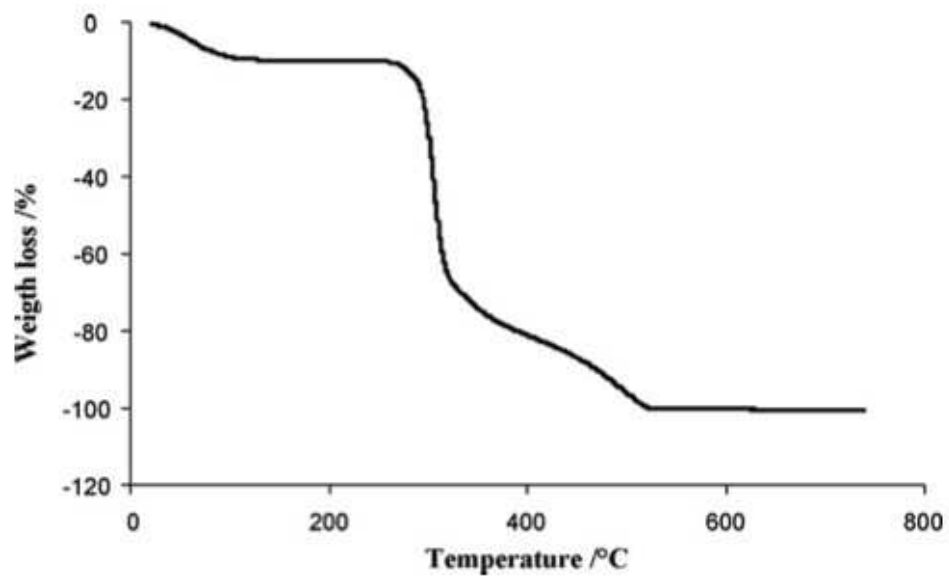


Figure V.11 : Thermal decomposition of corn starch during annealing in air [41].

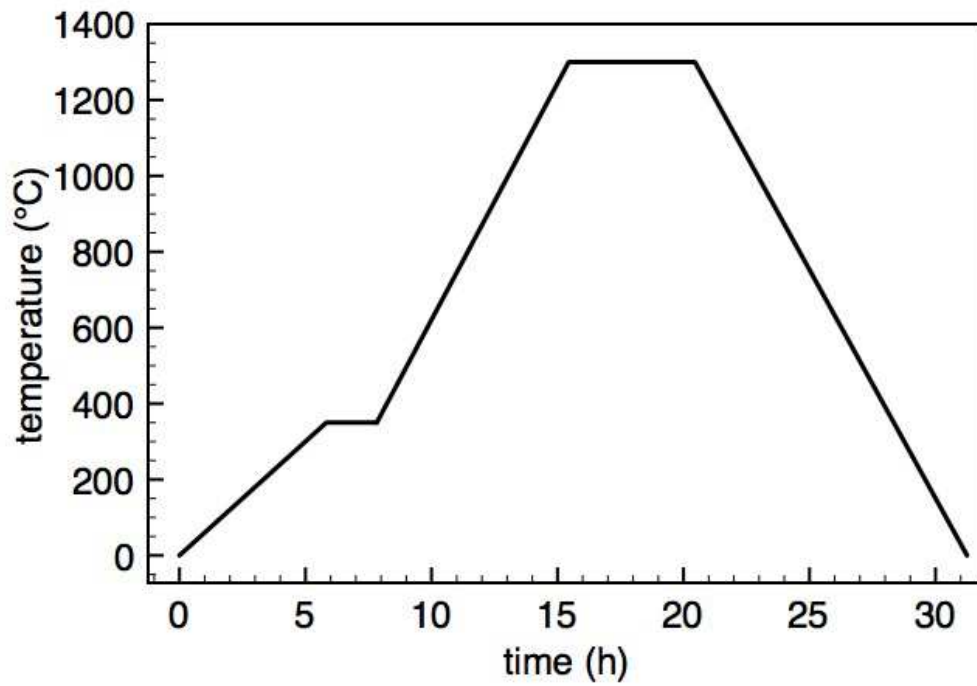
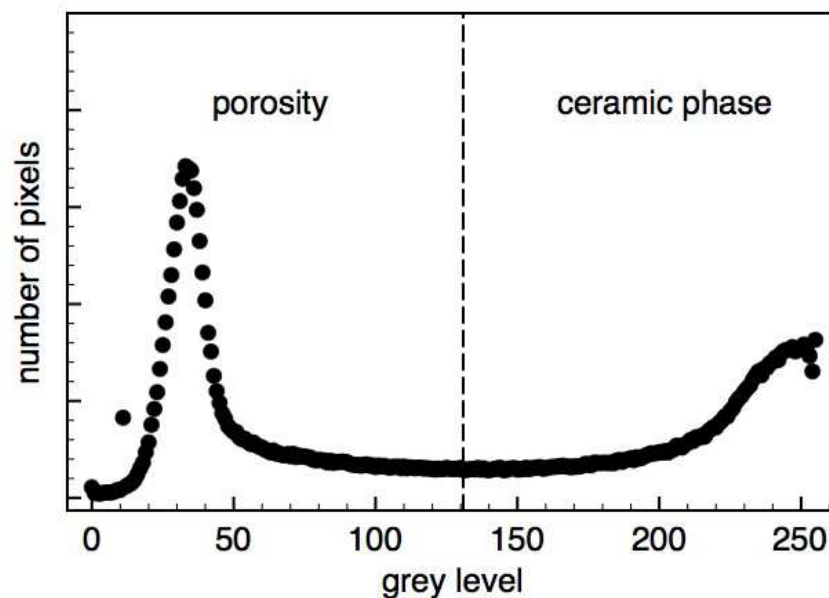


Figure V.12 : Sintering cycle used to fabricate the central membrane.

porosity of each sample was, therefore, estimated through analysis of images obtained by S.E.M. Using the software Image J, an automatic threshold based on an algorithm that can be found elsewhere [79], allowed to determine the porosity based on the difference of the grey level between the porous phase and the materials. The porosity is then given by the fraction between the black pixels that belong to the porous phase and the rest of the image. The grey level of any black and white picture varies from 0 and 255, being black the zero and white 255. All the other levels represent different shades from light to dark grey. In an image with good contrast, an object is well isolated from the background and therefore very few pixels have the grey level in the neighborhood of the object. This is the case of the image in figure V.10(b).

If we plot its histogram - the number of pixels corresponding to each grey level - of that image, it can be verified in figure V.13 that there is a clear decrease of the number of pixels in the intermediary grey levels.



**Figure V.13** : Histogram of figure V.10(b). It is represented the number of pixels that correspond to each grey level.

In order to determine in which grey level it is considered that a pixel belongs to the ceramic phase and no longer to the porosity, we use an iterative threshold developed by Ridler et al. [79]. The procedure divides the image into object and background by taking an initial threshold, then the averages of the pixels at or below the threshold and pixels above are computed. The averages of those two values are computed, the threshold is incremented and the process is repeated until the threshold is larger than the composite average [80]. This algorithm may be given by the expression V.4 and is the one available in the software ImageJ.

$$threshold = \frac{average\ background + average\ objects}{2} \quad (V.4)$$

Thus, keeping the same example of the sample in figure V.10(b), it is determined that the grey level 134 is the threshold that defines the boundary between porosity and ceramic phase. A detail of the original image and the result of the application of this threshold is shown in figures V.14(a) and (b), respectively.

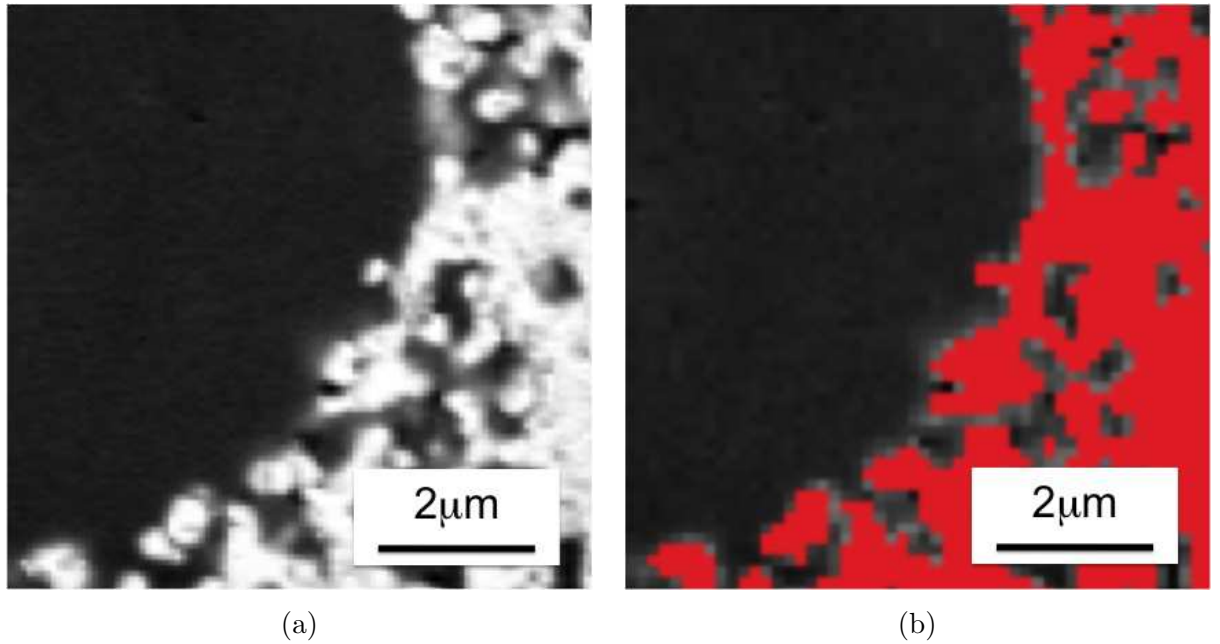


**Figure V.14** : Detail of an image of the central membrane (a) and the result of the application of the porosity threshold (b). In red are the pixels considered to belong to the ceramic phase and in black and dark grey the ones belonging to the porosity.

**Table V.1** : Composition of slurries used to calibrate the final porosity in the central membrane using corn starch.

	weight / g	short name
$\text{BaCe}_{0.85}\text{Y}_{0.15}\text{O}_{3-\delta}$	2.72	BCY15
$\text{Ce}_{0.85}\text{Y}_{0.15}\text{O}_{2-\delta}$	3.00	YDC15
poly(vinyl butyral)	1.40	PVB
poly(ethyleneglycol)	0.40	PEG
ethanol	5.50	-
corn starch	$0.3n, 0 \leq n \leq 6, n \in \mathbb{Z}$	-

This method is only a rough estimation of the porosity because it neglects one of the dimensions of the sample. In order to decrease the error of the procedure, each porosity estimation is the average of the values found for five different images. In order to be sure that the sample analyzed had an interesting volume of porosity, not too small that would not allow the evacuation of water, neither too high that would not allow the formation of percolating ion conducting paths, a calibration of the tape casting slurries was carried out. Thus, the volume of corn starch was varied and the porosity was estimated by the procedure previously explained. The composition of the slurries is gathered in table V.1.

The samples were sintered using the cycle shown in figure V.12 and their porosity was determined using the method explained above.

A relation between the volume of pore former and the final porosity of the sample was found for both pore formers, as it can be seen in figure V.15, where it is displayed the relation between the final porosity after sintering in the central membrane and the volume of corn starch as percentage of the volume of the ceramic powders.

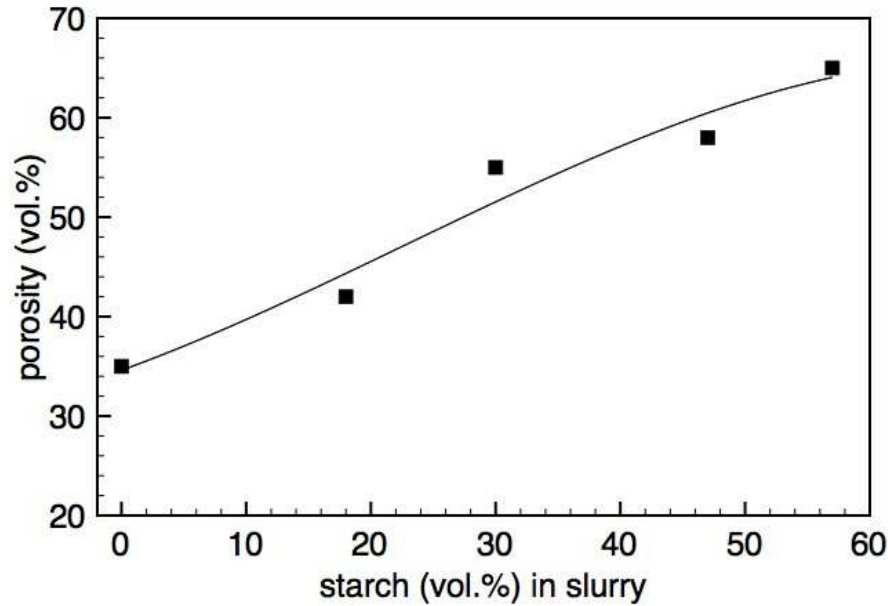


**Figure V.15** : Final porosity in the central membrane determined by image analysis as a function of the volume of corn starch in the slurry.

**Table V.2** : Composition of the slurry used to produce the sample analyzed by X-ray microtomography.

	weight / g	short name
$\text{BaCe}_{0.85}\text{Y}_{0.15}\text{O}_{3-\delta}$	1.81g	BCY15
$\text{Ce}_{0.85}\text{Y}_{0.15}\text{O}_{2-\delta}$	3.00 g	YDC15
poly(vinyl butyral)	1.40 g	PVB
poly(ethyleneglycol)	0.40 g	PEG
ethanol	5.50	-
corn starch	0.14	-

This curve was useful to fine-tune the slurry composition in order to obtain a relevant value of porosity. Taking into account these data about the porosity control using corn starch, the composition of the slurry used to produce the sample analyzed is shown in tableV.2.

The slurry was ball-milled for 4h. Tapes were cast with a thickness of 500  $\mu\text{m}$ , left to dry for 24h and punched in 25mm diameter discs. The samples were then sintered, using the cycle of figure V.12 over a powder bed on a  $\text{ZrO}_2$  support. After sintering, the samples were put in an epoxy resin and then put in vacuum to assure that the pores were filled. The resin was left to polymerize for 8h and afterwards the samples were extracted as discs with about 8 mm of thickness.

The dimensions of the cross section of the samples were determined by the attenuation coefficients of the ceramic materials, and the energy of the radiation that could be detected by the ESRF detectors. Thus, considering the materials used and the range of energy of the beam that crosses the sample, it was determined that the samples should have a cross section of  $300 \times 300 \mu\text{m}^2$ .

In order to reach the required dimensions the samples were polished in the thickness direction. Once the thickness of  $300\ \mu\text{m}$  was reached, a sample with  $300\ \mu\text{m}$  of width was cut using a micrometric saw. The height of the sample was left as high as possible as long as the sample was stable. As it can be seen in figure V.16, using this procedure, we obtained samples that could be self standing when using an appropriate sample holder. This was a very important point because the sample must stay still during the image acquisition, which can last from a few minutes to one hour.

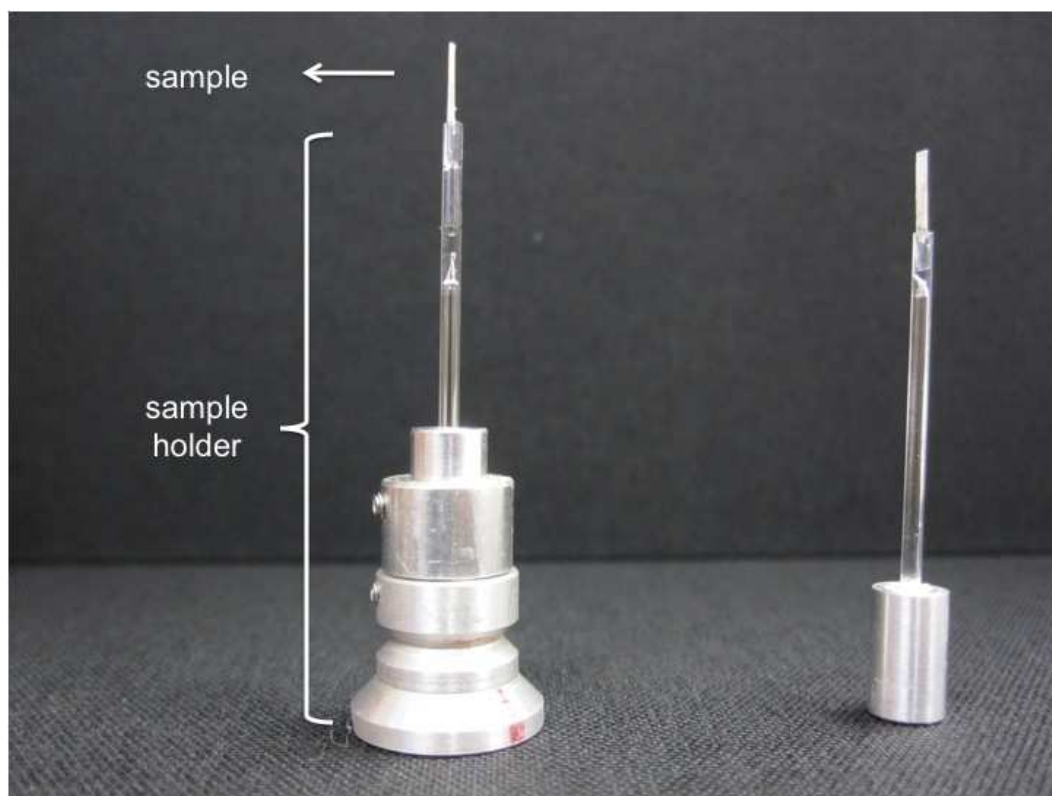


**Figure V.16** : Image of the sample in the sample holder before the X-ray microtomography image acquisition.

The last experimental factor yet to determine is the energy of the beam. Since our main objective is to distinguish the two materials in the ceramic phase and the porosity, the energy of the beam must be chosen to allow the best possible contrast between the three phases. The linear attenuation coefficient of a material varies with the energy of the beam and therefore each material will have a different interaction with the beam and that difference will be seen as a difference in the grey level of the image. The linear attenuation coefficients for the two ceramic materials of the central membrane are plotted as a function of the beam energy in figure V.17.

The first trials to obtain the images were carried out at 38 keV where, as it can be seen, there is the largest gap between the materials properties. However, it was verified that at this energy there was a high noise to signal ratio because the absorption is low. In fact, the difference between the energy of the beam coming from the source and the same beam after interacting with the sample is hardly detectable. The quality of the image was not adequate for the resolution that was necessary. Since the smallest pores and the powder particles size before sintering are near  $1\ \mu\text{m}$ , the resolution targeted for the images was  $0.28\ \mu\text{m}/\text{pixel}$ , which is the highest resolution possible in this synchrotron. Taking into account

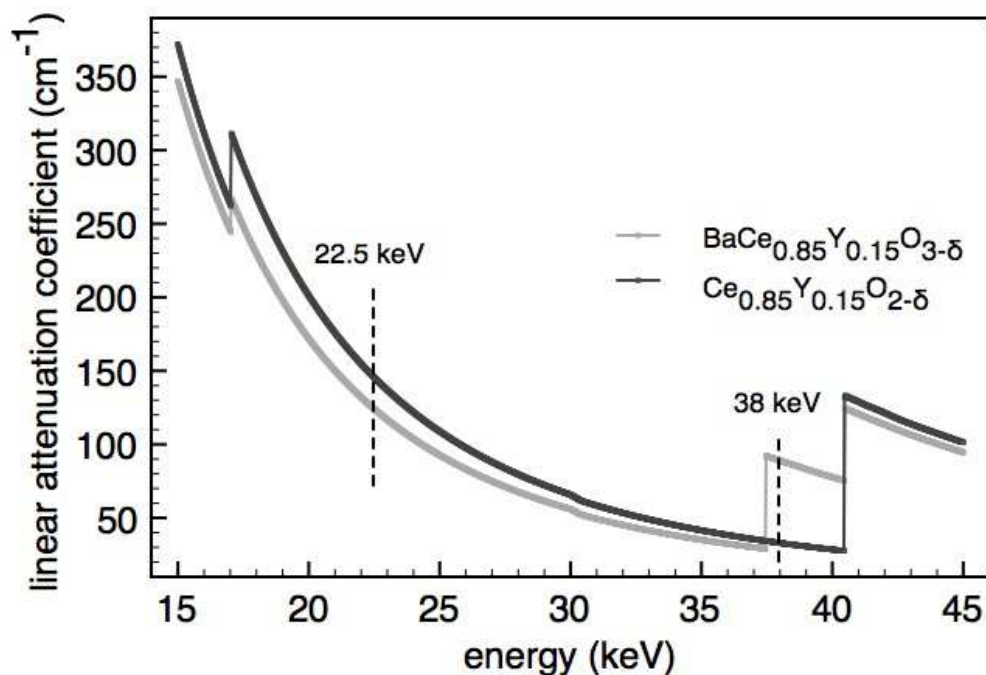


**Figure V.17** : Linear attenuation coefficients for  $\text{BaCe}_{0.85}\text{Y}_{0.15}\text{O}_{3-\delta}$  and  $\text{Ce}_{0.85}\text{Y}_{0.15}\text{O}_{2-\delta}$  as a function of the beam energy [81].

these factors, the beam energy chosen was 22.5 keV. Each sample had an acquisition time of 45min.

## V.4 X-ray microtomography results

The images obtained included zones where there was only the epoxy resin surrounding the sample that don't have any useful information. Thus, these images were cropped into images as the one shown in figure V.18. This image has  $887 \times 176$  pixels and for this sample, 442 images were obtained. The resolution is, as it was said before,  $0.28 \mu\text{m}/\text{pixel}$ .

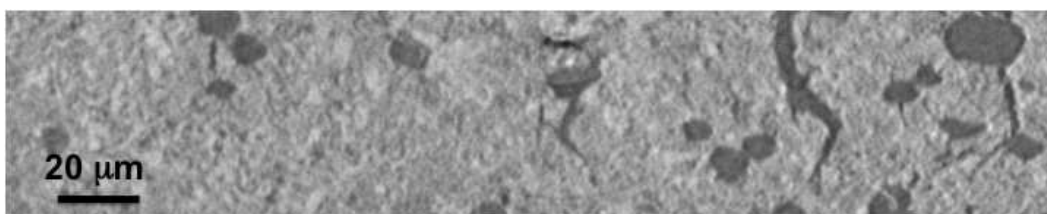


**Figure V.18** : 2D radiograph of the central membrane obtained by X-ray microtomography.

The first thing one can notice is that the contrast of this picture is very low, which can be seen in its histogram shown in figure V.19. The image average grey level is very clear and the difference between the grey levels is relatively hard to detect because all pixels are concentrated in a narrow section of the spectra.

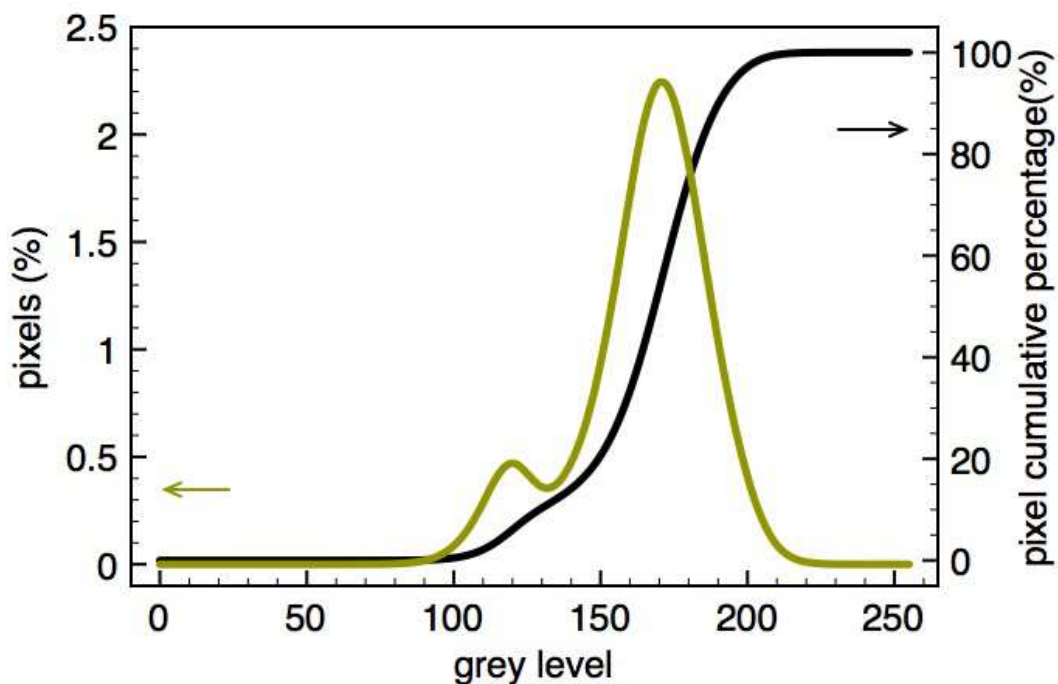


**Figure V.19** : Histogram of all the pictures obtained of the central membrane.

If the pixels grey level was equally distributed in the whole range of the spectra (between 0 and 255), the difference of between each phase would be more clear and the materials could be more easily identified. Instead, in this image, less than 0.1% of the pixels have a grey level lower than 90 and over 99.99% are below the grey level 230.

In order to increase the contrast of the image, its brightness was adjusted automatically using a tool available in the software ImageJ. This tool will redefine as 0 a certain grey value of the original image and will set a higher grey level as the new 255. The differences of grey levels in the new image will be proportional to the ones of the original image but they will be spread in the whole grey level spectra. Thus, the differences between the phases have higher contrast and are easily detectable. The result can be seen in figure V.20.

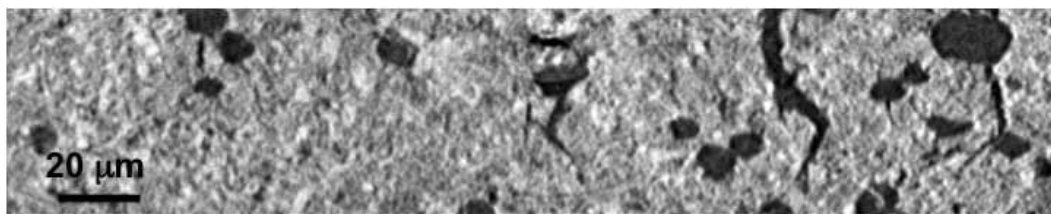


**Figure V.20** : 2D radiograph of the central membrane obtained after enhancement of the brightness and contrast.

The grey level 88 of the original image, below which there were 0.06% of all pixels, was set to 0. The grey level 215, below which there were 99.84% of the pixels, was set to 255 in the new image. The grey level of the image was spread in all the spectra, keeping the differences between them proportional. The histogram of the new image can be seen in figure V.21

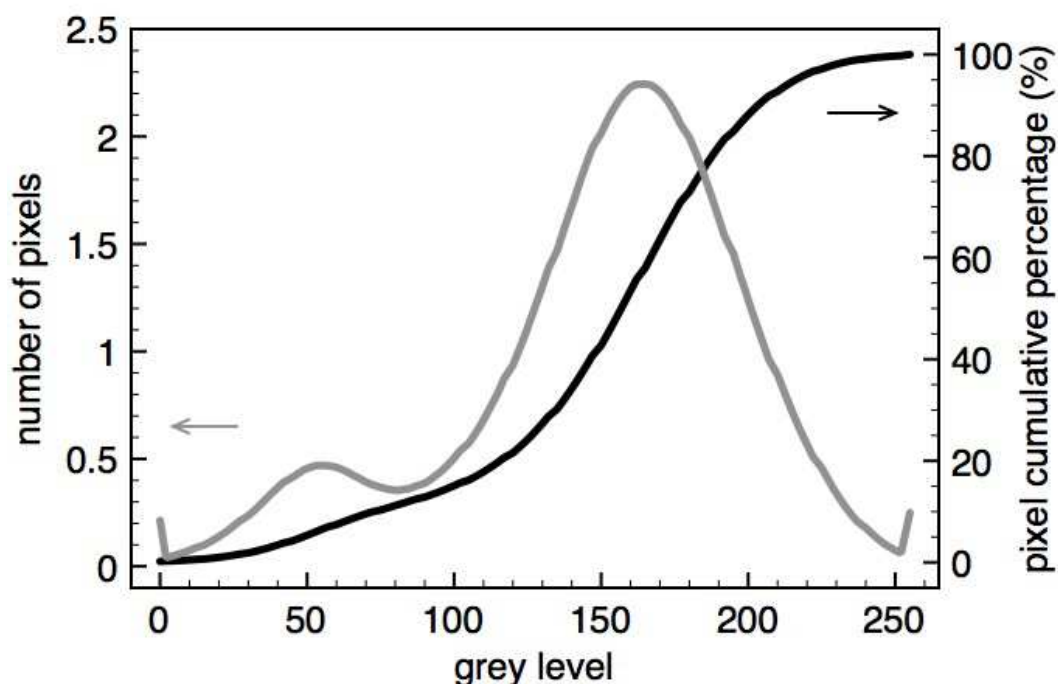


**Figure V.21** : Grey level distribution of the radiographs of the central membrane after enhancement of the brightness and contrast.

A comparison of the two histograms can be seen in figure V.22. They both have the same shape, so the original grey level distribution was respected. However, a slight saturation of the lowest and the highest grey level of the new image is verified in the histogram due to the attribution of these grey levels to pixels that, in the original image had a different grey level. These grey levels still represent only about 0.2% of the total of pixels.

With these 2D images, different softwares such as Avizo, ImageJ or Simpleware can be used to reconstruct the 3D structure of the samples, as it is illustrated in figure V.23

Now that the grey level distribution is optimized to allow better contrast, it is possible to identify each phase of the sample represented in the image, using its histogram. This can later be used to obtain the 3D image of the sample identifying each ceramic material and the porosity.

## V.5 Image segmentation

Through different methods and operations, an image can be treated in order to change its representation through which more useful information can be extracted. The interest of treating these images is to identify each of the three phases and then the triple phase boundaries, the places where they intersect. The sequence of operations that allowed to reveal these informations are here described.

### V.5.1 Porosity

The segmentation of the porous phase is the easiest of the three phases. The pores of the sample are filled with an epoxy resin that has a very different chemical structure than the

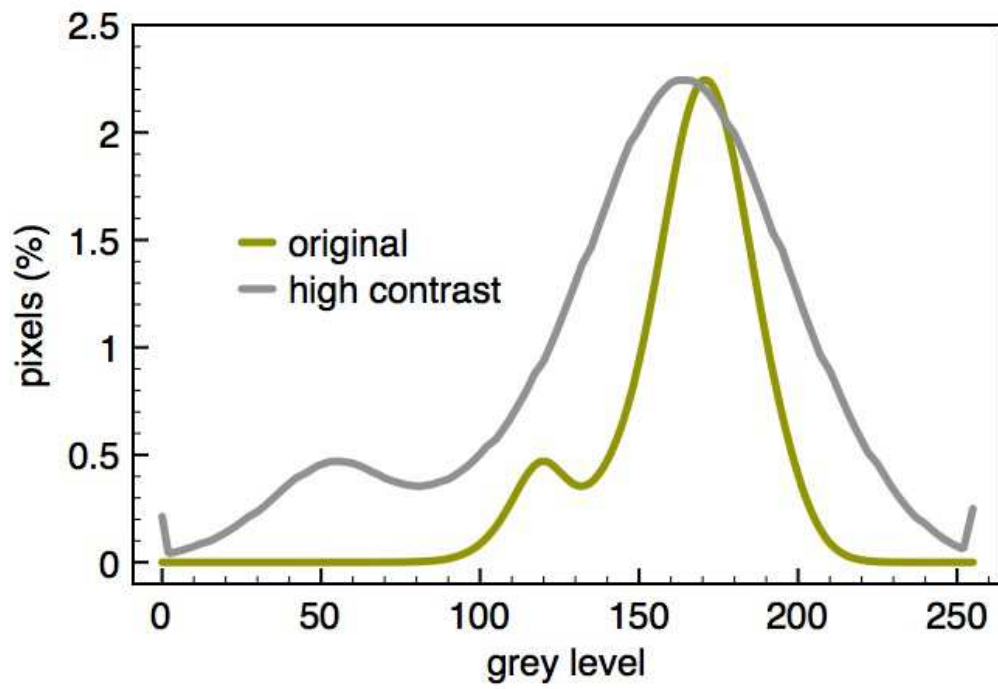


Figure V.22 : Comparison between the histograms of the original and the contrasted images.

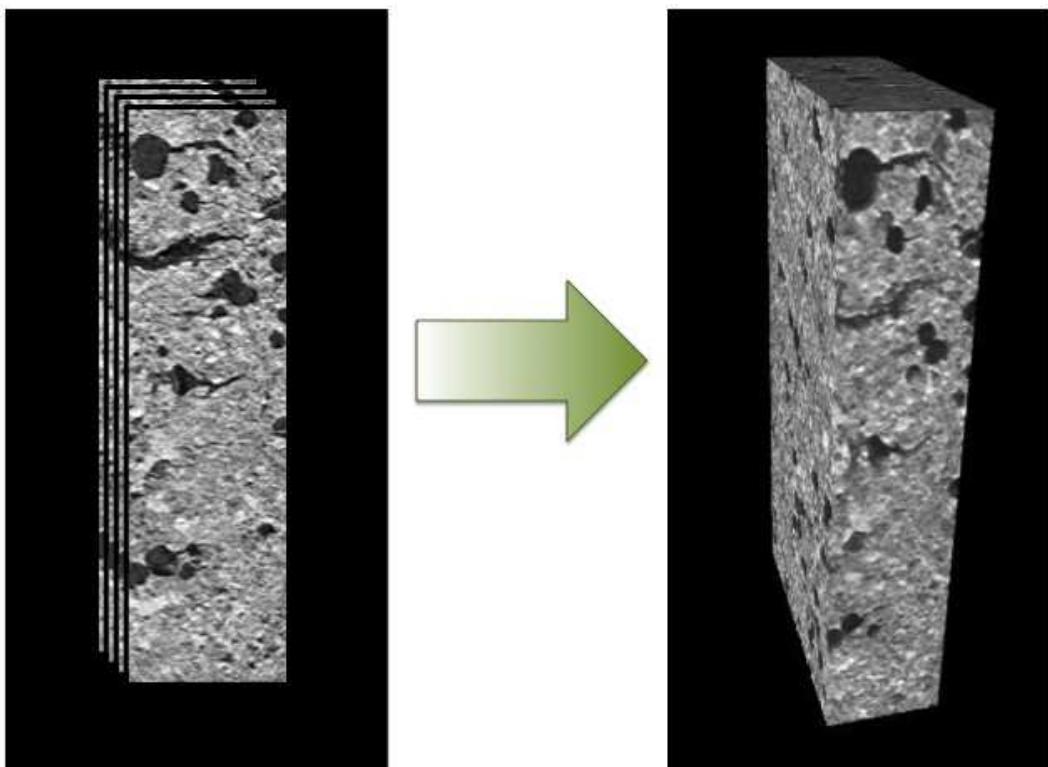
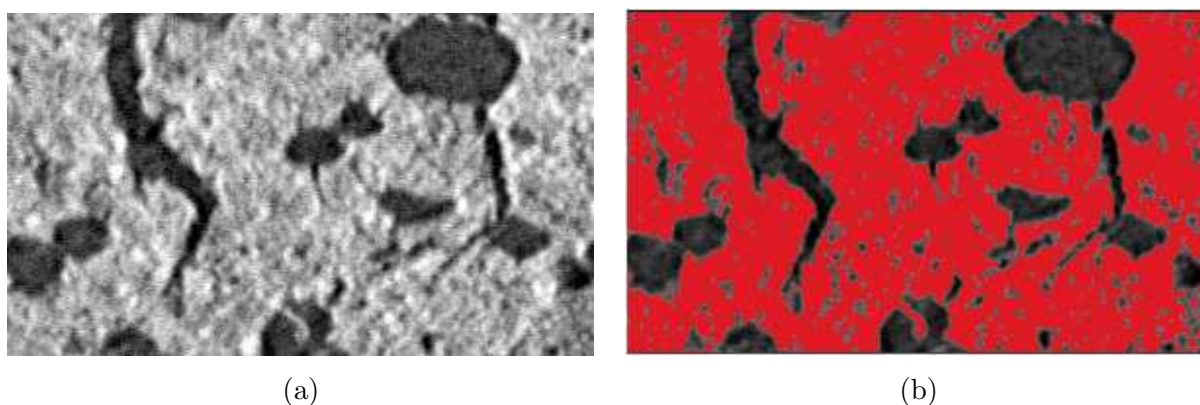


Figure V.23 : Illustration of the transformation of a set of 2D images into a 3D volume.

ceramic materials. Due to the long carbon chains with unsaturated bounds, these molecules can absorb a higher amount of energy than the ceramics. Therefore, when the radiation crosses the sample, a low amount is detected in the zones with high porosity and thus this phase appears in dark in the image obtained. As it happened in the B.S.E.-S.E.M. images, the porosity is well isolated from the ceramics due to the decrease of the number of pixels that have an intermediary grey level between the two phases, as it can be seen in figure V.22. The grey level boundary between porosity and ceramics can thus be determined using the same algorithm previously described and used in the B.S.E.-S.E.M. images. Applying this algorithm, available in the software ImageJ, it is found that the threshold for porosity is set at the grey level 132. A detail of the original image and the application of this threshold is shown in figure V.24.



**Figure V.24** : Detail of the original image of a central membrane (a) and the application of the porosity threshold found (b).

After applying this threshold to all the images obtained, the porosity in the central membrane section shown in figure V.24(a) can be represented in 3D, as it can be seen in figure V.25.

Using this algorithm was possible due to the chemical difference between the epoxy resin and the ceramics and the consequent difference of contrast. However this is not the case of the two ceramic materials used in the fabrication of the central membrane.

### V.5.2 Ceramic Materials

The ceramic materials used in the central membrane were chosen for their high ion conductivities but also for their chemical resemblance because diffusivity of different chemical elements could be avoided and the stability of their performances could be assured. However, in terms of X-ray microtomography imaging, this chemical resemblance implies a very similar absorption of the radiation. This can be verified in the figure V.17 where the linear absorption coefficients of both materials are plotted as a function of the energy of the beam. Only in two ranges of energy there is a clear difference of absorption between the two materials and where that difference is higher it was not possible to acquire good images because the absorption was too low comparing to the energy of the beam. Consequently, the contrast between the two ceramic materials is weaker than that of the porosity. The ceramics appear in the histogram as a continuous lump of grey levels. This means that the two materials have neighboring zones of absorption. The segmentation of these two phases will be done, changing manually the threshold of the grey levels.

Before determining the threshold to identify each ceramic material, a gaussian filter was

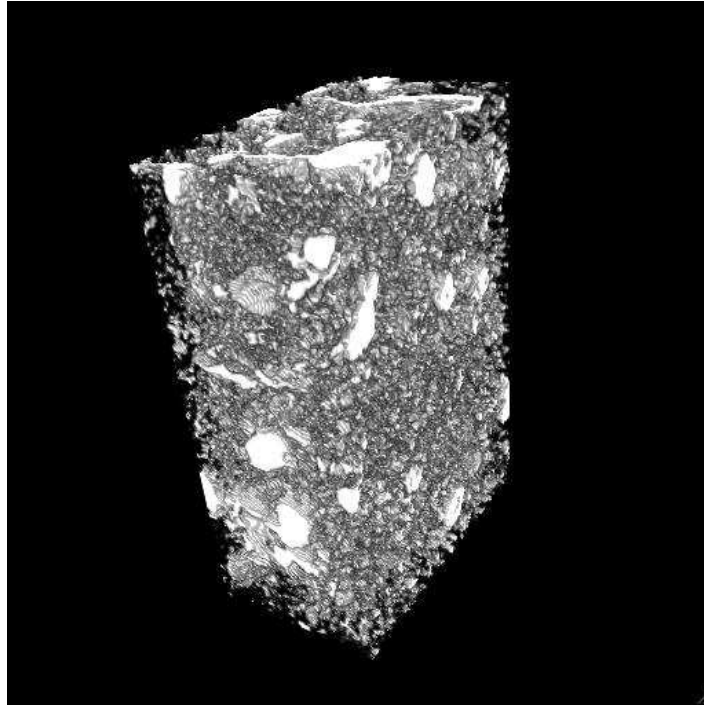


**Figure V.25** : 3D representation of the porosity in the central membrane.

applied to the image. A gaussian filter blurs the image by using a gaussian distribution to determine the transformation to apply to each pixel in the image. Each pixel of the original image receives the highest value of the distribution of standard deviation  $\sigma$  given by equation V.5 and the surrounding pixels receive smaller values as the distance  $x$  increases.

$$G(x) = \frac{1}{\sqrt{2\pi} \alpha} e^{-\frac{x^2}{2\alpha^2}} \quad (\text{V.5})$$

The resulting image respects the boundaries and edges of the original one and is less noisy and more uniform. This filter is available in the software ImageJ, in which one must choose the size of the filter or the diameter in which the neighboring pixels are affected by determining the standard deviation,  $\sigma$ . In this case, a gaussian filter with  $\sigma=1$  was applied. The difference between the original and the blurred image can be seen in figure V.26.

The image is now smoother, less noisy and the differences between the grey levels are easier to detect. The two ceramic materials can be distinguished in this image by thresholding. Knowing the linear attenuation coefficients of each material at the energy of the beam (22.5 keV), shown in figure V.17, it is expected that  $\text{BaCe}_{0.85}\text{Y}_{0.15}\text{O}_{3-\delta}$  appears brighter than  $\text{Ce}_{0.85}\text{Y}_{0.15}\text{O}_{3-\alpha}$  because it has a lower radiation absorption.

The materials different X-ray absorptions cause different grey levels in the images and, based on this, they were identified. The grey level that separates the two ceramics was 195 and the threshold for porosity had already been determined to be 132. The identification of each phase is illustrated in figure V.27.

This threshold was determined manually until the brightest pixels were chosen. Thus, the porosity was extracted by thresholding the image at grey level 132 and the  $\text{BaCe}_{0.85}\text{Y}_{0.15}\text{O}_{3-\delta}$  phase was also extracted by applying the threshold from grey level from 195 to 255. Each image was transformed into a binary image - an image only with black and white pixels - where the white pixels represent the phase identified. In order to extract  $\text{Ce}_{0.85}\text{Y}_{0.15}\text{O}_{3-\alpha}$  without

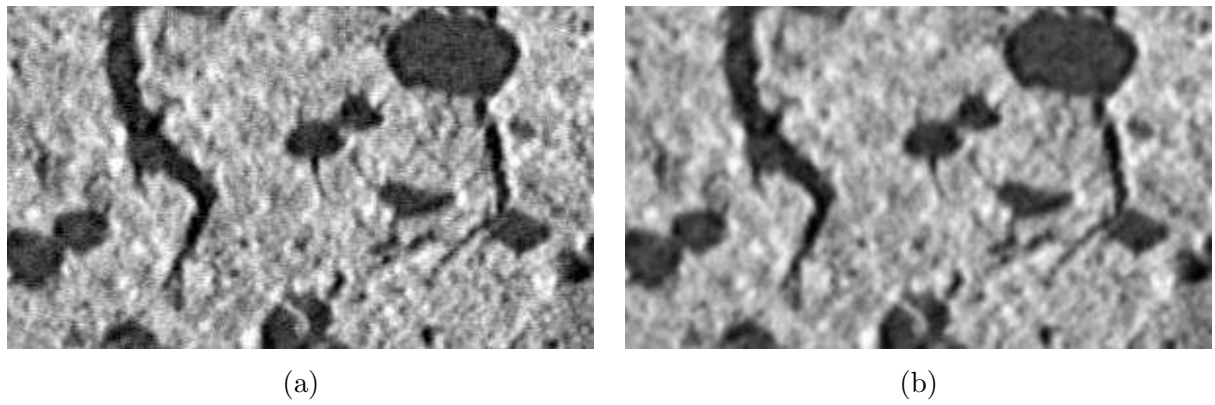


**Figure V.26** : The original section of the central membrane radiograph (a) and the same image after applying a gaussian filter of size 1.

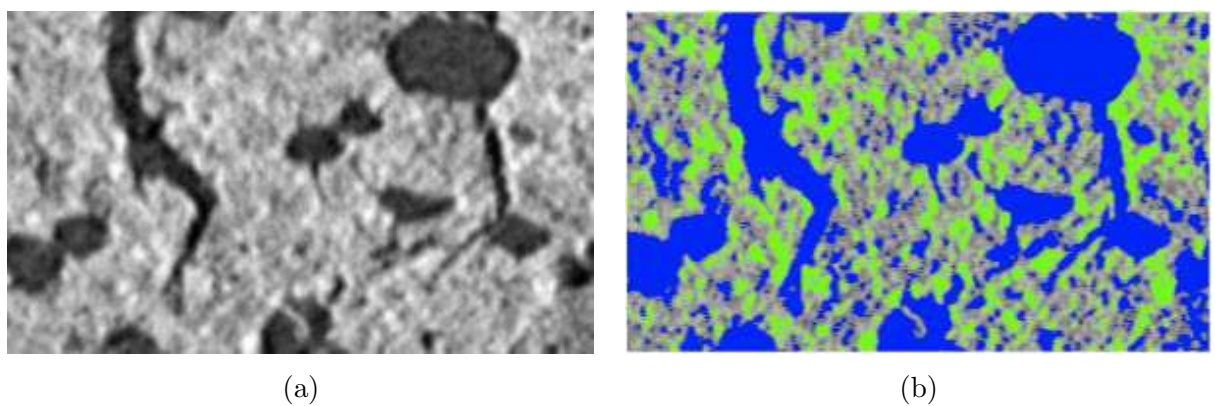


**Figure V.27** : Identification of the ceramic materials by thresholding: porosity is in blue, in grey is the  $\text{Ce}_{0.85}\text{Y}_{0.15}\text{O}_{3-\alpha}$  and in green is  $\text{BaCe}_{0.85}\text{Y}_{0.15}\text{O}_{3-\delta}$  .

intersecting the two other phases, it was extracted from the sum of the  $\text{BaCe}_{0.85}\text{Y}_{0.15}\text{O}_{3-\delta}$  and porosity binary images. The  $\text{Ce}_{0.85}\text{Y}_{0.15}\text{O}_{3-\alpha}$  phase is represented by the complementary of the sum of the other two phases. The sum of the two images can be done using ImageJ's function Process  $\rightarrow$  Image Calculator  $\rightarrow$  Add. The complementary of the sum of the two phases can be obtained by inverting the resulting image using Edit  $\rightarrow$  Invert, also in ImageJ.

However, it was verified that in the  $\text{Ce}_{0.85}\text{Y}_{0.15}\text{O}_{3-\alpha}$  phase image, there was constantly the presence of an *halo* that surrounds the porosity, as it can be seen in figure V.28. This halo is due to the bad contrast between the porous phase (the darkest phase) and the  $\text{BaCe}_{0.85}\text{Y}_{0.15}\text{O}_{3-\delta}$  phase (the brightest one). Ideally the interface between these two faces is binary, from 0 to 255, or more realistically, from the porosity grey level range to the  $\text{BaCe}_{0.85}\text{Y}_{0.15}\text{O}_{3-\delta}$  grey level range. But it was verified that the transition between the two phases goes through the grey levels of the  $\text{Ce}_{0.85}\text{Y}_{0.15}\text{O}_{3-\alpha}$  phase and therefore is wrongly identified as belonging to it.

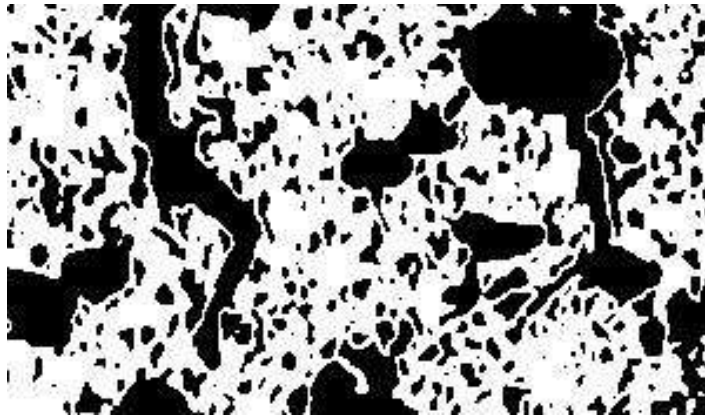


**Figure V.28** : Detail of the  $\text{Ce}_{0.85}\text{Y}_{0.15}\text{O}_{3-\alpha}$  phase identified in the central membrane.

In order to correct the halo, a sequence of morphologic image operations was developed in collaboration with D. Jeulin and C. Peyrega from the Mathematic Morphology Center of Ecole des Mines de Paris.

### V.5.2.1 Halo

The extraction of the halo required the use of simple image processing operations such as dilation, erosion, opening and closing. The sequence of operations and their effect on the original images is illustrated by generic representation of the images obtained by X-ray microtomography. The objective of this algorithm is to eliminate the halo that was wrongly identified as belonging  $\text{Ce}_{0.85}\text{Y}_{0.15}\text{O}_{3-\alpha}$  and to attribute it to the  $\text{BaCe}_{0.85}\text{Y}_{0.15}\text{O}_{3-\delta}$  phase.

The first step consists in an opening of the  $\text{Ce}_{0.85}\text{Y}_{0.15}\text{O}_{3-\alpha}$  image. This opening will actually be the intersection of 13 openings obtained using 13 segments in different directions in 3D. This allows obtaining a smoother opening than we would obtain if one single opening in one direction had been performed. The opening, a sequence of an erosion and a dilation, allows opening what in images appear as pores. When the dilation is applied, the pixels surrounding the pores are eliminated. The pore will be open depending on the thickness pixel wall that holds it and the size of the structural element used. If this pixel wall is completely eliminated, when the dilation is applied, it cannot be reconstructed because it was absent in the eroded image. The dilation cannot recall the original input image. The use of the opening is illustrated in figure V.29(a) and (b).

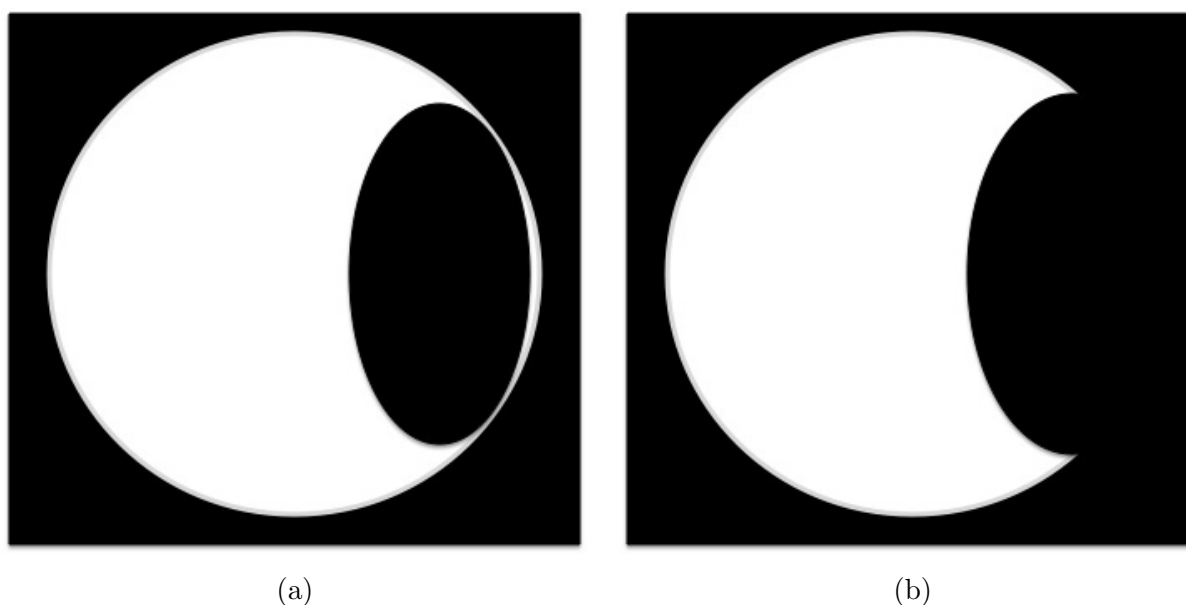


**Figure V.29** : A schematic representation of an halo (a) and a representation of the same image after removing the halo (b).

The region that is eliminated corresponds to the halo but its size depends obviously of the size of the structural element used. If this element is too large, than a part of the real  $\text{Ce}_{0.85}\text{Y}_{0.15}\text{O}_{3-\alpha}$  may be identified as belonging to the halo and the result will be fake. This region, a first approach of the halo can be obtained by the difference of the original and the opened  $\text{Ce}_{0.85}\text{Y}_{0.15}\text{O}_{3-\alpha}$  images, which in our generic case is equivalent to the region in white seen in figure V.30.

This halo is not correct yet because its size depends on the size of the structural element used and it may contain pixels that belong to the  $\text{Ce}_{0.85}\text{Y}_{0.15}\text{O}_{3-\alpha}$  material. Since the halo appears in the boundary between the porosity and the  $\text{BaCe}_{0.85}\text{Y}_{0.15}\text{O}_{3-\delta}$  phase, the pixels of the real halo are the ones that are simultaneously in the neighborhood of these two phases. In order to find these regions, a dilation was applied to the  $\text{BaCe}_{0.85}\text{Y}_{0.15}\text{O}_{3-\delta}$  image (see figure V.31). Then, a dilation was applied to the porosity image, see figure V.32.

These operations were carried out using a rhombioctahedron with 3 voxels of diameter (figure V.33)

The halo can be obtained by intersecting the dilated image of the porosity, the dilated image of  $\text{BaCe}_{0.85}\text{Y}_{0.15}\text{O}_{3-\delta}$  and the first halo extracted shown in figure V.30. In this way, we are sure that the voxels belonging to the halo are in the frontier between the porosity and the  $\text{BaCe}_{0.85}\text{Y}_{0.15}\text{O}_{3-\delta}$  phase which is exactly the zone where it can occur in the image. Those voxels that belonged to the halo but are not in this frontier, belong to the  $\text{Ce}_{0.85}\text{Y}_{0.15}\text{O}_{2-\delta}$  phase and will be correctly attributed to it.

Thus, the  $\text{BaCe}_{0.85}\text{Y}_{0.15}\text{O}_{3-\delta}$  phase will be the sum of the first image obtained by thresholding at grey level 195 and the final halo. The porosity had already been determined by thresholding at grey level 132. And the  $\text{Ce}_{0.85}\text{Y}_{0.15}\text{O}_{2-\delta}$  phase is again the complementary of the sum of the porosity image and the new  $\text{BaCe}_{0.85}\text{Y}_{0.15}\text{O}_{3-\delta}$  image containing the halo. The difference between the  $\text{Ce}_{0.85}\text{Y}_{0.15}\text{O}_{2-\delta}$  phase image before and after this treatment can be seen in figure V.34(a) and (b), respectively.

It was, however, verified that the images obtained in this way were too noisy to be realistic although a rhombicuboctahedron was used as a structural element and the opening was

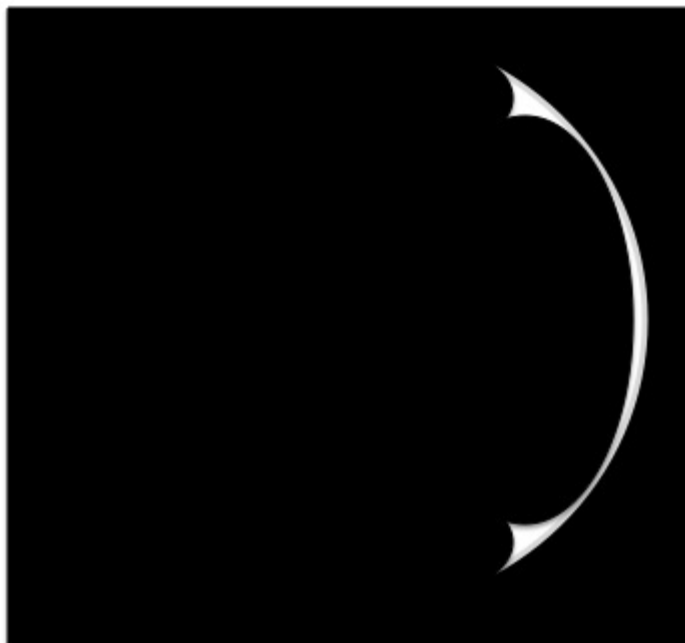


**Figure V.30** : The halo obtained by the difference between the opened and the original  $\text{Ce}_{0.85}\text{Y}_{0.15}\text{O}_{3-\alpha}$  images.

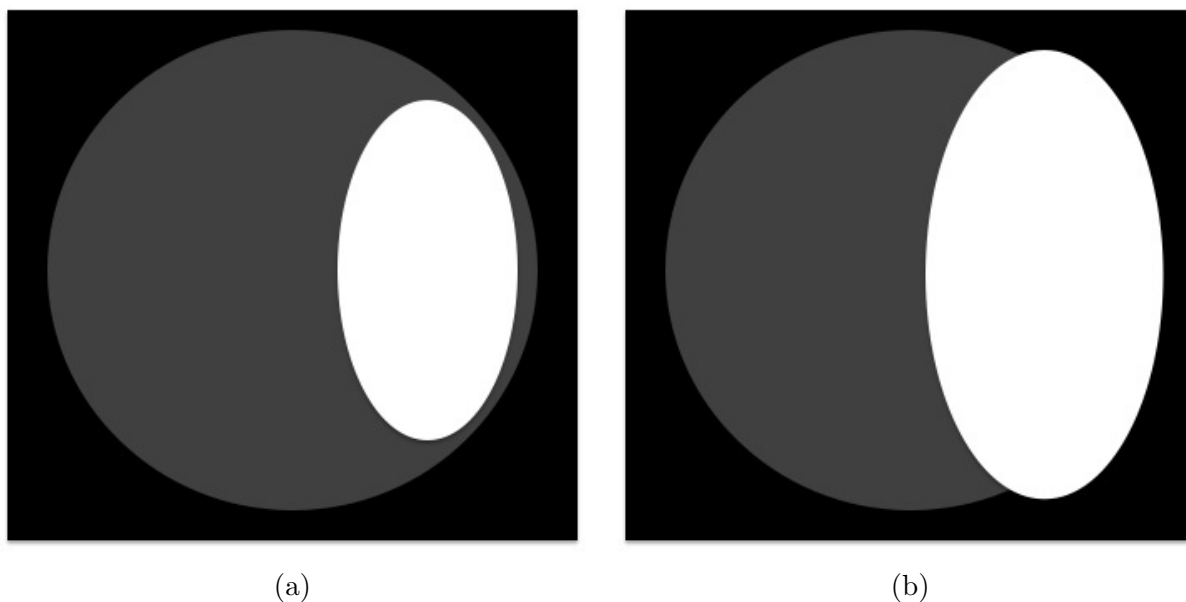


**Figure V.31** : Simplified representation of the central membrane with  $\text{BaCe}_{0.85}\text{Y}_{0.15}\text{O}_{3-\delta}$  in white,  $\text{Ce}_{0.85}\text{Y}_{0.15}\text{O}_{3-\alpha}$  in grey and the porosity in black (a). Illustration of the dilation of the  $\text{BaCe}_{0.85}\text{Y}_{0.15}\text{O}_{3-\delta}$  phase (b).

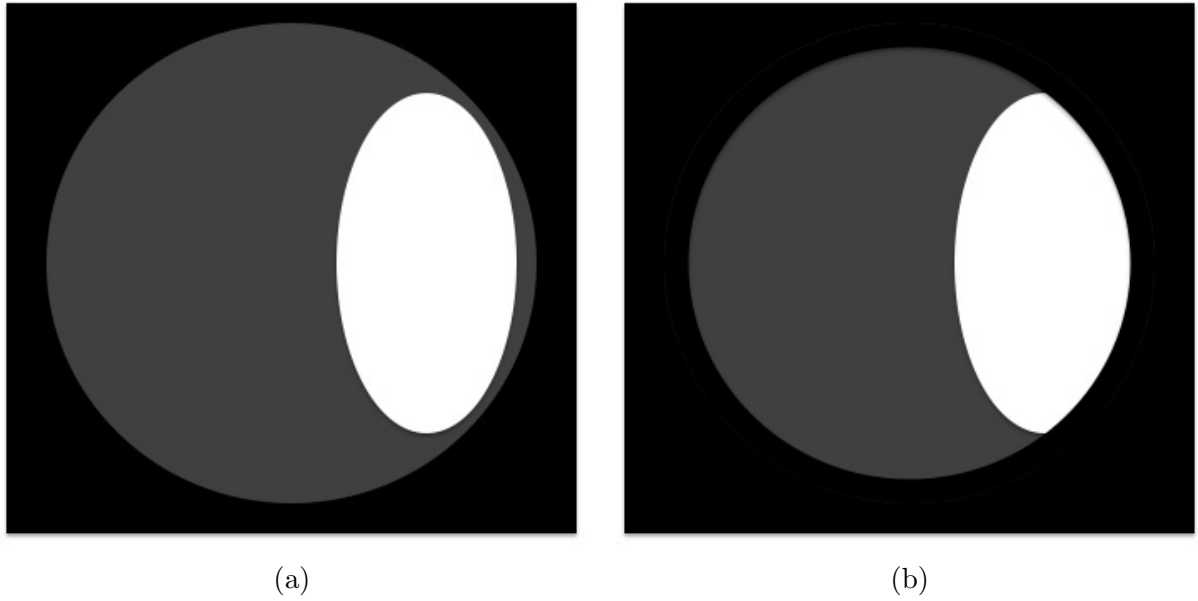


**Figure V.32** : The same simplified representation of the central membrane (a). Illustration of the dilation of the porosity phase (b).

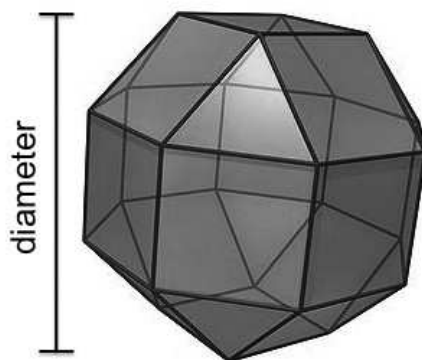


**Figure V.33** : Rhombicuboctahedron.

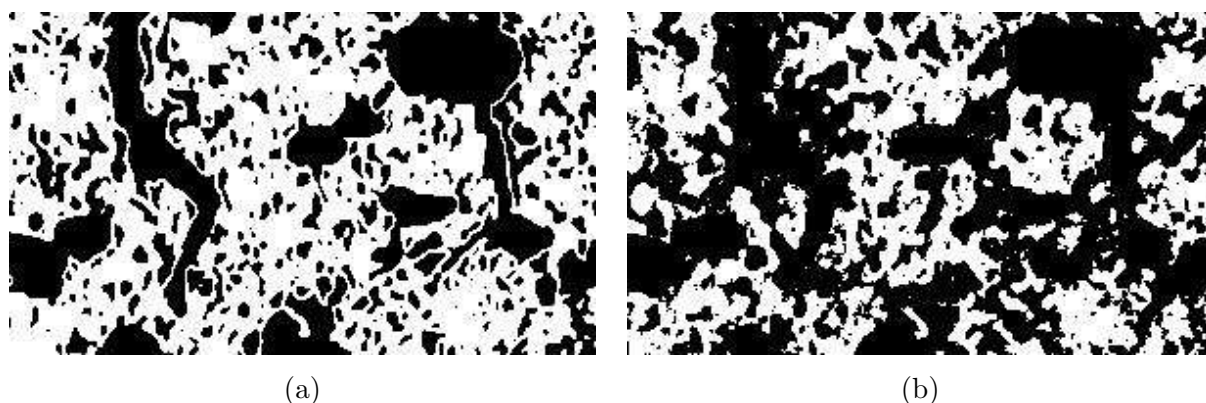


**Figure V.34** : 2D binary images of the  $\text{Ce}_{0.85}\text{Y}_{0.15}\text{O}_{2-\delta}$  phase identified by thresholding (a) and after applying the image processing algorithm developed (b).

obtained by the intersection of 13 openings in different directions. Therefore, an algorithm that can be applied using ImageJ was developed in order to smooth the images of the ceramic phases. The first step consists in applying a gaussian filter of size  $\sigma=1.5$  to the  $\text{BaCe}_{0.85}\text{Y}_{0.15}\text{O}_{3-\delta}$  binary image. The resulting image is no longer binary because a grey level is attributed to each pixel according to the weight determined by the gaussian distribution, as shown in figure V.35(a) and (b).

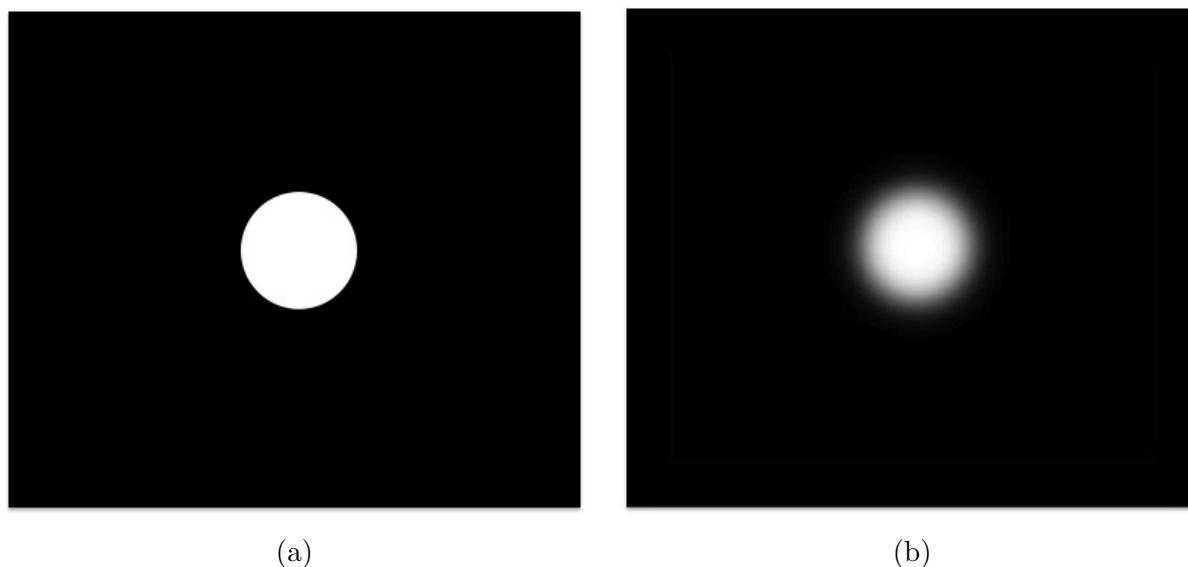


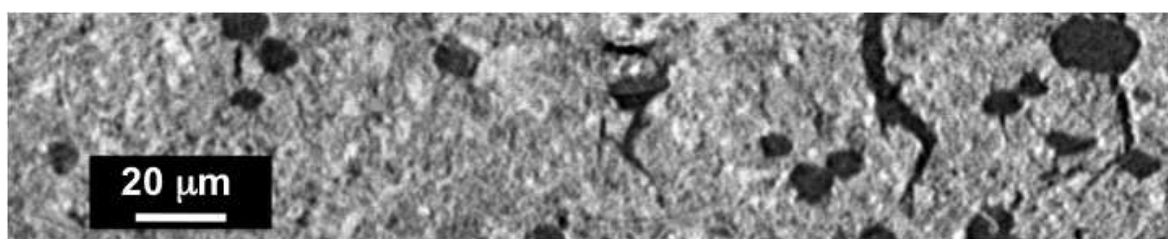
**Figure V.35** : Illustration of the application of a gaussian filter to the binary image in (a). A grey level gradient determined by the gaussian distribution of standard deviation  $\sigma$  is created (b). The resulting image is not binary.

The grey level gradient obtained in the frontier between the  $\text{BaCe}_{0.85}\text{Y}_{0.15}\text{O}_{3-\delta}$  phase, smooth its interface. In order to obtain a binary image again, an automatic thresholding is applied. The grey pixels become white and belong now to the  $\text{BaCe}_{0.85}\text{Y}_{0.15}\text{O}_{3-\delta}$  phase. However, this phase intersects now the porous phase. In order to identify these pixels, the intersection between the new  $\text{BaCe}_{0.85}\text{Y}_{0.15}\text{O}_{3-\delta}$  binary image and the porous phase is determined using the function Process  $\rightarrow$  Image Calculator  $\rightarrow$  And in ImageJ. The

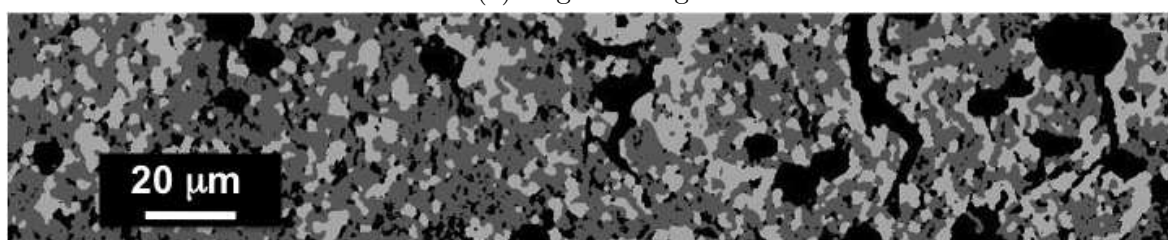
intersection of the two phases is subtracted to the  $\text{BaCe}_{0.85}\text{Y}_{0.15}\text{O}_{3-\delta}$  image and the two phases don't intersect anymore. This can be done using the function Process  $\rightarrow$  Image Calculator  $\rightarrow$  Subtract. Thus, the final smoother  $\text{BaCe}_{0.85}\text{Y}_{0.15}\text{O}_{3-\delta}$  image is obtained. The  $\text{Ce}_{0.85}\text{Y}_{0.15}\text{O}_{2-\delta}$  phase is extracted simply by determining the complementary of the sum of the other two phases and thus we are sure that the three phases are disjoint.

### V.5.3 Segmentation of the three phases

With the image processing operations defined to identify each phase represented in the image, it is now possible to compare the original radiograph with the phases identified by different grey levels. That comparison is shown in figure V.36(a) and (b).



(a) original image.



(b) processed image.

**Figure V.36** : Identification of the three phases in 2D images of the central membrane before (a) and after the identification of each phase by image processing (b).

Using all the images obtained, we can obtain the 3D representations of the original image and the reconstructed sample with the three phases identified, as seen in figure V.37(a) and (b).

The image processing operations sequence allowed identifying accurately each phase of the sample. It was verified that the porosity had been overestimated by B.S.E.-S.E.M. images. We expected to obtain a sample with a porosity with 40 vol.% of porosity and, after analyzing the 3D volume, it was found a value of 24%. Therefore the total volume percentage of the ceramic phase was higher than expected but what is remarkably accurate is the  $\text{BaCe}_{0.85}\text{Y}_{0.15}\text{O}_{3-\delta}$  to  $\text{Ce}_{0.85}\text{Y}_{0.15}\text{O}_{2-\delta}$  ratio (*BCY15/YDC15*) which is 8% higher than expected by the fabrication parameters. Thus, the  $\text{BaCe}_{0.85}\text{Y}_{0.15}\text{O}_{3-\delta}$  is slightly overestimated.

## V.6 Morphologic 3D Image Analysis

As it was shown before, through image processing operations, we could reconstruct the volume of a central membrane with the three phases identified. These images can be used to determine morphologic features of the sample that are important to predict the central membrane performance. These informations can be extracted from the images by using algorithms

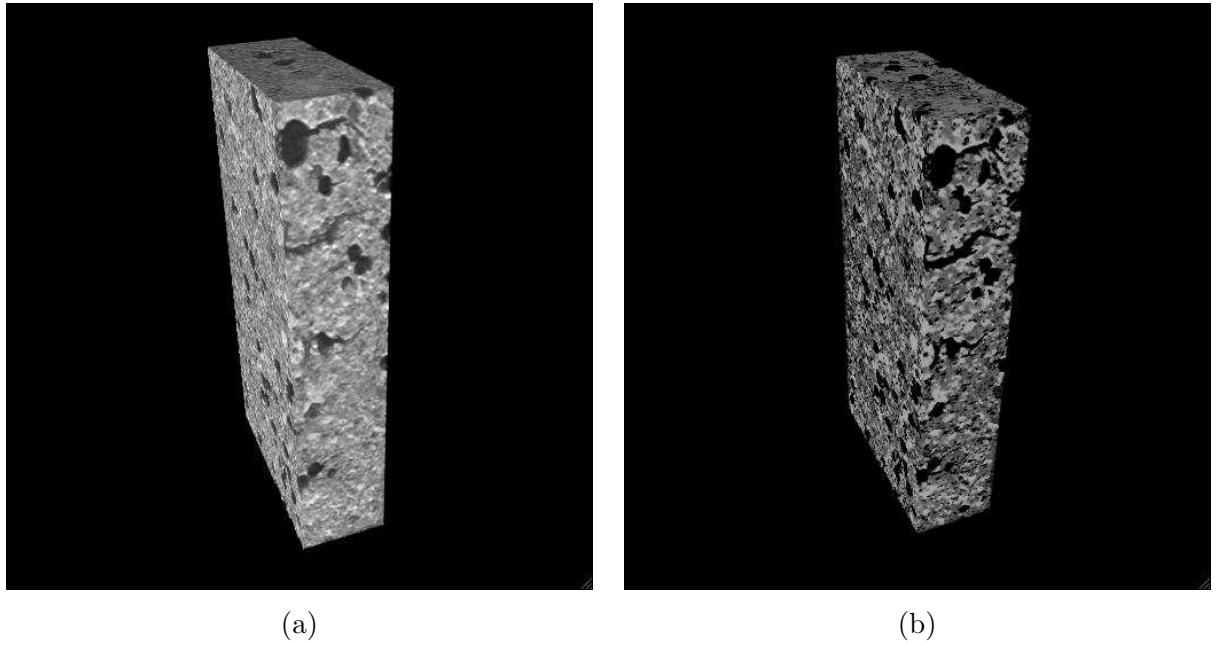


**Figure V.37** : Identification of the three phases of the central membrane in 3D: in (a) the volume obtained by X-ray microtomography and in (b) the same volume after image processing.

**Table V.3** : Comparison between the volume fraction of each phase in the sample and in the processed image. (\* estimated by B.S.E.-S.E.M. images)

	sample	processed image	difference
porosity (vol.%)	40 *	23.6	-59%
$\text{BaCe}_{0.85}\text{Y}_{0.15}\text{O}_{3-\delta}$ (vol.%)	24	31.9	+33%
$\text{Ce}_{0.85}\text{Y}_{0.15}\text{O}_{2-\delta}$ (vol.%)	36	44.5	+23.6%
<i>BCY15/YDC15</i>	0.67	0.72	+8%

developed by C. Peyrega for the software MorphM during his PhD thesis at the Center of Morphologic Mathematics from Ecole Nationale Supérieure des Mines de Paris [82].

### V.6.1 Percolation

Percolation is the ability of a fluid to flow through a porous structure. In the central membrane of an IDEAL-Cell, the percolations of the each of the three phases are very important for the cell's performance. It is clear that the porosity must percolate towards the exterior of the cell, so that when water is created, the central membrane has the ability to evacuate it. If the central membrane's porosity doesn't percolate, the water created will remain inside the structure. Water concentration, a product of the reaction, will increase and the driving force for its formation will decrease keeping the cell from working. The percolation of the each ceramic material is also important because it determines the ability of each ion to reach the active reaction sites, the triple phase boundaries. Through morphologic image analysis, we can determine the percentage of each phase that belongs to a percolating path in a given direction.

The algorithm used to determine percolation applies geodesic propagations into the studied media in the forward and backward directions using a sphere as a structural element. Only the paths that reach the opposite face of the volume in both directions are extracted, as illustrated in figure V.38.

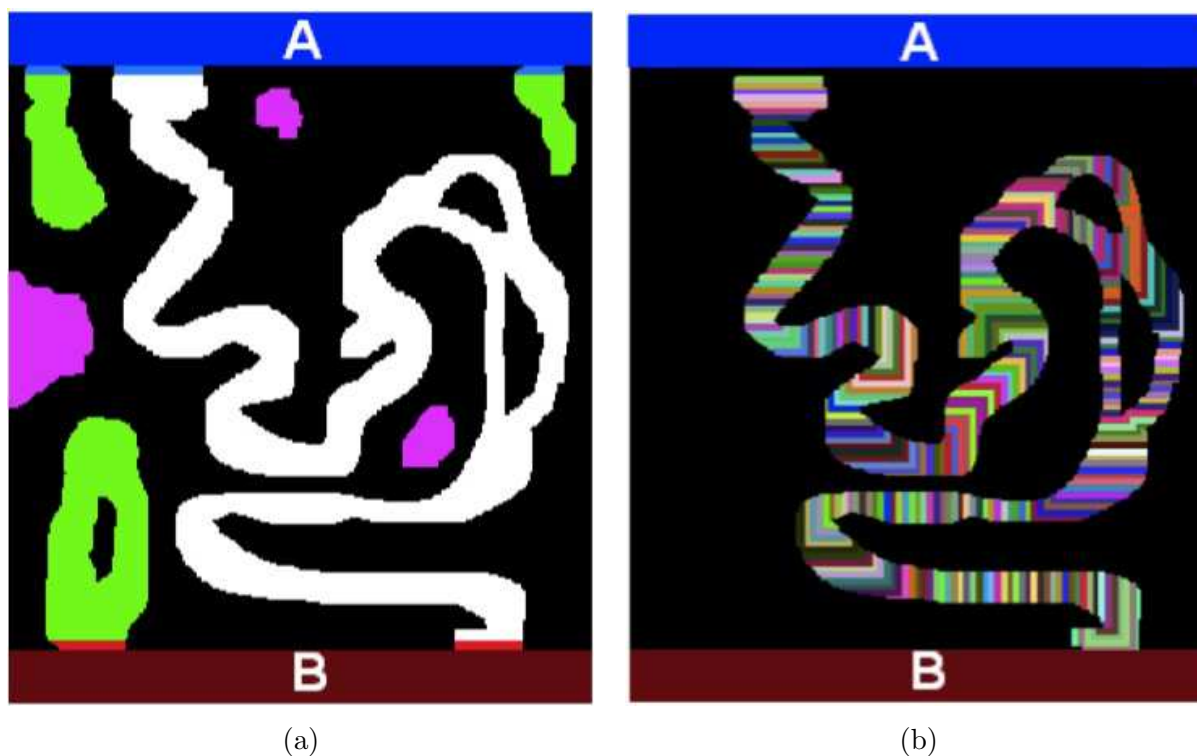


**Figure V.38** : Illustration of the algorithm used to determine the percolation of the medium shown in white, green and purple in (a). In (b) the only percolating path from A to B (source: C. Peyrega PhD thesis).

Using this algorithm, the percolation rate of each phase was determined in the three directions. The percolation rate is the percentage of the a given phase that belongs to a percolating path that connects two opposite faces in a certain direction. The three phases

are highly percolating, as shown in table V.4.

**Table V.4** : Percolation rate of each phase in the central membrane.

direction	BaCe <sub>0.85</sub> Y <sub>0.15</sub> O <sub>3-δ</sub>	Ce <sub>0.85</sub> Y <sub>0.15</sub> O <sub>2-δ</sub>	porosity
O <sub>x</sub>	97.8%	99.3%	85.0%
O <sub>y</sub>	97.0%	98.3%	84.5%
O <sub>z</sub>	97.6%	99.0%	84.9%

Thus, in any of the three directions, over 84% of the porous phase is connected to the opposite phase. This means that the water created in the membrane has a high probability of finding a path that allows it to be evacuated. The percolation ratios are even higher for the ion conducting phases: between 97% and 99% of the ceramic materials belong to percolating paths. This means that the ions can be conducted in almost the whole of the ceramic structure. These results are very encouraging concerning the central membrane performance.

### V.6.2 Tortuosity

A high percolation rate is important, it translates the possibility of a fluid or an ion to be transported between two extremities of a medium. However, the percolation rate doesn't contain any information about the length of the path traversed before reaching the end. Two structures with the same percolation rate can have very different abilities to evacuate water, for example. Imagine a medium in which the percolating paths length are very close to the shortest possible distance between the start and the end of that path. This structure can evacuate water more easily than another structure in which the percolating paths are two or three times longer than the shortest distance between the beginning and the end of the path. The shortest distance of a path, belonging to a medium X, that connects two points A and B, is called euclidean distance. The length of any given path belonging to the medium X connecting the same points A and B is called geodesic distance. The tortuosity ( $\tau$ ) of that path is given by the ratio of the geodesic to euclidean distances (equation V.6) and is a measure of the deviation of a path's length to its shortest possible value in a given medium.

$$\tau_{xAB} = \frac{\text{geodesic distance}_{xAB}}{\text{euclidean distance}_{xAB}} \quad (\text{V.6})$$

It's a morphologic parameter that has an influence on the central membrane performance and that has been taken into account in the model developed by Bessler *et al.* to describe the behavior IDEAL-Cell [70]. The model takes into account the kinetics of water formation, charge and mass transport in order to predict activation, ohmic and concentration polarizations in the cell. Charge transportation is described by Ohm law (equation V.7) in which the ion flow,  $\nabla N_{x,xCp}$  is a function of the effective conductivity of each of the ion conducting phases ( $\sigma_{xCp}^{eff}$ ) and its potential ( $\nabla \Phi_{xcp}$ ).

$$\nabla N_{x,xCp} = \frac{\sigma_{xCp}^{eff}}{2F} \nabla \Phi_{xcp} \quad (\text{V.7})$$

The effective conductivity of the ion conductors is determined from the materials bulk conductivities taking into account the porosity of the membrane ( $\epsilon$ ) and the tortuosity ( $\tau$ ) of the conducting paths (equation V.8).

$$\sigma_{xCp}^{eff} = \frac{\epsilon}{\tau} \sigma \quad (\text{V.8})$$

These same parameters are also important in the mass transport. Water flow in a porous media can be given by the Darcy's law (equation V.9) as a function of the water partial pressure gradient ( $\Delta P_w$ ) and the permeability of the structure, (B).

$$N_w = -\frac{P_w}{RT} \frac{B}{\mu} \Delta P_w \quad (\text{V.9})$$

If we consider that the central membrane is constituted of single size spherical particles closely and randomly packed, permeability can be given by the Blake-Kozeny empirical equation V.10 and porosity ( $\epsilon$ ), tortuosity ( $\tau$ ) and the diameter of the spherical particles ( $d_p$ ) play an important role.

$$B = \frac{d_p^2}{72\tau} \frac{\epsilon^3}{(1-\epsilon)^2} \quad (\text{V.10})$$

The lowest tortuosity of a path is thus 1 and the longer that path to connect two points is, the highest its tortuosity will be. The algorithm used does not determine the tortuosity of a structure or path but an histogram of tortuosities of an image. Thus, for each value of tortuosity  $\tau$ , it's determined how many pixels, in the percolating medium, belong to a path with that value of tortuosity [82]. Thus, the histograms of the tortuosities of each phase were determined and are here shown in figure V.39(a), (b) and (c).

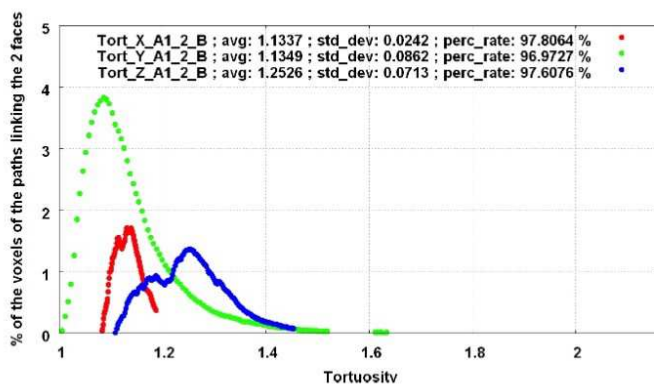
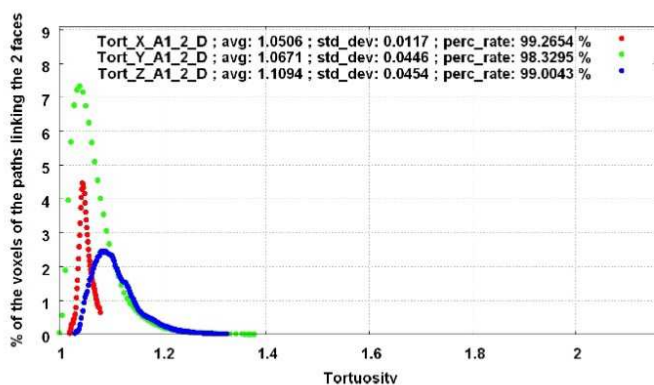
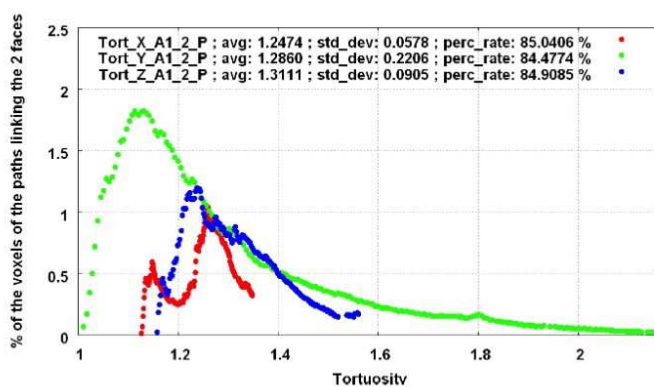
The tortuosities change slightly with the direction which indicates a small anisotropy of the structure. Most of the voxels belong to percolating paths with tortuosities between 1 and 1.4 which is very close to the corresponding euclidean distance. These results indicate that the central membrane has straight paths that allow an easy circulation of the ions through the central membrane and an easy evacuation of water from the central membrane towards the exterior of the cell.

### V.6.3 Active triple phase boundaries

The reaction in the central membrane takes place where the species involved - ions and water - can co-exist. These places are very similar to the reaction sites in SOFC electrodes, the so-called triple phase boundaries (TPBs), where a gas is diffused through the structure and reacts to produce ions and electrons that are, each of them, conducted by a different material. The case of the central membrane of an IDEAL-Cell is similar because the reaction takes place where the protons meet the oxygen ions that must be in contact with the porosity to allow the evacuation of the water created. We will also call these reaction sites triple phase boundaries. Not all of the TPBs can generate water continuously and keep the potential of the cell. Each ion conducting material must percolate towards its corresponding electrolyte to create a continuous path for the ions and the porosity must percolate towards the exhaust pipe to assure that the concentration of water is low in the membrane and the reaction is favorable. Thus, the active reaction sites in the central membrane are where the proton conducting material is in contact with the oxygen ion conducting material and with the porosity but also in which each of the ion conducting material percolates towards the corresponding electrolyte and the porosity percolates towards the exterior of the cell. A central membrane with high concentration of active triple phase boundaries will have higher performances. For this reason it is important to determine the active TPBs in a sample to improve the fabrication procedure.

This can be done using the processed 3D images obtained by X-ray microtomography, using image processing operations and the notion of percolation, explained before.

A sequence of image processing operations was determined to extract the triple phase boundaries without any notion of percolation. The first step is to dilate the binary images of the  $\text{Ce}_{0.85}\text{Y}_{0.15}\text{O}_{2-\delta}$  phase and of the  $\text{BaCe}_{0.85}\text{Y}_{0.15}\text{O}_{3-\delta}$ , using a cube of size 1 as structural

(a)  $\text{BaCe}_{0.85}\text{Y}_{0.15}\text{O}_{3-\delta}$  phase(b)  $\text{Ce}_{0.85}\text{Y}_{0.15}\text{O}_{2-\delta}$ 

(c) Porosity phase

**Figure V.39** : Histograms of the tortuosities of each phase of the central membrane. The tortuosities determined in the Ox direction are in red, in green in the Oy direction and in blue for the Oz direction.

element. Then each phase original binary image was subtracted to its dilated image. We obtain a binary image of the voxels that are in the neighborhood of each ceramic phase. Two images are thus obtained: one of the neighboring voxels of  $\text{Ce}_{0.85}\text{Y}_{0.15}\text{O}_{2-\delta}$  that belong to either  $\text{BaCe}_{0.85}\text{Y}_{0.15}\text{O}_{3-\delta}$  or to the porosity; and another image of the neighboring voxels  $\text{BaCe}_{0.85}\text{Y}_{0.15}\text{O}_{3-\delta}$  that thus belong to  $\text{Ce}_{0.85}\text{Y}_{0.15}\text{O}_{2-\delta}$  and to the porosity. However only the voxels that belong to the porosity are interesting to us. In order to distinguish which voxels in the neighborhood of ceramic material belong to the porosity and not to the other ceramic material, we use an image, such as figure V.37(b), in which each phase has a different grey level. Then we intersect, for example, the image of the neighboring voxels of  $\text{BaCe}_{0.85}\text{Y}_{0.15}\text{O}_{3-\delta}$  with the grey level image and we obtain the same voxels but with grey level of the corresponding phase. In order to obtain the voxels of the  $\text{BaCe}_{0.85}\text{Y}_{0.15}\text{O}_{3-\delta}$  neighborhood that belong to the porosity, a threshold at the porosity grey level (which is zero) is applied. The same sequence of operations is applied to the  $\text{Ce}_{0.85}\text{Y}_{0.15}\text{O}_{2-\delta}$  neighborhood image is done and we obtain the voxels of each ceramic material that belong only to the porosity. The triple phase boundaries are the voxels that belong to the porosity and are in the neighborhood of both  $\text{BaCe}_{0.85}\text{Y}_{0.15}\text{O}_{3-\delta}$  and  $\text{Ce}_{0.85}\text{Y}_{0.15}\text{O}_{2-\delta}$ . The triple phase boundaries are therefore the voxels resulting of the intersection of the two last images obtained. The total triple phase boundaries are shown in white in the figure V.40.

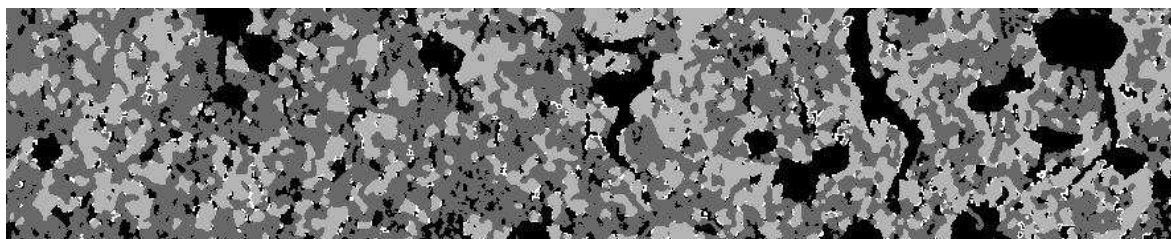


**Figure V.40** : 2D image of the central membrane in which the  $\text{BaCe}_{0.85}\text{Y}_{0.15}\text{O}_{3-\delta}$  phase is in light grey, the  $\text{Ce}_{0.85}\text{Y}_{0.15}\text{O}_{2-\delta}$  phase is in dark grey, the porosity is in black and the triple phase boundaries are in white.

In order to obtain the active triple phase boundaries, it is necessary to take into account the percolation of each phase in a given direction. The directions considered for the sample orientation are shown in figure V.41.

It was considered that the oxygen ion electrolyte was in the negative part of the Oy axis, i.e. below the central membrane. Therefore, the proton conducting electrolyte is above the central membrane at  $y=\delta y$ , considering that the membrane has a thickness of  $\delta y$ . Thus,  $\text{Ce}_{0.85}\text{Y}_{0.15}\text{O}_{2-\delta}$ , the oxygen ion conducting phase in dark grey in figure V.41 must percolate in the direction  $y=0 \rightarrow y=\delta y$  in order to allow the ions to be conducted from the electrolyte to the bulk of the central membrane structure. For the same reasons, the proton conducting phase, in light grey in figure V.41, must percolate from  $y=\delta y \rightarrow y=0$ . Porosity must allow the evacuation of water towards the exterior of the cell, thus, this phase must percolate in the Ox or Oz directions.

The voxels of the  $\text{BaCe}_{0.85}\text{Y}_{0.15}\text{O}_{3-\delta}$  phase that percolate in the  $y=0 \rightarrow y=\delta y$  direction are determined by a geodesic propagation. This consists in determining the percolation as it was done in V.6.1 but only in one direction. The voxels that don't belong to a percolating path that allow the conduction of protons from the electrolyte to the bulk of the central membrane are excluded. For the  $\text{Ce}_{0.85}\text{Y}_{0.15}\text{O}_{2-\delta}$  phase, the percolation is determined in the same way but in the  $y=\delta \rightarrow y=0$  direction. The percolating fraction of porosity was determined by geodesic propagations in the Ox and Oz directions. The total percolating

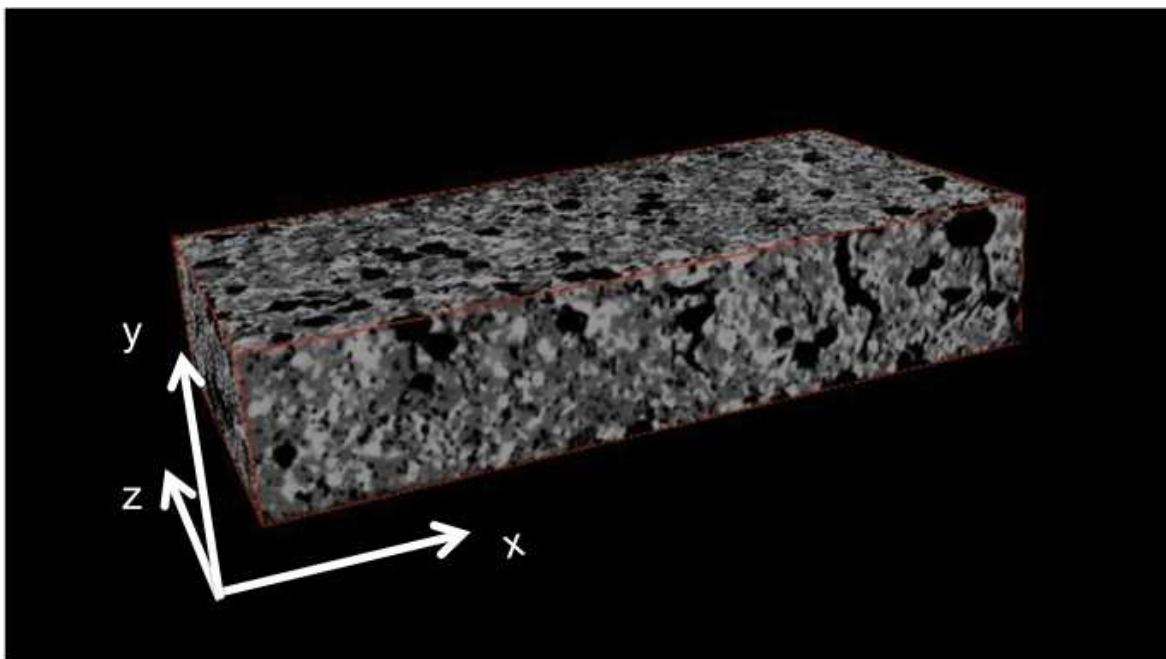


**Figure V.41** : 3D representation of the central membrane volume with the axis showing the directions considered in the percolation analysis.

porosity is the union, or the sum, of the two resulting images of the geodesic propagations in the two directions.

Three binary images were obtained: the porosity that percolates in the Ox and Oz directions, the  $\text{BaCe}_{0.85}\text{Y}_{0.15}\text{O}_{3-\delta}$  phase that percolates from  $y=0$  to  $y=\delta y$  and the  $\text{Ce}_{0.85}\text{Y}_{0.15}\text{O}_{2-\delta}$  phase that percolates from  $y=\delta y$  to  $y=0$ . In order to determine where these phases are in contact, the dilatation of each image was obtained using a cube of size one as structuring element. The intersection of the three images yields the voxels that are at the same time in the neighborhood of the three percolating phases. From these voxels, those that belong to total triple phase boundaries determined before, are the active triple phase boundaries. Thus the intersection of the image with the voxels in the neighborhood of the three percolating phases with the image of the total triple phase boundaries gives us the image of the active triple phase boundaries.

A detail of the central membrane 3D image with the three phases and the active triple phase boundaries identified is shown in figure V.42.

The image with the voxels that represent the active triple phase boundaries can be used to determine their length and density in the sample, since it is known that each voxels has a volume of  $0.28 \times 0.28 \times 0.28 \mu\text{m}^3$ . This sample has an active triple phase boundaries density of  $278 \text{ m/mm}^3$ , which represent 57.3% of the total triple phase boundaries.

## V.7 Discussion

In this chapter, a method based images obtained experimentally of the central membrane is proposed to determine the active triple phase boundaries. The limitations of the methods based on random structures were discussed. Although some of these methods can take into account different powder particle size distributions, they never translate the influence of

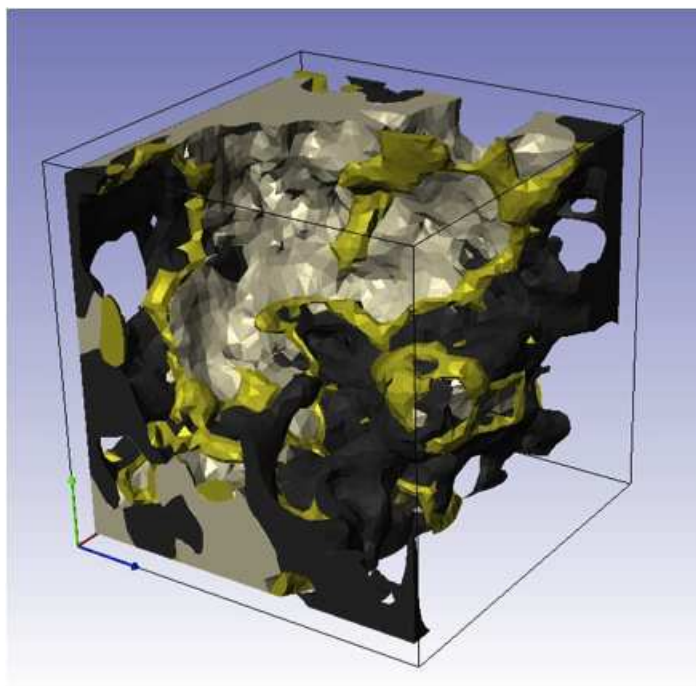


**Figure V.42** : Detail of the central membrane in 3D:  $\text{BaCe}_{0.85}\text{Y}_{0.15}\text{O}_{3-\delta}$  phase is in light grey,  $\text{Ce}_{0.85}\text{Y}_{0.15}\text{O}_{2-\delta}$  phase is in dark grey, the active triple phase boundaries are in yellow and the porosity is invisible.

the shaping technique in the layers morphology. A study based on images of a real SOFC anode was here shown. These images, obtained by F.I.B.-S.E.M., allows obtaining a volume of  $6 \times 5 \times 4 \mu\text{m}$  which is not representative of the sample. Thus it is very likely that the percolation of the phases is very easily reached in such a small volume. The authors obtained an active triple phase boundary density of  $2696 \text{ m}/\text{mm}^3$  that is probably overestimated.

The 3D images of the central membrane were obtained by X-ray microtomography. The sample was a  $\text{BaCe}_{0.85}\text{Y}_{0.15}\text{O}_{3-\delta} / \text{Ce}_{0.85}\text{Y}_{0.15}\text{O}_{2-\delta}$  composite. The porosity in the membrane was obtained by the use of corn starch as pore former. The experimental conditions such as the sample dimensions and the beam energy were optimized to obtain the best image quality and the best contrast between the two ceramic materials. An image processing algorithm was developed to identify each of the materials and the porosity in the membrane. Since the porosity was filled with an epoxy resin, this phase was very easily segmented from the original image. The segmentation of the two ceramics is the sensitive step of this procedure. If their very similar chemical composition is an advantage for the fuel cell performance stability because it avoids the diffusion of different chemical elements, their similar X-ray absorption make their image in the radiograph very similar and hard to distinguish. The fact that the powders particle size ( $\simeq 1 \mu\text{m}$ ) before sintering is very close to the image resolution ( $0.28 \mu\text{m}/\text{pixel}$ ) also makes the image segmentation a difficult task. As it was shown before, the histogram of the ceramic phase is a single continuous lump, therefore, there may be zones where the grey level of the materials are superposed.

The algorithm developed to extract the three phases of the image was accurate for this sample. The porosity obtained was lower than the expected one by the S.E.M.-B.S.E. image analysis. Since the contrast between porosity and ceramic phase is satisfying, the value obtained through the X-ray image is more accurate because a much more representative

volume of the sample is taken into account. The  $\text{BaCe}_{0.85}\text{Y}_{0.15}\text{O}_{3-\delta}$  to  $\text{Ce}_{0.85}\text{Y}_{0.15}\text{O}_{2-\delta}$  ratio was 8% higher than what was expected from the sample fabrication parameters. Therefore the  $\text{BaCe}_{0.85}\text{Y}_{0.15}\text{O}_{3-\delta}$  phase is overestimated in the processed image.

Using image processing operations and morphologic analysis, it was possible to determine parameters that are important to predict the central membrane and the IDEAL-Cell performances. It was determined that in average 98% of each ceramic phase percolates in the three directions of the volume. On the other hand around 85% of the porous phase percolates in the three directions of the sample. These are very high percolation rates of all the phases which indicates that this shaping procedure yields structures with good morphologies for the application. The histograms of tortuosities of each phase were also obtained. It was determined that, for each phase, most of the voxels belonged to paths with a tortuosity between 1 and 1.4. This low values of tortuosity show that the conduction of ions in the ceramics and the transport of water in the porosity are done in the central membrane through straight paths. This is another indicator of the good quality of the microstructures.

With the three phases segmented in a processed image, the active triple phase boundaries length of the central membrane was determined. It was found that the sample had an active triple phase boundary density of  $278 \text{ m/mm}^3$ . This value is about 10 times smaller than the one obtained by R. Wilson *et al.* in his study. There are different reasons for this. The materials used in the two studies are not the same and different powder morphologies yield different microstructures. R. Wilson studied an SOFC anode and therefore different criteria were used to determine the active triple phase boundaries. The most important fact is that we studied a  $248 \times 40 \times 124 \mu\text{m}^3$  which is  $10^4$  times bigger than the one studied by R. Wilson *et al.* Thus the sample volume here studied is more representative of the complete sample. It is likely that some of the paths found to be percolating by R. Wilson *et al.* will not be in volume 2 times bigger and that has a strong influence on the determination of the active triple phase boundaries.

## V.8 Conclusions

The morphology of a composite ceramic central membrane of an IDEAL Cell was studied through images obtained by X-ray microtomography. The images obtained represented  $248 \times 40 \times 124 \mu\text{m}^3$  of the sample. The three phases of sample were accurately identified using an algorithm of image process operations. The percolation rates and the tortuosities of the three phases were determined using morphologic image analysis. The ceramic phases had percolation rates over 97% whereas the porosity had a percolation rate of 85%. The three percolating phases had tortuosities between 1 and 1.4. The active triple phase boundaries density was determined. This sample had  $278 \text{ m/mm}^3$  of active triple phase boundaries.

This method allows the optimization of the shaping procedure to obtain microstructures with the best percolation rates, tortuosities and higher density of triple phase boundaries. It also allows studying a representative volume of the sample which is not the case of the, to our knowledge, only experimental-based method developed to this date. The method requires the use of a synchrotron due to the high resolution of the images required. Therefore, it is a technique that cannot be used nowadays routinely in a laboratory.

---

Les résultats de la modélisation électrochimique d'une cellule complète ont permis de montrer que la membrane centrale est le composant limitant de ce nouveau concept et que, contrairement aux dispositifs classiques (SOFC et PCFC), les électrodes ont des résistances de polarisation négligeables. Un des paramètres morphologiques qui impacte fortement les performances de la cellule est la densité de sites réactionnels de la membrane centrale. Dans ce chapitre une méthode analytique est proposée pour quantifier ce paramètre. Des images 3D représentatives de la membrane centrale ont été enregistrées par microtomographie RX à partir de monocouches obtenues par coulage en bande puis frittage. Des séquences de traitements d'image (seuillage, segmentation, etc.) ont rendu possible l'identification des trois phases constitutives, le conducteur protonique, le conducteur anionique et la porosité. En considérant la percolation de chacune des phases solides avec les électrolytes respectifs ainsi que celle de la porosité avec le milieu extérieur, la longueur des segments triples a pu être déterminées. L'échantillon présenté dans ce chapitre présente une densité de points triples de 278 m/mm<sup>3</sup>.

---



---

## Chapter -VI-

# Study of water evacuation in the central membrane

---

### Contents

---

<b>VI.1</b>	<b>Introduction . . . . .</b>	<b>140</b>
<b>VI.2</b>	<b>Experimental Procedure . . . . .</b>	<b>140</b>
<b>VI.3</b>	<b>Description of the samples . . . . .</b>	<b>141</b>
<b>VI.4</b>	<b>Model . . . . .</b>	<b>143</b>
	VI.4.1 Momentum transfer . . . . .	143
	VI.4.2 Mass Transfer . . . . .	146
<b>VI.5</b>	<b>Evaluation of the water evacuation . . . . .</b>	<b>148</b>
	VI.5.1 Problem . . . . .	148
	VI.5.2 Velocity Field . . . . .	150
	VI.5.3 Water evacuation . . . . .	152
	VI.5.4 Influence of the mesh density . . . . .	152
	VI.5.5 Influence of the pores shape . . . . .	155
	VI.5.6 Study of the samples anisotropy . . . . .	156
<b>VI.6</b>	<b>Discussion . . . . .</b>	<b>160</b>
<b>VI.7</b>	<b>Conclusions . . . . .</b>	<b>161</b>

---

## VI.1 Introduction

In the previous chapter, a method that allowed quantifying the active triple phase boundaries density of an IDEAL-Cell central membrane has been developed. Based on 3D images obtained by X-ray microtomography, this method measures the membrane's ability to allow the formation of water in the active triple phase boundaries. The function of the central membrane is not only the production of water but also its evacuation. It was seen in the previous chapter that the porosity of the central membrane has a percolation rate of about 85%, which indicates a good ability of the structure to evacuate water.

In this chapter, a method is proposed to quantify the ability of a porous membrane to evacuate water. The method can be used in order to adjust the shaping procedure. In the previous chapter two types of central membranes were produced: in chapter II the central membrane's porosity was created using graphite whereas in chapter V the pores were created introducing corn starch in the tape casting slurry. The pores created by the two pore formers are very different: they are small ( $\simeq 1\mu\text{m}$ ) without a particular shape for graphite and larger ( $\simeq 10\mu\text{m}$ ) and round-shaped for corn starch, as it can be seen in figure VI.1.

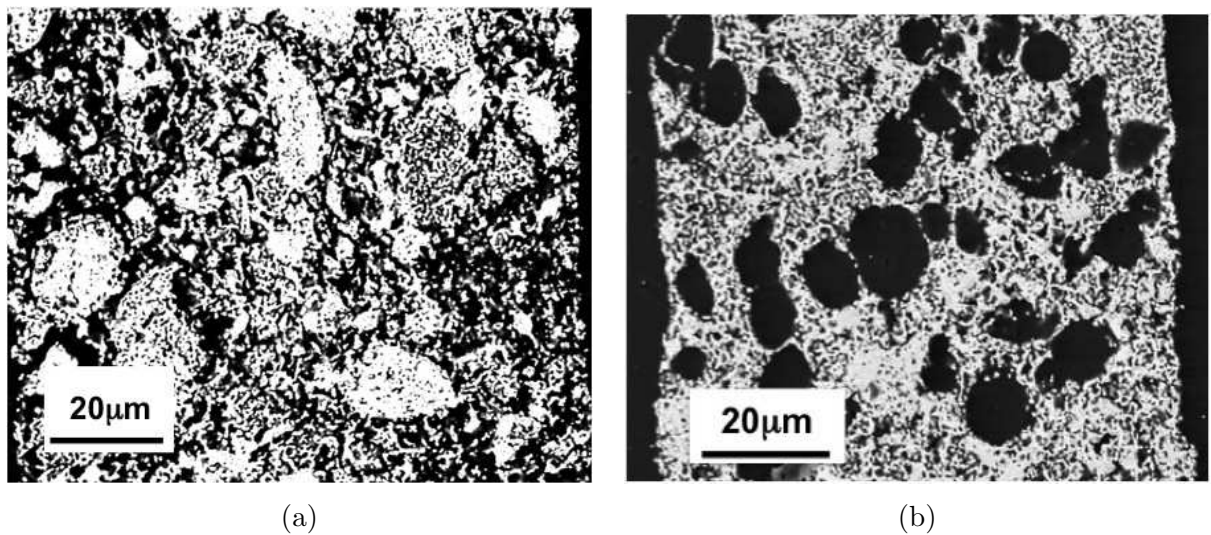


**Figure VI.1** : S.E.M. images of the central membrane using graphite (a) and corn starch (b) as pore former.

The objective is to use 3D images of these porous networks obtained by X-ray microtomography of two samples with the same porosity volume but different pore shapes and compare their ability to evacuate water solving fluid mechanics equations by the finite elements method.

## VI.2 Experimental Procedure

The samples studied were ceramic composite central membranes produced by tape casting and sintering. In one of the samples, the pore former used was graphite whereas in the other sample it was corn starch. In order to control the porosity in the central membrane using graphite as pore former, a calibration of the tape casting slurry was carried out. The sintering cycle used was optimized in chapter II and is shown in figure II.28. The samples in which corn starch was used as pore former were sintered according to the temperature cycle shown

in figure V.12. The calibration of the tape casting slurry composition using corn starch as pore former was carried out in chapter V.

The porosity in the central membranes after sintering was estimated through B.S.E.-S.E.M. images using the method described in part V.3. A relation between the graphite volume in the tape casting slurry and the porosity in the central membrane was found, as seen in figure VI.2.

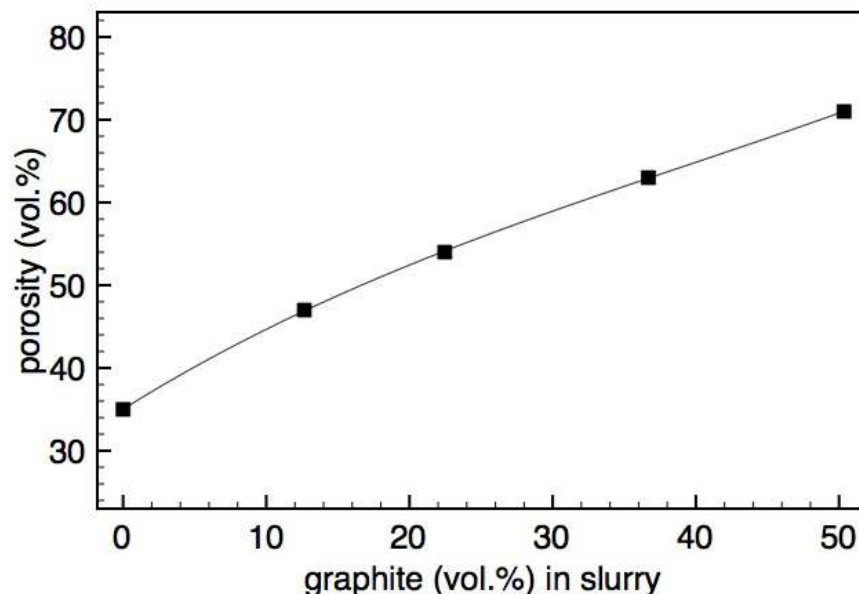


**Figure VI.2** : Final porosity in the central membrane estimated by analysis of B.S.E.-S.E.M. images using graphite as pore former.

The sintered samples, in which graphite and corn starch were used as pore formers, were put in an epoxy resin and then polished and cut to the X-ray microtomography required dimensions. This procedure was explained in V.3.

X-ray microtomography images were obtained using the same experimental conditions of the sample analyzed in chapter V.

### VI.3 Description of the samples

Ten samples were analyzed by X-ray microtomography: five in which corn starch was used as pore former and five in which the pores were created by the combustion of graphite. Since the objective is to study the flow of a fluid in the porosity of the central membrane, the porous phase was extracted using the method described in part V.5.1.

Amongst the samples obtained, one of each type was chosen to be studied. Both samples had a similar pore volume percentage - about 40% - and their tape casting slurry composition is gathered in table VI.2.

The samples had a volume of  $264 \times 17 \times 11 \mu\text{m}^3$  and  $280 \times 90 \times 140 \mu\text{m}^3$  and a porosity of 40% and 39%, as shown in table VI.2.

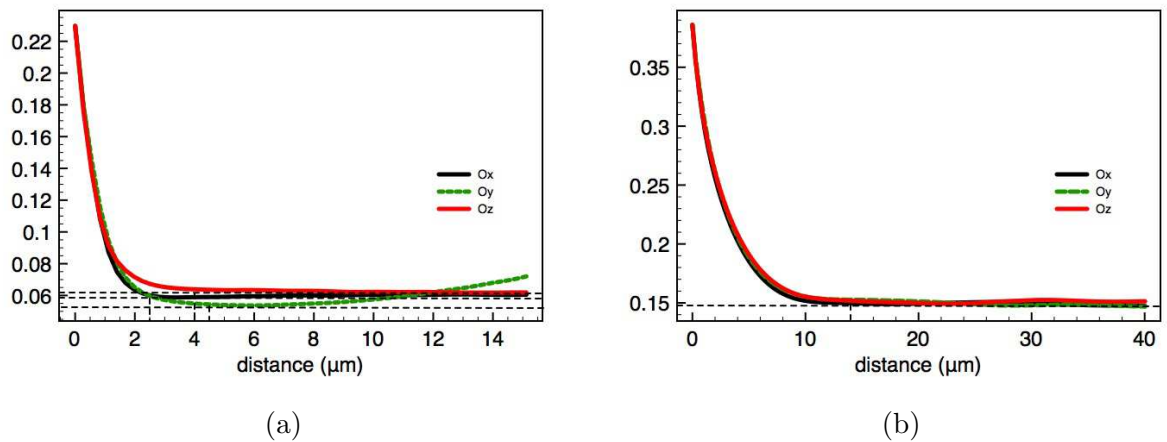
In order to take into account the scale of the microstructures, the covariances of the 3D images were plotted in different directions. The covariances change with direction of observation of the material, as it can be seen in figure VI.3(a) and (b).

**Table VI.1** : Tape casting slurry composition of the samples analyzed.

	sample A	sample B	short name
$\text{BaCe}_{0.85}\text{Y}_{0.15}\text{O}_{3-\alpha}$	2.72 g	4.07 g	BCY15
$\text{Ce}_{0.85}\text{Y}_{0.15}\text{O}_{2-\alpha}$	3.00 g	3.00 g	YDC15
poly(vinyl butyral)	1.40 g	1.40 g	PVB
poly(ethylene glycol)	0.40 g	0.40 g	PEG
ethanol	5.50 g	5.50 g	-
graphite	0.17 g	- g	-
corn starch	-	1.41 g	-

**Table VI.2** : Properties of the samples studied.

	sample A	sample B
pore former	graphite	corn starch
dimensions (pixels)	$944 \times 60 \times 40$	$998 \times 351 \times 500$
dimensions ( $\mu\text{m}$ )	$264 \times 17 \times 11$	$280 \times 98 \times 140$
porosity vol. %	40	39

**Figure VI.3** : Covariance diagram and covariance range for the porous phases of sample A (a) and sample B (b) in the directions Ox, Oy and Oz.

They reach an asymptotic value for a finite range, which measures the scale of the microstructures. The covariance range was determined for different directions and the results are shown in fig:VI.3. The maximum covariance ranges found were  $8 \mu\text{m}$  for sample A and  $15 \mu\text{m}$  for sample B. The large round-shaped pores of sample B lead to a larger covariance range.

**Table VI.3** : Covariance ranges in different different directions for samples A and B.

direction	sample A	sample B
x	2.5	14
y	4	14
z	4.5	14
zy $x\pi/4$	5	12
zy $x3\pi/8$	5	14
zy $x\pi/8$	<b>8</b>	14
xz $y\pi/4$	6	12
xz $y3\pi/8$	6	14
xy $z\pi/8$	5	12
xy $z\pi/4$	5	12
xy $z3\pi/8$	5	<b>15</b>
zy $x\pi/8$	<b>8</b>	13

## VI.4 Model

The evacuation of water in the central membrane porosity was simulated using momentum and mass transfer equations.

### VI.4.1 Momentum transfer

The net rate at which mass enters a control volume seen in (inflow - outflow), figure VI.4, must equal zero. The mass flow that enters and leaves the control volume is due to gross fluid motion. This mechanism is called advection. The rate at which mass enters the control volume through the surface perpendicular to  $x$  is given by  $(\rho u) dy$ , where  $\rho$  is the total density and  $u$  is the  $x$  component of the mass average velocity [83].

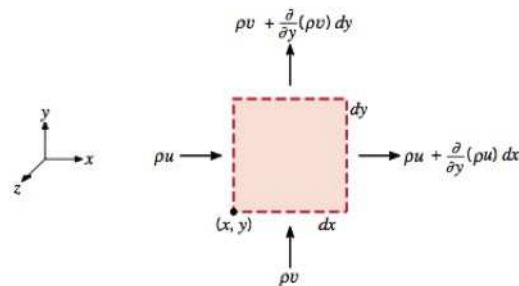


**Figure VI.4** : Differential control volume for mass conservation.

The mass flow at  $x + dx$ , the exit of the control volume, may be given by:

$$\left[ (\rho u) + \frac{(\delta u)}{\delta x} dx \right] dy$$

taking into account that  $\rho$  and  $u$  may vary with  $x$ . Using a similar result for the  $y$  direction, the mass conservation condition is given by:

$$(\rho u) dy + (\rho v) dx - \left[ \rho u + \frac{\delta(\rho u) dx}{\delta x} \right] dy - \left[ \rho v + \frac{\delta(\rho v) dy}{\delta y} \right] dx = 0$$

Canceling the terms and dividing by  $dx$ ,  $dy$  and  $dz$ , we obtain equation VI.1.

$$\frac{\delta(\rho u)}{\delta x} + \frac{\delta(\rho v)}{\delta y} = 0 \quad (\text{VI.1})$$

Since it was considered that the fluid is incompressible, the density  $\rho$  is constant and the continuity equation becomes equation VI.2.

$$\frac{\delta u}{\delta x} + \frac{\delta v}{\delta y} = 0 \quad (\text{VI.2})$$

For the forces acting on the control volume, the sum of all the forces must equal the net rate at which momentum leaves the control volume (outflow - inflow). Surface forces,  $F_s$ , that are proportional to the area, are due to the fluid static pressure as well as viscous stresses. The viscous stresses have two components, the normal stress ( $\sigma_{ii}$ ) and the shear stress ( $\tau_{ij}$ ), as shown in figure VI.5. The first subscript used to specify the stress components indicates the outward normal of the surface orientation and the second subscript indicates the direction of the force component.

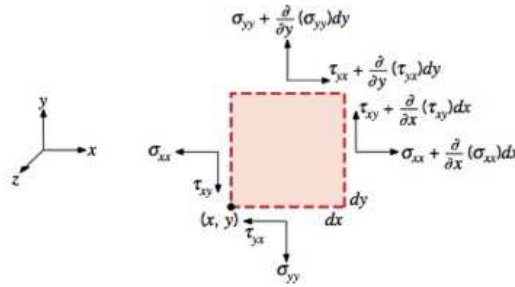


**Figure VI.5** : Normal and shear viscous stresses for a differential control volume.

The forces associated to the viscous stresses act between adjoining fluid elements and are a consequence of the fluid motion and viscosity. These stresses would vanish if the fluid velocity gradient was zero. The net surface forces - the fluid static pressure and the viscous stresses - are given by figure VI.3 and VI.4.

$$F_{s,x} = \left( \frac{\delta \sigma_{xx}}{\delta x} - \frac{\delta p}{\delta x} + \frac{\delta \tau_{yx}}{\delta y} \right) dx dy \quad (\text{VI.3})$$

$$F_{s,y} = \left( \frac{\delta \tau_{xy}}{\delta x} + \frac{\delta \sigma_{yy}}{\delta y} - \frac{\delta p}{\delta y} \right) dx dy \quad (\text{VI.4})$$

The fluid momentum fluxes must also be evaluated. In the direction  $x$ , the fluxes are shown in figure VI.6. The mass flow through the  $x$  surface, in the  $y - z$  plane, is  $(\rho u)$  and the corresponding  $x$ -momentum flux is  $(\rho u)u$ . Similarly, the  $x$ -momentum flux due to mass flow through the  $y$  surface, in the  $x - z$  plane, is  $(\rho v)u$ .

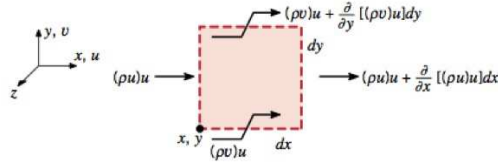


**Figure VI.6** : Momentum fluxes for a differential control volume.

The net rate at which  $x$  momentum leaves the control volume is given by:

$$\frac{\delta[(\rho u)u]}{\delta x} dx (dy) + \frac{\delta[(\rho v)u]}{\delta y} dy (dx)$$

The rate of change in the  $x$  momentum of the fluid is equal to the sum of the forces in the  $x$  direction. We obtain the equation VI.5.

$$\frac{\delta[(\rho u)u]}{\delta x} + \frac{\delta[(\rho v)u]}{\delta y} = \frac{\delta \sigma_{xx}}{\delta x} - \frac{\delta p}{\delta x} + \frac{\delta \tau_{yx}}{\delta y} \tag{VI.5}$$

Expanding the left-hand side derivatives, we obtain equation VI.6.

$$\rho \left( u \frac{\delta u}{\delta x} + v \frac{\delta u}{\delta y} \right) = \frac{\delta}{\delta x} (\sigma_{xx} - p) + \frac{\delta \tau_{yx}}{\delta y} \tag{VI.6}$$

The same equation is obtained for the  $y$  direction, as seen in equation VI.7.

$$\rho \left( u \frac{\delta v}{\delta x} + v \frac{\delta v}{\delta y} \right) = \frac{\delta \tau_{xy}}{\delta x} + \frac{\delta}{\delta y} (\sigma_{yy} - p) \tag{VI.7}$$

The terms on the right-hand side of equations VI.6 and VI.7 account for the viscous and pressure forces and the terms in the left-hand side represent the rate of momentum flow from the control volume.

The viscous stresses,  $\sigma_{ii}$  and  $\tau_{ij}$ , may be expressed as a function of flow variables. In figure VI.7, it is shown that normal stress,  $\sigma_{ii}$ , produces a linear deformation of the fluid, whereas shear stress,  $\tau_{ij}$ , produces an angular deformation. The magnitude of a stress is proportional to the rate at which the deformation occurs.

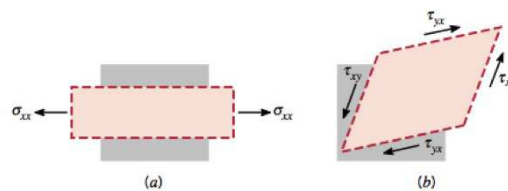


**Figure VI.7** : Deformations of a fluid due to viscous (a) and shear (b) stresses.

The deformation rate depends on the viscosity and the velocity gradient of the flow. For a newtonian fluid, the stresses are proportional to the velocity gradient being the viscosity the proportionality constant. Schlichting showed that the stresses can be given as function of viscosity and velocity gradients by equations VI.8, VI.9 and VI.10 [84].

$$\sigma_{xx} = 2\mu \frac{\delta u}{\delta x} - \frac{2}{3}\mu \left( \frac{\delta u}{\delta x} + \frac{\delta v}{\delta y} \right) \quad (\text{VI.8})$$

$$\sigma_{yy} = 2\mu \frac{\delta v}{\delta y} - \frac{2}{3}\mu \left( \frac{\delta u}{\delta x} + \frac{\delta v}{\delta y} \right) \quad (\text{VI.9})$$

$$\tau_{xy} = \tau_{yx} = \mu \left( \frac{\delta u}{\delta y} + \frac{\delta v}{\delta x} \right) \quad (\text{VI.10})$$

Substituting equations VI.8 to VI.10 in equations VI.6 and VI.7, the momentum equations become VI.11 for  $x$  and VI.12 for  $y$ .

$$\rho \left( u \frac{\delta u}{\delta x} + v \frac{\delta u}{\delta y} \right) = -\frac{\delta p}{\delta x} + \frac{\delta}{\delta x} \left\{ \mu \left[ 2 \frac{\delta u}{\delta x} - \frac{2}{3} \left( \frac{\delta u}{\delta x} + \frac{\delta v}{\delta y} \right) \right] \right\} + \frac{\delta}{\delta y} \left[ \mu \left( \frac{\delta u}{\delta y} + \frac{\delta v}{\delta x} \right) \right] \quad (\text{VI.11})$$

$$\rho \left( u \frac{\delta v}{\delta x} + v \frac{\delta v}{\delta y} \right) = -\frac{\delta p}{\delta y} + \frac{\delta}{\delta y} \left\{ \mu \left[ 2 \frac{\delta v}{\delta y} - \frac{2}{3} \left( \frac{\delta u}{\delta x} + \frac{\delta v}{\delta y} \right) \right] \right\} + \frac{\delta}{\delta x} \left[ \mu \left( \frac{\delta u}{\delta y} + \frac{\delta v}{\delta x} \right) \right] \quad (\text{VI.12})$$

Solving equations VI.1, VI.11 and VI.12, a representation of the two-dimensional velocity field can be obtained. A three-dimensional velocity field may be obtained applying the same equations to the  $z$  direction.

#### VI.4.2 Mass Transfer

As it is shown in the control volume in figure VI.8, mass transfer may occur by advection (with the mean velocity of the mixture) and by diffusion (relative to the mean motion) in each of the coordinate directions [83].

The species conservation principle requires that the net rate at which species A enters the control volume due to advection in the direction  $x$  is given by equation VI.13.

$$\begin{aligned} \dot{M}_{A,adv,x} - \dot{M}_{A,adv,x+dx} &= (\rho_A u) dy - \left[ (\rho_A u) + \frac{\delta(\rho_A u)}{\delta x} dx \right] dy \\ &= -\frac{\delta(\rho_A u)}{\delta x} dx dy \end{aligned} \quad (\text{VI.13})$$

The flow of species A by diffusion can be given by Fick's Law, equation VI.14.

$$N_A'' = D_{AB} \frac{\delta \rho_A}{\delta x} \quad (\text{VI.14})$$

If we consider the flow of an incompressible fluid (constant  $\rho$ ), the net rate at which species A enter the control volume by diffusion in the  $x$  direction is given by equation VI.15.

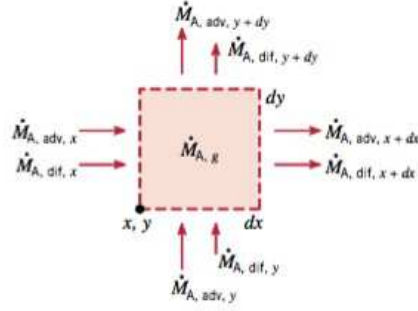


**Figure VI.8** : Differential control volume for species conservation.

$$\begin{aligned} \dot{M}_{A,dif,x} - \dot{M}_{A,dif,x+dx} &= \left( -D_{AB} \frac{\delta \rho_A}{\delta x} \right) dy & (VI.15) \\ &- \left[ \left( -D_{AB} \frac{\delta \rho_A}{\delta x} \right) + \frac{\delta}{\delta x} \left( -D_{AB} \frac{\delta \rho_A}{\delta x} \right) dx \right] dy = \frac{\delta}{\delta x} \left( D_{AB} \frac{\delta \rho_A}{\delta x} \right) dx dy \end{aligned}$$

Equations VI.13 and VI.15 may also be obtained for directions  $y$ .

Thus, considering the control volume represented in figure VI.8, if we consider the principle of the species conservation, we obtain equation VI.16.

$$\begin{aligned} \dot{M}_{A,adv,x} - \dot{M}_{A,adv,x+\delta x} + \dot{M}_{A,adv,y} - \dot{M}_{A,adv,y+\delta y} & & (VI.16) \\ + \dot{M}_{A,dif,x} - \dot{M}_{A,dif,x+\delta x} + \dot{M}_{A,dif,y} - \dot{M}_{A,dif,y+\delta y} + \dot{M}_{A,g} &= 0 \end{aligned}$$

where  $\dot{M}_{A,g}$  is the mass of A generated in the control volume that will be considered zero.

Substituting the equations VI.13 and VI.15 and their equivalent for the  $y$  direction in equation VI.16, we have equation VI.17.

$$\frac{\delta(\rho_A u)}{\delta x} + \frac{\delta(\rho_A v)}{\delta y} = \frac{\delta}{\delta x} \left( D_{AB} \frac{\delta \rho_A}{\delta x} \right) + \frac{\delta}{\delta y} \left( D_{AB} \frac{\delta \rho_A}{\delta y} \right) \quad (VI.17)$$

Developing the terms on the left-hand side, substituting from the overall continuity equation VI.1 and considering that the total density  $\rho$  is constant, equation VI.17 is transformed into equation VI.18.

$$u \frac{\delta(\rho_A)}{\delta x} + v \frac{\delta(\rho_A)}{\delta y} = \frac{\delta}{\delta x} \left( D_{AB} \frac{\delta \rho_A}{\delta x} \right) + \frac{\delta}{\delta y} \left( D_{AB} \frac{\delta \rho_A}{\delta y} \right) \quad (VI.18)$$

This equation may be expressed in its molar form by equation VI.19.

$$u \frac{\delta(C_A)}{\delta x} + v \frac{\delta(C_A)}{\delta y} = \frac{\delta}{\delta x} \left( D_{AB} \frac{\delta C_A}{\delta x} \right) + \frac{\delta}{\delta y} \left( D_{AB} \frac{\delta C_A}{\delta y} \right) \quad (VI.19)$$

In this equation  $u$  and  $v$  are the velocities in  $x$  and  $y$  directions, respectively, that are determined in each point of the control volume by equations VI.11 and VI.12.

## VI.5 Evaluation of the water evacuation

The equations that describe the momentum and mass fluxes were presented in the previous section. The conditions that were used to evaluate the evacuation in the central membrane will be described here.

### VI.5.1 Problem

In an IDEAL-Cell central membrane, water is created in the active triple phase boundaries, that were quantified in chapter V and then evacuated through the porosity that is connected to the exterior of each unit cell. In order to evaluate the ability of a central membrane produced by tape casting and sintering to evacuate the water vapor, only the water transportation inside the control volume was taken into account. It was considered that water is created in one boundary of the membrane and that it must cross it to the opposite side. Thus, the model used proposes a situation in which at  $t = 0$  there is only air flowing inside the central membrane. Then, water vapor is introduced in one boundary. The amount of water increases with time until it reaches, at  $t = t_0$ , the maximum concentration,  $C_0$ , according to the expression VI.20

$$C(t) = C_0 e^{-\left(\frac{t-t_0}{a}\right)^2} \quad (\text{VI.20})$$

The water concentration profile will have the generic shape shown in figure VI.9.

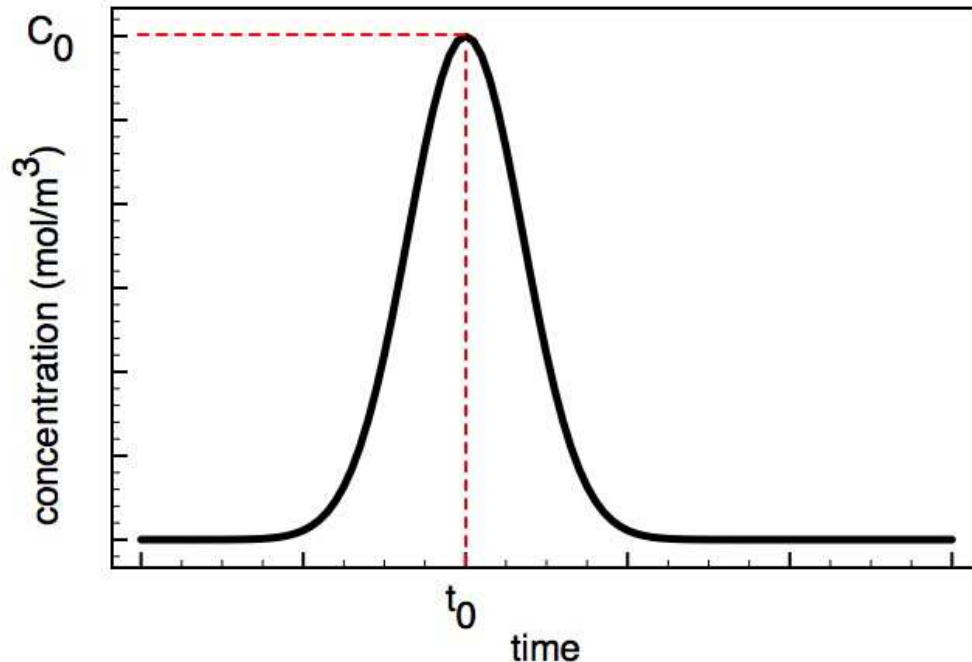


**Figure VI.9** : Water vapor concentration profile at the inlet boundary of the control volume.

In operating conditions, water is created at  $600^\circ\text{C}$ . Considering that the temperature inside the membrane is constant and homogeneous, water is created as steam. Since water's critical point is  $374^\circ\text{C}$  and 22 MPa, at  $600^\circ\text{C}$ , regardless the pressure is, water is wether a gas or a supercritical fluid for which there is no distinct liquid and gas phases (see figure VI.10).

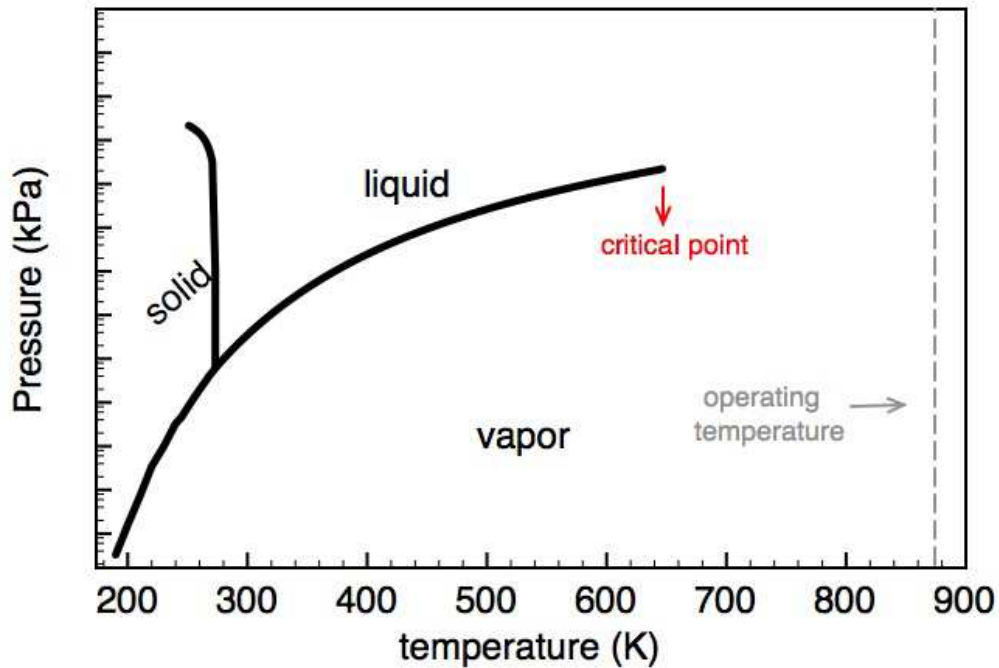


**Figure VI.10** : Water phase diagram. Water's critical temperature is below the IDEAL-Cell operating temperature.

Since physical data such as the diffusion coefficient of water in air at 600°C could not be found in the literature, it was considered that the system is at 300°C. This allowed to obtain reliable data necessary for the calculation but represents a deviation of the operating conditions of the cell. The constants used to run the model are gathered in table VI.4.

**Table VI.4** : Physical constants used in the model.

	value
density ( $\rho$ )	0.362 kg/m <sup>3</sup>
viscosity ( $\eta$ )	21.4 $\mu$ Pa.s
initial velocity ( $v_0$ )	0.001 m/s
concentration ( $C_0$ )	0.6 mol/m <sup>3</sup>
diffusion coefficient ( $D_{H_2O-air}$ )	0.873x10 <sup>-4</sup> m <sup>2</sup> /s
$t_0$ , in C(t)	40
$a$ , parameter in C(t)	10

It was considered that temperature and pressure are constant inside the membrane. Density remains constant during the flow and therefore the fluid is considered incompressible.

The momentum and mass equations were solved on 3D structures of the central membrane using the finite element method. The 3D images of the central membrane were too large to solve the calculation because they demand very large computer resources. Therefore, the volumes of the samples were chosen from the original images. The dimensions of the volumes respected the covariance ranges of each structure. Thus, the volume of sample A used has

a volume of  $8 \times 8 \times 8 \mu\text{m}^3$  and the volume of sample B has a volume of  $15 \times 15 \times 15 \mu\text{m}^3$ . The volumes extracted from the complete images had porosity volumes very similar to those of the original samples. Sample A has a porosity of 40% and the volume extracted to simulate the water flow, shown in figure VI.11(a), has a porosity of 39%. Sample B has a porosity volume of 39% and the volume used in calculations, shown in figure VI.11(b) has a porosity of 42%.

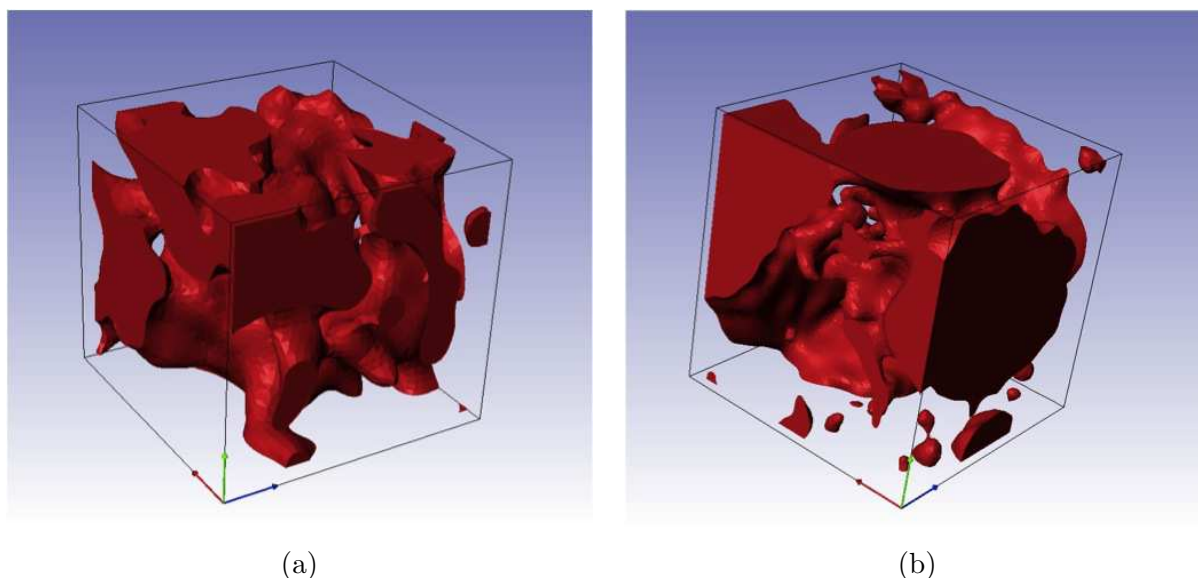


**Figure VI.11** : The volume of sample A in (a) and B in (b) used to simulate water evacuation. Volume A represents  $8 \times 8 \times 8 \mu\text{m}^3$  and volume B represents  $15 \times 15 \times 15 \mu\text{m}^3$  of the original sample.

These volumes were meshed using the software Simpleware that allows converting an image into a mesh compatible with COMSOL Multiphysics that was used to simulate the water flow. Simpleware also allows some basic morphological operations. Thus, using the filter *remove islands*, it was possible to eliminate the parts of the porosity that were isolated and therefore didn't contribute the evacuation of water. The volumes as used in the simulations are shown in figure VI.12(a) and (b).

## VI.5.2 Velocity Field

The equations that allow to obtain the velocity profile in the samples, shown in part VI.4.1, were applied in 3D using the necessary constants shown in table VI.4. These equations are available in the Incompressible navier-stokes model available of the Chemical Engineering Module. One surface of the sample was considered an entry (*inlet*) and the opposite one was considered an flow exit (*outflow*). All other boundary surfaces were considered *wall*, i.e. the velocity is zero in contact with these boundaries [85]. The velocity field obtained is shown in figure VI.13.

It is considered that velocity is zero in the fluid layer in contact with the wall surfaces. The interaction with the neighboring fluid layers depends on the shear and viscous stresses that are related with the fluid viscosity and velocity, as shown in equations VI.8, VI.9 and VI.10. Thus, the closer a fluid layer is from the membrane wall, the slower its speed will be, and that's why in the less narrow sections of the porosity the velocity is higher, as it can be seen in figure VI.13.

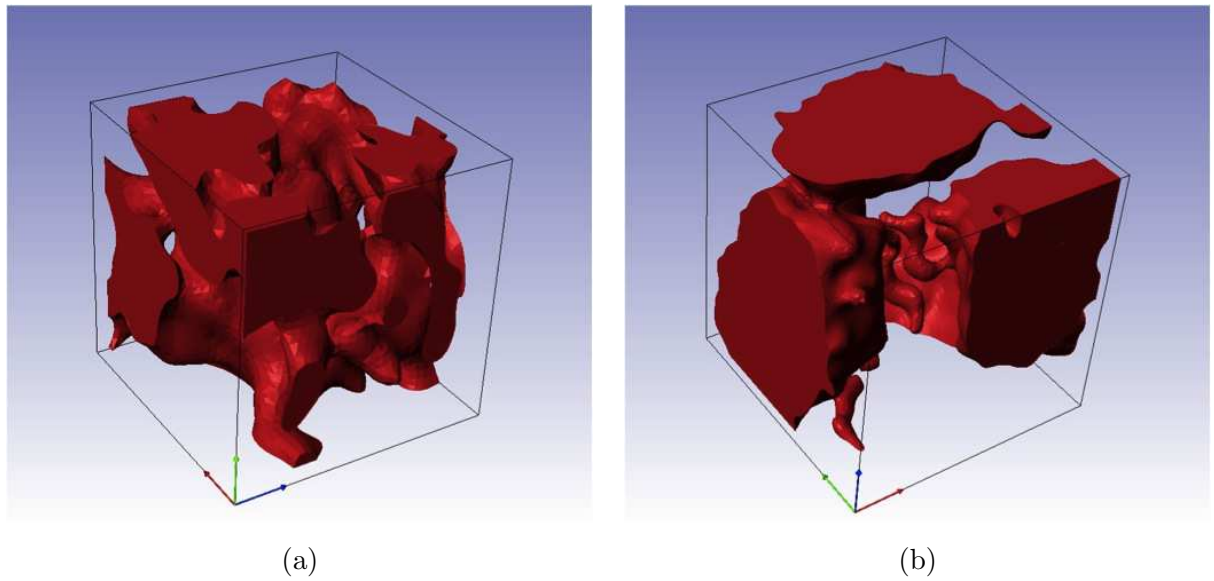


**Figure VI.12** : Volume of sample A (a) and B (b) after removing the disconnected volume fractions.

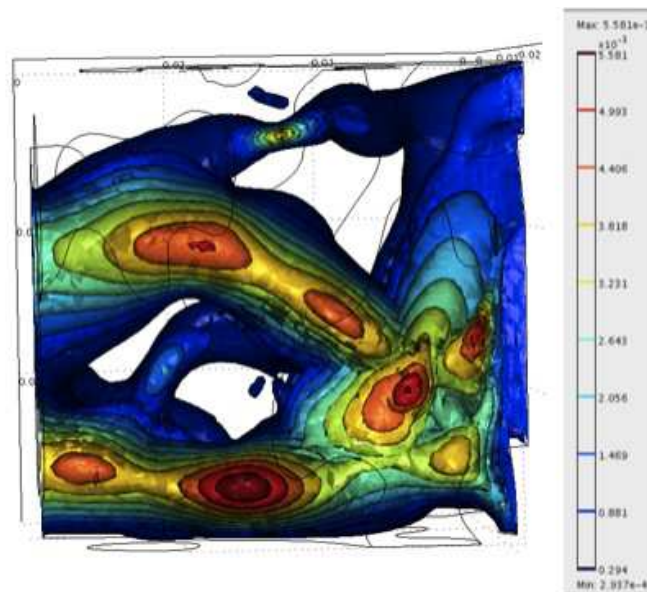


**Figure VI.13** : Velocity field obtained for sample A.

### VI.5.3 Water evacuation

Using the solution for the velocity obtained, the evolution of water concentration could be obtained. Using the inlet water concentration given by equation VI.20 and the constants in table VI.4, the equations shown in part VI.4.2 were applied in 3D through the Convection and diffusion module of the Chemical Engineering Module. The same surface previously considered a flow inlet was now considered as a *concentration* boundary, whereas the outlet boundary surface is a *convective flux* boundary. All other boundaries are considered walls and therefore don't allow the flow of matter through their surface [85].

The water concentration in the membrane as function of time is shown in figure VI.14. At  $t = 1$  s, water enters the control volume with velocity  $v_0$  through the boundary on the right-hand side. According to what was defined in the model, the fluid will cross the structure and will leave on the opposite side. Thus, the concentration in the membrane increases progressively (see  $t = 10$  s and  $t = 30$  s) until it reaches its maximum value at  $t = 40$  s in the inlet boundary, as defined by the constant  $t_0$  in the concentration,  $C(t)$ , equation VI.20. After  $t = 40$  s, water concentration decreases in the inlet boundary and so it does also in the rest of the membrane structure as water is evacuated through the outlet boundary (see  $t = 50$  s) until it reaches practically zero at  $t = 100$  s.

The water concentration profiles at inlet boundary and the average water concentration at the outlet boundary are shown in figure VI.15.

We can verify that water crosses the volume in a few seconds because the peak of concentration in the outlet boundary is just offset of a few seconds comparing to the inlet concentration peak. The shape of the of the water concentration profile at outlet is the same of the one at the inlet which means that the path between the two boundaries is very straight and doesn't retain the fluid.

### VI.5.4 Influence of the mesh density

From the 3D images of the central membrane, meshes with different densities (number of elements per volume) can be obtained using the software Simpleware. A denser mesh yields a more precise solution but with a longer calculation time. However if a mesh that is less dense allows obtaining the same result of a denser mesh, the time needed to compute a good quality solution for the problem will be shorter. Thus, the sample image was transformed into meshes with three different densities: normal, medium and coarse (see figure VI.16).

Calculations to obtain the water concentration profile at the outlet boundary surface were determined for the three different mesh densities samples. The results are shown in figure VI.17

The result is the same for the mesh densities tested. The features of each mesh and the calculation time for each solution are listed in table VI.5.

**Table VI.5** : The three meshes used and the calculation times for each of them.

mesh	n° of elements	mesh density	calculation time	
			velocity profile	water evacuation
normal	40431	79 elements/ $\mu\text{m}^3$	292 s	377 s
medium	13746	27 elements/ $\mu\text{m}^3$	100 s	129 s
coarse	3615	7 elements/ $\mu\text{m}^3$	79 s	95 s

Since the same result is obtained for the three meshes, the following calculations were carried out using a coarse mesh because it allows obtaining the results faster.

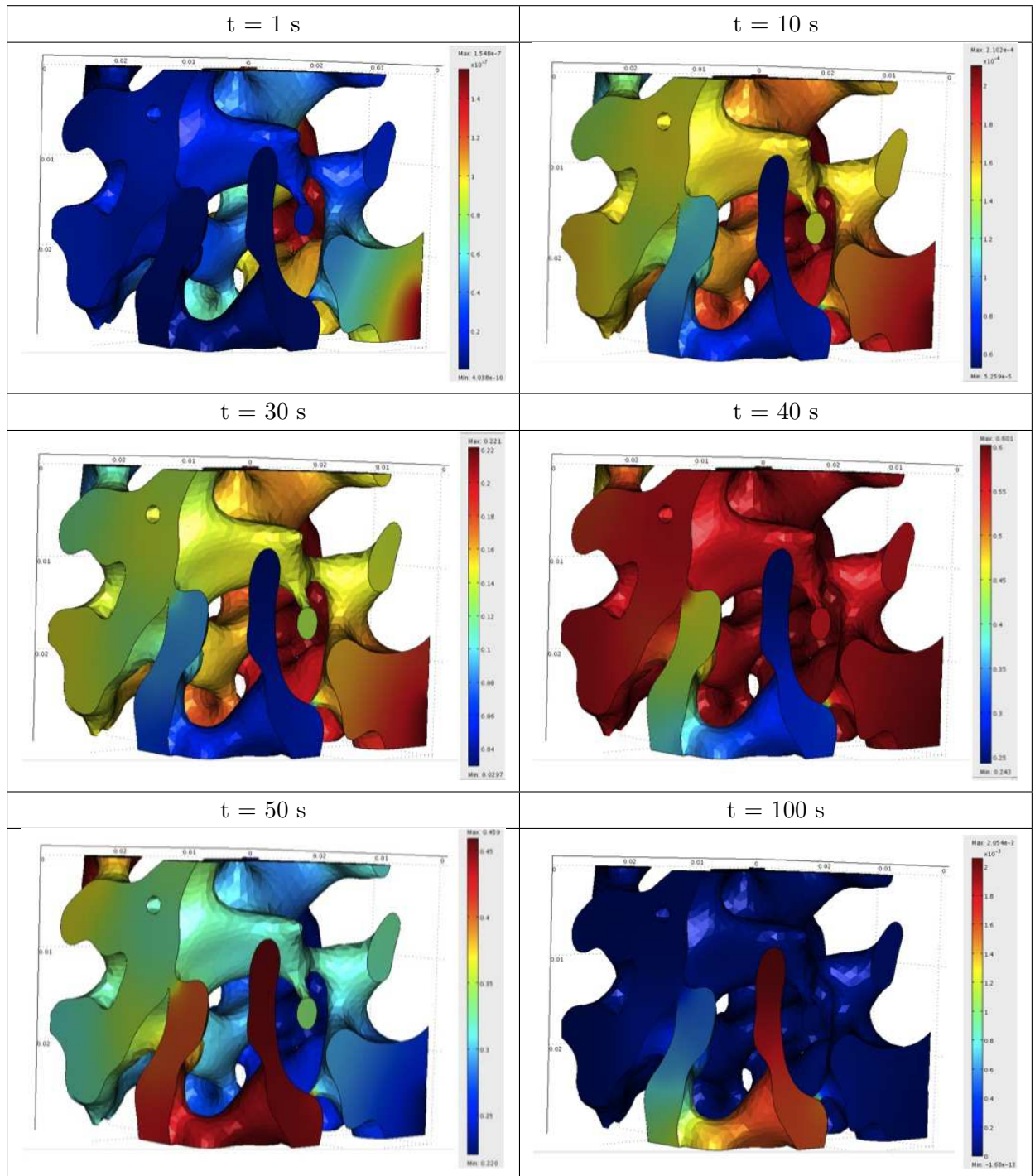


Figure VI.14 : Water concentration in sample A as function of time.

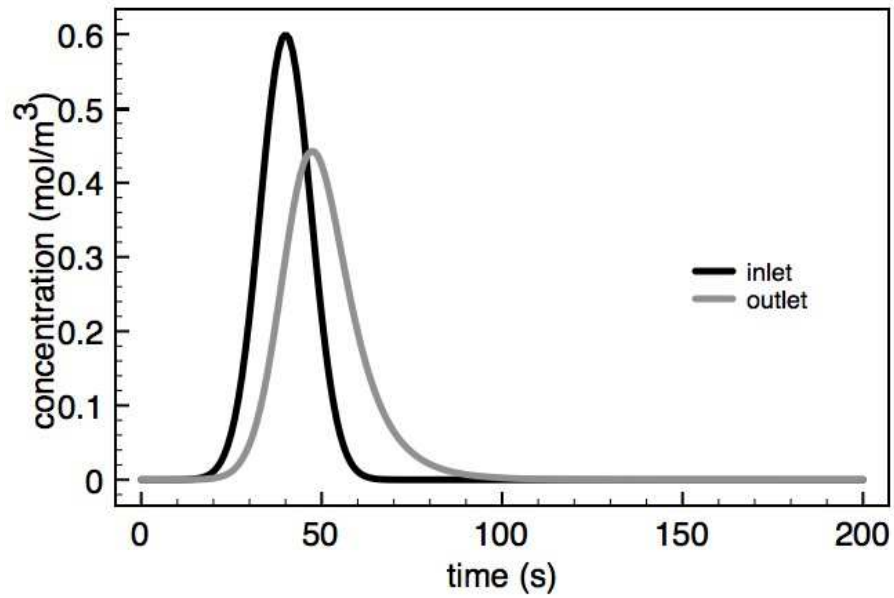


Figure VI.15 : Water concentration profile at the inlet and outlet of sample A.

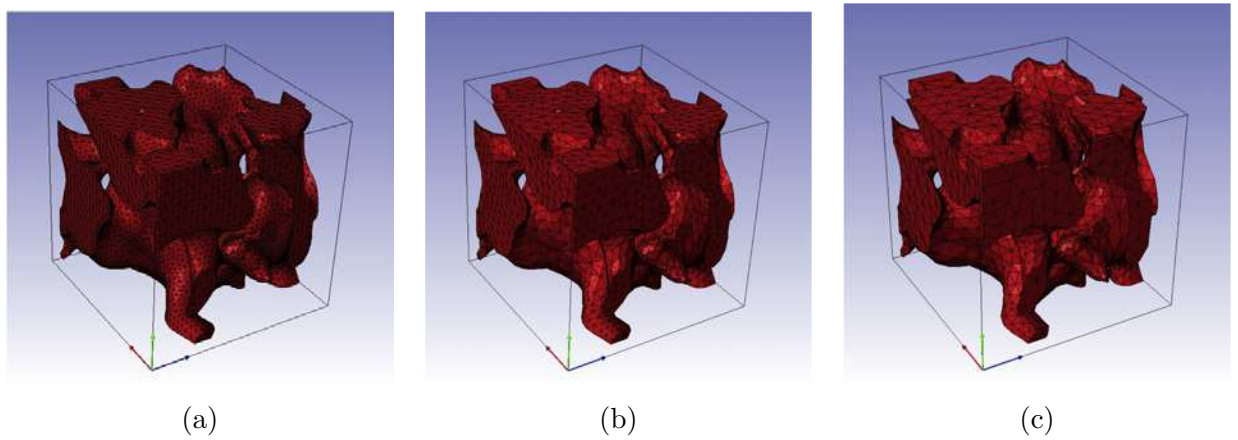
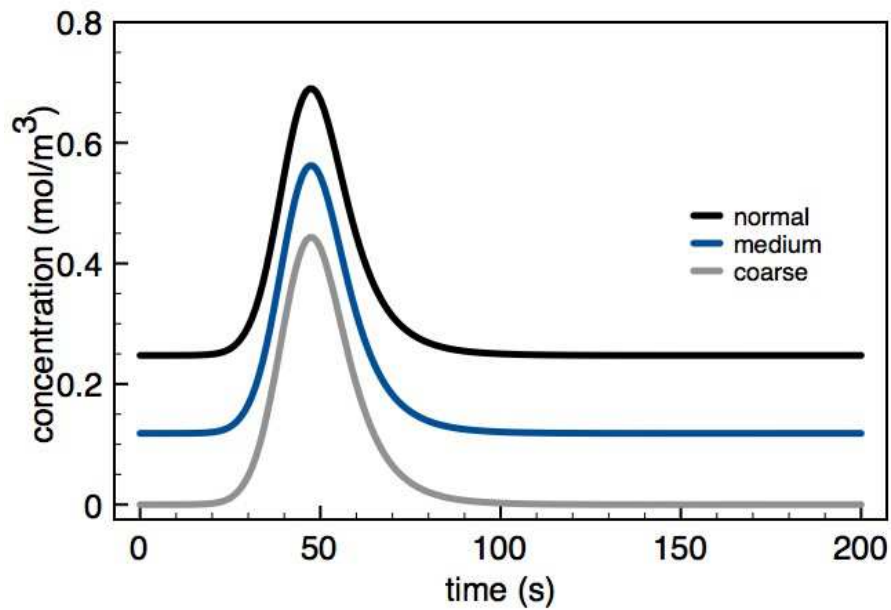


Figure VI.16 : The three mesh densities obtained: normal (a), medium (b) and coarse (c).



**Figure VI.17** : Water concentration profiles at the outlet of sample A using three different mesh densities.

### VI.5.5 Influence of the pores shape

The model developed was applied to the samples A and B, in figures VI.18(a) and (b) in order to compare the ability to evacuation of water of each type of porous structure.

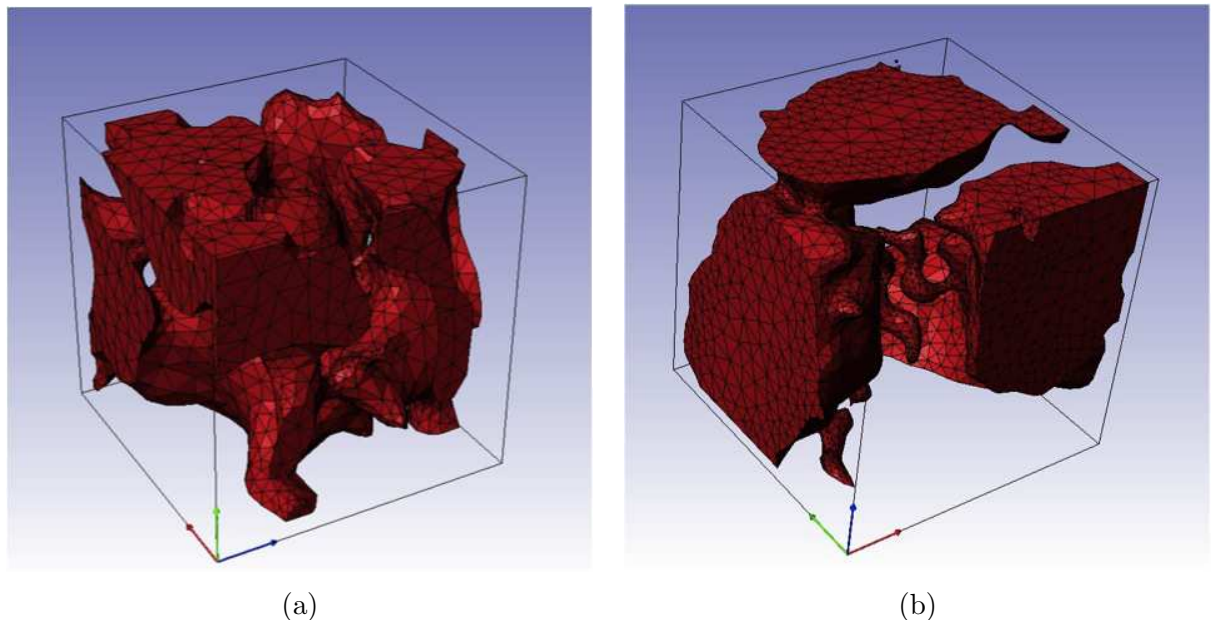


**Figure VI.18** : Water evacuation was compared in these two samples. In (a) the graphite was used as pore former whereas in (b), corn starch was used.

The velocity field obtained for sample B is shown in figure VI.19.

Using the solution for the velocity, the water concentration profile was obtained for sample B as a function of time. In figures VI.20(a) and (b), two images representing water flow in

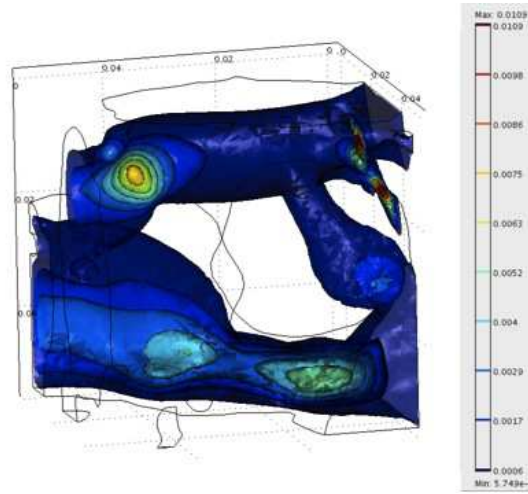


**Figure VI.19** : Velocity field in the sample B.

sample B at different times are shown. In figure VI.20(a), we can see the moment when the inlet water concentration reaches its maximum,  $C_0$ , and in figure VI.20(b), the final part of the water flow, when the concentration is higher at the outlet of the control volume.

The average water concentration at the outlet boundary was plotted as function of time, as it can be seen in figure VI.21.

Although the water concentration reaches the maximum value  $C_0$  at the inlet boundary (see figure VI.20(a)), water is diluted in the larger pores created by corn starch in the membrane and it never reaches that value at the outlet boundary. The evacuating paths also seem to be less straight, more tortuous, because the water concentration profile at the outlet has a completely different shape from the one at the inlet boundary.

### VI.5.6 Study of the samples anisotropy

In the previous sections, the ability of a membrane to evacuate water was studied by imposing an inlet surface boundary and an outlet boundary on it opposite side. It was thus considered that water was evacuated in a certain direction, let's call it  $O_x$ . All the other surfaces were considered walls through which there was no mass flow. The results obtained may depend of the flow direction considered. In order to study if the influence of the direction of the flow imposed, the same calculations of velocity field and evolution of water concentration in central membrane were carried out, imposing the inlet and the outlet boundary surfaces in the  $O_y$  and  $O_z$  directions.

These calculations were carried out for both samples A and B in the three directions. The evolution of the average water concentration in the outlet surface boundary is plotted in figure VI.22(a) and (b).

In order to compare the results obtained for the water evacuation in the two samples in the different directions, a criteria was defined. For each sample, it was determined the time  $t$  for which 95% of the water inserted in the sample was evacuated through the outlet boundary surface. The amount of water that enters the sample can be given by the inlet concentration, since it was considered that the density was constant and therefore the volume is constant. The integral of the inlet concentration function in time is thus proportional to the amount of water that enters the sample, as shown in eq.VI.21.

$$n_{in} = \int_0^t n_{in}(t) dt = V \times \int_0^t C_{in}(t) dt \quad (\text{VI.21})$$

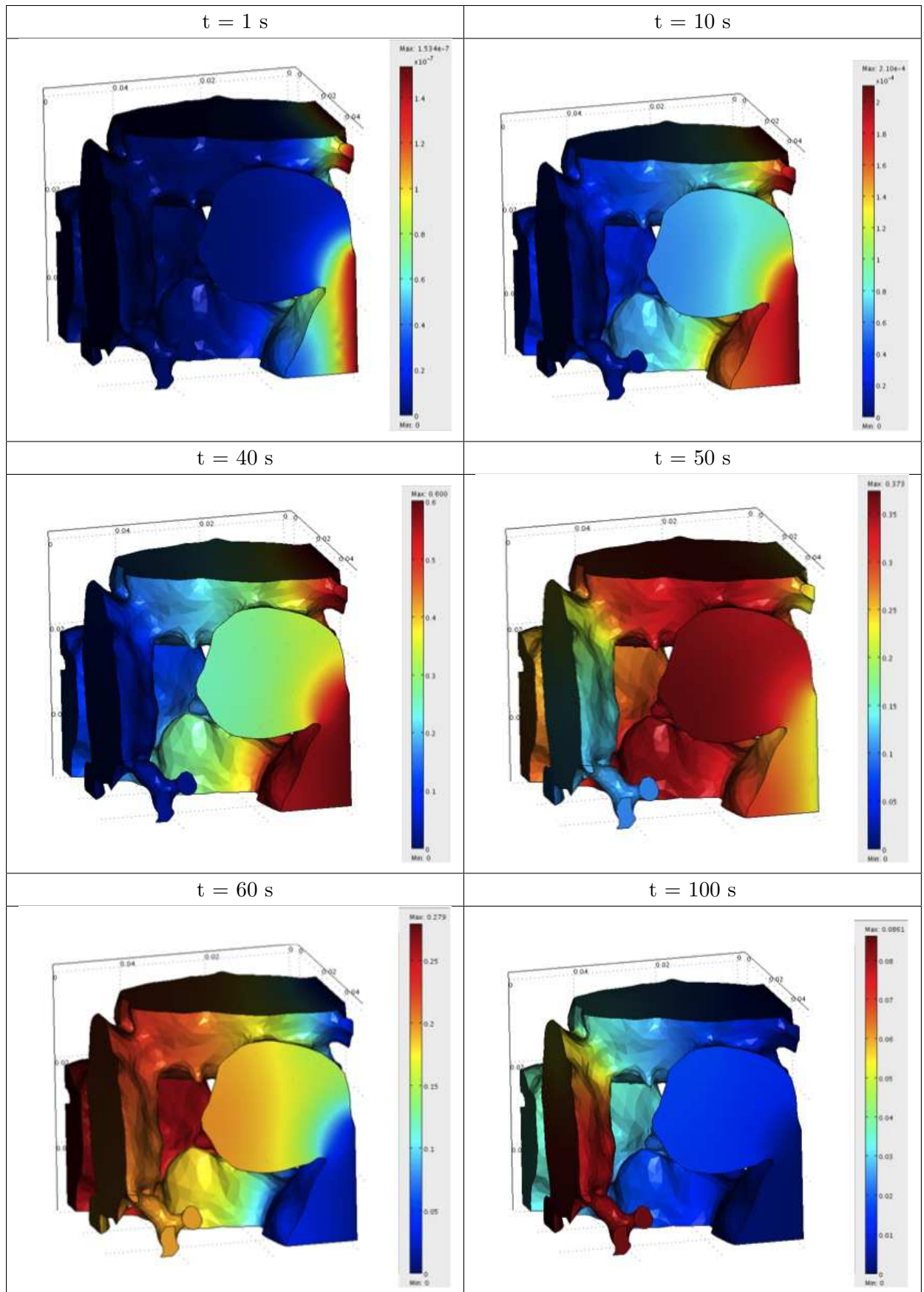
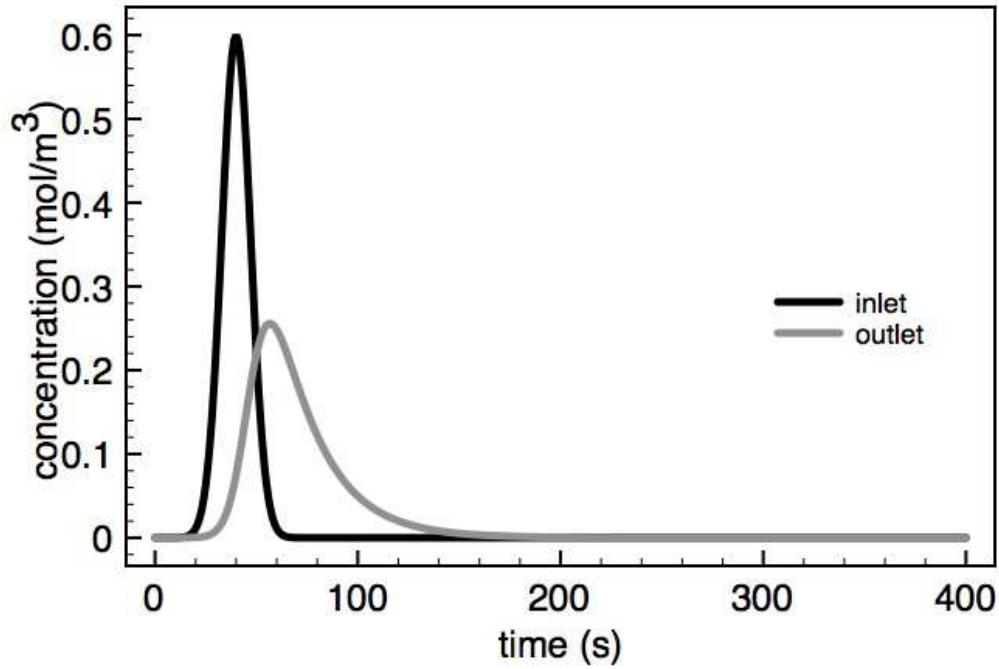


Figure VI.20 : Evacuation of water as function of time for sample B.



**Figure VI.21** : Water concentration at inlet and outlet of sample B as a function of time.

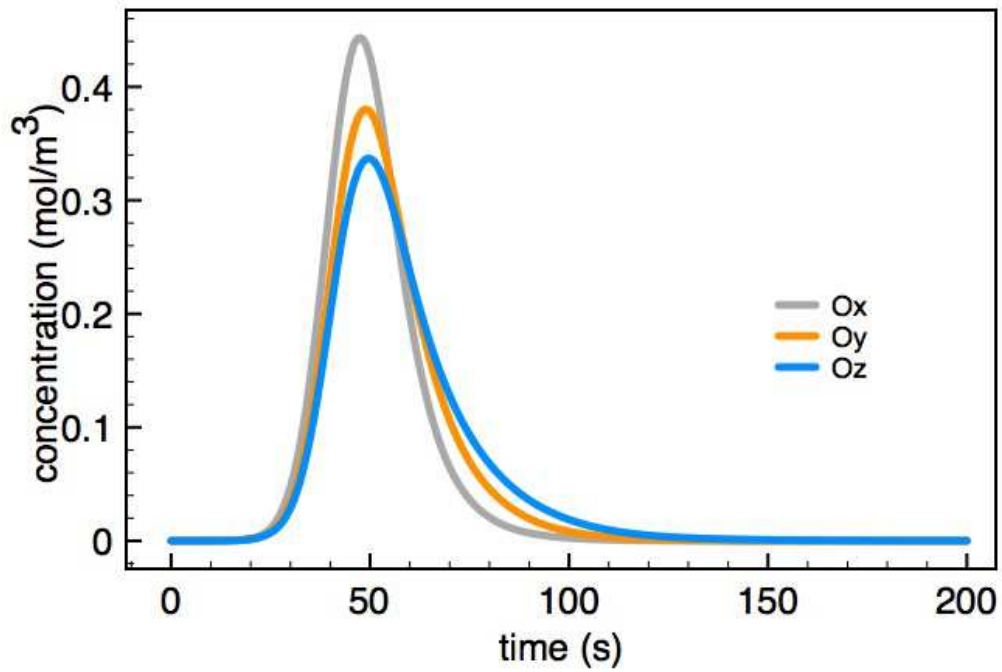
The amount of water,  $n_{out}$ , that is evacuated from the sample may be determined using an expression similar to equation VI.21 since the function of the water outlet concentration is known. Thus,  $t_{95}$ , is the time  $t$  for which 95% of the water that enters the sample, determined by equation VI.21, equals amount of water that is evacuated from the sample, determined by the integral of the outlet water concentration function, as shown in eq.VI.22. The integral of the inlet water concentration was determined from  $t=0$  to  $t=200$  because it was considered that its value remained unchanged for higher values of  $t$ , as it can be seen for example in figure VI.21.

$$t_{95} = t : 0.95 \times \int_0^{200} C_0 e^{-\left(\frac{t-40}{10}\right)^2} dt = \int_0^t C_{out}(t) dt \quad (\text{VI.22})$$

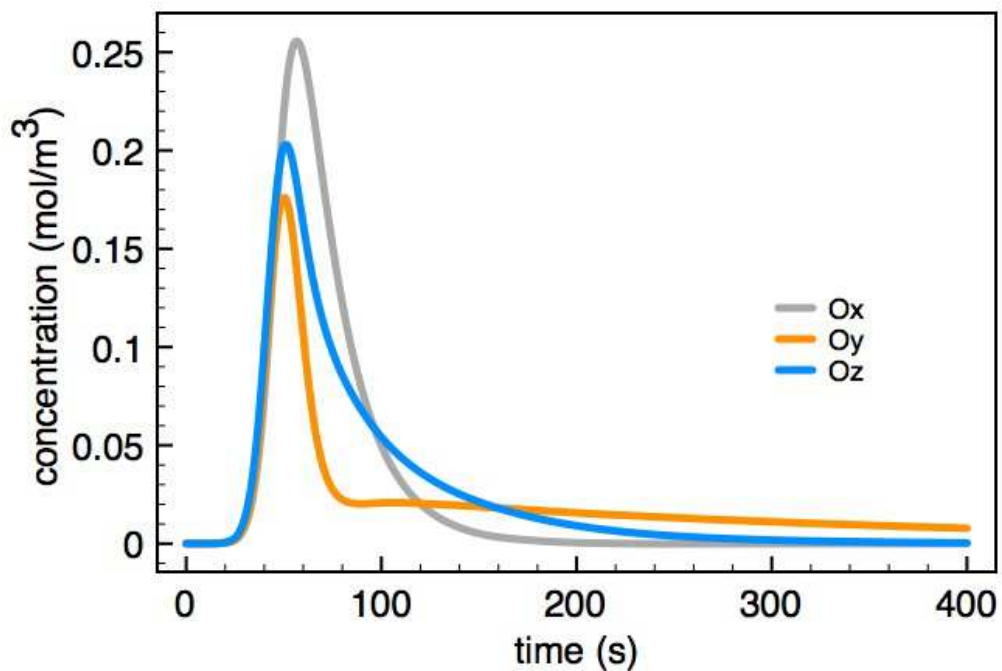
The value  $t_{95}$ , is a measure of the ability of a structure to evacuate water: the faster the water leaves the sample, the better the performance of the structure is. The values, determined integrating the outlet water concentration functions as a function of time, are gathered in table VI.7. In order to be compared, the  $t_{95}$  values are divided by the volume of the corresponding sample:  $8 \times 8 \times 8$  for sample A and  $15 \times 15 \times 15$  for sample B.

**Table VI.6** : Time ( $t_{95}$ ) at which 95% of the water is removed from the membrane.

direction	sample A	sample B
Ox	70 s	112 s
Oy	79 s	660 s
Oz	87 s	195 s



(a)



(b)

**Figure VI.22** : Water concentration at the outlet surface boundary as a function of time for different directions in samples A (a) and B (b).

**Table VI.7** : Values of  $t_{95}$  divided by the sample volume.

direction	sample A	sample B
Ox	0.14	0.03
Oy	0.15	0.20
Oz	0.17	0.06

## VI.6 Discussion

In this chapter it is proposed a method to measure the ability of the central membrane of an IDEAL-Cell to evacuate the water produced. Two samples with different porosity shapes were tested: sample A has smaller pores ( $\simeq 1\mu\text{m}$ ) created using graphite as pore former and sample B that has larger ( $\simeq 15\mu\text{m}$ ) and round-shaped pores for which corn starch was used as pore former. The samples were composite ceramic structures produced by tape casting and sintering. The sintering cycles has been determined for both types of samples in the previous chapters. The tape casting slurry compositions had already been calibrated to relate the porosity estimated by image analysis in the sintered membrane when corn starch was used as pore former. The same calibration was carried out for the slurries for which graphite was used as pore former. Five samples of each type were produced. 3D images of these samples were obtained by X-ray microtomography using the the same experimental conditions that were described in chapter V. Therefore the samples had to be prepared using epoxy resin and then cut to  $300\mu\text{m}\times 300\mu\text{m}$  squared base parallelepipeds.

The 3D images of each sample were extracted using the procedure explained in chapter V. From all the samples analyzed, one of each type, with similar porosity volume were chosen to be compared. Thus, sample A had 40 vol.% of porosity and in sample B that value was 39%. The covariances of each sample were plotted in different directions. The covariances had a finite range for which they reached an asymptotic value. For sample A the maximum covariance range is  $8\mu\text{m}$  and for sample B that range is  $15\mu\text{m}$ . The size of the large round-shaped pores of sample B explain this result.

Water flow in the central membrane was simulated using momentum and mass transfer equations solved by the finite elements method in COMSOL Multiphysics. The model developed describes a situation in which only air flows through the membrane until  $t = 0\text{s}$ . Then water concentration increases in the inlet boundary and is evacuated in a given direction on the opposite surface, the outlet surface boundary. The model assumes some simplifications of the real operating conditions. The IDEAL-Cell operates above water critical temperature, at  $600^\circ\text{C}$ . Thus, at this temperature, water is wether a gas or a supercritical fluid. The diffusion coefficient of water in air,  $D_{H_2O-air}$  at  $600^\circ\text{C}$ , can not be found in the literature. Therefore, it was considered that the system operates at  $300^\circ\text{C}$  and the thermodynamic and physical data necessary for the model were used for this value of temperature. Since at the real operating conditions, water is a gas or a supercritical fluid in which distinct gas and liquid do not exist, it was considered that water condensation does not occur and that the density of the fluid remains constant inside the membrane.

The meshes of the porosity images were obtained using the software Simpleware. The complete 3D images obtained by X-ray microtomography were too large and the calculations on these structures demanded very important computer resources. Therefore, a fraction of the complete porosity volume was extracted in each sample. In order to assure the representativity of the original samples, these volumes respected their covariance range and porosity volume. Thus the volume chosen to represent sample A had 39vol.% of porosity and dimensions of  $8\times 8\times 8\mu\text{m}^3$ . The volume that represents sample B has 42 vol.% of porosity

and dimensions of  $15 \times 15 \times 15 \mu \text{ m}^3$ .

The first step of the calculation is to determine the velocity field inside the membrane. Velocity has the value  $v_0$  in the inlet surface boundary and zero in the fluid layer that is in contact with wall surfaces of the structure. The velocity in each point of the mesh depends on the fluid properties and therefore on the viscous and shear stresses between the fluid layers. The highest velocities are thus obtained for the larger porous paths.

Using the solution obtained in the velocity profile, the evolution of water concentration in each point of the membrane can be determined. Water concentration increases in the inlet surface boundary until it reaches its highest value  $C_0$  at  $t = 40$  s. The concentration determined in each point the membrane depends on the speed and the diffusion coefficient. An average water concentration at the outlet surface boundary was determined as function of time.

The calculation time depends on the density of the mesh. The more elements per  $\mu \text{ m}^3$  exist the longer but more precise the calculation will be. Three different mesh densities were obtained for sample A and it was verified that the results were the same for each of them. Thus, calculations were carried out with a coarse mesh density of 7 elements/ $\mu \text{ m}^3$ . Using this mesh density the velocity profile is obtained in 79 s and the water concentration evolution was determined in 95 s for sample A.

The velocity field and water concentration evolution are determined considering an inlet and an outlet surface boundaries that are opposed to each other according to a given direction. The ability of each sample to evacuate water was determined in three different directions: Ox, Oy and Oz. In order to compare these results it was defined a criteria to measure the water evacuation in the membrane. For each membrane it was defined the time  $t$  for which the water evacuated from the membrane reached 95% of the water inserted in the sample. It was verified that the evacuation of water depends for both samples of the direction in which it occurs. Water is evacuated in between 70 s and 87 s for sample A and in between 112 s and 195 s for sample B. In sample A, the outlet water concentration profile is very similar to the inlet water profile: it reaches its highest value, close to  $C_0$ , and decreases rapidly close to the rate at which it increases. In sample B, water increases rapidly at the the outlet surface until a maximum value smaller than  $C_0$ , as if water was diluted inside the large round pores. After reaching this smaller concentration maxima, water concentration decreases leaving residual water concentration inside the structure. The values of  $t_{95}$  found for sample A are lower than those of sample B because the volume of the first sample is also lower than the volume of the latter. Thus, these results cannot be directly compared. When the values of  $t_{95}$  are divided by the volume of each sample, we realize that the larger pores of sample B allow a faster evacuation of water than the narrow pores of sample A.

These results don't represent exactly what happens in the central membrane because it was considered that the system is at a different temperature, that the density of the fluid is constant and that none of the materials have an hydrophilic behavior. However, they allow to compare the ability of these two structures with different morphology to evacuate water.

## VI.7 Conclusions

A method to quantify the ability of the central membrane of an IDEAL-Cell is proposed in this chapter. The procedure implies the fabrication of the samples by tape casting and sintering, the acquisition of 3D images of the microstructures by X-ray microtomography, meshing those images to obtain a finite element structure using the software Simpleware and solving momentum and mass transfer equations with COMSOL Multiphysics.

Two structures with different morphologies were studied: samples A with smaller pores without a specific shape and sample B with larger round-shaped pores. It was found that, in a

structure of the type of sample B, water is diluted inside the larger pores and evacuated more efficiently. In sample A, water reaches the initial concentration value  $C_0$  inside the structure and it is evacuated with a concentration profile very similar to the inlet concentration. The evacuation efficiency of this type of structure with narrow pores is more dependent of the water concentration at the inlet.

This method relies on the use of representative volumes of the complete samples images and admits certain simplifications of the real operating conditions of IDEAL-Cell. Thus, it can not be considered the an exact representation of the water flow in the central membrane but it allows to compare, in the same conditions, the water evacuation properties of the microstructures obtained.

---

Dans ce chapitre, une méthode par élément fini est présentée pour évaluer l'aptitude de la membrane centrale de la cellule IDEAL-Cell à évacuer l'eau formée. La procédure implique au préalable la fabrication des échantillons par coulage en bande puis frittage, l'acquisition par tomographie RX des images représentatives de la microstructure et le maillage de ces images (en utilisant le logiciel Simpleware) afin d'obtenir une structure par éléments finis pour laquelle les équations de vitesses et de transfert de masse ont été résolues à l'aide de COMSOL Multiphysics. Deux structures de morphologie différentes ont été étudiées : l'une avec de petits pores de forme aléatoire et l'autre accommodant de plus larges pores de forme sphérique. Les résultats montrent que, dans la deuxième structure, l'eau est diluée dans les larges pores et plus aisément évacuée. Cette méthode est fortement dépendante du volume représentatif considéré dans l'image complète du matériau et prend en compte certaines simplifications des conditions réelles de fonctionnement de la cellule.

---



---

## Conclusions – Prospects

---

The growth of energy consumption in the world allowed an important improvement in our life quality in the last decades. However, the continuation of the current trends in energy consumption will have a serious impact in the planet sustainability. One of the possible solutions to produce energy with a low impact for the planet are fuel cells. In this field, research efforts have been focused in the improvement of performances by synthesizing new materials with better electrical or electrocatalytic properties and optimizing shaping methods that allow developing more efficient microstructures.

The work presented in this text is part of an effort of a research consortium that, since 2008, works in the development of a new concept of intermediate temperature fuel cell. As described in the text, this concept consists in reassembling the anode part of a PCFC and the cathode part of a SOFC by means of a porous central membrane wherein water is formed and evacuated.

At Mines ParisTech Materials Center, the activities developed were focused in two aspects: the fabrication of prototypes and the characterization of the central membrane.

## Main results

### Fabrication of prototypes

The first objective of this project was to demonstrate the IDEAL-Cell concept. Our first efforts were dedicated to the fabrication of the prototypes. IDEAL-Cell is a five-layered structure of two porous electrodes, two dense electrolytes and one porous central membrane. The material of each functional layer was chosen for its performances reported in the literature. The proton electrolyte material is  $\text{BaCe}_{0.85}\text{Y}_{0.15}\text{O}_{3-\delta}$  (BCY15) and the oxygen electrolyte chosen is  $\text{Ce}_{0.85}\text{Y}_{0.15}\text{O}_{2-\delta}$  (YDC15). The anode is a NiO-BCY15 composite. For the cathode, different solutions based in  $\text{La}_{0.4}\text{Sr}_{0.6}\text{Co}_{0.2}\text{Fe}_{0.8}\text{O}_{3-\delta}$  (LSCF48) were tested. The central membrane, the innovative step of this concept was a composite of the two electrolyte materials (BCY15 and YDC15) since its function is to allow the conduction and recombination of  $\text{H}^+$  and  $\text{O}^{2-}$  ions. The prototypes were fabricated by tape casting, cold pressing and sintering. Different tape casting slurry compositions were developed for each layer considering the powder morphology and the final microstructure required. Each material was characterized and the sintering behavior was studied in order to determine the appropriate thermal treatments.

The proof of concept (PoC) prototypes were simplified complete cell structures of two dense electrolytes and one porous composite central membrane in which platinum electrodes were coated. This configuration allowed stable performances that were not affected by the electrodes performances. Two types of samples were produced: self supported samples and proton electrolyte supported samples. These prototypes were shaped to allow a qualitative proof of the concept. They respect the four criteria previously stated to prove that this new concept is a fuel cell. The criteria are: (i) a stable open circuit voltage, (ii) a stable polarization curve, (iii) a specific impedance fingerprint for water formation and (iv) detection of water exhausted from the cell as a result of its operation.

Once the concept was demonstrated, the work was focused on the development of the electrodes. A NiO-BCY15 anode was developed by tape casting and sintering. It has an area specific resistance of  $21.1 \Omega \cdot \text{cm}^2$  at  $611^\circ\text{C}$  which is much higher than what is reported in the literature for equivalent anodes. Three different cathodes were developed based on LSCF48. The best performing cathode obtained is a LSCF48-YDC15 composite that has an area specific resistance of  $0.99 \Omega \cdot \text{cm}^2$  at  $594^\circ\text{C}$ .

After developing the proof of concept prototypes and the electrodes separately, all the compartments that compose the IDEAL-Cell has been fabricated using the shaping tools

available. The next logical step was the fabrication of a complete cell. The success of such task depends on the homogeneity of the materials sintering temperature and therefore of its morphology and chemical nature. Producing flat cells with adequate microstructures is particularly difficult due to the fact that each material has a different sintering behavior. The samples successfully produced have at least one support layer that assured the mechanical stability of the structure during sintering. However this keeps such a cell from reaching higher performances. The metal-support approach tried in chapter IV is a promising path to obtain cells with a mechanical support and optimized ceramic layers. However, the high density of the electrolytes, mostly the proton electrolyte, was not achieved and the high temperatures at which the cells were sintered threatened the nickel support chemical and mechanical stability.

### Characterization of the central membrane

The central membrane is the innovative part of the IDEAL-Cell concept. It's a dedicated membrane where water is formed and evacuated. According to the first modeling results, this is the rate-limiting compartment of the cell. Its ability to allow water formation and evacuation keeps a driving force for the cell operation. It was thus important to characterize the microstructures produced by tape casting and sintering.

In order to determine the ability of the membrane to produce water, a method based on 3D images obtained by X-ray microtomography is proposed. The method allows quantifying the active triple phase boundaries, the sites where the electrochemical reaction takes place. In 3D images of the central membrane, each phase (BCY15, YDC15 and porosity) was identified through their different grey level and an appropriate image treatment algorithm. The images have a resolution of  $0.28 \mu\text{m}/\text{pixel}$ , which is in the size range of the powders particles before sintering. The phase segmentation is thus a critical point of this method. Using binary images for each phase and using a notion of percolation, the active triple phase boundaries length was determined. A triple phase length density of  $278 \text{ m}/\text{mm}^3$  was obtained for the sample analyzed.

The ability of the central membrane to evacuate water was studied using 3D images of the porous phase of two different samples. With different pore shapes - large and round or small without particular shape - two samples with the same porous volume were studied. The co-variances of the images were determined in different directions in order to determine representative volume elements of each sample. These images were then meshed and momentum and mass transfer equations were solved using a fluid dynamics simulation software. The results obtained allow concluding that large round-shaped pores allow a faster water evacuation in the central membrane and therefore this type of structure would allow reaching higher performances.

### Prospects

After over three years of work, IDEAL-Cell is no longer in the proof of concept phase. The objective of further activities must be the quantitative improvement of the performances. In order to reach this, the fabrication procedure must be improved and stabilized. The use of tape casting and sintering to produce a complete IDEAL-Cell will require the homogenization of the sintering behavior of the different materials. This can be achieved by changing the powders morphology, by using a sintering aid or by changing the chemical nature of the materials. Decreasing the particle size of the materials may allow decreasing the sintering temperature but reaching a highly dense layer will be more difficult. This kind of compromise must be reached for BCY15. Due to its chemical nature, this is the material that does not allow reaching better microstructures using sintering. The use of a sintering aid or simply

another proton conducting material that has a lower sintering temperature may be necessary to produce complete cells with better performances. In terms of materials performances, further investigations must be done to study the anode. With an area specific resistance of  $21.1 \Omega \cdot \text{cm}^2$ , this anode will soon be the rate-limiting structure of the IDEAL-Cell. This high resistance may be due to the formation of an insulating phase at the BCY15-NiO interfaces during sintering. Lowering the sintering temperature may avoid the reactivity between these two materials.

The method developed to measure the active triple phase boundaries density has the advantage of allowing to analyze representative volumes of samples obtained experimentally. There are not many studies that allowed obtaining this kind of information. When the fabrication procedure of IDEAL-Cell will be stabilized, this method can be used to correlate the microstructures obtained to the electrochemical performances. The method proposed has three drawbacks. The images have to be acquired in a synchrotron. The limited access to such equipment doesn't allow applying this procedure iteratively, in a frequent basis, to optimize the microstructures obtained. The grey level contrast in the images depends on the materials different chemical nature. Therefore, the choice of the materials in a composite layer would be limited by these factors. The last inconvenient of this method is that, even using a powerful equipment such as the synchrotron of the ESRF, the resolution of the images is near to the particle size of the powders used. The quality of the images obtained is highly dependent of the stability of the acquisition.

The study of water evacuation in the central membrane by computational fluid dynamics may also be improved. Further simulations can be done in different volume element sizes in order to verify volumes used are representative of the whole sample. Ideally, permeability experiments should be carried out in similar samples in order to verify the results obtained by simulation.

# Bibliography

- [1] NASA. Nasa astronomy picture of the day web site.
- [2] British Petroleum. Bp statistics: Statistical review of world energy.
- [3] United Nations. United nations data.
- [4] World Bank Group. World bank group.
- [5] IEA. International energy agency.
- [6] NASA. Nasa: Goddard institute for space studies.
- [7] GENI. Global energy network institute.
- [8] A. Kirubakaran, S. Jain, and R.K. Nema. A review in fuel cell technologies and power electronic interface. *Renewable and Sustainable Energy Reviews*, 13:2430–2440, 2009.
- [9] National Energy Technology Laboratory. Fuel cell handbook. Technical report, U.S. Department of Energy, 2004.
- [10] D. Hallyday, R. Resnick, and J. Walker. *Fundamentals of Physics*. 6th edition, 2006.
- [11] W. Grover Coors. Protonic ceramic fuel cells for high-efficiency operation with methane. *Journal of Power Sources*, 118:150–156, 2003.
- [12] H. Iwahara, T. Esaka, H. Uchida, and N. Maeda. Proton conduction in sintered oxides and its application to steam electrolysis for hydrogen production. *Solid State Ionics*, page 359, 1981.
- [13] Project consortium. Ideal-cell: Innovative dual membrane fuel-cell, description of work, proposal n°213389. Technical report, 2007.
- [14] J. Tolchard. Solid: Protons. *Encyclopedia of Electrochemical Power Sources*, pages 188–194, 2009.
- [15] K.D. Kreuer. On the complexity of proton conduction phenomena. *Solid State Ionics*, pages 149–160, 2000.
- [16] Hiroyasu Iwahara. Technological challenges in the application of proton conducting ceramics. *Solid State Ionics*, (289-298), 1995.
- [17] K.S. Knight. Structural phase transitions, oxygen vacancy ordering and protonation in doped  $\text{BaCeO}_3$ : results from time-of-flight neutron powder diffraction investigations. *Solid State Ionics*, 145:275–294, 2001.
- [18] K.D. Kreuer. Aspects of the formation and mobility of protonic charge carriers and the stability of perovskite-type oxides. *Solid State Ionics*, 125:285–302, 1999.

- [19] G. Ma, T. Shimura, and H. Iwahara. Simultaneous doping with  $la^{3+}$  and  $y^{3+}$  for  $ba^{2+}$ – and  $ce^{4+}$ –sites in  $baceo_3$  and ionic conduction. *Solid State Ionics*, 120:51–60, 1999.
- [20] J. Hafsaoui. *Membrane duale de reformage et de filtration pour la production d'hydrogene par reaction de craquage de methane*. PhD thesis, Ecole Nationale Supérieure des Mines de Paris, february 2009.
- [21] E Ivers-Tiffée. Solide: Oxygen ions. *Encyclopedia of Electrochemical Power Sources*, pages 181–187, 2009.
- [22] J.A.Kilner. Fast oxygen transport in acceptor doped oxides. *Solid State Ionics*, 129:13–23, 2000.
- [23] J.A. Kilner and B.C.H. Steele. *Nonstoichiometric Oxides*. Academic Press, 1981.
- [24] J. Faber, C. Geoffrey, A. Roux, A. Sylvestre, and P. Abelard. *Applied Physics*, A49:225, 1989.
- [25] D.Y. Wang, D.S. Park, J. Griffith, and A.S. Nowick. *Solid State Ionics*, 2:95, 1981.
- [26] J.A. Kilner. *Solid State Ionics*, 8:201, 1983.
- [27] V.V. Kharton, F.M.B. Marques, and A. Atkinson. Transport properties of solid electrolyte ceramics: a brief review. *Solid State Ionics*, 174:135–149, 2004.
- [28] Richard E. Mistler and Eric R. Twiname. *Tape Casting - theory and practice*. The American Ceramic Society, 2000.
- [29] R. Costa. *Contribution a la mise en forme d'une pile a combustible du type P.C.F.C*. PhD thesis, Centre des Materiaux, Mines ParisTech, 2009.
- [30] Rodrigo Moreno. The role of slip additives in tape-casting technology: part i - solvents and dispersants. *The American Ceramic Society Bulletin*, 71(10):1521–1530, october 1992.
- [31] A.Sanson, P. Pinasco, and E. Roncari. Influence of pore formers on slurry composition and microstructure of tape cast supporting anodes for sofc. *Journal of the European Ceramic Society*, 28:1221–1226, 2008.
- [32] Loey A. Salam, Richard D. Matthews, and Hugh Robertson. Pyrolysis of polyvinyl butyral (pvb) binder in thermoelectric green tapes. *Journal of European Ceramic Society*, 20:1375–1383, 2000.
- [33] C. Gabrielli. Identification of electrochemical processes by frequency response. Technical report, Solartron, 1980.
- [34] Z. Stoynov and D. Vladikova. *Differential Impedance Analysis*. Marin Drinov Academic Publishing House, 2005.
- [35] I. Epelboin, M. Keddam, O.R. Mattos, and H. Takenouti. The dissolution and passivation of fe and fe-cr alloys in acidified sulphate medium: influences of ph and cr content. *Corrosion Science*, 19:1105–1112, 1979.
- [36] Z. Stoynov, D. Vladikova, G. Raikova, A.S. Thorel, A. Chesnaud, J. Abreu, M. Viviani, A. Barbucci, S. Presto, and P. Carpanese. Impedance spectroscopy studies of dual membrane fuel cell. *Journal of Electrochemical Acta*, 2011.

- [37] J.W. Gibbs. *Thermodynamische Studien*. 1986.
- [38] Milan Zunic, Laure Chevalier, Aleksandar Radojkovic, Goran Brankovic, Zorica Brankovic, and Elisabetta Di Bartolomeo. Influence of the ration between ni and bace<sub>0.9y0.1</sub>O<sub>3-δ</sub> on microstructural and electrical properties of proton conducting ni-bace<sub>0.9y0.1</sub>O<sub>3-δ</sub> anodes. *Journal of Alloys and Compounds*, 509:1157–1162, 2011.
- [39] W.Z. Zhu and S.C. Deevi. A review on the status of anode materials for solide oxide fuel cells. *Materials Science and Engineering*, A362:228–239, 2003.
- [40] R.J. Gorte, J.M. Vohs, and S. McIntosh. Recent developments on anodes for direct fuel utilization in sofc. *Solid State Ionics*, 175:1–6, 2004.
- [41] M.-L. Fontaine, Y. Larring, R. Haugrud, T. Norby, K. Wiik, and R. Bredesen. Novel high temperature proton conducting fuel cells: Production of la<sub>0.995</sub>sr<sub>0.005</sub>nbo<sub>4-δ</sub> electrolyte thin films and compatible cathode architectures. *Journal of Power Sources*, 188:106–113, 2009.
- [42] G.C. Mather, F.M. Figueiredo, D.P. fag, T. Norby, J.R. Jurado, and J.R. Frade. Synthesis and characterisation of ni-srce<sub>0.9yb0.1</sub>O<sub>3-δ</sub> cermet anodes for protonic ceramic fuel cells. *Solid State Ionics*, 158:333–342, 2003.
- [43] Jan Rossmeisl and Wolfgang G. Bessler. Trends in catalytic activity for sofc anode materials. *Solid State Ionics*, 178:1694–1700, 2008.
- [44] A. Bieberle and L.J. Gauckler. *Solid State Ionics*, 146:23, 2002.
- [45] R.M.C. Clemmer and S.F. Corbin. Influence of porous composite microstructure on the processing and properties of solid oxide fuel cell anodes. *Solid State Ionics*, 166:251–259, 2004.
- [46] S.K. Pratihari, R.N. Basu, S. Mazumder, and H.S. Maiti. In M. Dokyia (Eds.) S.C Singhal, editor, *Proceeding of the Sixth International Symposium on Solid Oxide Fuel Cells (SOFC-VI)*, volume 17-22, page 513, 1999.
- [47] Swadesh K. Pratihari, A. Das Sharma, R.N. Basu, and H.S. Maiti. Preparation of nickel coated ysz powder for application as an anode for solid oxide fuel cells. *Journal of Power Sources*, 129:138–142, 2004.
- [48] T.H. Lee, S.E. Dorris, and U. Balachandran. Thin film preparation and hydrogen pumping characteristics. *Solid State Ionics*, 176:1479–1484, 2005.
- [49] Stephen J. Skinner. Recent advances in perovskite-type materials for sofc cathodes. *Fuel Cells Bull.*, 3:113–121, 2001.
- [50] E. Maguire, B. Gharbage, F.M.B. Marques, and J. A. Larincha. Cathode materials for intermediate temperature sofc. *Solid State Ionics*, 127:329–335, 2000.
- [51] M. Godickemeyer, K. Sasaki, L.J. Gauckler, and I. Reiss. *Solid State Ionics*, 86-88:691–701, 1996.
- [52] M. Mogensen, T. Lindegaard, and U.R. Hansen. *Journal of Electrochemical Society*, 41:2122, 1994.
- [53] L.M. Navarro, F.M.B. Marques, and J.R. Frade. *Journal of Electrochemical Society*, 144:267, 1997.

- [54] H. Inaba and H. Tagawa. *Solid State Ionics*, 83:1, 1996.
- [55] L.-W. Tai, M.M. Nasrallah, H.U. Anderson, D.M. Sparlin, and S.R. Sehlin. Structure and electrical properties of  $\text{La}_{1-x}\text{Sr}_x\text{Co}_{1-y}\text{Fe}_y\text{O}_3$ . part 1. the system  $\text{La}_{0.8}\text{Sr}_{0.2}\text{Co}_{1-y}\text{Fe}_y\text{O}_3$ . *Solid State Ionics*, 76:259–271, 1995.
- [56] L.-W. Tai, M.M. Nasrallah H.U. Anderson, D.M. Sparlin, and S.R. Sehlin. Structure and electrical properties of  $\text{La}_{1-x}\text{Sr}_x\text{Co}_{1-y}\text{Fe}_y\text{O}_3$ . part 1. the system  $\text{La}_{1-x}\text{Sr}_x\text{Co}_{0.2}\text{Fe}_{0.8}\text{O}_3$ . *Solid State Ionics*, 76:273–283, 1995.
- [57] F. Tietz, V.A.C. Haanappel, A. Mai, J. Mertens, and D. Stover. Performance of lscf cathodes in cell tests. *Journal of Power Sources*, 156:20–22, 2006.
- [58] M.C. Tucker. Progress in metal-supported solid oxide fuel cells: A review. *Journal of Power Sources*, 195:4570–4582, 2010.
- [59] A. Momma, Y. Kaga, T. Okuo, K. Fujii, K. Hohjyo, and M. Kanazawa. *Bull. Electrochem. Lab*, 63:103–113, 1999.
- [60] A. Mineshige, K. Fukushima, S. Okada, T. Kikuchi, M. Kobune, T. Yazawa, K. Kikuchi, M. Inaba, and Z. Ogumi. *Electrochem. Solid State Letter*, 9:427–429, 2006.
- [61] C. Hwang, C.-H. Tsai, C.-H. Lo, and C.-H. Sun. *Journal of Power Sources*, 180:132–142, 2008.
- [62] T. Ishihara, J. Yan, M. Enoki, S. Okada, and H. Matsumoto. *Journal of Fuel Cell Science Technology*, pages 031205–1–031205–3, 2008.
- [63] Y.W. Ju, H. Eto, T. Inagaki, and T. Ishihara. In *ECS Transactions*, volume 2, pages 719–726, 2009.
- [64] J. Yan, M. Enoki, H. Matsumoto, and T. Ishihara. *Electrochimica Acta*, 52(1645-1650), 2006.
- [65] T. Ishihara, J. Yan, M. Shinagawa, and H. Matsumoto. *Electrochimica Acta*, 52:1645–1650, 2006.
- [66] P. Bance, N.P. Brandon, B. Girvan, P. Holbeche, S. O’Dea, and B.C.H. Steele. *Journal of Power Sources*, 131:86–90, 2004.
- [67] H.C. Park and A.V. Virkar. *Journal of Power Sources*, 186:133–137, 2009.
- [68] P. Szabo, J. Arnold, T. Franco M. Gindrat, A. Refke, A. Zagst, and A. Ansar. In *ECS Transactions*, volume 25, pages 175–185, 2009.
- [69] N. Minh and T. Takahashi. *Science and Technology of Ceramic Fuel Cells*. Elsevier, 1995.
- [70] T. Ou, F. Delloro, C. Nicolella, W. G. Bessler, and A. Thorel. Mathematical model of mass and charge transport and reaction in the central membrane of the ideal-cell. In *ECS Transactions*, volume 25, pages 1295–1304, 2009.
- [71] Xiaohua Deng and Anthony Petric. Geometrical modeling of the triple-phase boundary in solid oxide fuel cells. *Journal of Power Sources*, 140:297–303, 2005.

- [72] J.R. Wilson, W. Kobsiriphat, R. Mendonza, H.-Y. Chen, J.M. Hiller, D.J. Miller, K. Thornton, P.W. Voorhees, S.B. Adler, and S.A. Barnett. Three-dimensional reconstruction of a solid-oxid fuel-cell anode. *Nature Materials*, 5:541–544, 2006.
- [73] Ben Kenney, Mikelis Valdmanis, Craig Baker, J.G. Pharoah, and Kunal Karan. Computation of tpb length, surface area and pore size from numerical reconstruction of composite solid oxide fuel cell electrodes. *Journal of Power Sources*, 189:1051–1059, 2009.
- [74] NIST. X-ray absorption coefficients data, <http://physics.nist.gov/physrefdata/xraymasscoef/chap2.htm>
- [75] X-ray interaction, <http://www.ndt-ed.org/educationresources/communitycollege/radiography/physics>
- [76] ESRF. E.s.r.f. web site.
- [77] Avinash C. Kak and Malcolm Slaney. *Principles of Computerized Tomographic Imaging*. IEEE Press, 1988.
- [78] Princeton. Phase contrast imaging technique, <http://www.princetoninstruments.com>.
- [79] T.W. Ridler and S. Calvard. Picture thresholding using an iterative selection method. In *IEEE Transactions on systems*, volume 8, pages 630–632, 1978.
- [80] Pacific Wiki. Imagej 3d package.
- [81] NIST. X-ray mass interaction, <http://www.nist.gov/pml/data/xraycoef/index.cfm>.
- [82] C. Peyrega. *Prediction des proprietes acoustiques de materiaux fibreux heterogenes a partir de leur microstructure 3D*. PhD thesis, Ecole Nationale Supérieure des Mines de Paris, 2010.
- [83] Frank P. Incropera and David P. Dewitt. *Fundamentals of Heat and Mass Transfer*. Wiley Higher Education, 5<sup>th</sup> edition, 2001.
- [84] H. Schlichting. *Boundary Layer Theory*. ed. Mc-Graw-Hill, 7<sup>th</sup> edition, 1979.
- [85] Comsol. *Comsol Multiphysics: Model Library*. Comsol, 2005.
- [86] W.G. Bessler, J. Warnatz, and D.G. Goodwin. *Solid State Ionics*, 177:3371, 2007.
- [87] J.P.P. Huijsmans. Ceramics in solid oxide fuel cells. *Current Opinion Solid State and Materials Science*, 5:317–323, 2001.
- [88] F. Tietz, H.-P. Buchkremer, and D. Stover. Components manufacturing for solid oxide fuel cells. *Solid State Ionics*, 152-153:373–381, 2002.
- [89] W. Munch, K.D. Kreuer, G. Seifert, and J. Maier. Proton diffusion in perovskites: comparison between  $\text{BaCeO}_3$ ,  $\text{BaZrO}_3$ ,  $\text{SrTiO}_3$  and  $\text{CaTiO}_3$  using quantum molecular dynamics. *Solid State Ionics*, pages 183–189, 2000.
- [90] Research Services Branch. Imagej: User guide.
- [91] G. Schiller, R.H. Henne, M. Lang, R. Ruckdaschel, and S. Scharper. *Fuel Cells Bull.*, 3:7–12, 2000.
- [92] A.S. Thorel, A. Chesnaud, M. Viviani, A. Barbucci, S. Presto, P. Piccardo, Z. Ilhan, D. Vladikova, and Z. Stoyanov. Ideal-cell, a high temperature innovative dual membrane fuel-cell. In *ECS Transactions*, 2010.

- [93] Project consortium. Ideal-cell project: Periodic consortium report y2. Technical report, 2010.
- [94] Q.-U. Huang, R. Hui, B. Wang, and J. Zhang. A review of ac impedance modeling and validation in sofc diagnosis. *Electrochimica Acta*, 52:8144–8164, 2007.
- [95] K.D. Kreuer, E. Schonherr, and J. Maier. Proton and oxygen diffusion in baceo<sub>3</sub>-based compounds: a combined thermal gravimetric analysis and conductivity study. *Solid State Ionics*, 70-71:278–284, 1994.
- [96] S.P.S. Badwal and K. Foger. Solid oxide electrolyte fuel cell review. *Ceramics International*, 22:257–265, 1996.
- [97] H.-J. Neef. International overview of hydrogen and fuel cell research. *Energy*, 34:327–333, 2009.
- [98] A. Boudghene Stambouli and E. Traversa. Solid oxide fuel cells (sofcs): a review of an environmentally clean and efficient source of energy. *Renewable and Sustainable Energy Reviews*, 6:433–455, 2002.
- [99] J.M. Andujar and F. Segura. Fuel cells: history and updating. a walk along two centuries. *Renewable and Sustainable Energy Reviews*, 13:2309–2322, 2009.
- [100] A. Demin and P. Tsiakaras. Thermodynamic analysis of a hydrogen fed solid oxide fuel cell based on a proton conductor. *International Journal of Hydrogen Energy*, pages 1103–1108, 2001.
- [101] USDOE. United states of america, department of energy, October 2010.
- [102] UNESCO. Unesco: Institut for statistics.
- [103] W.F.Smith. *Principles of Materials Science and Engineering*. mcGraw-Hill, second edition, 1990.
- [104] Rodrigo Moreno. The role of slip additives in tape-casting technology: part ii - binders and plasticizers. *The American Ceramic Society Bulletin*, 71(11):1647–1656, october 1992.
- [105] R. Gerhard-Anderson and A.S. Nowick. *Solid State Ionics*, 5:547, 1981.
- [106] J.P.P. Huijsmans. Ceramics in solid oxide fuel cells. *Current Opinion Solid State & Materials Science*, 5:317–323, 2001.
- [107] K.D. Kreuer. On the development of proton conducting materials for technological applications. *Solid State Ionics*, 97:1–15, 1997.
- [108] H. Iwahara, T. Esaka, H. Uchida, and N. Maeda. *Solid State Ionics*, (359), 1981.

## Appendix I : Electrochemical impedancy spectroscopy obtained for the anode

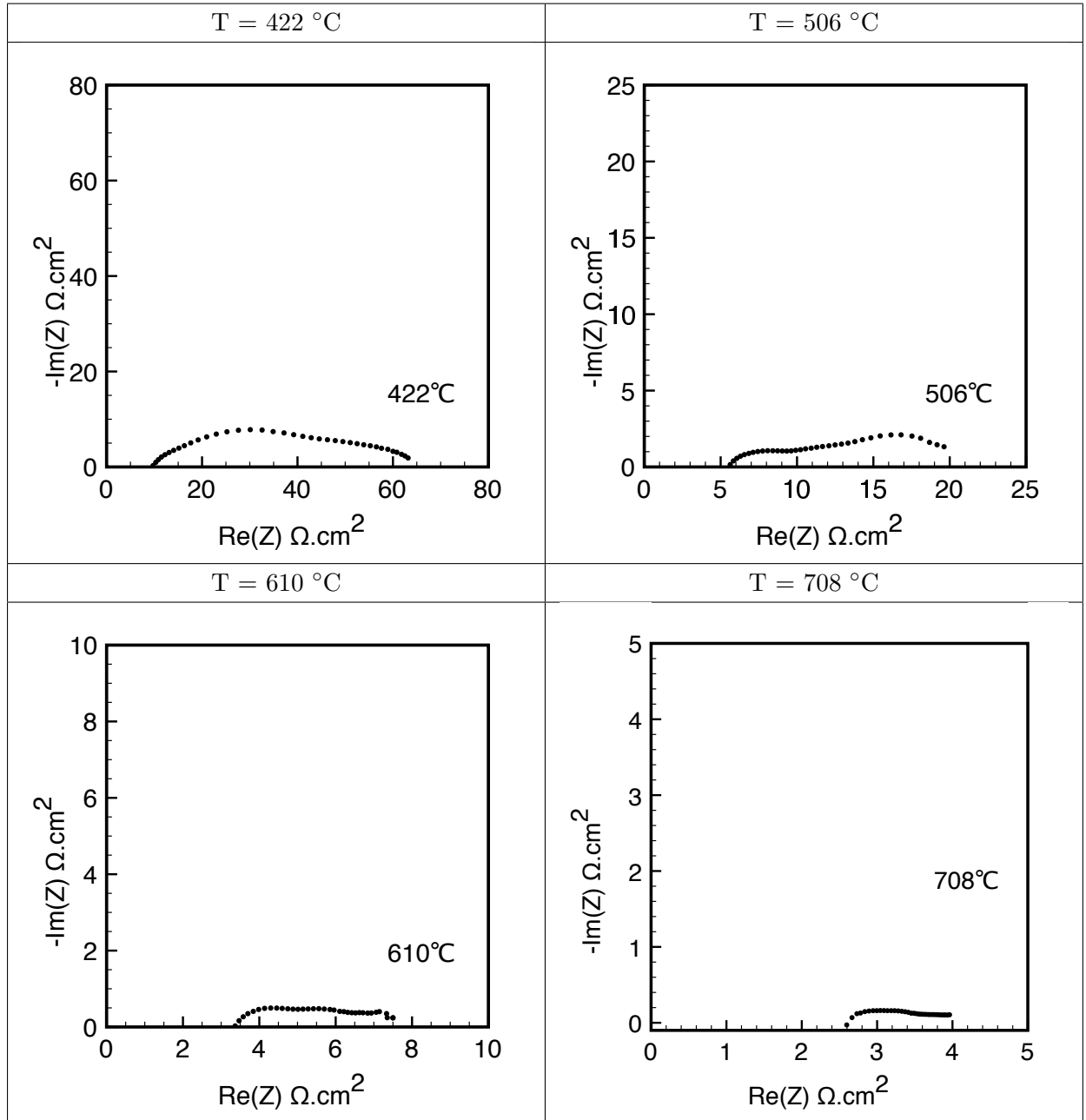


**Figure VI.23** : Nyquist plots obtained for the NiO -  $\text{BaCe}_{0.85}\text{Y}_{0.15}\text{O}_{3-\delta}$  at different temperatures.

## Appendix II : Electrochemical impedancy spectroscopy obtained for the cathodes developed

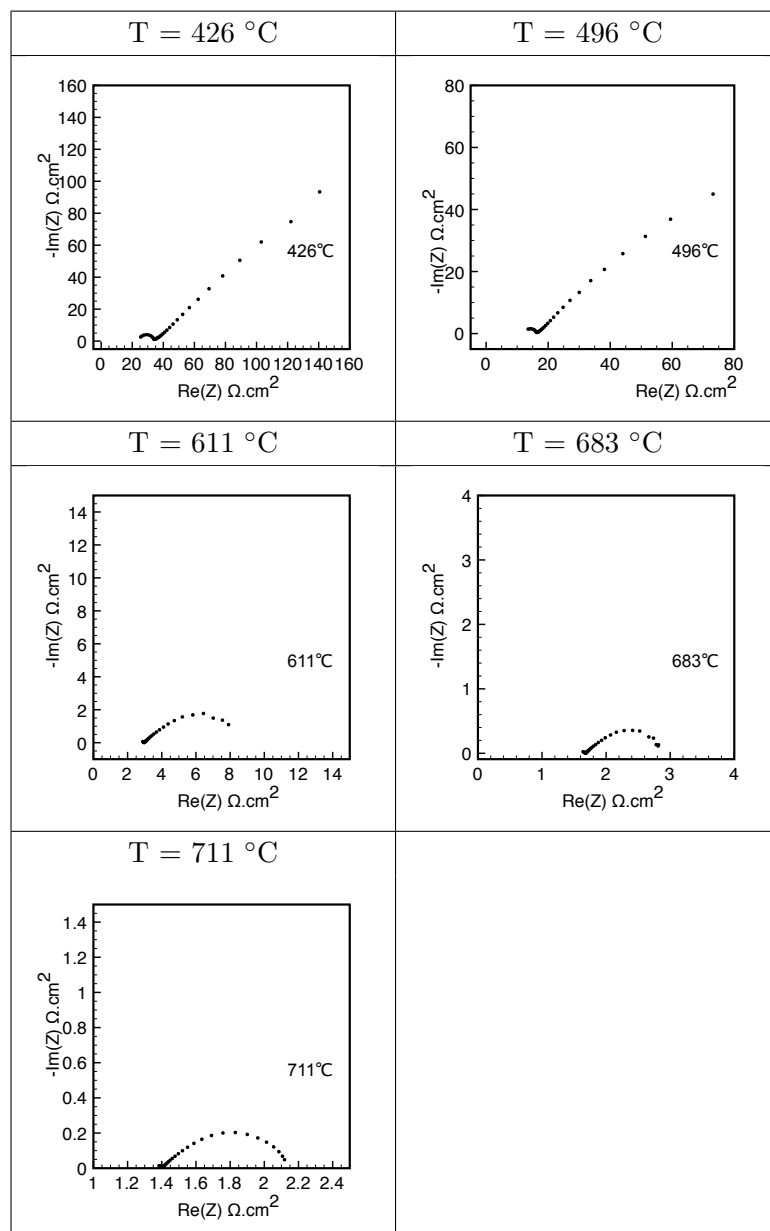


**Figure VI.24** : Nyquist plots obtained for the  $\text{La}_{0.40}\text{Sr}_{0.60}\text{Co}_{0.20}\text{Fe}_{0.80}\text{O}_{3-\delta}$  cathode at different temperatures.

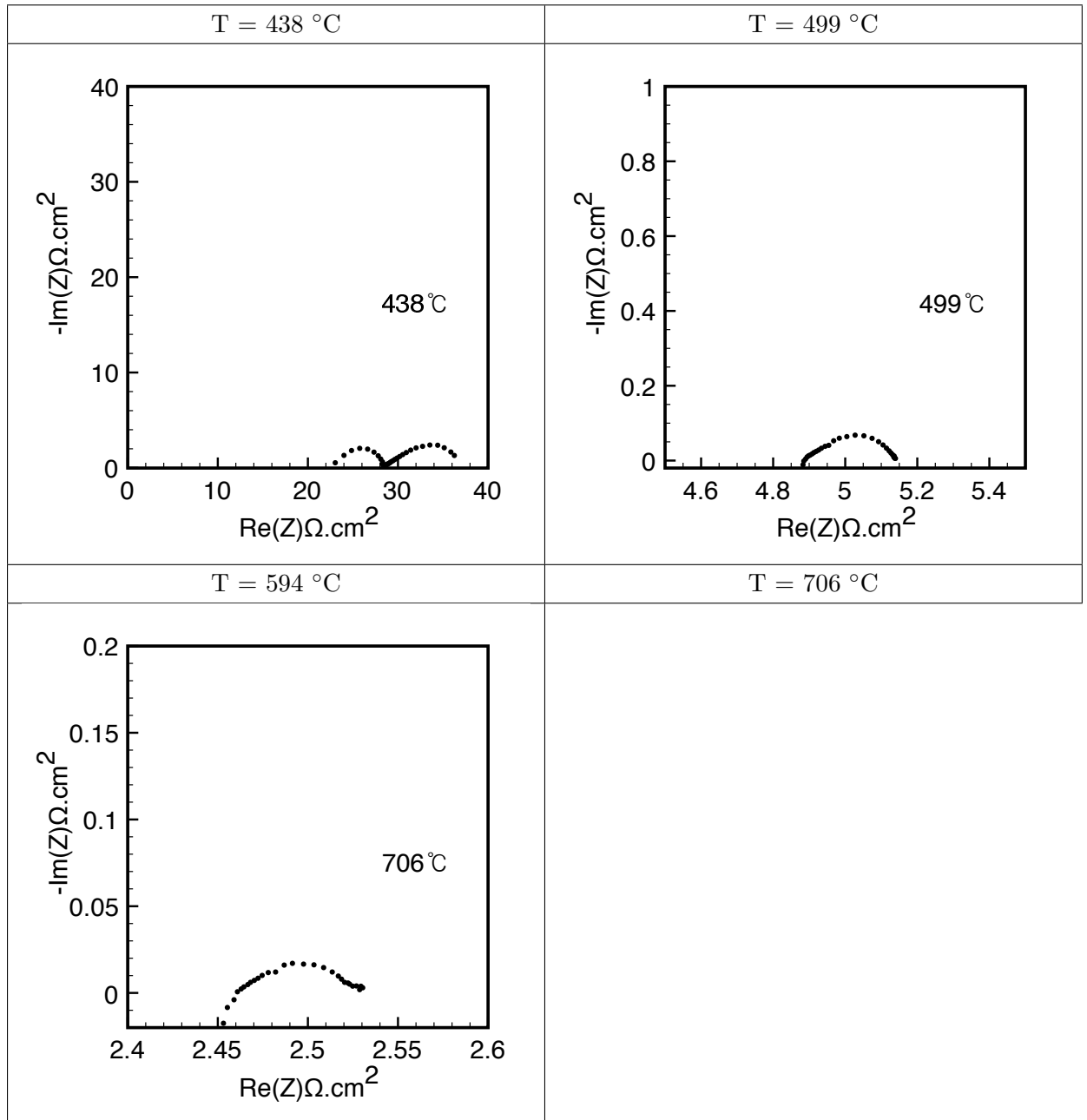


**Figure VI.25** : Nyquist plots obtained for the  $\text{Ce}_{0.85}\text{Y}_{0.15}\text{O}_{2-\delta}/\text{La}_{0.40}\text{Sr}_{0.60}\text{Co}_{0.20}\text{Fe}_{0.80}\text{O}_{3-\delta}$  at different temperatures.

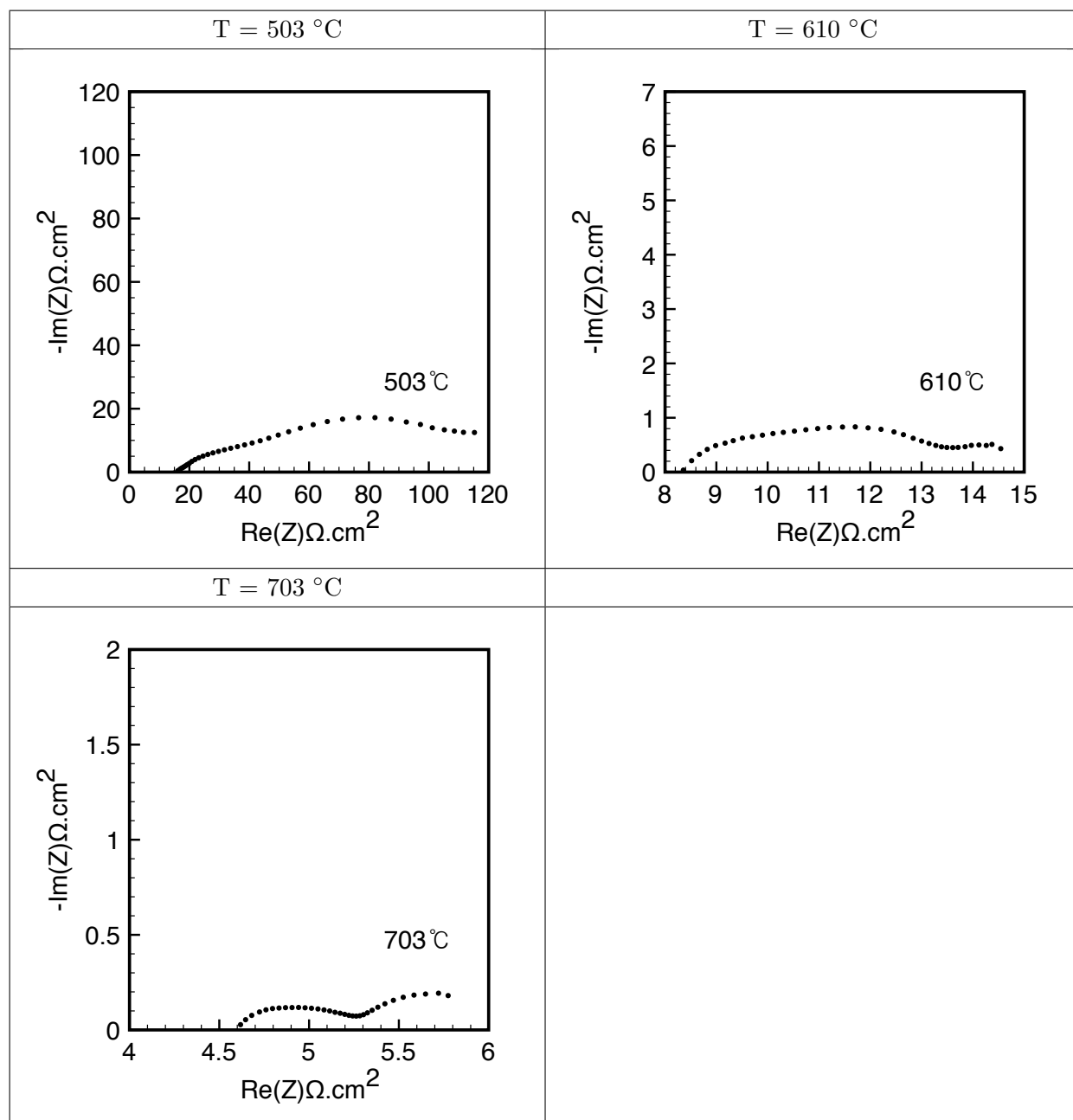


**Figure VI.26** : Nyquist plots obtained for the  $\text{BaCe}_{0.85}\text{Y}_{0.15}\text{O}_{3-\delta}/\text{La}_{0.40}\text{Sr}_{0.60}\text{Co}_{0.20}\text{Fe}_{0.80}\text{O}_{3-\delta}$  at different temperatures.

## Contribution au développement d'IDEAL-Cell, un nouveau concept de pile à combustible à température intermédiaire

**Résumé :** Une pile à combustible est un système électrochimique (générateur d'énergie) qui permet la conversion directe et en continu, de l'énergie chimique libérée lors d'une réaction d'oxydation d'un combustible, en électricité et en chaleur, et ce avec un très faible (voire aucun) impact sur l'environnement.

Diverses stratégies ont été envisagées pour améliorer la performance de ces dispositifs parmi lesquelles l'intégration de matériaux architecturés innovants présentant une formulation chimique et une microstructure propices à l'obtention de meilleures propriétés électrique ou électro catalytique. Une autre voie permettant d'atteindre le même objectif est ce à quoi aspire ce travail en proposant le développement d'un concept de pile à combustible fonctionnant à température intermédiaire. Ce nouveau concept se base sur la jonction de la partie anodique d'une PCFC avec la partie cathodique d'une SOFC, par l'intermédiaire d'une membrane centrale dans laquelle l'eau est formée puis évacuée. Les activités dans le cadre de cette thèse se sont orientées vers la fabrication de prototypes, pour la preuve du concept, et la caractérisation de la membrane centrale.

Les prototypes pour la preuve du concept sont des assemblages multicouches simplifiés par rapport à la cellule complète, pour lesquels les deux électrodes ont été substituées par un dépôt de platine. Ces premiers modèles ont été testés et les résultats montrent qu'ils se comportent comme une pile à combustible, en respectant 4 critères prédéfinis : (i) une tension en circuit ouvert (OCV) stable, (ii) une courbe de polarisation stable, (iii) une signature sur les spectres d'impédance complexe typique de la formation d'eau et (iv) une mesure et quantification de l'eau évacuée en fonction du courant traversant la cellule.

L'aptitude de la membrane centrale à former et évacuer l'eau a été évaluée par analyse quantitative de la longueur de ces sites réactionnels actifs. La méthode proposée est basée sur l'analyse des images 3D de la membrane centrale, enregistrées par microtomographie X. L'écoulement de l'eau à travers la structure poreuse de la membrane a été étudié. Pour cela, les images 3D de deux microstructures distinctes ont été utilisées pour résoudre les équations de la vitesse d'écoulement et de transfert de masse par la méthode des éléments finis.

**Mots clés :** IDEAL-Cell, coulage en bande, frittage, microtomographie à rayons X.

## Contribution to the development IDEAL-Cell, a new concept of intermediate temperature fuel cell

**Abstract:** Fuel cells are electrochemical devices that allow the conversion of chemical energy directly into electric energy with low impact to the environment.

The improvement of fuel cell performances has been done through the synthesis of new materials with better electrical or electrocatalytic properties and the optimization of shaping methods that allow developing more efficient microstructures.

A third path to reach the same objective is proposed in the work here presented: the development of IDEAL-Cell, a new concept of intermediate fuel cell. This concept consists in the anode part of a PCFC connected to the cathode part of a SOFC through a porous central membrane in which water is formed and evacuated. The activities developed were focused in two aspects: the fabrication of prototypes and the characterization of the central membrane.

The proof of concept (PoC) prototypes were simplified complete cell structures of two dense electrolytes and one porous composite central membrane in which platinum electrodes were coated. They respect the four criteria previously defined as necessary to demonstrate the new concept : (i) a stable open circuit voltage, (ii) a stable polarization curve, (iii) a specific impedance fingerprint for water formation and (iv) detection of water exhausted from the cell as a result of its operation.

The ability of the central membrane to allow the formation of water is determined by the measurement of the active reaction sites length. The method proposed is based on the analysis of 3D images of the central membrane obtained by X-ray microtomography. The water flow through the porous structure of the central membrane was studied. 3D images of two different types of structures were used to solve momentum and mass transfer equations through the finite element method.

**Keywords:** IDEAL-Cell, tape casting, sintering, X-ray microtomography.